JOURNAL OF

METALS

IN TWO SECTIONS—SECTION 1

September 1955

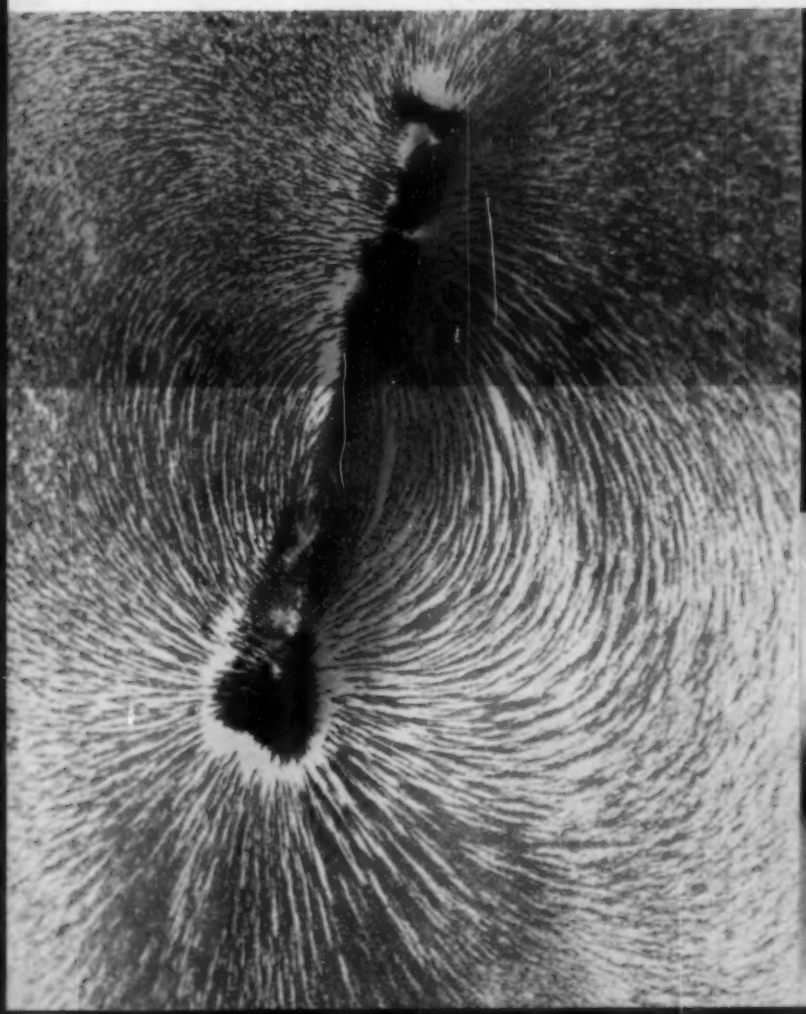

PRODUCTS that are improving the efficiency and speeding production in American industry

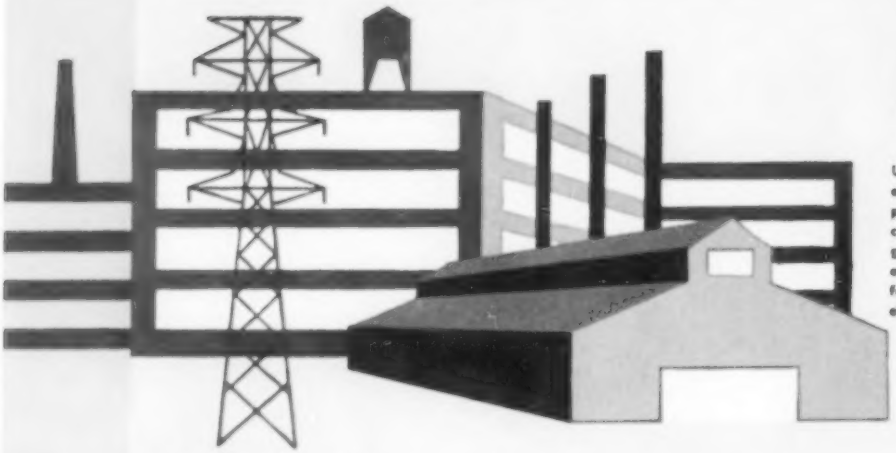

USG® Brushes are available in production or replacement lots in carbon, carbon-graphite, electrographitic, pure graphite and metalgraphite grades for all types of rotating electrical equipment.

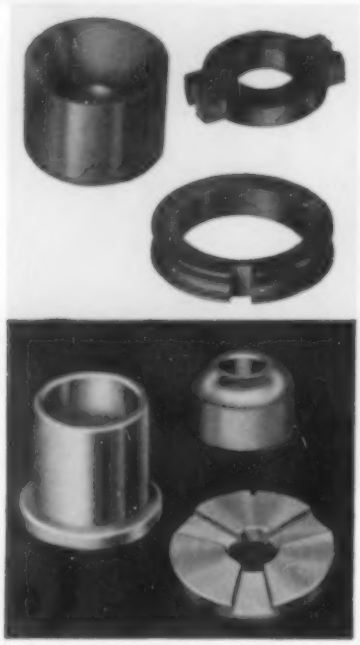

GRAPHITAR® (carbon-graphite) is a versatile engineering material of carbon-graphite composition offered in many grades for bearings, seals, piston rings, pump vanes, thrust washers, valve seats, pistons, bushings.

Metallurgical graphite grades for carbon control in iron and steel melting, mold coatings, hot topping compounds, Cordip®, Mexaloy® for refractory mixtures and other MEXICAN® products.

GRAMIX®: Sintered-metal bearings, gears, cams, slides, rollers, bushings and machine parts available in ferrous and non-ferrous alloys. The metal with the built-in lubrication.

206

OUR 101ST YEAR

THE UNITED STATES GRAPHITE COMPANY

DIVISION OF THE WICKES CORPORATION • SAGINAW, MICHIGAN

JOURNAL OF

METALS

Published to provide a continuing, authoritative, and up-to-date record of technological, engineering, and economic progress in all branches of the metals industry by the
Metals Branch
American Institute of Mining and Metallurgical Engineers, Inc.
29 West 39th Street, New York 18

• • •

ALVIN S. COHAN
Manager of Publications
Editor, JOURNAL OF METALS

EDWIN M. WEISS
Associate Editor

• • •

M. SNEDEKER G. M. ZILL
Assistant Editors

GRACE PUGSLEY Production Manager
W. J. SEWING Asst. Prod. Mgr.

• • •

METALS BRANCH COUNCIL

J. H. Scaff Chairman
J. S. Smart, Jr. IMD Chairman
A. W. Thornton ISD Chairman
A. W. Schlechten EMD Chairman
P. T. Stroup M. E. Volin
J. S. Marsh D. S. Eppelsheimer

EDITORIAL ADVISORY COMMITTEE

J. S. Smart, Jr. Chairman
W. A. Dean Evan Just
J. C. Kinnear, Jr. John Marsh
T. D. Jones M. Tenenbaum

TECHNICAL PUBLICATIONS COMMITTEES

Robert Aborn AIME Chairman
M. A. Jones ISD Chairman
S. J. Dickinson EMD Chairman
W. R. Hibbard, Jr. IMD Chairman
E. J. Kennedy, Jr. Secretary

• • •

WARREN V. SMITH
Eastern Advertising Manager

BOB WILSON
Western Advertising Manager
84 E. Randolph St., Chicago

• • •

The AIME Publishes:
Journal of Metals
Mining Engineering
Journal of Petroleum Technology

VOL. 7, NO. 9 SEPTEMBER, 1955

COVER

Magnets, domains, and their force through space inspired the cover by Harry Brocke this month. For more on this subject turn to page 948.

NEWS

Books for Engineers	928	Drift of Things	940
Industrial Notes	930	Reporter	943
Coming Events	930	IMD Fall Meeting Program	977
Employment Service	932	AIME News	980
Trends	938	Personals	982

TECHNICAL FEATURES

Iron and Steel Produced From Pyrrhotite Tailings Opens Up Potential Market — B. G. Hunt, A. Turner — 944

Domain Structures Suggest Key to Enigma of Magnetic Force — C. D. Graham, Jr. — 948

Sound Uranium Ingots Cast Using Consumable Electrode Arc-Melting — F. R. Lorenz, W. J. Hurford — 952

Ore Blending at Shipping Dock Insures Uniform Blast Furnace Burden — M. W. Griswold — 956

Analytical Control of Bessemer Blow Reported Possible With New Techniques — 960

TRANSACTIONS

Temperature Gradient Zone Melting — W. G. Pfann — 961

Phase Equilibria in the System FeO-Fe_2O_3-SiO_2 — A. Muan — 965

This issue of JOURNAL OF METALS is in two Sections:
Section 1—Magazine Section 2—Transactions Section

Published the first day of each month by the American Institute of Mining and Metallurgical Engineers, Inc., 29 West 39th Street, New York 18, N. Y. Telephone: PEnnsylvania 6-9220. Subscription $8 per year for non-AIME members in United States and North, South and Central America; $10, foreign; $6 for AIME members, or $4 additional in combination with a subscription to "Mining Engineering" or "Journal of Petroleum Technology." Single copies, 75 cents; single copies foreign, $1.00; special issues, $1.50 . . . The AIME is not responsible for any statement made or opinion expressed in its publications . . . Copyright 1955 by the American Institute of Mining and Metallurgical Engineers, Inc. . . . Registered cable address, AIME New York . . . Indexed in Engineering Index, Industrial Arts Index and Chemical Abstracts . . . Reentered as second-class matter Sept. 21, 1949, at the post office at New York, N. Y., under the Act of March 3, 1879. Additional entry established at Manchester, N. H.

Books for Engineers

ORDER YOUR BOOKS THROUGH AIME—Address Irene K. Sharp, Book Department. Ten per cent discount given whenever possible. Order Government publications direct from the agency concerned.

How to Train Engineers in Industry (Executive Research Survey No. 4), *National Society of Professional Engineers*, $2.00, 72 pp., 1955—An analysis of the experience of more than 200 companies and the opinions of many individual leaders in the training field. It covers, among other things, typical training programs, how to train the trainers, and guidance toward professionalism.

Solar Energy Research, edited by Farrington Daniels and John A. Duffie, *University of Wisconsin Press*, $4.00, 290 pp., 1955—Based in part on a symposium held at the University of Wisconsin in 1953, this volume includes reports by 31 contributors on the present status of the utilization of solar energy. Space heating, power plants, large scale furnaces, and a wide range of other uses of solar energy are discussed in the 11 sections into which the book is divided. A bibliography is included.

Metals Reference Book, by Colin J. Smithells, 2 vols., *Interscience Publishers Inc.*, $25.00, 1955—A convenient and comprehensive summary of a wide range of physical, mechanical, and electrical data relating to metallurgy and metal physics. In this new edition, new values have been substituted where more recent and reliable information has become available, several sections have been added covering elastic properties and damping capacity, physical properties of molten salts, and friction. Presentation is largely in tabular form, with brief monographs included where information could not otherwise be adequately given.

Progress in Low Temperature Physics, by C. J. Gorter, Vol. 1, *Interscience Publishers Inc.*, $8.75, 418 pp., 1955—Eighteen papers by research specialists present concise surveys of various aspects of the three main fields involved—magnetism, properties of liquid helium, and superconductivity. In addition such allied topics as the electronic specific heat in metals, velocity and absorption of sound in condensed gases, and transport phenomena in gases are presented. There is a combined subject index and the author index covers the extensive bibliographies.

The Metal Beryllium, edited by D. W. White, Jr. and J. E. Burke, *American Society for Metals*, $8.00, 703 pp, 1955—Owing to the increasing interest in beryllium a group of ASM conference papers together with some additional material has been edited to provide an overall reference book on the subject. The several chapters deal with the importance of beryllium, its ores, reduction of the ores, fabrication of the metal, properties, metallography, corrosion, alloys and cermets, health hazards, chemistry, and the special problem of brittleness of the metal. Each chapter includes a bibliography.

Brazing Manual, by Committee on Brazing and Soldering, American Welding Society, *Reinhold Publishing Corp.*, $4.75, 193 pp., 1955—This book makes available a compilation of all the technical information on the eight brazing processes. Complete information is given on each of these: torch brazing, twin-carbon brazing, furnace brazing, induction brazing, resistance brazing, block brazing, and flow brazing. An appendix in chart form lists properties of brazeable metals and alloys, and for the first time brazing fluxes and atmospheres are standardized into types according to their compositions and uses.

Industrial and Manufacturing Chemistry, 3 vols., *Philosophical Library Inc.*, $50.00, 1955. **Part I, Organic**, by G. Martin, sixth edition, revised by E. I. Cooke, 752 pp. **Part II,** (vol. 1, 600 pp., vol. 2, 491 pp.) **Inorganic,** by G. Martin, sixth edition, revised by W. Francis — Volumes embrace both American and British practice and cover the whole range of subjects with which the industrial chemist and manufacturer is concerned. This work is intended to meet the requirements of all businessmen interested in chemical processes, of manufacturers, consulting chemists, patent workers, technical lawyers, and fire insurance inspectors. Much of the information is published in book form for the first time, and many of the descriptions of new processes and modern plants were privately obtained through the courtesy of industrial chemists and of leading firms in Europe and America. Statistics are a feature of the book as well as a comprehensive index.

Bibliographic Survey of Corrosion, 1950 to 1951, *National Assn. of Corrosion Engineers*, $12.50 (members $10.00), 435 pp., 1955—This compilation of 4454 abstracts is the fourth in a series covering 1945 to 1951. As in previous volumes, the abstracts are arranged by specific subdivisions under the eight main groups of the NACE filing system: general, testing, corrosion phenomena, corrosive environments, preventive measures, materials of construction, equipment, and industries. An author index and a detailed subject index complete the volume.

Electro-technology, by M. G. Say, *Philosophical Library Inc.*, $6.00, 167 pp., 1955—Presents in a concentrated form the electrotechnical basis of the phenomena that are important in light and heavy electrical engineering. An introductory section deals with conduction and magnetic and electric field effects, and a comprehensive list of definitions is given. The second part of the book gives a complete guide to the handling of circuit problems. A feature is the collection of network theorems helpful for those who work out electrical quantities in all types of circuits and networks.

PROFESSIONAL SERVICES
Limited to AIME members, or to companies that have at least one AIME member on their staffs. Rates $40 per year per inch.

DR. B. EGEBERG
Metallurgical Consultant
Reg. Prof. Engr.
Steel & Metals
Operations — Research
Meriden, Conn.

LEDOUX & COMPANY
Chemists Assayers Spectroscopists
SHIPPERS' REPRESENTATIVES
Mine Examination Analyses
359 Alfred Ave. Teaneck, New Jersey

MAX STERN
Consulting Engineer
Expert for Scrap Recovery and Shipwrecking — Modernization of Plants and Yards for Ferrous and Nonferrous Metal Scrap
149 Broadway New York 6, N. Y.

H. L. TALBOT
Consulting Metallurgical Engineer
Extraction and Refining of Base Metals
Specializing in Cobalt and Copper
Room 330, 84 State St., Boston 9, Mass.

DR. E. TSUTSUMI
Registered Japanese Patent Attorney & Metallurgical Consulting Engineer
Patent Matters—Research . . . technical text translated from Japanese into English or vice versa: 2¢ per English word.
C. P. O. Box 1545 Tokyo, Japan

50-ton crane becomes 85-ton crane

with no increase in size

United States Steel's Edgar Thomson Works in Braddock, Pennsylvania, needed new and heftier crane equipment to handle larger ladles. One requirement was four new crane trolleys which were to operate on the same bridges, if possible, and in exactly the same clearances as before.

The trolleys had to be stronger but no larger than before; so ordinary steel wouldn't do. Needed, was a steel of *exceptional strength* which could be *welded easily*. Lots of alloy steels could have met the strength requirements; but USS "T-1" Steel was the *only* steel that could supply not only the required strength, but good weldability as well.

"T-1" Steel plate—in ¼" and 1" thicknesses—was used in box girders and lateral stiffener plates of the trolleys. This change increased the crane capacity from 50 to 85 tons with no increase in size.

The structure was welded with AWS E12015 electrodes. It was as easy as welding carbon steel. No stress relief was needed. And the welds developed the full yield strength of the steel: 90,000 psi. minimum.

Remember this story when you must weld very high strength parts —parts that must operate at temperatures as high as 900°F. or as low as 40°F. below zero, parts that must withstand tremendous impact abuse, abrasion or tensile stress. Then consider USS "T-1" Constructional Alloy Steel. For full particulars write: United States Steel, Room 4842, Pittsburgh 30, Pa.

UNITED STATES STEEL CORPORATION, PITTSBURGH · COLUMBIA-GENEVA STEEL DIVISION, SAN FRANCISCO
TENNESSEE COAL & IRON DIVISION, FAIRFIELD, ALA. · UNITED STATES STEEL SUPPLY DIVISION, WAREHOUSE DISTRIBUTORS
UNITED STATES STEEL EXPORT COMPANY, NEW YORK

SEE THE UNITED STATES STEEL HOUR. It's a full-hour TV program presented every other week by United States Steel. Consult your local newspaper for time and station.

USS "T-1" CONSTRUCTIONAL ALLOY STEEL

USS

UNITED STATES STEEL

Industrial Notes

• No. 3 blast furnace of the Sharon Steel Corp. is now equipped with high top pressure blowing. In addition, a modern gas washer was installed to eliminate dirt and dust discharged into the air during various periods of furnace operation. These improvements in the furnace, costing in excess of a half million dollars, will increase Sharon's iron capacity.

• A publication, *How Zinc Controls Corrosion*, issued by the American Zinc Institute describes the many ways zinc lengthens the life of steel products and reduces maintenance costs. Drawings, charts, and photographs together with brief comments present the corrosion control characteristics of zinc coatings, zinc pigments, and zinc anodes. An extensive selection of farm, industrial, marine, and building applications of zinc is reviewed. Copies can be obtained without charge from: American Zinc Institute, Inc., 60 E. 42nd St., N. Y.

• *Thompson Products, Inc., Cleveland, has turned to vacuum metallurgy for help in developing new high purity metals that will make tougher and longer lasting components. At present activity is directed principally to the improvement of high temperature alloys currently used for gas turbine engines. Future activity will be directed toward the development of new alloys whose compositions present difficult or insurmountable problems when air melting or casting is attempted.*

• Harbison-Walker Refractories Co. will begin immediate construction of a refractories plant in Lima, Peru. Associated with Harbison-Walker in the new company to be known as Refractarios Peruanos, S.A. are Cerro de Pasco Corp. and Miguel Dammert Muelle of Peru. Harbison will have the majority interest in the company and will supply the supervisory and technical management. The plant will be operated largely by Peruvian personnel.

• Aid in solving critical metallurgical problems may be found in a booklet on the vacuum melting process published by the Utica Drop Forge & Tool Corp. Utica has been in volume production of vacuum melted alloys for months and the information and experience gained is of interest to all concerned with metallurgy and product design. A free copy can be obtained from: Fred Hale, Utica Drop Forge & Tool Corp., Utica 4, N. Y.

• New stainless steel design handbook offered by alloy metal wire div., H. K. Porter Co., Inc., covers in detail the properties, specifications, applications, and design data on the company's 20 grades of stainless steel wire, rod, and strip. Title of the book is, *Functional Selection of Stainless Steels*, and it includes properties charts, size and weight charts, and other tabular data to help the design engineer select the right grade of steel for a particular application. For a free copy write to: E. H. Mann, alloy metal wire div., H. K. Porter Co. Inc., Prospect Park, Pa.

• *South Works of U. S. Steel Corp. celebrated its 75th Anniversary August 17 to 18. Construction of South Works, the oldest steel plant in Chicago, began on Mar. 22, 1880. Steelmaking operations began Mar. 26, 1881, employing about 2000 persons. Now more than 14,000 persons work at the plant and it ranks as the third largest steel mill in the world with a capacity of 5½ million ingot tons a year.*

• Technical data and tooling information on the production of aluminum parts on automatic screw machines is described in a booklet published by Kaiser Aluminum & Chemical Sales, Inc. Drawings and illustrations show proper tool angles for machining the various aluminum alloys suitable for screw machines. Tables cover speeds and feeds for cutting, skiving, cut-off, drilling, reaming, boring, counterboring and trepanning, recessing, box tools and hollow mills, threading, thread rolling, cross slide knurling and turret knurling. Available on request from: Technical Editor, Kaiser Aluminum & Chemical Sales, Inc., 228 N. LaSalle St., Chicago 1.

• A newly revised booklet, *Tool Steels for the Non-Metallurgist*, is available from the Crucible Steel Co. of America. Written to present a practical understanding of tool steels, the text describes the six basic classifications of tool steels and the numerous grades within the general classifications. Heat treating techniques are described and pertinent information is given in various tables. Copies can be obtained from: Advertising Dept., Crucible Steel Co. of America, P.O. Box 88, Pittsburgh 30, Pa.

• *American Iron & Steel Institute has issued a section of the* Steel Products Manual *covering* Alloy Steel: Semifinished: Hot Rolled and Cold Finished Bars. *The booklet includes chapters on products and manufacturing processes, blooms, billets and slabs, hot rolled bars, cold finished bars, quality descriptions and test, chemical ranges and limits, H-steels, and general information on alloy steel. Information on the manual can be obtained from: American Iron & Steel Institute, 350 5th Ave., New York 1.*

Coming Events

Sept. 1, AIME, Utah Uranium Subsection, Arches Cafe, Moab.

Sept. 6-16, Machine Tool Show, Chicago.

Sept. 6-9, Western Area Development Conference, Multnomah Hotel, Portland.

Sept. 14-16, Porcelain Enamel Institute, annual shop practice forum, Deshler-Hilton Hotel and Ohio State University, Columbus.

Sept. 16, AIME, Oregon Section, Burns Restaurant, Portland.

Sept. 23-24, AIME, NOHC, Southern Ohio Section, Deshler-Hilton Hotel, Columbus.

Sept. 24, AIME, Adirondack Section, Plattsburg Elks Club, New York.

Sept. 25-28, American Institute of Chemical Engineers, Lake Placid Club, Lake Placid.

Sept. 26-30, Atomic Industrial Forum, trade fair, Sheraton-Park Hotel, Washington, D. C.

Sept. 29, AIME, NOHC, Western Section, Rodger Young Auditorium, 936 W. Washington Blvd., Los Angeles.

Oct. 2-5, AIME, MGGD fall meeting and Black Hills regional meeting, Ind. Min. Div., Alex Johnson Hotel, Rapid City.

Oct. 6-8, AIME, Rocky Mountain Minerals Conference, Hotel Newhouse, Salt Lake City.

Oct. 13-14, Engineers' Council for Professional Development, annual meeting, King Edward Hotel, Toronto, Canada.

Oct. 14-15, National Society of Professional Engineers, fall meeting, Peabody Hotel, Memphis.

Oct. 17-19, AIME, IMD, fall meeting, Adelphia Hotel, Philadelphia.

Oct. 17-21, National Metal Exposition and Congress, Philadelphia.

Oct. 17-21, National Safety Congress and Exposition, Conrad Hilton, Congress, Morrison, and LaSalle Hotels, Chicago.

Oct. 20-21, National Noise Abatement Symposium, Armour Research Foundation, Illinois Institute of Technology, Chicago.

Oct. 24-25, Steel Founders Society of America, fall meeting, Greenbrier, White Sulphur Springs.

Oct. 24-29, Societe Francaise de Metallurgie, autumn metallurgical meeting, Paris, France.

Oct. 27-28, National Conference on Industrial Hydraulics, annual meeting, La Salle Hotel, Chicago.

Oct. 27-29, AIME, Ind. Min Div., fall meeting, Hotel Charlotte, Charlotte.

Oct. 31-Nov. 2, National Lubricating Grease Institute, annual meeting, Edgewater Beach Hotel, Chicago.

Nov. 1-5, World Symposium on Applied Solar Energy, Westward-Ho, Phoenix.

Nov. 4, AIME, Pittsburgh Local Section, off-the-record meeting, Pittsburgh.

Nov. 9-11, Industrial Management Society, time and motion study and management clinic, Sherman Hotel, Chicago.

Nov. 13-18, ASME, annual meeting, Congress, Conrad Hilton, and Sheraton-Blackstone Hotels, Chicago.

Nov. 16, AIME, NOHC, Western Section, Rodger Young Auditorium, 936 W. Washington Blvd., Los Angeles.

Nov. 17-18, American Society for Quality Control, mid-west conference, Schroeder Hotel, Milwaukee.

Nov. 28-Dec. 1, Air Conditioning and Refrigeration Institute, exposition, Auditorium, Atlantic City.

Dec. 10-16, International Atomic Exposition, Cleveland Public Auditorium, Cleveland.

Feb. 20-23, 1956, AIME, annual meeting, Statler and New Yorker Hotels, New York.

PHILIPS
100 KV
Electron Microscope

The Philips EM-100 Electron Microscope first introduced smart comfortable styling with all operating controls accessible for convenient use. Four significant improvements provide added features unmatched by any other electron microscope.

A new Front End Plate Camera is optionally available and will fit any existing EM-100 Microscope. The film cassette holds either five 3¼" x 4" glass plates or six 4" x 5" cut films. Direct micrographic recordings may be made at magnifications up to 100,000 diameters. A film counter is included to prevent double exposures. A single-action lever speedily removes the cassette from the field while automatically changing the film.

A new 20 Angstrom lens is likewise adaptable to all existing EM-100 Microscopes. The new lens utilizes a short focal-length objective which has been designed for interchangeability with previous lenses for applications requiring the highest possible definition.

The Wide-field Adaptor, operated through a footswitch, enables the operator to select any given area of a specimen under reduced magnification and instantaneously return to high magnification for the area selected.

A Binocular Microscope is available which positions in front of the circular viewing screen. The microscope is equipped with objective lenses permitting either 3.5 or 7x magnification and aids in determining sharpest possible image focus. When removed it serves as a microscope for specimen preparation.

By efficient planning and scientific combination of facilities, additions are being constantly made to the existing basic EM-100 design, thus maintaining its reputation as outstanding in functional electron microscope design.

Increased field size permits simple area selection.

Release of footswitch returns high magnification.

Front end plate camera offers 100,000X film magnification.

Removeable microscope also aids in specimen preparation.

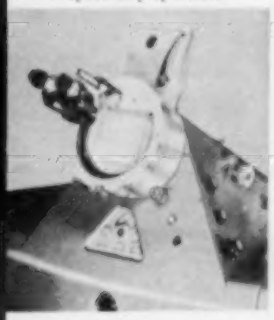

A Norelco PRODUCT

NORTH AMERICAN PHILIPS COMPANY, INC.

Serving Science and Industry

750 South Fulton Avenue, Mount Vernon, N. Y.

In Canada: Rogers Majestic Electronics Ltd., 11-19 Brentcliffe Road, Leaside, Toronto 17, Ontario

—Personnel Service—

THE following employment items are made available to AIME members on a nonprofit basis by the Engineering Societies Personnel Service Inc., operating in cooperation with the Four Founder Societies. Local offices of the Personnel Service are at 8 W. 40th St., **New York 18**; 100 Farnsworth Ave., **Detroit**; 57 Post St., **San Francisco**; 84 E. Randolph St., **Chicago 1**. Applicants should address all mail to the proper key numbers in care of the New York office and include 6c in stamps for forwarding and returning application. The applicant agrees, if placed in a position by means of the Service, to pay the placement fee listed by the Service. AIME members may secure a weekly bulletin of positions available for $3.50 a quarter, $12 a year.

——POSITIONS OPEN——

Metallurgical Engineer, B.S. degree, young, with experience, for production (quality control) and development work in the field of vacuum melted materials. Steel mill experience and knowledge of high temperature alloys desired but not a necessary requirement. Location, New York State. W1962.

Plant and Sales Managing Engineer for small nonmetallic crushing, drying, and bagging plant treating bentonite. Salary, $9600 a year. Location, Wyoming. W1944.

Mineral Dressing Engineers, graduate metallurgical engineers, with minimum of five years experience in mineral dressing or process metallurgy. Company operates an AEC laboratory. Salary commensurate with experience and training. Location, New England. W1924.

Metallurgist or Metallurgical Engineer, recent graduate, for manufacturing research laboratory of progressive steel castings company. Opportunity to do applied research and pilot plant work on metallurgy of cast steels, development of new molding techniques, and casting processing methods. Apply by letter indicating educational background, military status, and experience. Location, Midwest. W1912C.

Chemist who is familiar with spectrography and has had some ex-

SENIOR
ENGINEER
Metallurgical Research

For Materials Research and Radiation Studies Group of the Aircraft Nuclear Propulsion Department.

A senior research position is now open in an advanced project . . . the application of nuclear energy to the field of flight. The engineer who qualifies will be responsible for research designed to provide improved metals and alloys for use in an aircraft nuclear power plant.

The job requires a degree in physical metallurgy or metallurgical engineering and 8 to 10 years experience in working with high temperature or corrosion resistant metals and alloys. (If directly related, time spent on obtaining an advanced degree may be considered part of this experience.)

PUBLICATION OF RESEARCH RESULTS IN THE APPROPRIATE CLASSIFIED OR OPEN LITERATURE IS ENCOURAGED.

Send complete resume to:
TECHNICAL PERSONNEL
Aircraft Nuclear Propulsion Dept.

GENERAL ELECTRIC
Cincinnati 15, Ohio

METALLOGRAPHER

Young graduate metallurgist with at least one to two years experience in industry. Nonferrous experience desirable but not absolutely essential. We are willing to train to some extent, provided the applicant possesses the necessary qualifications. This position offers an outstanding opportunity for advancement and growth with an expanding organization. In reply please furnish full particulars regarding background and experience. State salary requirements. Direct reply to:

Employment Supervisor
KAISER ALUMINUM & CHEMICAL CORP.
Trentwood Works
Spokane 69, Washington

METALS RESEARCH LABORATORIES
Technical Personnel Requirements

RESEARCH ENGINEER: Ph.D. or Sc.D. in chemical engineering or extractive metallurgy for duties focused on the technology of extremely pure metal compounds and their subsequent reduction to metals. The engineer will have responsibility for bench-scale to pilot-scale work on unit operations such as leaching, chlorination, distillation, melting, high-temperature furnace work, solvent extraction, and ion exchange. Ability in preliminary design is desirable. Send resume of education, experience and salary expectations to: M. L. Baas, Metals Research Laboratories of the Electro Metallurgical Company, P.O. Box 580, Niagara Falls, New York.

RESEARCH ENGINEER OR RESEARCH METALLURGIST: Sc.D. or M.S. in mineral engineering or metallurgical engineering to conduct research leading to better methods of mineral recovery. Process and flow-sheet development for newly located orebodies will be required, along with supervision of specific research problems on comminution, flotation, electrostatic and magnetic separation, smelting, leaching or other unit operations. Applicant must have demonstrated ability for initiating and directing experimental work in the fields of mineral dressing or extractive metallurgy. Two to three years' experience as a research engineer is desirable. Send resume of education, experience, and salary expectations to: M. L. Baas, Metals Research Laboratories of the Electro Metallurgical Company, P.O. Box 580, Niagara Falls, New York.

METALLURGISTS

The Research and Development Division of a large specialty steel manufacturer, in western Pennsylvania, has several openings for qualified personnel.

Supervisor Magnetic Materials Research: Ph.D. in physics or metallurgy, plus 5 years' minimum experience in research or development of magnetic materials. Should be familiar with powder metallurgy techniques and the manufacture and testing of high permeability materials as well as permanent magnet materials.

Silicon Steel Research Supervisor: Degree in metallurgy or physics, plus 5 years' minimum experience in research or development of steels for the electrical industry. Skilled in research methods, report writing and metallurgical processes.

Research Metallurgists: B.S. degree or higher, plus 5 years' minimum experience in research or development of metals and alloys. Requires ability to outline and conduct research and development programs.

Associate Metallurgists: B.S. in metallurgy or physics, plus 4 years' minimum experience research in metals. Skilled in research techniques, report writing, and comprehension of metallurgical processes.

Send complete resume giving educational background, experience, and salary desired to:

Box J-25M AIME
29 West 39th St., New York 18

perience with physical testing and metallurgy, to supervise a small laboratory and expedite production. Salary open. Location, Long Island, N. Y. W1867.

Process Development Metallurgist. Must have background in melting metallurgy or physical chemistry of metals required. To lead program of process development involving molten metal reactions, melting thermodynamics, effects of soluble gases, etc. for vacuum melted high temperature and specialty alloys. Well equipped pilot plant and supporting laboratory facilities available. D1136.

Metallurgist, who specialized in thermic treatments and processing of metals for the manufacture of armaments and ammunition. Salary open. Location, South. W1810(b).

Welding or Metallurgical Engineer, 30 to 45, to supervise development projects and preproduction work on advance turbojet engine parts and components. Must have experience in fusion and resistance welding of stainless steel, super alloy, and titanium alloy. Salary, $6000 to $9000. Location, Ohio. C3469.

TITANIUM

Capital available for research into the reduction of titanium ores. Please submit background experience.

Box J-26M AIME
29 West 39th St. New York 18, N. Y.

GALVANIZING METALLURGIST. Immediate opening with a fully integrated steel mill in the Pittsburgh district for a technical graduate with experience in continuous galvanizing. Will supervise metallurgical function of the line including all phases of process and quality control and customer technical service. Please reply with complete resume of background and salary requirements to Director of Technical Services, Jones & Laughlin Steel Corporation, Pittsburgh 30, Pa.

PROCESS DEVELOPMENT METALLURGIST

Challenging new supervisory position in expanding Research and Development Department. Technical investigation and evaluation of new or improved processes for smelting, refining, and processing. Metallurgical or chemical engineering background with advanced scientific training in process metallurgy. Attractive salary. Address reply to Director of Technical Services.

JONES & LAUGHLIN STEEL CORPORATION
Pittsburgh 30, Pa.

Supervisor Minerals Beneficiation, metallurgical or mining engineer, up to 45. Must have had at least four years experience in mineral beneficiation work, and knowledge of metallic and nonmetallic mining. Will develop and direct minerals beneficiation program, and formulate policies regarding minerals and encourage use of these services by operating divisions. Salary, $7500 to $12,000 a year. Employer may negotiate placement fee. Considerable traveling. Location. Chicago. C3310.

Engineers. (a) Sales Metallurgist, precision castings, with metallurgical background and be familiar with needs of industry in the precision casting field; able to initiate sales policies and promotion of new ideas in this industry. Salary open. (b) Foundry Metallurgist, to take charge of all foundry operations of investment casting company, experienced with ferrous and nonferrous alloys and, if possible, with high vacuum technique; capable of initiating alloy development programs. Salary open. Location, Midwest. W1835.

Field Engineer, metallurgy, 25 to 35, for smelter of precious metals. Must have at least two years experience in heat treating, brazing or welding. Knowledge of electronics helpful. Salary, $4200 to $6000 a year. Employer will pay placement fee. Location, Chicago. C3407.

are you producing

321 STAINLESS STEEL

Titanium Stabilized

low aluminum residual in this steel tends to lessen the formation of the detrimental Sigma phase.

this can be more easily accomplished by the addition of low carbon Ferro Titanium which is low in Aluminum.

TAM, as a principal supplier of low carbon Ferro Titanium, is equipped to supply your requirements. Our broad experience in the application of LCFT may also be of value to you.

Why not write our New York office for the latest technical information as well as prices and deliveries.

TAM PRODUCTS
Registered U. S. Pat. Off.

TITANIUM ALLOY MFG. DIVISION
NATIONAL LEAD COMPANY

Executive and Sales Offices:
111 Broadway, New York City

General Offices, Works and Research Laboratories:
Niagara Falls, New York

MCA offers Quick delivery

of all forms for all uses

TUNGSTEN

Ferro-Tungsten

Tungstic Oxide

Tungstic Acid

Ammonium Para-Tungstate

Sodium Tungstate

Tungsten Metal Power

Now that Tungsten high-speed steel can be supplied as needed, manufacturers have returned to it for the well-defined uses in which it surpasses all other materials. Processed in the U. S. A., MCA Tungsten offers a consistently uniform product assuring excellent results.

As recognized authorities in the application of Molybdenum, Tungsten, Boron, Rare Earths, and the alloys and chemical elements of these materials, MCA assures confidential and immediate response to inquiries.

An informative book, entitled "Tungsten Steels", has been prepared by the Molybdenum Corporation. It deals with both scientific and practical considerations, and recommends procedures found to yield best results. A copy will be mailed on request.

MOLYBDENUM

CORPORATION OF AMERICA

Grant Building **Pittsburgh 19, Pa.**

Offices: Chicago, Cleveland, Detroit, Los Angeles, New York, Pittsburgh, San Francisco
Sales Representatives: Edgar L. Fink, Detroit; Brumley-Donaldson Co., Los Angeles, San Francisco
Subsidiary: Cleveland-Tungsten, Inc., Cleveland, Ohio

MCA

MORGAN CONSTRUCTION COMPANY WORCESTER, MASS.

ROLLING MILLS • MORGOIL BEARINGS • WIRE MILLS • REGENERATIVE FURNACE CONTROL • EJECTORS • GAS PRODUCERS

H. H. Wood, Rep., Koppers Bldg., Pittsburgh, Pa. *English Rep.*, International Construction Co., 56 Kingsway, London W. C. 2, Eng.

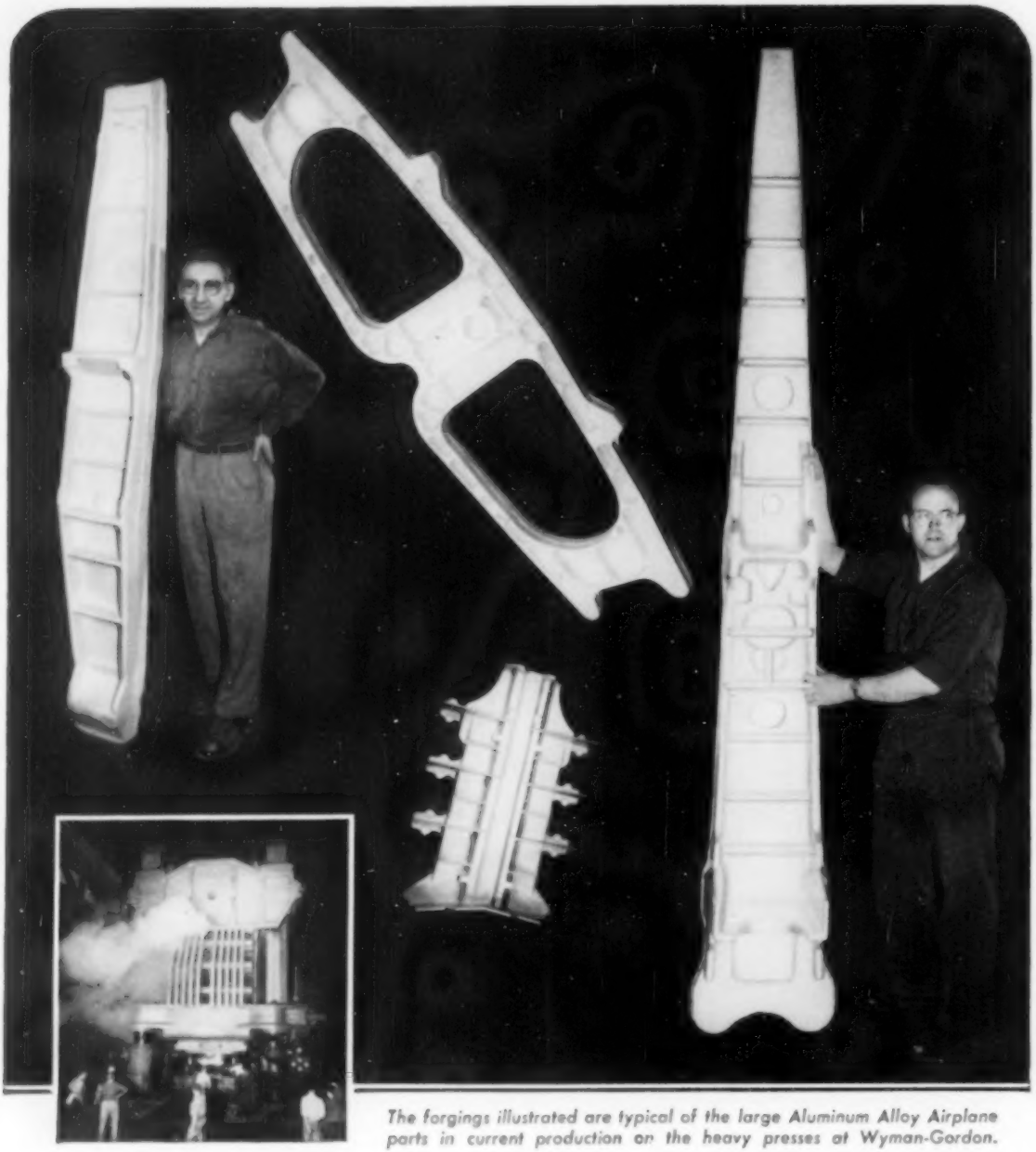

The forgings illustrated are typical of the large Aluminum Alloy Airplane parts in current production on the heavy presses at Wyman-Gordon.

A new era in the art of forging has been demonstrated as production goes forward on this 35,000-ton closed die forging press. Larger forgings with thinner sections and closer tolerances than heretofore possible open new concepts in forging design. Wyman-Gordon continues to pioneer by — Keeping Ahead of Progress.

WYMAN-GORDON CO.

Established 1883

FORGINGS OF ALUMINUM • MAGNESIUM
STEEL • TITANIUM

WORCESTER 1, MASSACHUSETTS
HARVEY, ILL. • DETROIT, MICH.

Heroult
ELECTRIC MELTING FURNACES

TOPS FOR PRODUCTION OF HIGH GRADE STAINLESS, ALLOY AND RIMMING STEELS

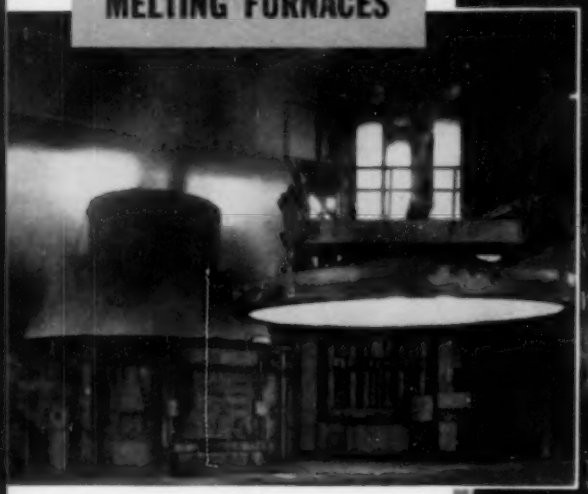

World's Largest Electric Furnaces

. . . now in operation!

INSTALLED in the ultra-modern mill of McLouth Steel Corporation, in Detroit, these giant *200-Ton* Heroults are the largest electric melting furnaces ever built. With an inside shell diameter of 24'6", they have a rated charge capacity of 400,000 pounds, and each is designed for efficient operation on 25,000 to 33,000 KVA transformer capacity. Featuring a swing-type roof, these furnaces are equipped with the finest, most up-to-date mechanism and electrical controls available.

McLouth's adoption of electric furnaces of this size sets a precedent. It is a "first" which should conclusively prove that, in addition to closer control, higher uniformity, better performance, and greater safety, large capacity Heroult Electric Furnaces are an economically sound investment—even for high tonnage steel-making.

We welcome an opportunity to help you select and install the furnace best suited to your particular requirements.

ASK FOR NEW CATALOGUE. *Contains latest information on modern electric furnaces—types, sizes, capacities, rating, etc. Write Pittsburgh Office for free copy.*

AMERICAN BRIDGE DIVISION, UNITED STATES STEEL CORPORATION
GENERAL OFFICES: 525 WILLIAM PENN PLACE, PITTSBURGH, PA.

Contracting Offices in New York, Philadelphia, Chicago, San Francisco and other principal cities.
United States Steel Export Company, New York

USS

UNITED STATES STEEL

STARTING salaries for beginning engineers continue to increase according to figures compiled by the Illinois Institute of Technology. Tabulations show that the starting pay of the 1955 June engineering graduate with a B.S. degree climbed to $381 per month as compared to the $363 received by the 1954 June graduate. The following table gives the beginning salary figures for IIT engineers.

Average Beginning Salary Figures For IIT Engineers in Dollars Per Month

Engineering Field	June 1954	June 1955
Metallurgical	377	404
Electrical	386	416
Civil	375	380
Mechanical	373	377
Industrial	356	371
Chemical	362	365
Architectural	365	353
Fire Protection and Safety	338	348

All averages are based on a 40-hr work week and apply to engineering graduates with some practical experience. Nearly all engineering students at Illinois Tech hold part-time or summer jobs during their academic career.

One of the more noteworthy trends demonstrated by the survey is the desire by organizations to secure a greater number of engineering graduates for eventual advancement to managerial and supervisory positions. The move in that direction is underscored by the increasing demand by industry for experienced engineers for executive positions.

The survey also pointed up that engineers and specialists are not the only college graduates getting higher salaries. Reports from half of IIT business and economic majors showed their average starting wage to be $369 per month. A year ago it was $343 and in June 1953, $327.

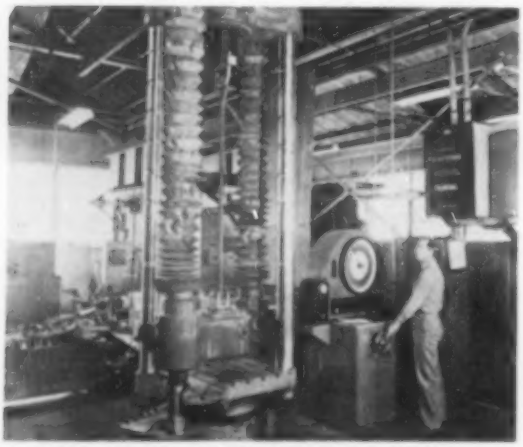

Proof loading in tension on an aircraft arresting hook is performed on a 440,000 lb Baldwin universal testing machine at Axelson Mfg. Co. Canvas pantaloons protect tension members of machine from dirt sifting in from the foundry next door.

IN THE space of a half dozen years, lithium has grown from an almost obscure chemical element to a multimillion dollar business. Production facilities are being expanded to startling capacities and speculation in lithium deposits is at an all time high.

Is the lithium industry being overexpanded? L. G. Bliss, vice president of Foote Mineral Co. answers, "We all remember a somewhat analogous case in aluminum. The largest producer of this metal announced an ambitious expansion program some years ago when it was in a market unable to support such expansion . . . Commercial markets developed that were not visualized when capital commitments were made, and so it may be in the field of lithium."

Polishing up his crystal ball, Mr. Bliss offered the following observations: Commercial acceptance of lithium in metallurgy has been retarded by economics. With expansion in production facilities the trend of lithium pricing is now in the right direction to awaken earlier interests. Lithium may have a use as a scavenger or, as some metallurgists believe, as an alloying constituent in the ferrous and nonferrous industries. The literature already indicates that considerable work has been done in these fields since the development by the Germans many years ago of lithium containing bearing metal.

For several years investigations have also been made to determine the effect of the addition of lithium fluoride and/or lithium carbonate to the bauxite-cryolite bath. In the atomic energy field it could well be that lithium will become the friendly rival of uranium. Moving from the plant to the kitchen Mr. Bliss points out that in the new field of dry bleaches, dry lithium hypochlorite more nearly matches the desirable properties of liquid sodium hypochlorite than other proprietary dry compounds now being offered. Use will also increase in such applications as enamel, porcelain, and glass.

Mr. Bliss states that if his fleeting pictures from the crystal ball are true, lithium will create a new and large basic industry. "Life with lithium in the future will not be static," he concludes, ". . . we believe it is already dynamic."

◆◆◆◆◆◆

EVERYDAY the average person is exposed to thousands of words on meetings at the summit, rumors of a coal strike, and the political assault on WOC's. Important as these are there is very little the average person can do about them. Not so the subject of a recent speech by J. A. Stephens, U.S. Steel Corp.'s vice president for industrial relations.

Mr. Stephens brought into prospective the entire problem of communication and the fundamental need for providing something of value for the human mind. "Any community possessing little or no library service," he said, "is an incomplete community, regardless of how many swimming pools, television sets, or sports cars it may have. It is depriving

itself and especially its children the right to explore literature of enduring value—literature that has made the human spirit soar above even the grubbiest kind of everyday existence."

Public libraries have been the principal victims of the great pinch on local tax resources resulting from the enormous rise in Federal taxation. Mr. Stephens said he believed that library development in the U. S. could be stimulated if business and industrial leaders in the smaller industrial cities took the initiative in working with public librarians to establish business information services. This type of business-industry-library cooperation has already been developed in numerous large cities.

However, Mr. Stephens emphasized, "Industrial management looks upon libraries not so much as reservoirs of practical data, but as priceless repositories of knowledge about the institutions of society we must cherish and defend—and knowledge about institutions and ways of thought that are hostile to human freedom and that we must know about in order to combat them effectively. It is the responsibility of those in business and industry, in their role as citizens, to safeguard libraries and to fight for the libraries' right to make available literary material presenting diverse points of view. . ."

◆◆◆◆◆◆

A FAR CRY from the small gasoline engine used to provide emergency power for rural areas and small industries is the turbo-mobile power plant capable of developing 5500 kw of electrical power. This unit, developed for the Bureau of Yards and Docks of the U. S. Navy as an emergency unit, was designed by Clark Bros. Co. of Olean, N. Y., one of the Dresser Industries.

The emergency power unit is mounted in a railroad car, can be moved at high speed in any freight or passenger train service, and is ready to operate within 24 hr after reaching the desired site. The only items necessary for successful operation are a fuel source and a transmission line. This gas turbine driven unit is designed to operate on a wide range of liquid and gaseous fuels, in combination or interchangeably.

The Clark turbo-mobile power plant can be used to meet emergencies arising from natural causes such as floods, fires, tornadoes, hurricanes, and earthquakes. In the event of war, the mobile power plants could be moved in on ships to base areas, and units could be standing by in this country near key manufacturing plants, or large cities.

The gas turbine used to drive the generator in the power unit is also well suited to the drive of centrifugal compressors in the refining, gas transmission, and process industries. It is specifically designed for continuous, long-life operation with or without regeneration.

The gas turbine consists of an axial flow compressor and axial flow turbine with two shafts. The first (high pressure) turbine consisting of two stages operating at 5000 rpm drives the axial flow compressor supplying combustion air. The second turbine running independently drives the load generator at 3600 rpm. The rotating blades are forged and shrouded reducing interstage losses. The stator blades are precision cast and attached to carrier rings with controlled clearances permitting thermal expansion without strain or distortion. The turbine is designed for normal operation at an inlet temperature of 1350°F.

Only minor preparation at the site before startup is required, and only one trained operator is required to start and operate the plant.

In addition to the 5500 kw unit built for the U. S. Navy, a 6200 kw unit has recently been sold to the Comision Federal de Electricidad in Mexico. In Mexico, mobile power is considered to be the answer for supplying power to cities and areas separated by long distances, where it is not economical to build transmission lines to interconnect all areas. Mobile steam and Diesel plants have been used, but they are not an entirely satisfactory answer, and it is felt that the gas turbine unit, which is satisfactory from a size viewpoint, does not require water, and may be moved and placed in operation in hours, will provide the solution.

Clark Bros. Co., which is celebrating its 75th year of service, started as a manufacturer of agricultural tools and pumps. They have since continuously adjusted and expanded the business, merging with Dresser Industries in 1937. Their big interest today is building new and improved compressors, engines, and turbines.

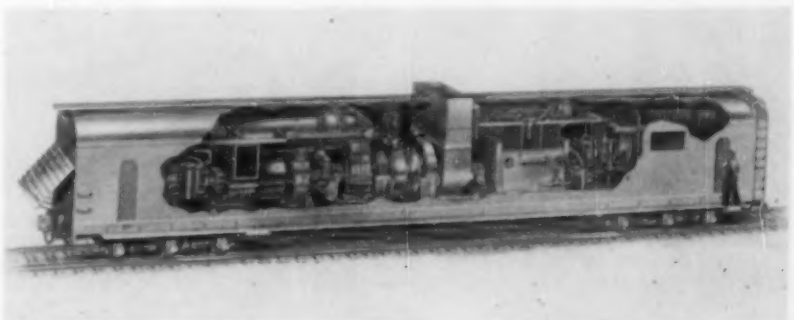

This cutaway shows the Clark turbo-mobile power plant mounted in a specially designed railway car. At the left is Diesel engine used to start unit, Clark gas turbine, generator, exciter, fuel pumps, and control room.

Drift of Things

THE Second Metallwerke Plansee in Reutte, Austria was scheduled to follow the Joint Metallurgical Societies Meeting in Europe. Some 250 attended from many countries including a dozen Americans from the Joint Metallurgical Meeting and a number who came direct. There were 130 registrants from Austria, 68 from Germany, 31 from England, 20 from the USA, 15 from Sweden, 14 from France, 12 from Switzerland, and from 1 to 6 from each of the following: Luxembourg, Spain, Italy, Belgium, Holland, Japan, Ireland, and Norway.

The technical sessions were well planned covering varying phases of powder metallurgy and related subjects from fundamental research to operating techniques. Translations of papers and discussions were provided for those who were not linguists. The attendance indicates the completeness of the exchange in information between scientists and producers throughout much of the world. The technical sessions were held at the Metallwerke Plansee plant in Reutte. Reutte is a small city in the Tirolean Alps of Austria—a beautiful setting for either a meeting or a plant.

One evening an exhibition of Tirolean dancers was provided, a treat whether one had seen such dancing before or not. The meeting opened and closed with a dinner. It should be noted that Dr. Paul Schwarzkopf, founder and owner of American Electro Metal Co. in Yonkers, N. Y. and Metallwerke Plansee Gesellschaft in Reutte, is an excellent host. His staff members too, from both companies, did everything possible to supply technical information or to provide for the comfort of the registrants. At the close of the meeting plans were made to provide for an international powder metallurgy society to insure the continuation of these valuable meetings.

Ernest Kirkendall

Dr. Paul Schwarzkopf, fourth from left, was host at the International Seminar on Powder Metallurgy in Reutte, Germany. The meeting was held following the Joint Metallurgical Societies Meeting in Europe, and some of the Americans attending are shown with Dr. Schwarzkopf.

Photographs of the Joint Metallurgical Societies Meeting in Europe that were received too late for inclusion in the August issue of JOURNAL OF METALS, p. 865, are shown below.

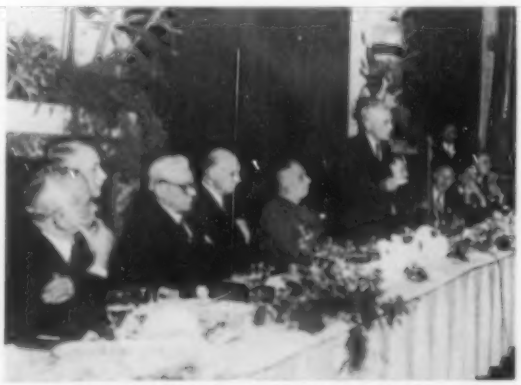

John Chipman, Chairman-elect of the Iron & Steel Div., AIME, responds on behalf of the Americans to the welcome of the Centre National de Recherches Metallurgiques at the Luncheon held at Le Manoir in Liege, Belgium, June 13, 1955.

The banquet in the Orangerie in the Palace of Versailles, June 18, 1955. Insert shows a portion of the speakers table at the banquet. From left to right: Ernest Kirkendall, Mme. la Comtesse de Vitry, M. R. Terrel, Mrs. George Roberts, R. de Vitry, president of Societe Francaise de Metallurgie, the host society, and Mrs. J. B. Austin.

NOW!

X-ray inspection anywhere!

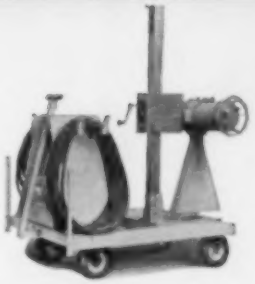

Truck-mounting of OX-175 with elevating tube stand converts this rugged, dependable, portable x-ray unit into a *mobile* inspection tool for laboratory and shop.

Simply staged and remotely controlled, the *portable* OX-175 provides positive check of the welds on this oil storage tank.

with industry's most versatile x-ray unit — General Electric's OX-175

Fifty feet off the ground . . . or inside a 15-inch opening — General Electric's new OX-175 is the answer to almost any radiographic inspection procedure. Light weight and small tubehead size — plus control-cable lengths up to 200 feet — permit checking of welds, castings or assemblies in the shop or in the field.

There are three models to choose from . . . any of ten types of mountings. And note this — with its flat target tube, the OX-175 produces a 360° field of radiation that can radiograph an entire circumferential weld in one exposure.

Your G-E x-ray representative will show you how the OX-175 can extend your range of x-ray inspection. Call him today, or write X-Ray Department, General Electric Company, Milwaukee 1, Wisconsin, for Pub. AY94.

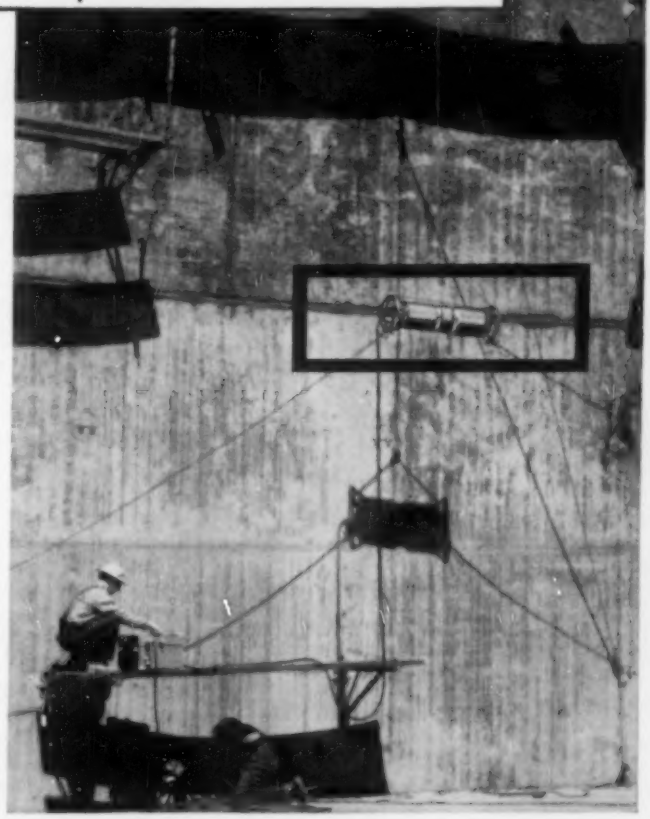

Progress Is Our Most Important Product

GENERAL ELECTRIC

Lifting capacity of this Austin-Western crane was increased 350% by replacing cylindrical worm gearing with Cone-Drive gearing. The boom lifting mechanism is driven by a 6" center distance 50:1 Cone-Drive Gearset powered by hydraulic motor. A similar 5" center distance 40:1 Cone-Drive unit swings the crane.

350% more lifting capacity with help from nickel alloys

DON'T ADD BULK or deadweight to increase load capacity.

Cone-Drive gearsets that raise and swing the boom of this crane show how you can strengthen an assembly while making it more compact.

Cone-Drive mates a nickel alloy steel worm with gearing of chill-cast nickel alloyed bronze. Added to bronze, nickel imparts extra life and strength, raises elastic properties, and increases shock resistance as much as 25 to 50 per cent.

Likewise, nickel contributes much to the worm. Cone-Drive worms are medium-carbon nickel-chromium-molybdenum steel, heat treated to a minimum hardness of 32 Rockwell C and 140,000 psi tensile strength.

The nickel content in this steel helps make possible a surface that resists wear and spalling . . . and a core with the toughness to withstand severe overloads.

In many a metal, you can improve specific properties by use of nickel alone or in combination with other alloy elements. When you have a metal problem, whatever the difficulty, send us details. We'll be glad to give you suggestions based on our wide experience in this field.

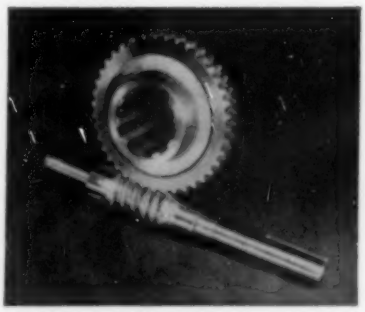

Give compact units stamina by designing to use high mechanical properties of nickel alloys. Above is such a unit, produced by Cone-Drive Gears Division of Michigan Tool Co., Detroit 12, Mich.

INCO **THE INTERNATIONAL NICKEL COMPANY, INC.** 67 Wall Street New York 5, N.Y.

Victor Chemical Works, Chicago, has developed a new alloy, ferrophosphorus, to increase the density of concrete walls forming the protective shielding for atomic hot cells. Ordinary concrete for this purpose would have to be 6 to 8 ft thick, but when mixed with concrete, ferrophosphorus produced a density of 290 to 300 lb per cu ft, twice that of ordinary concrete.

Columbia-Southern Chemical Corp. of Pittsburgh and Imperial Chemical Industries Ltd. of England plan to construct a $10 million titanium plant at Natrium, W. Va. Companies will introduce a new sodium reduction method to produce granular titanium. Plans call for a processing plant with a 5000 ton capacity.

Reynolds Metals Co. is beginning the largest expansion program in its history. A $250 million program to increase its annual primary aluminum products by 270 million lb to a total of 1.1 billion lb includes a new 200 million lb primary reduction plant to be built in the Ohio River Valley.

Elgin National Watch Co. has developed a button-sized expendable battery that delivers 1.15 v for two years. Using indium as an anode and an undisclosed material for the cathode, the microcell opens up new possibilities in military and industrial applications.

Chromium coating of titanium has been successfully accomplished by Tiarco Research Laboratories of Clark, N. J. Named the Bayliq process, the method should be valuable in counteracting the galling tendency of titanium in sliding contacts.

In the plant wide expansion program of Wickwire Spencer div. of Colorado Fuel & Iron Corp. three open hearths are being enlarged from 110 to 175 tons per heat. New turboblowers, each costing $1 million, will increase the efficiency of the furnaces.

Steel capacity in the six countries of the European Coal and Steel Community is expected to increase from 51 to between 57 or 58 million metric tons by 1958. Steel industries of the community employ approximately 406,000 persons.

U. S. Bureau of Mines has announced a $250,000 research program in rare earth metals. The Rare and Precious Metals Experiment Station at Reno, Nev., is investigating the properties of these metals with a view to developing methods of extraction and possible commercial uses.

A liquid metal fuel reactor with a potential of 7.8 mill per kw hr using uranium and bismuth was described by Brookhaven scientists at Geneva. A solution of uranium in bismuth was selected because of the low melting point and low neutron capture cross-section of bismuth.

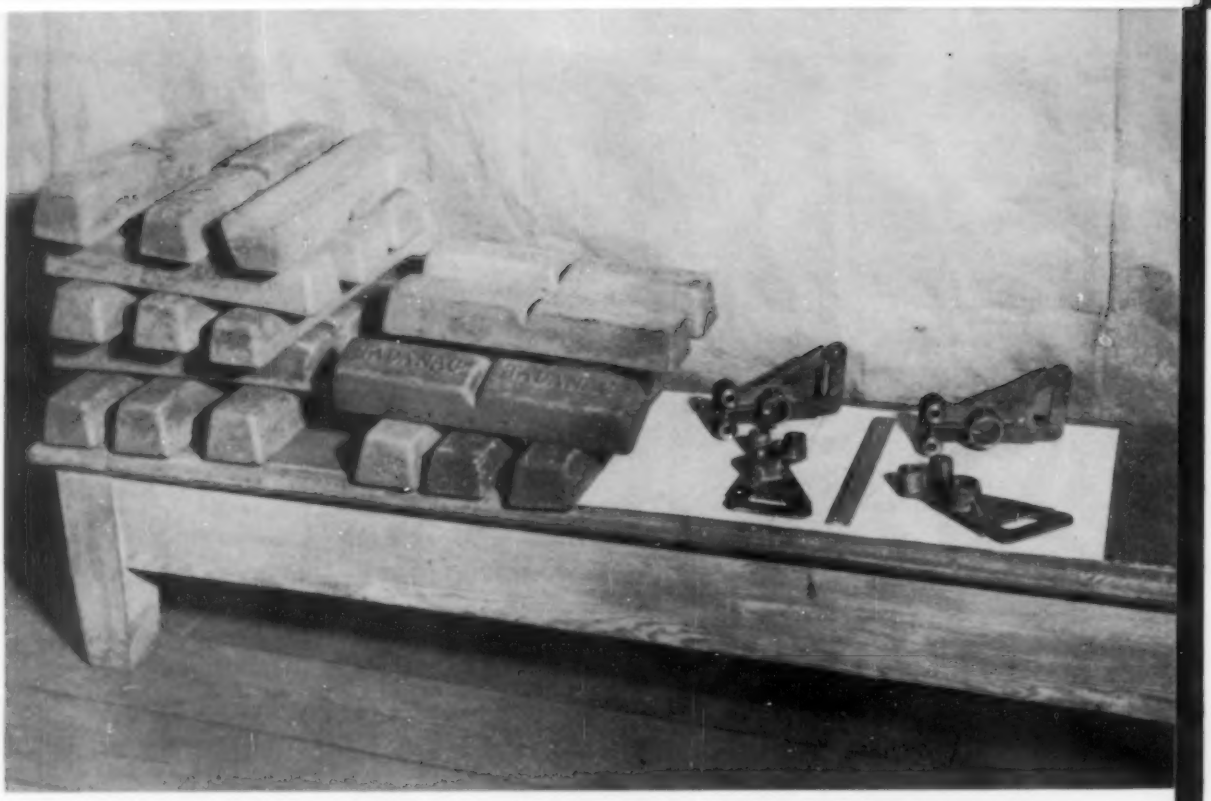

Pig iron produced from Cominco's iron oxide calcine was made into mild carbon steel in a basic electric furnace. Ingots and special castings showed no abnormal characteristics.

Iron and Steel Produced From Pyrrhotite Tailings Opens Up Potential Market

by B. G. Hunt and A. Turner

IRON SULPHIDE concentrate is produced in the process of separating lead and zinc from the ore at Cominco's Sullivan mine at Kimberley, B. C. A certain amount of this iron concentrate is roasted to provide SO_2 for sulphuric acid manufacture. The iron oxide calcine from the roaster was used to produce approximately 6 tons of pig iron. The residual elements in the calcine were not present in excessive proportions and some of the iron was converted into mild carbon steel.

The iron oxide calcine from the suspension roasters is so finely divided that addition of some coarse hard material is necessary to hold the charge open and permit proper roasting. In tests made by Sintering Machinery Corp., good results were obtained, using 50 pct return sinter in sintering feed, and this quantity is assumed to be satisfactory. The return sinter must of course be crushed and a part of the limerock flux would be added with this, and the balance directly to the furnace.

Because insufficient sulphur is present to provide the necessary heat, coke breeze was added. The tests indicated that 4 to 5 pct of the weight of material sintered would be required. Representative calcine was not available for the test program and so typical iron concentrates were used, which required the removal of much more sulphur. The iron concentrate was desulphurized and sintered in an oil-fired rotary kiln, 4 ft diam x 48 ft long. Two passes

B. G. HUNT and A. TURNER are Pilot Plant Engineer and Research Engineer respectively, Research and Development Div., The Consolidated Mining & Smelting Co. of Canada Ltd., Montreal, Quebec, Canada. This paper was presented at the AIME Pacific Northwest Regional Conference, Spokane, Apr. 28 to 30, 1955.

Table I. Analyses and Quantity of Materials Involved in Smelting Pig Iron

Material	Wt, Lb	Analysis, Pct						Weight, Lb					
		Fe	CaO	SiO_2	Al_2O_3	MgO	Mn	Fe	CaO	SiO_2	Al_2O_3	MgO	Mn
In													
Sinter	20,818	58.5	1.8	10.7	2.97	0.45	0.79	12,179	373	2228	618.3	93.7	164.5
Coke	5,055	2.0	0.9	8.4	4.3	—	—	101	45	427	215.9	0.5	—
Limerock	5,073	0.9	49.7	4.6	1.1	0.35	—	44	2523	233	84.0	17.6	—
Total								12,324	2942	2888	888.2	111.8	164.5
Out													
Pig Iron	12,704	93.42	—	2.08*	—	—	0.77	11,868	—	265	—	—	97.3
Slag	7,742	7.0**	41.3	34.8	12.9	1.2	0.76	542***	3197	2694	998.7	92.9	58.8
Baghouse and Flue Dust	849	6.0	9.1	8.6	—	—	—	33	50	47	—	—	—
Unaccounted Loss or Gain	—	—	—	—	—	—	—	+119	+306	+418	+110.5	−18.9	−8.5
Total	—	—	—	—	—	—	—	12,324	2942	2888	888.2	111.8	164.5

* Silicon. ** Total iron comprising 4.0 pct metallic iron and 3.0 pct iron oxide. *** Total iron comprising 310 lb metallic iron and 232 lb iron oxide.

were required, the final product being a good physical sinter. The main operating controls were temperature, controlled by the oil burner, and feed rate. The first pass discharge temperature was maintained at 1500° to 1600°F, which accomplished a satisfactory sulphur elimination without any sintering of the product.

If the material is sintered before complete removal of the sulphur it becomes more difficult to get the sulphur as low as desired. Thus when the feed rate was controlled at 500 lb per hr, the sulphur in the product was 5 to 10 pct while at 400 lbs per hr the sulphur was reduced to 2 to 5 pct. For the second pass the discharge temperature was raised to a minimum of 2000°F in order to sinter the product. A feed rate of about 400 lb per hr resulted in a sulphur in the product of 0.1 to 0.4 pct.

Electric Furnace Reduction

The smelting was done in a single phase 75 kw furnace. This furnace consisted of a rectangular steel shell lined with magnecon brick to give a shaft of about 9 in. wide x 18 in. long x 30 in. deep. Below the slag level an inner lining of carbon was provided by baking in Soderberg paste. One taphole was installed level with the bottom of the shaft. Two manually operated 4 in. diam electrodes introduced the power to the furnace. Power was supplied by a 75 kw tap transformer though subsequent experience indicated that a 100 kw transformer would have been more adequate.

The furnace charge was calculated from the analyses of sinter, limerock, and coke, and batches were weighed out, mixed and charged. Feeding was at a suitable rate to keep the shaft fairly full. The furnace was tapped about every 1½ hr using an oxygen lance to open the taphole, all slag and iron being drained out each time. Tapping temperature was about 2800°F. After the first tapping the taphole was plugged with a wooden plug which made subsequent tapping much easier.

The quality of the sinter had a marked effect on the furnace operation, and best results were obtained with a well-graded sinter free from fines.

Some difficulty was experienced with the slag. This was partly due to the small scale of the operation, and partly to the lack of power to maintain the required temperatures. Normally iron slags should be less than 1 pct Fe instead of the 7 pct that was averaged during these tests. Part of this iron, 4 pct of the slag by analysis, was present as metallic iron that had been reduced but had not had the opportunity to settle out of the slag. Table I indicates an iron recovery to pig iron of 96.3 pct which

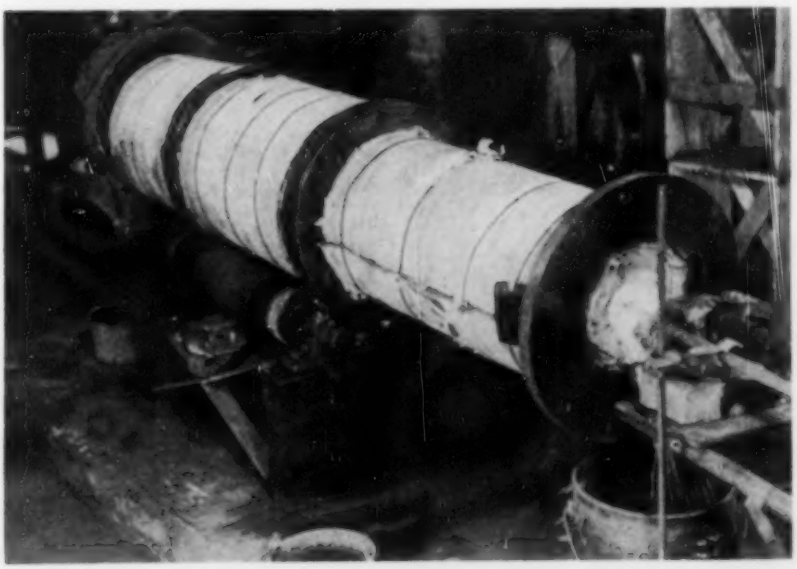

Iron concentrate was desulphurized and sintered in an oil-fired rotary kiln 4 ft diam x 48 ft long. Two passes were required.

Table II. Analyses of Impurities in Smelting Process

Material	Wt, Lb	Analysis, Pct						Weight, Lb					
		Pb	Zn	As	Sb	Sn	Cu	Pb	Zn	As	Sb	Sn	Cu
In													
Sinter	20,810	0.524	0.320	0.024	0.023	0.023	0.033	109.1	67.7	5.0	5.2	4.8	6.7
Out													
Pig Iron	13,704	0.0069	<0.006	0.025	0.008	0.025	0.07	0.9	0.6	3.2	1.1	3.2	8.9
Slag	7,742	0.53	0.15	0.031	0.094	0.040	—	42.8	11.6	2.4	8.0	3.1	—
Flue Dust	540	11.8	26.4	0.35	0.89	0.40	—	64.8	144.9	1.9	4.9	2.2	—

theoretically could have been raised by 2.5 pct to a total of 98.8 pct.

The small furnace with a small bath of slag and metal provided little opportunity for settling. Settling may also have been inhibited by the stirring action of the power. When the melt is tapped and both slag and metal run out, mixing may occur, and rapid freezing may prevent any further separation. The separation of metallics and slag is also influenced by the fluidity of the slag. The fluidity is partly a function of temperature which can be made higher when adequate power is available. The remaining iron, 3 pct of the slag, is present as iron oxide and indicates to what extent reduction did not go to completion, in this case 1.9 pct. This is dependent upon the time of contact, which in this operation was about 2 hr. This could be improved upon in a full sized furnace where the time of contact would be greater.

In sintering to remove sulphur, various amounts of the impurities are driven off. The greater part of the lead and most of the arsenic is removed. Most of the zinc, antimony, tin and copper remain with the sinter.

The behavior of the impurities during smelting is shown in Table II. The lead is distributed mainly between the slag and the fume, and due to its low solubility only a minor amount appears in the pig iron. A small amount of lead appears as metallic lead seeping out through the tap hole. Analysis of this is shown in Table III and the high tin content should be noted. With continued furnace operation a greater portion of the lead could be expected to collect in this manner as the furnace lining becomes saturated. It is unlikely that the concentration of lead in the pig iron would go any higher due to its low solubility.

The zinc present tends to leave the system almost entirely with the fume, due to its high vapor pressure in the metallic state. At any event the pig iron is consistently low in zinc, well below any concentration that might cause concern.

Because of their tendency to form stable compounds with iron when in the reduced state both arsenic and tin reported in the pig iron to the extent of nearly half the amount present in the system. A smaller proportion of antimony was also present, probably due to the same cause. However, the actual concentrations are not high enough to affect the quality of the pig iron. Confirming what can be expected from its particular characteristics practically all the copper present migrates to the pig iron. Even so the concentration is not particularly abnormal.

The analysis of the pig iron is given in Table II. In general it may be described as equivalent to a high quality low phosphorus premium grade pig iron. The silicon content would place it in the grade of a No. 2 foundry pig but operating conditions in a commercial furnace could be adjusted to give varying quantities of silicon at will.

Steel Production

The analysis of the pig iron produced and an examination of its microstructure indicated no significant abnormalities. Use of this experimentally produced iron in the foundry at Trail gave high quality castings. However, because of the association of unusual elements in the raw material, not normally found in iron ore, it seemed prudent to obtain a definite and independent evaluation of the pig iron for steelmaking. Arrangements were therefore made for a detailed investigation to be carried out in the laboratories of the Mines Branch of the Canadian Dept. of Mines and Technical Surveys at Ottawa.[1]

Mild carbon steels were made in a basic electric furnace using Cominco pig iron, structural steel scrap, and commercial pig iron in varying proportions in the different heats. Ingots poured from the steel were forged from approximately 5½ in. in diam to slabs 2½ in. in thickness. The forging qualities of the steel made with Cominco pig iron appeared equal to the steel made without Cominco pig iron.

Table III. Typical Analyses of Materials, Pct

Material	Fe	SiO_2	CaO	Al_2O_3	MgO	S	Mn	Pb	Zn	As	Sb	Sn	Cu	W
Iron concentrates	47.9	8.8	1.2	2.8	0.6	34.4	0.4	1.1	0.6	0.27	0.07	0.008	—	0.1
Iron sinter	58.5	10.7	1.8	2.97	0.45	0.1	0.79	0.524	0.325	0.024	0.025	0.023	0.033	—
Kiln flue dust	40.5	—	—	—	—	—	—	7.2	1.2	1.91	0.08	0.1	—	—
Pig iron*	—	—	—	—	—	0.05	0.77	0.0069	<0.006	0.025	0.008	0.025	0.07	<0.1
Slag**	7.0	24.8	41.3	12.9	1.2	—	0.76	0.53	0.15	0.031	0.094	0.040	—	—
Furnace flue dust	6.0	8.6	0.1	—	—	—	—	11.8	26.4	0.35	0.89	0.40	—	—
Lead bullion***	—	—	—	—	—	—	—	98	—	0.05	2.0	6.6	0.2	—

* Also contained 3.55, 2.08, and 0.08 pct respectively of C, Si, and P. ** Also contained 4.0 and 3.0 pct respectively of Fe and FeO.
*** Also contained <0.005, 0.04, and 21.1 oz per ton respectively of Bi, Au, and Ag.

The steel slabs 2½ in. thick were hot rolled to 1 in., ½ in. and ¼ in. thick plate. Visual and microscopic examination showed normal characteristics on all heats. Inclusions, microstructures and grain sizes on the as-rolled and normalized plate were normal.

Short time tensile tests were made on as-rolled and normalized plate at room temperature, 400°, 800°, 1200°, and 1600°F. Some lowering of the tensile ductility was found at 1200° and 1600°F but this is not unusual in the short-time testing of mild steel at elevated temperatures.

Hot bend tests were made on as-rolled plate, and the checking characteristics at 1600°, 1800° and 2100°F appeared similar in all heats.

Transition curves were plotted from the results of Charpy V-notch impact tests on as-rolled plate from all heats and normalized plate from two heats. The curves of the steel in the as-rolled condition were all within an acceptable band.

Weldability tests, using the Controlled Thermal Severity Weldability test, developed by the British Welding Research Assn. indicated that all steels had similar weldability.

Availability of Iron Concentrate

The ore from the Sullivan mine contains lead and zinc sulphides associated with a considerable proportion of iron sulphide. In the treatment of this ore at the Sullivan concentrator coarse size waste rock is first eliminated in a sink and float plant, then the lead and zinc are successively separated as sulphide concentrates by differential flotation. The tailings from this operation, which are predominantly pyrrhotite with varying proportions of pyrite and siliceous gangue and residual amounts of lead and zinc minerals, contain approximately 0.04 pct Sn as cassiterite, the coarser particles of which are recoverable.

The flotation tailings, amounting to some 6000 tons per day, are treated in a 33 ft Dorr hydroseparator for removal of low grade slimes. The underflow amounting to 2500 to 3000 tons per day is passed on to a flotation section to remove an iron sulphide concentrate and leave flotation tailings containing recoverable tin. This *iron concentrate*, amounting to 1200 to 1700 tons per day contains 47 pct Fe and 32 to 33 pct S. About 400 tons per day is roasted to provide acid for the Kimberley phosphate plant and the remainder is stored in the *iron tailing* storage area.

Economic Considerations

It is evident that the recovery of iron from this high sulphide product must be integrated with an operation which will consume sulphuric acid. When the Kimberley fertilizer dept. was completed in September 1953, the recovery of iron was brought one step nearer practical realization. Even so, the scale of operation of the fertilizer plant, which determines the quantity of iron oxide produced at the roasting plant, sets a limit to the quantity of iron that can be produced. This eliminates the possibility of a conventional iron blast furnace producing 500 to 1000 tons of pig iron per day and leads to the consideration of the electric furnace process.

An electric furnace process based on 100 tons of iron per day would have a number of advantages at Kimberley. The scale of operation is more in keeping with the supply of iron oxide. Furthermore the operation would use electric power, which Cominco has in abundance at moderate cost, and it would be well-located with respect to the only B. C. source of metallurgical coke at Michel. With the advantages of raw materials and power, it is apparent that the Kimberley location is as well situated as any in B. C. or in the Pacific Northwest for small scale production of pig iron. The potential market for the product is a matter of some uncertainty. Western markets are relatively small and have been so dominated by scrap metal that outlets for pig iron have not developed normally.

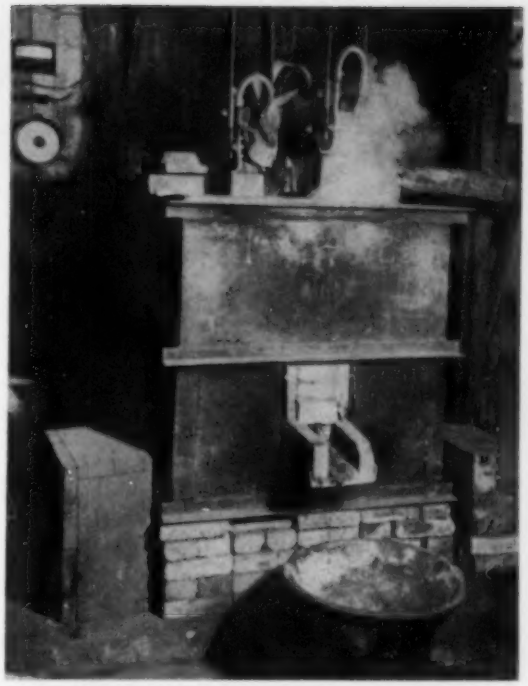

Smelting was done in a single phase 75 kw furnace. Shaft is 9 in. wide x 18 in. long x 30 in. deep. Two 4-in. diam electrodes introduce power to the furnace.

The general pattern of development for such an operation at Kimberley has been apparent for some years. The use of the electric furnace for smelting pig iron is not new, but has been developed into commercially successful operations in Europe. The engineering and metallurgical problems associated with the process are understood, and have been solved. The novel feature of the present scheme is the presence of residual lead and zinc, with smaller quantities of arsenic, antimony, tin, and copper in the iron concentrates which are the primary raw materials for the process. The deportment of these elements could be predicted with some degree of confidence and the pilot plant tests established without doubt the possibility of making an acceptable standard grade of pig iron free from deleterious effects arising from the presence of abnormal nonferrous metals.

Reference

[1] B. G. Hunt, E. J. Kwasney, W. P. Campbell, and S. L. Gertsman: Experimental Production of Iron and Steel from Cominco Iron Concentrates. *Canadian Mining & Metallurgical Bulletin* (May 1955) **48**, pp. 281 to 291.

Domain Structures Suggest Key to Enigma of Magnetic Force

by C. D. Graham, Jr.

NO ONE knows when man first stumbled onto the mysterious phenomenon of magnetism. *Stumbled* is perhaps an appropriate word, for one legend holds that an ancient shepherd named Magnes first discovered magnetism when the iron nails in his shoes stuck to the ground in a region rich in magnetic ore.

Magnes was doubtless confused by his discovery. He had every right to be. Even today, scientists and engineers who constantly work with magnets are sometimes nagged by the feeling that the whole business is highly improbable. The idea that two pieces of metal can attract one another across an empty space seems basically absurd. This apparent flouting of the teachings of experience doubtless accounts for both the fascination of toy magnets and for the long search by science for an understanding of the origin of the mysterious forces of magnetism.

Absurd or not, magnetism is here to stay. In a society based increasingly on electric power, magnetism is essential—for electricity and magnetism go always hand in hand. From the generator at the power station, through the transformers and switchgear of the distribution system, through the electric meter in the basement and right out to the speaker on a hi-fi rig, magnets and magnetic materials are at work. In relays and rolling mills, swagers and synchrotrons, science and technology depend on magnetism.

How much do scientists know about this useful mystery of magnetism? One is apt to be impressed with the accomplishments of all these heavy thinkers when one counts up the books and papers written on magnetism and magnetic materials in the 136 years which have elapsed since Hans Christian Oersted first twitched a compass needle with an electric current in a nearby wire. On the other hand when one looks at the mountain of uncertainties, assumptions, and unknowns which still lie ahead, one is not so sure.

Fortunately for the peace of mind of technical people everywhere, some progress has been made both in developing useful magnetic materials and in understanding the fundamental nature of magnetism. Generally speaking, these two have been separate developments. Magnetic materials have been found and improved by the sledge-hammer technique of trying things until you find one that works —being guided by experience and counting heavily on luck. Science has played a very minor part in this development.

It is a commonplace observation that in metallurgy, the science is far behind the art. It is, however, also widely held that this state of affairs may be changing. In recent years, for example, understanding of the mechanical properties of metals has been greatly accelerated by the development of the dislocation concept. One of the great advantages of the dislocation theory, as of all useful theories, is that it provides a common basis for thinking about a number of different properties. It seems safe to say that if the behavior of dislocations in metals under various conditions were better understood comprehension (and control, within limits) of a wide variety of mechanical properties such as strength, fatigue life, creep resistance, and hardness would be evident.

C. D. GRAHAM, JR. is associated with the General Electric Research Laboratory, The Knolls, Schenectady, N. Y.

The Ferromagnetic Domain

A comparable state of affairs exists in the field of magnetic materials. It is now universally accepted that the key to the behavior of magnetic materials is the ferromagnetic *domain*. All magnetic materials contain domains. These domains are small regions in the material which are completely magnetized. Domains are perfect magnets; they are always magnetized, and always completely magnetized. A domain cannot be demagnetized except by heat. An externally applied field may change the direction but not the magnitude of its magnetization.

A magnet made out of a series of isolated domains, all magnetized in one direction, should be many times more powerful than any magnet now in use. In fact, very considerable progress has already been made toward producing such *fine particle* magnets. But in ordinary materials, like the iron nails in the shepherd's shoes, the domains are not isolated and their moments or magnetizations are not all aligned in one direction. Normally the domain magnetizations are distributed in various directions so that the net magnetization of the whole sample is zero. In this way a piece of iron appears to be unmagnetized even though it is made up of a collection of very powerful permanent magnets.

Fig. 1—Diagram of a simple domain configuration in a grain of magnetic metal. The arrows represent direction of magnetization in each domain.

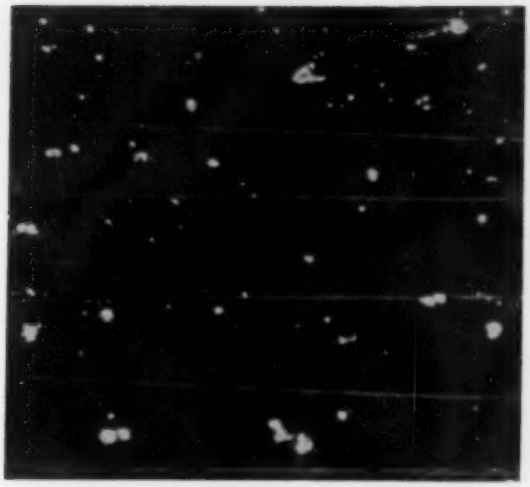

Fig. 2—Simple domain structure in a grain of silicon-iron is shown under dark field illumination magnified 150X. Surface of grain is parallel to 110 plane.

In a single grain, domains are normally magnetized only in certain crystal directions. One possible arrangement of domains in a grain is illustrated in Fig. 1. It can be seen that each domain magnetized in a given direction is exactly balanced by another domain of equal volume magnetized in the opposite direction.

People working on domains have an advantage over people working on dislocations. It is possible to see domains directly under a microscope. Figs. 2 and 3 are photographs of domains in two grains of silicon iron. The resemblance between Fig. 2 and the center part of Fig. 1 is clear. The photographs also illustrate some of the properties of domain boundaries. For example, domain boundaries as viewed on the surface of a grain are usually straight lines, or nearly so, and the lines meet one another at definite, reproducible angles. The observed domain structure in a grain is closely connected with the crystal orientation of the grain. In fact, only on grains of certain simple orientations are the surface domain patterns simple enough to be interpreted without confusion.

Domains are observed by the powder or Bitter pattern technique in which a colloidal suspension of a ferromagnetic material, usually magnetite, is placed on the electropolished surface of the specimen. The colloidal particles collect along the lines where domain boundaries intersect the surface since these are the regions of greatest field strength. Electropolishing is necessary to eliminate the surface strains produced by mechanical polishing, which could easily obscure the true domain structure. The lines of colloidal particles are visible under the microscope. Dark field illumination is usually employed so that the boundaries appear light against a dark background as in Figs. 2 and 3.

Actually, the advantages of direct observation are no longer completely denied to dislocation enthusiasts. In favorable cases, individual dislocation sites can be revealed as etch pits by the use of certain reagents. Fig. 4 shows these dislocation etch pits in silicon iron.

The most important fact about domain boundaries is that they move. When a magnetic field is applied to a soft magnetic material, the domains magnetized parallel or nearly parallel to the field will grow at the expense of other domains. This growth produces a net magnetization in the direction of the applied field, as illustrated for a simple case in Fig. 5.

This picture of the magnetization process amounts to saying that the mechanism by which magnetic materials magnetize is by the motion of domain boundaries—at least in the steeply rising portion of the magnetization curve which is of greatest importance in most materials. The problem of understanding magnetization is thus reduced to the more concrete problem of understanding domain boundary movements.

Just as a knowledge of dislocation behavior should lead to an understanding of mechanical properties, so a knowledge of domain behavior should lead to an understanding of magnetic properties. If anything, the prospects for magnetics research are the brighter of the two, since domains are large enough to be observed directly and easily.

Areas of Research

Domain wall motions are known to be responsible for magnetic properties and a workable method for observing domain boundaries is available. Armed with these two pieces of information, it should be

Fig. 3—Simple domain structure in a grain of silicon-iron is shown under dark field illumination magnified 150X. Surface of grain is parallel to 110 plane.

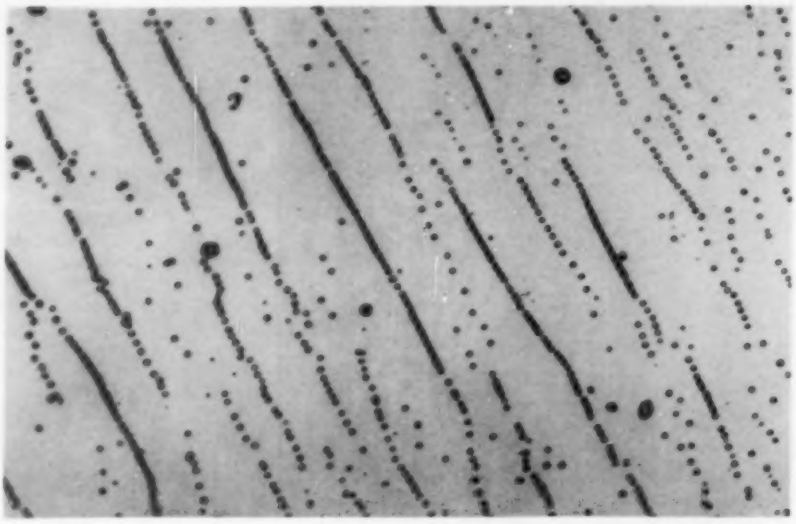

Fig. 4—Etch pits on dislocation sites in a silicon-iron grain are shown magnified 750X. Photographs are by C. G. Dunn and W. R. Hibbard, Jr.

possible to devise a research program that might lead to the elimination of much of the trial-and-error development characteristic of work on magnetic materials.

Preferred orientations, or textures, are known to have a pronounced effect on magnetic properties. The reason is clear enough: since domains are normally magnetized parallel to certain crystal directions, changing the crystal orientations will change the domain structure. In particular, by having one of the favored crystal directions, called *easy* directions, parallel to the applied field, it is possible to make the magnetization process easier. The result, in terms of magnetic properties, is to raise the knee of the magnetization curve (which means obtaining a higher flux density for a given applied field) and also to reduce the power losses when the material is used in electrical equipment such as transformers. *Grain-oriented* silicon steels are currently used in large quantities as transformer core materials because of their superior properties along the rolling direction.

However, it is not clear just how *perfect* a texture should be to give the best combination of properties. Nor is it certain that the present texture is the best possible one for all applications. To approach this problem from the domain point of view, it will be necessary to observe domain structure and domain boundary motion in single crystals and bicrystals of controlled orientation. This kind of experiment could yield information about the nature of the texture and the proper degree of perfection required for a given purpose. Given these specifications, the metallurgist could concentrate his efforts on producing a given material of known value, rather than on juggling variables in the hope that an improvement in properties will result.

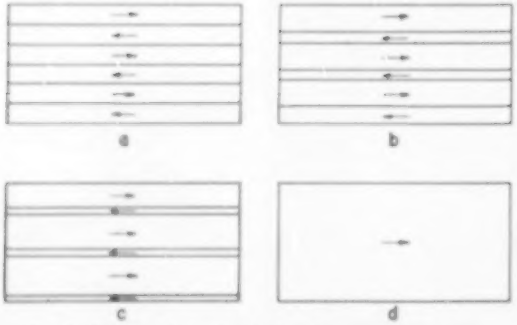

Fig. 5—Diagram shows domain boundary movements during magnetization: a. no applied field, b and c. increasing field applied from left to right, and d. still higher applied field causing saturation of the specimen.

One of the most persistent problems in the metallurgy of magnetic materials is the effect of grain size. The confusion surrounding this point has two major causes. First, it is difficult to change grain size without also altering some other property of a material, particularly when the grain size heat treatments involve high temperatures and reducing atmospheres, as in the case of iron. Second, grain size probably affects magnetic properties in more than one way. One effect of grain boundaries is to inhibit the motion of domain walls, which leads to increased coercive force and higher losses. Even when the domain structure in a grain is simple, wedge-shaped *closure domains* are frequently found at grain boundaries, as shown in Fig. 6. The magnetization process involves the rearrangement of these domains, so that their presence makes magnetization more difficult. From this point of view, grain boundaries are undesirable in soft magnetic materials, and should be eliminated. This means that the grain size should be large. Or perhaps the texture should be made so perfect that the grain boundaries separate grains of almost identical orientation; such grain boundaries might no longer be a serious obstacle to domain boundary movements. Direct observation of domain boundaries in motion at grain boundaries of various kinds should give the answer.

On the other hand, grain size appears to influence domain size. A fine-grained material has more domain wall per unit volume than a coarse-grained material. There is good reason to think that transformer core losses are reduced by increasing the number of domain walls, so from this point of view a fine-grained structure seems desirable. It does not appear possible to observe domain boundaries directly by the powder method if the boundaries are moving under 60 cycle excitation, but there are in-

direct means of studying domain wall motions in simple cases by the magnetic changes so produced. In this way it is possible to approach the relation between domain size and magnetic properties under ac conditions.

Inclusions are a known source of trouble in soft magnetic materials. It is often possible to observe closure domains around inclusions, as shown in Fig. 7, and the mechanism by which such a domain structure can inhibit domain wall motion is understood. Theory, however, does not say much about the effects of inclusion size or shape on domain wall motion, and here a direct experimental approach should be possible. By observing domain wall behavior around inclusions of various kinds and sizes, one might be able to identify the most harmful inclusions and to note the inclusion size and distribution which will minimize power losses.

The effects of internal stresses are understood less than any of the variables considered above. The nature of an internal stress resulting from local deformation, unequal contraction on cooling, or some other source, involves the arrangement of dislocations in the metal, and this arrangement is not generally known. Thus from a theoretical point of view, the problem is difficult because the form of the stress field is unknown. The experimental approach is also difficult, since stresses generally distort the domain structure so severely that it is impossible to interpret. A number of workers have investigated the effects of uniform stress on domain structure. Another possible approach would be to observe domain behavior in the vicinity of a localized distortion such as a slip line.

Cooling magnetic materials through the Curie temperature while applying a magnetic field sometimes produces marked changes in magnetic properties. However, the mechanism by which these changes occur is not always clear. Certainly the magnetic annealing must affect the domain structure, but the nature of the change and the process by which it takes place have not been established. A series of simple experiments in this field could be of enormous importance in the development of magnetic materials.

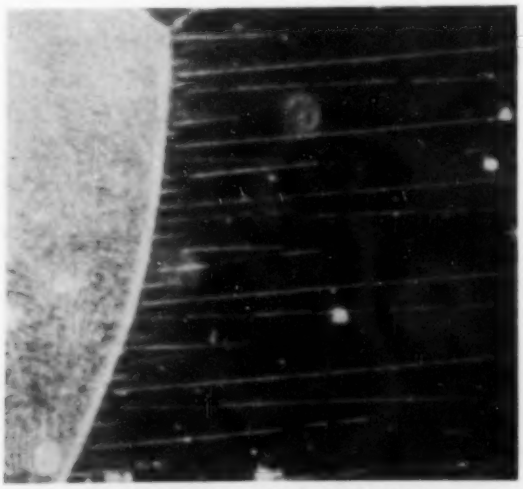

Fig. 6—Domain structure at grain boundaries are shown in silicon-iron magnified 150X. Heavy curved line is the grain boundary. Note wedge-shaped closure domains extending into the central grain from the grain boundary.

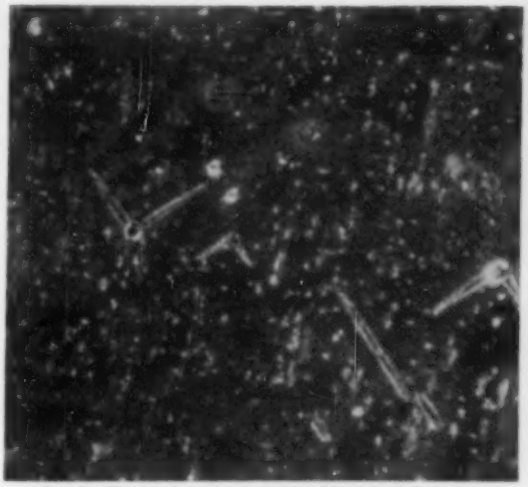

Fig. 7—Closure domains around inclusions in silicon-iron are shown. Note double wedges radiating in a V from the inclusions. Small light spots in background are particles used to make domain walls visible.

Most of this discussion has concerned soft magnetic materials, but the same general considerations must apply to permanent magnet alloys. The difference, of course, is that for permanent magnets one needs to make domain motion difficult, so that the material, once magnetized, cannot be easily demagnetized. It is difficult to observe domains directly in good permanent magnet materials, since they are usually complex alloys, highly strained. Information gleaned from studies of domains in soft materials, however, should be of value in understanding and improving permanent magnet materials.

Conclusion

Since domain boundary movements are responsible for most important magnetic properties, the study of domain structure and domain boundary motions under various conditions can be of the greatest possible value in understanding, predicting, and controlling the properties of magnetic materials. Among the variables which may be approached by the observation of domains are the effects of textures, grain size, inclusions, internal stresses, and magnetic annealing. In particular, knowledge of the effects of metallurgical structure on domain behavior should make it possible to predict in advance the structure required to produce the magnetic properties needed for a particular application. As this stage is approached, the trial-and-error method of improving magnetic materials will slowly give way to the simpler, more direct, and more economical procedure of working to produce a given structure, with reasonable confidence that it will possess the required properties.

References

The general subject of magnetism, with emphasis on magnetic materials, is thoroughly covered by R. M. Bozorth: *Ferromagnetism* (1951) D. Van Nostrand, New York. Specific treatment of the domain theory is given by K. H. Stewart: *Ferromagnetic Domains* (1954) Cambridge Univ. Press, Cambridge. C. Kittel: Physical Theory of Ferromagnetic Domains (1949) *Rev. Mod. Phys.*, **21**, p. 541. Experimental details on the observation of domain walls are given by H. J. Williams, R. M. Bozorth, and W. Shockley: Magnetic Domain Patterns on Single Crystals of Iron (1949) *Phys. Rev.*, **75**, p. 155.

Cast structure is shown on a machined and etched longitudinal section through consumably melted 70 w/o Zr-30 w/o uranium ingot.

Sound Uranium Ingots Cast Using Consumable Electrode Arc-Melting

by F. R. Lorenz and W. J. Hurford

SOUND uranium ingots have been successfully produced by melting derby uranium with the consumable electrode arc-melting process. This process is also clean and easy to control when remelting uranium previously vacuum induction melted and cast.

Although no data are available on the difference in the quality of the ingots produced from the two types of melting stock, the improved nature of the operation in remelting previously vacuum melted stock would indicate that a better quality might be obtained. It should be possible to make sound large diameter uranium ingots by similar methods.

Westinghouse Atomic Power div. first utilized arc-melting in 1949 when small laboratory furnaces for the nonconsumable electrode (tungsten tip) arc-melting of zirconium were placed in operation and has since been active in the development of techniques for numerous applications of nonconsumable and consumable electrode arc-melting. Consumable electrode remelting has been used as an integral part in the production of fuel alloys for various reactor projects. The first recognition at Westinghouse Atomic Power div. of the possibilities for consumable melting of uranium was in 1952, and in November of that year, the first melts of natural uranium were made by the consumable electrode process. Since that time a wide variety of uranium and uranium alloy remelts have been made by this method. The alloys have been principally additions of zirconium or molybdenum to uranium, and the alloy electrodes have been made either by non-consumable electrode arc-melting or by vacuum induction melting.

F. R. LORENZ and W. J. HURFORD are Supervisory Engineer and Section Manager respectively, Westinghouse Atomic Power div., Westinghouse Electric Corp., Pittsburgh.

Uranium Melting Practice

The first uranium arc-melting program was concerned primarily with production of ingots of low carbon bearing uranium suitable for fabrication into slabs which could then be processed to uranium foil. Uranium derbies (metal in the as-reduced conditi n, approximately 4 in. thick and 8 in. diam) were prepared for melting by sawing ½ in. from the top in order to remove the high magnesium and slag bearing material. This was followed by forging into a consumable electrode of about a 2½-in. octagonal section and cutting to a 26-in. length. Electrode fabrication was done by heating the uranium in a carbonate salt bath (39 pct K_2CO_3, 33 pct $NaCO_3$, 28 pct Li_2CO_3) at 1220°F and forging on a press. At first the end of the forged bar was shaped into a square section and attached to the water-cooled copper electrode by the copper collet assembly illustrated in Figs. 1 and 2. These figures also show the uranium butt end remaining after completion of a melt. Because of the difficulty in consistently obtaining a good fit into the collet, some of the consumable electrodes were attached by drilling and tapping one end of the forged uranium bar and then screw-

Fig. 1—Components of copper collet assembly shown after a melt are: retaining ring, collet which screws onto plug at end of water cooled electrode, and uranium butt.

ing this onto a threaded plug at the end of the water-cooled electrode assembly. Fig. 3 is a schematic arrangement of a typical consumable electrode furnace similar to the one used for this work, and Fig. 4 is a photograph of the laboratory furnace used for this work.

In addition to the melting of derby uranium stock, some work was done with the remelting of vacuum induction cast ingots to obtain sound, larger diameter ingots.

The furnace operating procedure for a melt of uranium going from a 2½-in. diam electrode to a 4-in. diam ingot is outlined as follows:

A—Evacuate furnace system to about 20 microns and purge with helium.

B—Repeat A.

C—Evacuate to 20 microns, refill to atmospheric pressure with a mixture in the ratio of 1 helium:1 argon.

D—Reduce system pressure to about 15 in. Hg.

E—Lower the electrode assembly, with the power on, until an arc is established by striking a layer of metal chips which has been placed on the mold bottom. The arc is usually established with about 800 amp.

F—The electrode is withdrawn after striking the arc to maintain 25 to 30 arc v, and as the metal starts to melt off, the electrode is lowered as it is consumed in order to maintain an arc of 25 to 30 arc v and 2300 amp. This condition gives a melting rate of about 7 lb per min in converting an electrode of 2½-in. diam to an ingot of 4-in. diam, or a power consumption of 0.16 kw hr per lb.

G—Shutdown is achieved by reducing the power in increments of 600 amp to make the ingot top sound and free of shrinkage cavities.

H—The ingot is removed by inverting the copper mold. If difficulty is experienced because of scored and worn molds, the removable mold bottom (sealed with an O ring assembly) is taken off and the ingot pushed out.

Results Obtained From Melting Uranium by Consumable Electrode Arc-Melting Process

A—Uranium melting can be accomplished in either a partial vacuum or an inert atmosphere. Uranium is cast in a water-cooled copper mold, and the arc is established and maintained from a uranium electrode. These conditions obviate the melting contamination caused by certain atmospheres, by the graphite or refractory crucibles of induction melting, or by the tungsten tip in the non-consumable electrode type of arc-melting.

B—When the melting cycle is properly controlled sound uranium ingots are produced having no primary or secondary pipe or shrinkage cavities. Soundness is achieved with the additional cost and time for the remelt, and some surface conditioning treatment is also necessary. However, this could be accomplished with almost no sacrifice of material by a welding treatment to remelt the surface.

C—Larger diameter ingots can be produced from smaller ones cast by other means without resort to any intermediate processing such as rolling out to strip or rod and chopping prior to remelting by nonconsumable electrode arc methods.

D—Raw as-reduced metals, such as derby uranium, can be converted into useful solid shapes by fabricating an electrode from the raw material and then melting and casting into an ingot.

E—Method provides a satisfactory means for remelting certain alloys to achieve homogeneity of alloying addition.

I—Water flow around the mold assembly during melting is maintained at an absolute minimum just above that flow required to prevent localized boiling on the mold surface.

Description of Uranium Ingots

The consumable electrode arc-melting technique produced ingots of 4-in. diam that were entirely satisfactory for the intended purpose of providing stock for the fabrication of uranium foil.

A 4-in. diam ingot is shown in Fig. 5 and a longitudinal section of a similar 80-lb ingot is illustrated

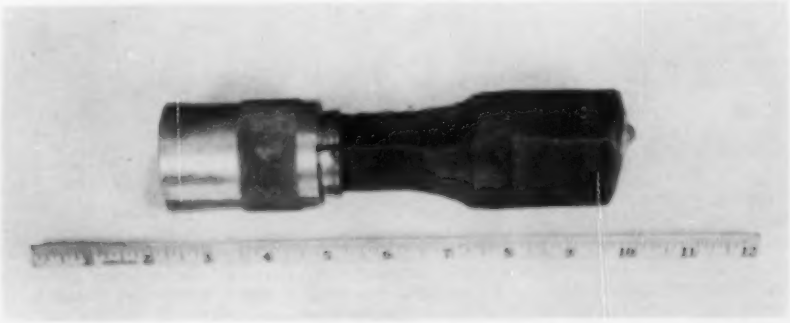

Fig. 2—Collet and butt of forged uranium derby electrode are shown assembled after completion of a melt.

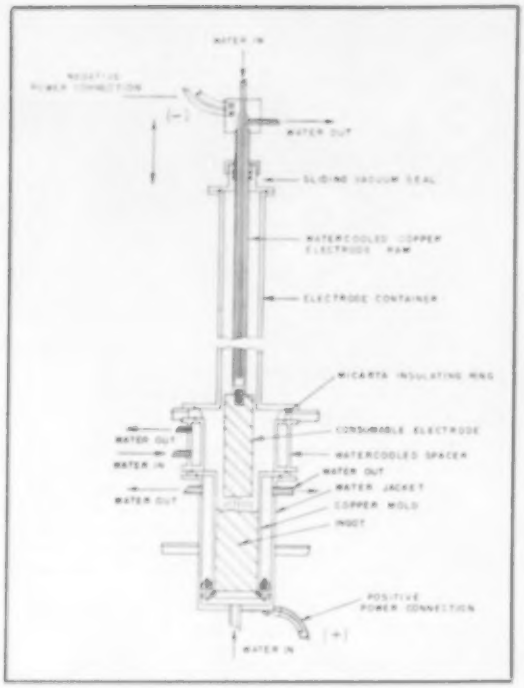

Fig. 3—Diagram of consumable electrode arc melting furnace illustrates component parts.

in Fig. 6. An ingot surface representative of the worst condition from this process which occurs when melting derby stock is that shown in Fig. 5 which shows the pock marks or blisters resulting from splatter of molten metal up onto the cold mold wall above the rising molten pool on top of the casting. These spots do not usually remelt when the molten metal of the ingot advances past them, but additional experience will minimize this condition by proper control of the melting conditions. The ingots made during this investigation were cleaned up on the surface by machining 1/16 in. off the radius to eliminate these blisters. Depending upon the amount of hot work done to the ingot and the subsequent use of the stock produced, surface conditioning might not be necessary under certain circumstances.

The surface can be improved by a weld-conditioning treatment which has been used quite successfully on zirconium ingots ranging in size from 4-in. (40 lb) to 12-in. diam (1000 lb). This consists of mounting the ingot in a jig in a controlled atmosphere chamber so that it can be rotated in such a manner that an overlapping spiral path can be remelted under a welding torch. This can be done automatically and effectively remelts the entire surface to some depth, determined by the welding conditions, thus eliminating the small holes under the surface which are associated with the freezing of small droplets of metal splashed on the mold wall during the melt.

The longitudinal section (top and bottom halves) of the uranium ingot shown in Fig. 6 is representative of the degree of soundness achieved by this melting technique. There is no pipe or shrinkage cavity. Only a very slight degree of sub-surface porosity exists under the surface blisters and is readily removed by a light skinning operation or by the weld-conditioning mentioned previously. A very thin layer of porosity is present under the top ingot surface. This particular ingot was made by remelting an electrode cast from a vacuum-induction melt. The melt is considerably cleaner and easier to control than one made by using raw derby uranium. The latter is accompanied by a considerable evolution of volatiles which tend to make the arc quite unstable, and this results in increased splatter on the mold wall to produce the type of surface as on the ingot in Fig. 5.

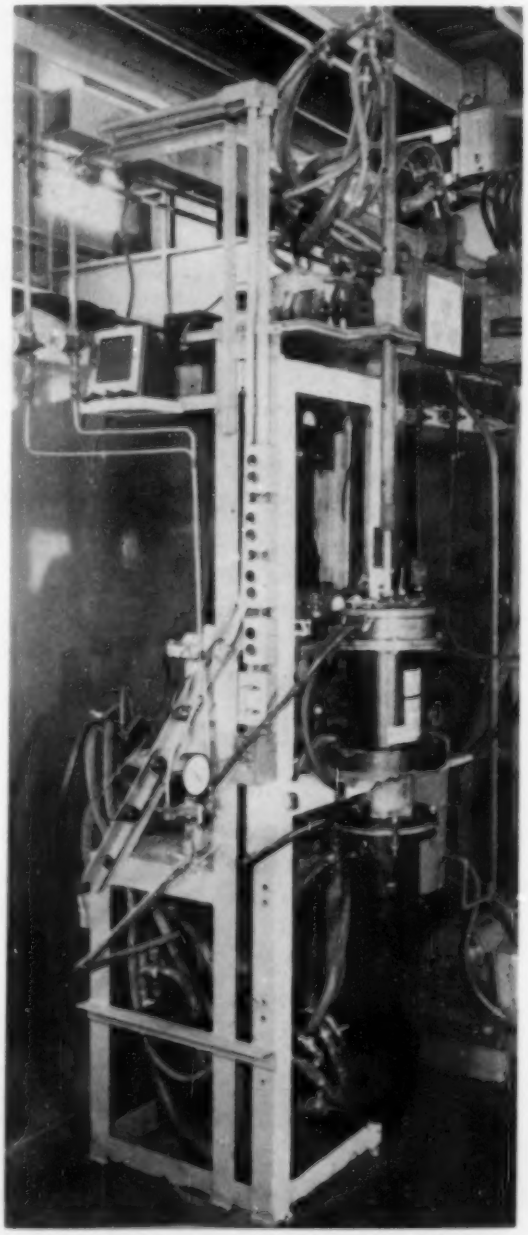

Fig. 4—Laboratory consumable electrode arc furnace modified from standard nonconsumable type furnace by the addition of deep spacer.

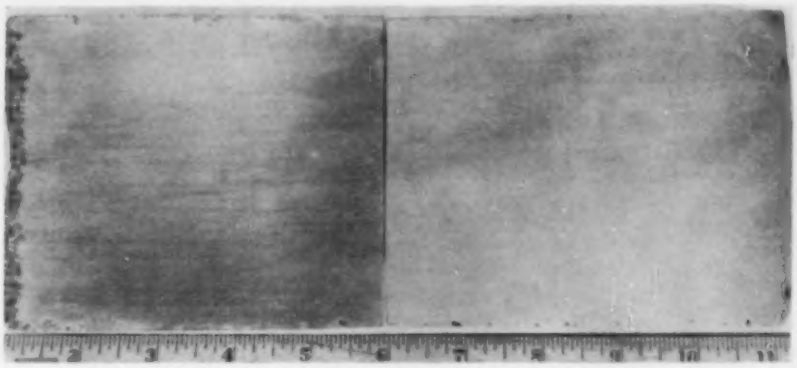

Fig. 6 — Machined and etched longitudinal section through consumably melted 4-in. diam uranium ingot is shown. Top of ingot is at left. Dark spots are etching stains around voids.

The 4-in. diam ingots produced from consumable electrodes of forged derby uranium, in this investigation, were used to produce some rather good uranium foil. The ingots were forged, rolled to slabs, and machined to ¼x5½x20 in. These slabs were then rolled in a series of operations to produce foil 0.001-in. thick x 5-in. wide. The material handled very nicely in the final rolling on a Sendzimir mill.

Considerations for Production Applications

For the purpose of producing large ingots, the furnace construction is such that the electrode container height is limited only by the overhead room required to raise and lower the electrode assembly. It is practical to make long electrodes by welding together cast or forged bars as needed to produce such ingots. Welding of uranium electrodes has been done successfully for bars of 2½-in. diam in a helium atmosphere box and should be adaptable to welding in air provided proper ventilation is provided. An inert gas shield would probably be of value if gaseous contamination of the weld became a problem. Zirconium and zirconium alloy electrodes are customarily welded together in air.

Fig. 5—As cast, 4-in. diam natural uranium ingot is shown as produced by consumable electrode arc melting process.

The as-reduced metal might be used directly as electrodes by welding together derbies that had been conditioned by pickling to remove slag from the outside. In some instances it might be necessary to flatten the top and bottom by either machining or upsetting on a forge in order that a welded electrode might be fabricated. This type of operation would probably be rather difficult.

The furnace system for a given capacity furnace is much more compact than is a vacuum-induction melting unit of similar capacity. The floor space required is minimized, the system volume is also smaller, requiring lower capacity vacuum pumping systems. It must be recognized, however, that since the melt is accomplished in an inert atmosphere of approximately 1/3 atmospheric pressure and that the entire mass of metal is never molten at any instant, the metal does not have opportunity for appreciable removal of volatiles and light, floatable impurities as in vacuum-induction melting. For large diameter ingots, it is known that the depth of molten metal is usually greater than 6 in. When the electrode metal contains appreciable quantities of volatiles which are not removed by a single consumable melt or when the ingot cast therefrom is porous because of residual gases, the single melted ingot can be used as an electrode and can be consumably remelted to a larger diameter ingot which will probably be sound. A double melting process such as this is currently being used to produce sound ingots from sponge zirconium which contains large amounts of volatile materials and which yields porous ingots after only a single consumable melt. Depending on the requirements for the metal, it might then be better to vacuum-induction melt and cast electrodes which would be remelted by the consumable electrode arc-melting method.

Acknowledgment

The work described was carried out in connection with the investigation of methods for melting materials used in the manufacture of components for nuclear reactors under AEC Contract AT-11-1-GEN-14.

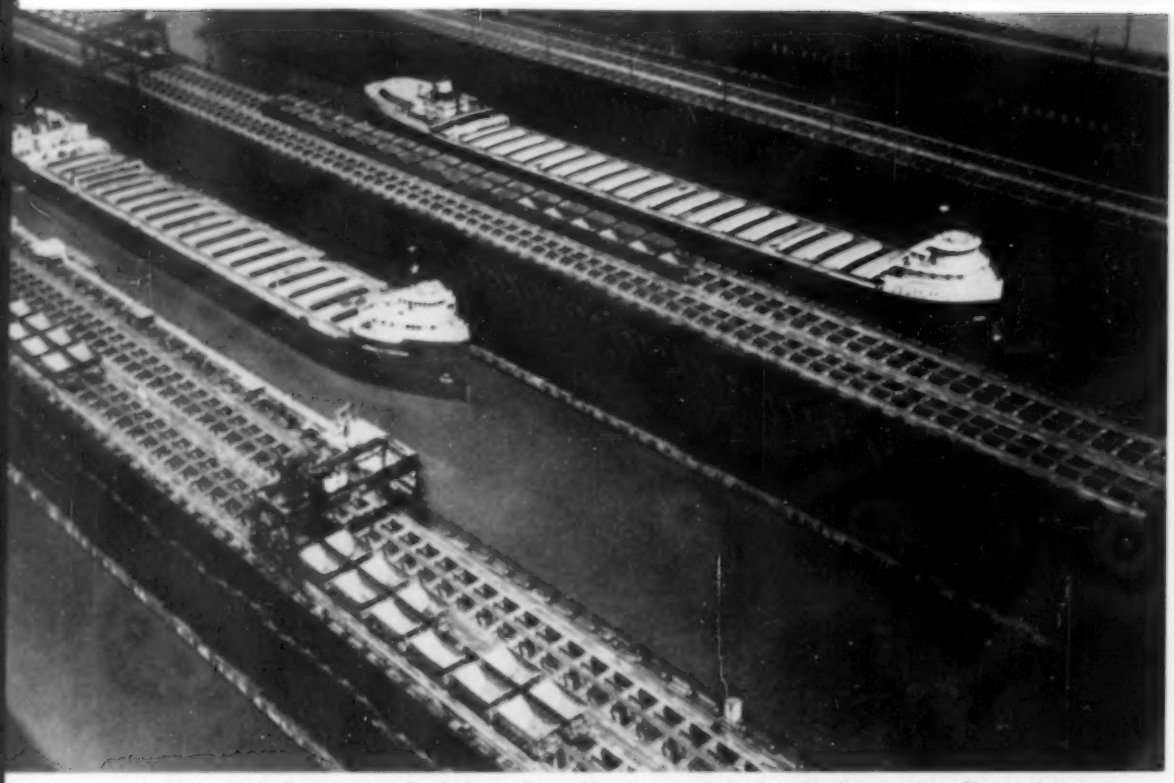

Aerial view of the Great Northern Ore Docks at Allouez, Wis. show magnitude of ore blending operation. Photograph is courtesy of *Skillings Mining Review*.

Ore Blending at Shipping Dock Insures Uniform Blast Furnace Burden

by Myron W. Griswold

CONTINUOUS efficient operation of a blast furnace in producing a desirable grade of pig iron is dependent, to a large degree, on the uniformity of the raw materials with which the furnace is burdened. Coke, ore, and limestone are the primary raw materials charged into the furnace. By the nature of their origin, coke and limestone tend to be more uniform in their analysis than the ores.

The extreme lack of uniformity of the Minnesota ores, as produced, necessitates using various methods to produce a uniform shipping grade. The ore grading dept. supplies the ore boats with cargoes of constant analysis. Each cargo is well blended so that there is a minimum analytical variation from hatch to hatch. In this way the blast furnace dept. is greatly aided in producing a constant output of desirable pig iron.

Ores are analyzed for iron, phosphorus, silica manganese, alumina, and moisture. In order to obtain a representative sample for analysis, each car of ore is sampled at either 18 or 24 points. In the 18 point method, a rope with knots at 18-in. intervals is cast diagonally across the top of the car. A ¼-lb scoop of ore is then taken from directly underneath each of the 18 knots. In the 24 point method, a rope with eight knots spaced at 24-in. intervals is used. This rope is cast along the length of the car three times, once at the peak and once on each slope about two-thirds of the way down from the peak to the

M. W. GRISWOLD is Ore Grader, Iron Mining Dept., Inland Steel Co., Ironton, Minn. This paper was presented at the AIME Blast Furnace, Coke Oven and Raw Materials Committee Meeting, Philadelphia, Apr. 18 to 20, 1955.

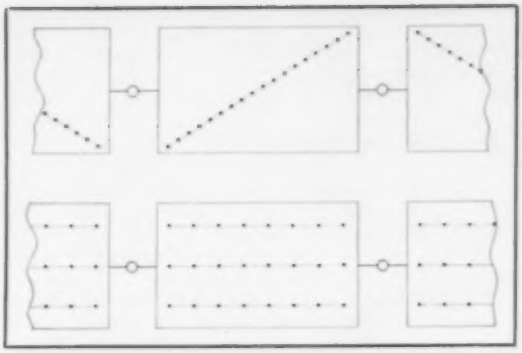

Fig. 1—Sampling points in the 18 and 24 point methods are shown. Inland's furnaces are burdened on these results rather than on Lower Lakes analysis as formerly.

side of the car. Each time the rope is cast a ¼-lb sample is taken from beneath each of the eight knots.

For economy in analytical cost, cars are grouped for sampling. Non-uniform ores are combined into groups of five and uniform ores may be combined into groups of seven cars. Hence in a five car group, the sample consists of either 90 or 120 scoops and in a seven car group the sample consists of either 126 or 168 scoops. Whether the 18 or 24 point method is used is a matter of company preference as either gives accurate results. Inland has concluded that the Upper Lakes sampling and analysis methods are so accurate that all furnaces are now burdened on these results rather than on Lower Lakes analysis as formerly. Fig. 1 illustrates both of these methods.

Grades of Ore Shipped

Except for certain specialty grades which are shipped from time to time, Inland ships two grades of blast furnace ore from the state of Minnesota. The first in point of tonnage is the Leslie which is a Mesabi Range low phosphorus non-Bessemer grade shipped through the Great Northern Ore Docks at Superior, Wis. The second is the Anderson grade which is a high phosphorus manganiferous grade originating primarily on the Cuyuna Range and shipped through the Northern Pacific Ore Dock at Superior. The makeup of these two grades each year is somewhat of a compromise between what the blast furnace dept. would like and what the raw materials dept. has available. The Leslie typically consists of an aggregate of about 2 million tons with a natural percentage analysis of about 49.00 iron, 0.060 phosphorus, 10.50 silica, 0.70 manganese, and

Table I. Typical Season Allotment of Leslie Grade

Ore	Tonnage†	Fe	P	SiO_2	Mn	Al_2O_3
A	120,000	45.00	0.080	8.20	0.60	7.20**
B	380,000	50.30	0.050	12.40	0.60	1.10
C	190,000	47.10	0.050	8.10*	1.10	1.80
D	30,000	46.50	0.030*	10.50	1.50**	0.90*
E	130,000	46.80	0.070	9.50	1.30	1.60
F	80,000	43.00*	0.080	12.20	0.70	4.00
G	10,000	49.00	0.060	10.70	0.80	1.00
H	60,000	47.80	0.070	10.90	0.70	2.40
I	260,000	49.50	0.070	11.70	0.70	1.60
J	140,000	49.70	0.050	9.70	0.70	1.10
K	15,000	44.30	0.060	15.70**	0.90	2.10
L	200,000	51.40**	0.050	12.10	0.40*	1.00
M	235,000	45.90	0.090**	8.50	0.50	5.66
Average		48.31	0.063	10.50	0.71	2.43

† Total, 1,850,000 tons. * Denotes extreme low. ** Denotes extreme high.

Table II. Ore Order for a 16,000 Ton Cargo

Ore	Tonnage	Fe	P	SiO_2	Mn	Al_2O_3
B	1700	50.30	0.050	12.40	0.60	1.10
C	2400	47.10	0.050	8.10	1.10	1.80
E	1500	46.80	0.070	9.50	1.30	1.60
F	1000	43.00	0.080	12.30	0.70	4.00
I	3200	49.50	0.070	11.70	0.70	1.60
L	3200	51.40	0.050	13.10	0.40	1.00
M	3000	45.90	0.090	8.50	0.50	5.66
Average		48.33	0.065	10.55	0.71	2.41
Guarantee	—	48.31	0.063	10.50	0.71	2.43

2.25 alumina. During the 1954 shipping season this tonnage came to Inland from 10 different producers and with widely varying analyses. The Anderson usually consists of about 500,000 tons analyzing in the aggregate about 45.00 iron, 0.20 phosphorus, 11.50 silica, 3.0 manganese, and 2.0 alumina. This grade in 1954 came from eight different producers.

In the blending of any given grade it is impossible to place equal emphasis on all the elements. It is necessary, therefore, to decide which elements are of primary importance and which are secondary. Fortunately, by exercising close control over two or three elements in the cargo, the others will, usually, fall within allowable limits. It is believed that more uniform operation of the blast furnace results when the slag forming elements are held in close control. Because of this and because the Leslie grade constitutes almost one-half of all the ores used by Inland, silica and alumina are placed in the primary classification. Iron is watched closely but will be allowed to deviate in order to hold the slag forming elements constant. The goal is to hold the silica and alumina within 0.05 pct of the guarantee and iron within 0.25 pct. If these three elements are within these pre-

Table III. Number of Cars and Pockets Required for a 16,000 Ton Cargo

Ore	Tonnage	Cars
B	1,700	31
C	2,400	44
E	1,500	27
F	1,000	18
I	3,200	58
L	3,200	58
M	3,000	54
Total	16,000	290

$$\frac{290 \text{ Cars}}{5 \text{ Cars per Pocket}} = 58 \text{ Pockets}$$

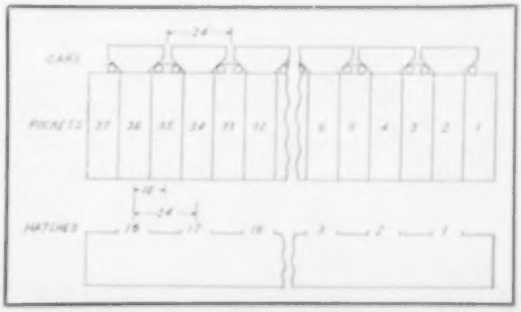

Fig. 2—Diagram shows relative position of ore cars to dock pockets and dock pockets to vessel hatches. Even numbered pockets contain Leslie ore and odd numbered pockets other ores.

Table IV. Pocket Analysis of a Well Graded Cargo

Run	Ores	Fe	P	SiO_2	Mn	Al_2O_3
A	B, L, & I	50.50	0.055	12.20	0.50	1.00
B	C & E	47.00	0.065	8.60	1.20	1.70
C	F & M	45.00	0.080	9.50	0.60	6.00
D	B, L, & I	50.50	0.055	12.20	0.50	1.00
E	Various	48.30	0.065	10.50	0.71	2.40
Average		48.26	0.065	10.60	0.70	2.42
Guarantee		48.31	0.063	10.59	0.71	2.43

scribed limits, the phosphorus and manganese will usually be near grade.

Because the Anderson is primarily a manganese grade the order of priority here is first, manganese; secondly, silica and alumina. If these three elements are on grade, the iron and phosphorus will usually fall into line. Because the principles involved and the problems encountered are identical, regardless of which elements are given priority, the grading of a typical Leslie cargo will be discussed. The shipping grade is an aggregate tonnage made up of many ores and satisfying, as nearly as possible, the blast furnace requirements but modified by what ores are available to the raw materials dept. A recent Leslie season allotment is given in Table I.

Individual component ore guarantees vary in iron between 43.00 and 51.40, in phosphorus between 0.030 and 0.090, in silica between 8.10 and 15.70, in manganese between 0.40 and 1.50, and in alumina between 0.60 and 7.20. While each producer attempts to deliver ore of guaranteed analysis for each cargo, this goal is impossible to attain and the variations within each cargo will greatly exceed the variations in the season's guarantee. Over the season it should be expected that irons will vary in individual samples from about 35.00 to 63.00 and silicas from 3.00 to 28.00. The ore grader's problem, then, is to blend the lows with the highs so that each cargo is of the guaranteed analysis and so that there is a minimum of variation from hatch to hatch within the cargo.

Grading of the Cargo

While there are boats of all sizes and designs carrying ore down the lakes, a 16,000-ton 18 hatch boat will be considered typical. The first step in the process is to order a combination of ores which will average out to the grade guarantee. All the ores in the makeup are not available at all times and also, to simplify accounting, the number of ores ordered for each cargo is held to a minimum consistent with making the guarantee. Table II illustrates a typical order.

Orders are placed a week to 10 days in advance of the boat arrival, whenever possible, although sudden switches in the vessel schedule by the vessel dept. may result in orders for much quicker delivery. Ores are usually delivered by the producers

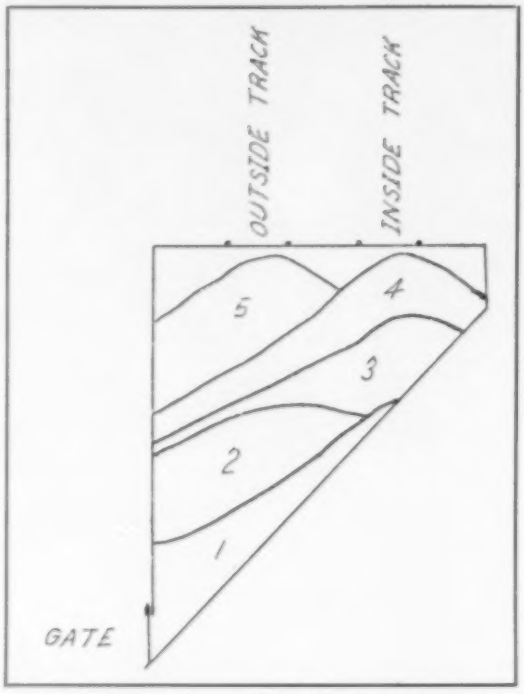

Fig. 3—Cross-section of ore pocket shows dumping sequence and position assumed by ores in the pocket.

from one to three days in advance of the boat arrival. In delivering the ore the producer gives Inland the sample numbers, the name of the mine, and the sample analyses. The dock is notified that these cars have been turned over to Inland for their disposition.

Blending of the ores is accomplished at the ore docks. All docks at the head of the lakes are built jutting out into the harbor so that boats may be loaded on both sides. While docks are of all sizes, the average would have about 175 pockets on each side. Each pocket has a capacity of five cars. The car capacity is 55 tons so each pocket will hold about 275 tons. Pocket bottoms slope towards the outside for gravity emptying, and the face of each pocket is equipped with a shut-off gate and spout to conduct the ore into the hold of the dock. Two railroad tracks run the length of the dock over each set of pockets so that the loaded cars may be spotted in position and bottom dumped directly into the pockets. Pockets are placed on 2-ft centers along the dock but since the cars are 24 ft overall, only alternate pockets are used for any given cargo. The modern ore boats have their hatches built on 24-ft

Table V. Pocket and Section Analysis of a Three Section Cargo, Pct*

	Section X 18 Pockets					Section Y 18 Pockets					Section Z 22 Pockets				
Run	Fe	P	SiO_2	Mn	Al_2O_3	Fe	P	SiO_2	Mn	Al_2O_3	Fe	P	SiO_2	Mn	Al_2O_3
A	50.50	0.055	12.20	0.50	1.00	50.50	0.055	12.20	0.50	1.00	50.50	0.055	12.20	0.50	1.00
B	47.00	0.065	8.60	1.20	1.70	47.00	0.065	8.60	1.20	1.70	47.00	0.065	8.60	1.20	1.70
C	45.00	0.080	9.50	0.60	6.00	45.00	0.080	9.50	0.60	6.00	45.00	0.080	9.50	0.60	6.00
D	50.50	0.055	12.20	0.50	1.00	50.50	0.055	12.20	0.50	1.00	50.50	0.055	12.20	0.50	1.00
E	46.00	0.065	11.00	0.71	4.00	51.50	0.065	6.30	0.71	1.00	47.56	0.065	13.53	0.71	3.24
Average	47.80	0.068	10.70	0.70	2.74	48.90	0.065	9.70	0.70	2.14	48.11	0.065	11.21	0.70	2.39

* Cargo Average: 48.26, 0.065, 10.60, 0.70, and 2.42 pct respectively of Fe, P, SiO_2, Mn, and Al_2O_3.

centers; this integrates with the 24 ft between loaded pockets. Fig. 2 illustrates the relative position of the ore cars, pockets, and boat hatches in position for loading. It should be pointed out in connection with this sketch that by the time the boat arrives for loading, the pockets have been filled and the empty cars withdrawn.

The pocket cross-section illustrated in Fig. 3 shows the sequence of dumping of the cars and the position that the ore from each car assumes in the pocket. The first, third, and fourth cars are dumped from the inside track and the second and fifth cars are dumped from the outside track. This sequence of dumping results in better intermixing of the ores as the pocket is discharged into the vessel hold.

Based on a weight of 55 tons per car, Table III gives the number of cars of each ore, the total number of cars in the cargo, and the number of pockets required for the cargo being discussed. In order to assure the best possible blending of the various constituents in the ores, the dock is instructed by the grading office as to the order of dumping the cars into the dock pockets. The first car dumped into the pocket is referred to as the **A** car and the sum of all the **A** cars is called the **A** run. There will, likewise, be a **B**, **C**, **D**, and **E** run. In order to assure the free flow of the ore out of the pocket, the **A** run should be made up of wash ore concentrates or other material of coarse, rocky structure. Wash ores are typified by high iron, high silica, and low alumina. Ores **B**, **L**, and about ½ of ore **I** would be of this type. Fifty-eight cars of uniform analysis would be selected from these ores for the **A** run. To offset the high iron and high silica in the **A** run, 58 cars would be selected for the **B** run which are lower in these two elements. These 58 cars would come primarily from ores **C** and **E**.

The third car in the pocket receives the best intermixing so this position is reserved for the most off-grade material. In the cargo this would be the high alumina cars in ores **F** and **M**. While the alumina guarantees in these ores are 4.60 and 5.66 respectively, some samples would be higher in alumina than others and for the **C** run 58 cars would be selected with the highest alumina analysis. There would be about another 58 cars of wash ore left and these would go to make up the **D** run. As a result of the careful selection of the first four runs, it is usually found that the 58 cars remaining for the **E** run are quite uniform and near grade. Table IV illustrates the expected pocket analysis if proper selection has been made for each run.

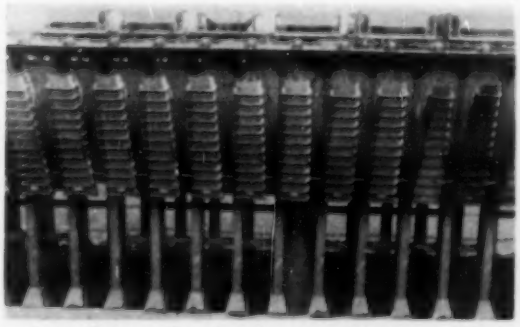

Fig. 4—Side view of ore dock shows cars spotted over pockets for dumping. Pockets are 12 ft center to center.

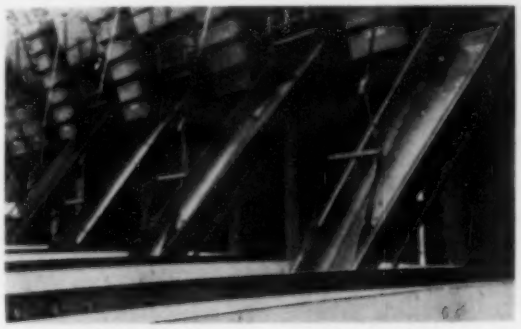

Fig. 5—Ore spouts lowered to discharging position deliver ore from pockets to vessel hold.

Whatever lack of uniformity there is between samples within the various runs is minimized by the fact that there will be more than one pocket loaded into each hatch. In the cargo under consideration there are 58 pockets for an 18 hatch boat. If the boat is loaded uniformly from end to end, each hatch will receive three pockets with four pockets remaining for boat trimming. The law of averages determines that if one pocket in a hatch deviates from the average, the addition of one, two, or three more pockets will bring the resulting hatch analysis closer to the cargo average. Figs. 4 and 5 show a view of ore docks and spouts.

Sectioning the Cargo

It is normal to be able to select four runs of uniform analysis but, oftentimes, there are wide variations in the ores remaining for the **E** run. If this situation is encountered, a method known as sectioning is used. To use a simple illustration, there might be an excessive number of high alumina cars remaining for the **E** run. In the sectioning method the 18 cars remaining for the **E** run with the highest alumina would be placed in the first 18 pockets to be loaded into the boat. Thus each hatch would receive one and only one high alumina pocket. These 18 pockets would be called section **X** and the remaining 40 pockets would be called section **Y**. The pockets of section **Y** would be slightly deficient in alumina but the hatch to hatch variations would be reduced to a minimum. At times it is necessary to break the cargo into three sections, if, for example, an excess of low silica cars remain for the **E** run. Table V illustrates a three section cargo with section **X** off-grade in alumina, section **Y** off-grade in silica, and section **Z** containing the balance.

It will be noted from Table V that there are wide variations in the **E** run and these are reflected in the section analyses. However, the boat would still get one car of section **X** and one car of section **Y** in each hatch and finish with section **Z**. The resulting cargo would be uniform from hatch to hatch and would make an acceptable furnace feed. Sectioning should be used only when absolutely necessary because it throws a large additional switching charge onto the railroad and also slows down the movement of ore through the docks. In times of heavy shipments, it is vital that every car be emptied and returned to the mines with the greatest possible dispatch. In cases of extreme analytical variations the sectioning method may be extended to runs other than the **E** run. The methods and problems remain identical when sectioning other runs.

Analytical Control of Bessemer Blow Reported Possible With New Techniques

IN THE Bessemer converter process the entire operation of converting iron into steel takes less than 20 min. This is the great advantage of the process, but the very rapidity of the conversion is often a problem because analytical control of the melt during a blow is very difficult.

In recent years, a number of attempts have been made to overcome this weakness of the converter process by devising ways and means of observing the bath temperature or by subjecting the converter flame to a spectroscopic examination. Wever and Koch[1] et al. have described experiments carried out at the works of the Dortmund-Hoerde Huttenunion A.G. at Dortmund, Germany.

Radiation Pyrometer

A radiation pyrometer was mounted at the outer end of a long, pivoted probe. This could be lowered over and into the mouth of the converter and retracted out of the way before the vessel was tilted.

It was found that when the final bath temperature was checked with an immersion pyrometer at the conclusion of the blow, the difference between this reading and the final reading obtained while the blow was in progress was seldom more than ±10°C.

The results obtained have indicated clearly how the elimination of the different metalloid elements influences the rise in temperature of the converter bath. In the early stages the oxidation of silicon brings the temperature up by approx 100°C. Although carbon oxidation is a strongly exothermic reaction the loss of CO from the surface of the bath removes a large proportion of the heat generated. In the remaining 4 min the oxidation of the phosphorus (the after blow) pulls the temperature up by approx another 200°C.

Flame Spectroscopy

Parallel with the continuous measurement of the bath temperature in the converter, a spectroscopic technique was developed for the continuous observation of the converter flame and a continuous recording of its condition. The light from the flame passes through a prism and is split up. Observations are confined to two separate ranges of the spectrum, in the violet end to the wavelengths 4100 to 4170Å and in the red end to the wavelengths 7025 to 7325Å. The light in these two ranges is directed onto two separate photometric devices which are linked by a compensator. They are so arranged that a continuous record is made of the ratio of the intensity of red light to the intensity of violet light being emanated by the converter flame.

During the silicon and carbon oxidation the converter flame emits a steady radiation in the 4100 to 4170Å field. The radiation arises primarily from the carbon monoxide, but during the dephosphorization period another steady emission in the range 7025 to 7325Å takes place and the ratio of red to violet radiation increases considerably. Towards the end point of conversion, however, there comes a reversion to a greater intensity of violet radiation and the value of the intensity ratio falls slightly.

Converter Fume

The behavior of the converter flame radiation as determined by these methods has been shown to be attributable to the production of different types of fine iron oxide fume during the progress of conversion. The variation in radiation wavelength can be attributed to the fine particles of fume that act as centers of lightscatter according to Rayleigh's principle. During the early period of the blow the fume is very finely divided and the scatter is thus in the shortwave range. As the carbon is eliminated and the afterblow takes place the size of the fume particles increases and the radiation scatter is thus pushed over to the longer wavelengths. In the final stages the production of a proportion of fine fume leads to the shorter wavelength scatter and a slight reduction of the red to violet radiation intensity ratio.

The ways in which intensity of flame radiation and the corresponding fume particle size vary correlate very closely with the variation in bath temperature throughout the course of the blow. From this it was concluded that the production of converter fume is due to the intensely high temperature which is generated at the point where the blast enters the metal. This temperature is sufficient to cause actual volatilization of the metal which is then converted to oxide actually in the vapor phase. The perfectly spherical particles which make up the fume are strong evidence of this and the higher the temperature of the bath, the larger the sphere can become before it is ejected to the cooler parts of the converter and growth therefore ceases.

It was found that if the bath temperature at the moment of maximum long wave radiation intensity is known, then an accurate prediction of the final phosphorus content can be made. Provided that both the continuously recording radiation pyrometer and the spectroscopic photometers are functioning properly, it is possible by this means to operate the basic Bessemer converter with a degree of analytical control approaching that of the much slower open hearth furnace.

Reference

[1] F. Wever, W. Koch, H. Hofermann, B. A. Steinkopf, H. Knuppel, K. E. Mayer, and G. Weithoff: *Stahl u. Eisen*, May 5, 1955, pp. 549 to 559.

This article was originally printed in The Iron & Coal Trades Review (London) Vol. 170, June 17, 1955, p. 1413.

Temperature Gradient Zone Melting

by W. G. Pfann

Under certain conditions, a molten zone can be made to move through a solid by impressing a stationary temperature gradient across the solid. This phenomenon can be utilized in fabricating semiconductive devices, growing single crystals, joining, boring fine holes in solids, measuring diffusivities in liquids, small scale alloying, and purification. Fundamentals and exemplary applications are outlined.

A NEW aspect of the travel of a molten zone through a solid is considered in this paper. Whereas, in previously described zone melting techniques,[1-4] zones were usually caused to move by changing the position or temperature of a heat source, in the present technique a zone is made to move by impressing a temperature gradient across it. For example, a thin layer of molten Al-Si alloy, sandwiched between two silicon slabs having a temperature gradient normal to the layer, will travel through the hotter slab. One feature of *temperature gradient zone melting*, as this technique will be called here, is that zones of unusually small dimensions can be maintained. This leads to such diverse uses as have been listed in the abstract. In this paper fundamentals of the movement of a molten zone in a temperature gradient, and some practical applications thereof, are outlined.

Assumptions

The movement of a molten zone through a solid body of solvent substance in which a temperature gradient exists will be discussed. The length of the zone will be its dimension in the direction of motion. The *direction* of the temperature gradient will be toward the region of higher temperature. To be considered is a binary or higher order solute-solvent system in which the concentration of solute in the molten zone is sufficient to produce a lowering of the freezing temperature of the solvent which is at least of the order of the temperature range impressed on the charge. While we discuss primarily molten zones in a solid matrix, the principles are applicable to solid or vaporous zones in a solid matrix, a requirement being that the diffusivity in the zone be substantially greater than in the matrix. Diffusion of solute into the surrounding solid will be assumed negligible. In general, its presence will not basically alter the conclusions to be drawn.

For illustration, a system represented by the partial constitutional diagram of Fig. 1a will be discussed, in which k, the distribution coefficient defined in the figure, is constant and less than unity. However, the technique is applicable to any solute-solvent system in which one component lowers the melting point of another component.

W. G. PFANN, Member AIME, is associated with Murray Hill Laboratory, Bell Telephone Laboratories Inc., Murray Hill, N. J.

Discussion of this paper, TP 4021E, may be sent, 2 copies, to AIME by Jan. 1, 1956. Manuscript, Sept. 29, 1954. Philadelphia Meeting, October 1955.

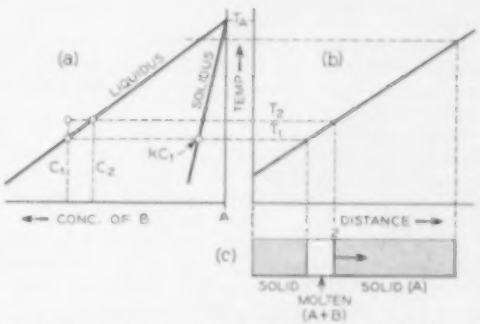

Fig. 1—Temperature gradient zone melting scheme shows: a—portion of phase diagram, b—temperature gradient in system, and c—physical system comprising molten zone containing *A* and *B* traveling through solid *A*.

Movement of a Molten Zone in a Temperature Gradient

Consider, in the system AB of Fig. 1, where B is designated the *solute* and A the *solvent*, the effect of sandwiching a thin layer of solid B between blocks of solid A and placing the whole in a temperature gradient such that the temperature of the layer is above the lowest melting temperature of the system. Surrounded by an excess of A, the layer will dissolve A, becoming molten, and expand in length.* As solution of A continues, at both interfaces, the mean solute concentration in the zone will move to the right in Fig. 1a, until at temperature T_1 the liquid at the cooler interface reaches the liquidus concentration C_1. Solution of A thereupon ceases because the liquid T_1 is saturated with A. The liquid at the hotter end of the zone, being at temperature T_2, is not saturated with A at concentration C_2. Hence solution of A continues there and concentration C_2 is approached. A concentration gradient therefore is set up in the zone, causing A to diffuse toward the cool end and B toward the hot end. As a result, the liquid at the cool interface becomes supersaturated and a layer of crystalline A containing concentration kC_1 of B in solid solution freezes. Since a source of A

* While this wording may seem to suggest that, in the zone, A is the solute, the author will nevertheless hold to the convention stated previously that A is the solvent, wherever the term solute or solvent is used.

The Transactions papers appearing in the Journal of Metals during 1955 will subsequently appear in AIME Transactions Volume 203, and may be permanently referenced to that volume.

Fig. 2—Sketch shows short temperature gradient produced by heaters at temperatures T_1 and T_2.

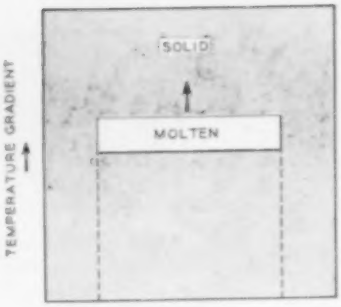

Fig. 3—Diagram illustrates molten zone of rectangular cross-section traversing a solid in the direction of the temperature gradient.

exists at the hot end and a sink for A at the cool end of the zone, diffusion of A through the zone continues and as a result the molten zone travels through the solid in the direction of increasing temperature.

Length of Zone: As the zone travels through the temperature gradient, its mean composition follows the liquidus and its length l is influenced by two opposed effects:

1—Its solubility for A increases as it moves up the liquidus. This effect tends to *increase* l. The tendency for increase in l will be *small* if the slope of the liquidus, dT/dC, is large and if the concentration of A in the zone is small.

2—Its content of B decreases through loss of B in the frozen solid, and hence the amount of A which it can dissolve tends to decrease. This effect tends to *decrease* l. The tendency for decrease in l will be small if the solubility of B in solid A is small.

Thus, l may increase or decrease as the zone travels, depending on whether effect 1 or 2 is dominant.

Compositional Changes: Consider a molten zone, containing components A and B and traversing a block of solid A, as in Fig. 1. The main factor determining the concentration distribution of B in the traversed solid is the temperature range in the block. Since the zone advances by climbing along the liquidus and since to traverse the block it must traverse the range of temperature in the block, it follows that the range of solute concentration in the traversed solid will be that corresponding to this temperature range on the liquidus multiplied by k. Hence smaller temperature gradient, that is, smaller range of temperature in a given block, results in a more uniform solute concentration. However, at smaller temperature gradient, the rate of zone travel will be lower as well and hence, with this particular scheme, a compromise between uniformity and speed may be necessary.

Changes in composition of the zone of Fig. 1 are related to changes in zone length in a way which may be seen as follows: If, as the zone advances, it enters regions of higher temperature, then the concentration of B in the traversed solid C_s, must decrease, as is evident from the phase diagram. In such a case, the zone length l may increase, remain constant, or even decrease. On the other hand, if the zone advances at constant temperature—and it is shown subsequently that this is possible—C_s must remain constant, even though B is steadily being lost by the zone. This is accomplished by a reduction in l at just such a rate as to maintain constant concentration in the zone. This action is quite analogous to the method described in ref. 1 of decreasing l at a linear rate to maintain uniformity of solute concentration in a charge of pure solvent being traversed by a zone containing solute. A feature of temperature gradient zone melting is that such reduction in l occurs automatically and can in practice be carried to $l = 0$.

One reason for sweeping a zone through a solid is to distribute solute in the latter. The desired solute may be a major component of the zone, as B in the system AB used for illustration, or it may be an additional minor constituent C, such as a donor or acceptor element desired in a semiconductor. In the latter case, the starting charge could be an alloy of B and C or of A, B, and C. Here B could serve principally as a carrier, producing a molten zone from which C would be distributed.

Rate of Travel of Zone: The main factors influencing the rate of travel of the zone are: the temperature gradient dT/dx, the slope of the liquidus dT/dC, and the diffusivity D in the liquid. High travel rate is favored by large dT/dx and D, small dT/dC. The heat of fusion and the thermal conductivity will, in certain cases, affect the rate by their influence on the temperature gradient in the zone. If these quantities are large, the travel rate will tend to be low.

The way in which the temperature gradient is impressed on the zone can appreciably affect the travel rate. Consider a short temperature gradient, produced by external moving heaters with a molten zone in the gradient, as in Fig. 2. The zone, in such a situation, would move to the right, eventually stopping at the shoulder of the curve at T_2. If, while the zone is moving, the temperature gradient is displaced to the right as shown by the dashed curve, then the composition of the zone would rise less rapidly along the liquidus than would be normal for a stationary gradient. In principle, the zone could be held at one temperature for its entire travel distance. This technique has the following important feature: It permits traversal of a charge at the high rate corresponding to a high temperature gradient, while at the same time permitting the low variation in concentration typical of a low temperature gradient.

Another means of producing the desired displacement of a temperature gradient is to lower the mean temperature of the system as the zone advances.

Shape of Zone: Consider a molten zone of more or less rectangular cross-section, thin in the direction of motion and moving through a solid charge of cross-section greater than that of the zone, as shown in Fig. 3. As the zone travels, surface tension of the liquid will tend to make it spherical, while crystalline anisotropy will tend to make it lie along certain planes or directions. Lattice defects such as grain boundaries or dislocations may tend to cause it to move faster at such defects or spread along them.

In general, however, despite these forces, the shape of the zone will tend to remain the same in a uniform temperature gradient because the temperature gradient has a stabilizing effect on zone shape. In order for the zone to change its shape, parts of its boundary must move with respect to others. But the zone is essentially saturated at its sides and tends to be stable there and can move its forward and rear interfaces in but one direction: the direction of the temperature gradient. As a result of this stability of form, a very thin molten zone, of the order of 10^{-2} cm or less in length and of the order of 1 cm^2 or more in area, can be made to travel many zone lengths without major change in form.

If the temperature gradient is not uniform (lines of heat flow being nonparallel), a flat zone like that of Fig. 2 will be unstable and will tend to break up or elongate. Practical implications of this are: 1—if a flat zone is wanted, the temperature gradient should be uniform and 2—by using diverging lines of heat flow, a zone of very small lateral dimensions can be produced as a zone in such a temperature field will tend to elongate and to contract laterally.

Applications

Semiconductive Devices: Temperature gradient zone melting makes possible a new approach to the fabrication of semiconductive devices such as diodes and transistors. It has certain advantages over existing techniques in producing conventional designs and it makes possible new designs involving complex *p-n* junction shapes.

A large area *p-n* junction which was made by sandwiching an 0.005 in. sheet of aluminum between two 0.1 in. blocks of silicon and placing the whole in a temperature gradient is shown in Fig. 4. The alloy layer has traveled most of the way through the upper block, depositing behind it single crystal *p*-type silicon having the orientation of the lower *n*-type block which served as a seed. The freezing of the Si-Al eutectic has resulted in a partial break-up of the originally continuous zone and has cracked the neighboring silicon. A feature of the temperature gradient technique is that thicker layers can be grown than in the usual alloy technique[5,6] and hence that solidification strains occur far from the *p-n* junction, where they are much less harmful. In practice the zone can be swept to the outer surface of the block, where it can either be removed or used as an electrical connection to the swept region.

Line or dot zones, small in one or two lateral dimensions, respectively, can be swept through a block without major change of form. By this means, a thin *p*-type layer or thin *p*-type rods or lines can be produced in an *n*-type block. Fig. 5 is a cross-section of a *p*-type layer about 0.006 in. thick produced by sweeping an aluminum line zone through a block of *n*-type germanium. Penetration rates for aluminum-rich line zones traveling through germanium were about 1.5 mm per hr at a temperature gradient of about 100°C per cm.

It has been observed that if the zone is small, ~0.003 in. in one or more lateral dimensions as in Fig. 5, the crystal orientation of the block being traversed prevails, even if a seed of different orientation is used. This self-seeding feature is desirable in making *n-p-n* junctions because it eliminates grain boundaries which would tend to impair the electrical properties of the junction. It should be noted that the *p-n* barrier forms at the side of a line zone, in contrast to the large area barrier of Fig. 4 which formed for the most part at the initial location of an area zone.

A line or dot zone need not travel through a block; it may traverse its surface as well if the temperature gradient is imposed parallel to or slightly away from the surface. By this means, *p-n* junctions parallel to a surface can be produced.

A coating of complex shape can be deposited on the surface of a block and then swept through the block, normal to the surface, to produce internal *p-n* or *n-p-n* barriers of corresponding form.

Molten zones will follow the direction of maximum temperature gradient quite faithfully. By changing the direction of the gradient as a zone travels, it can be made to follow a complex path.

Single Crystals: From the foregoing it is clear that temperature gradient zone melting can be used to grow a single crystal; and, in fact, temperature gradient techniques, using much larger volumes of liquid, have been reported.[7] Use of a short large area molten zone for this purpose has a number of advantages, among which are:

1—The apparatus is simple and has no moving parts and even the temperature need not be altered.

2—The volume of liquid is so small that a container is unnecessary and contamination and nucleation therefrom are avoided.

3—Since the volume of liquid is small, since the temperature drop in the liquid is small, and since stirring and convection are absent, the probability of spontaneous nucleation is minimized.

On the other hand, a foreign substance will be present in solid solution—although innocuous ones can be used—and excessive temperature gradients can cause strains.

Joining: The method of Fig. 4 may be regarded as a joining method in which the molten zone acts as

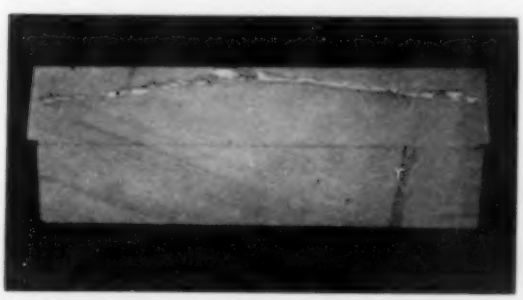

Fig. 4—Large area *p-n* junction was produced by sweeping an aluminum-rich zone through upper silicon slab. Original magnification, X8. Area reduced approximately 35 pct for reproduction.

Fig. 5—Thin *p*-type layer was produced by sweeping an aluminum line zone through an *n*-type germanium block. Cross-section was perpendicular to line zone. Original magnification, X75. Area reduced approximately 35 pct for reproduction.

a *solder* to join the two blocks but, unlike conventional solder layers, then migrates through one of the blocks so it can be removed. By this means mechanical, chemical, thermal, or electrical weaknesses of soldered joints can be eliminated. It should be remembered, however, that a solid solution of the zone solute will be left in the traversed block.

Extremely thin layers can be moved. For example, fractional mil layers of gold can be moved through a 100 mil slab of germanium by the temperature gradient technique.

Measurement of Diffusivities in Liquids: It was pointed out by Reiss[8] that, since convection is negligible in these thin layers, transport occurs entirely by diffusion and hence the temperature gradient technique provides a method of measuring diffusivities in liquids. The flux F of a diffusing component—for example, silicon diffusing through a thin aluminum-rich layer—may be written as the sum of two terms. One is a chemical term, proportional to the concentration gradient in the layer; the other is a thermal term, proportional to the temperature gradient and the concentration in the layer. The flux is readily obtained by measuring the travel rate of the layer. The concentration gradient, dC/dX, may be written as $(dC/dT)(dT/dX)$, where dC/dT is obtainable from the slope of the liquidus and dT/dX is obtainable from the applied temperature gradient and the ratio of thermal conductivities of liquid and solid, which must be known or measured. While the process occurs over a range of temperature and concentration, these ranges can be small so that a condition of constant temperature and concentration can be closely approached. There is little basis theoretically for predicting whether thermal diffusion will aid or oppose chemical diffusion, although calculations based on published thermal diffusion coefficients[9] indicate that the thermal term should be relatively small, of the order of a few percent of the chemical term. It is intended to treat this problem more fully in a later publication. However, data obtained by Wernick[10] on the movement of gold and aluminum-rich zones through germanium and silicon give diffusivities D in the 10^{-4} cm^2 sec^{-1} range when D is calculated from $F = D\,(dC/dX)$, which neglects thermal diffusion.

Zone Refining: The temperature gradient technique can be used to advantage as a means of zone refining. One or a series of short large area zones can be swept through a solid charge to remove undesired impurities (which are not necessarily soluble in the charge). Thin layers of solute substance can be stacked between thin layers of charge at the cool end of a temperature gradient and then swept through the remainder of the charge. Representative travel rates may be a few millimeters per hour in a temperature gradient of the order of 50°C per cm. A series of different solutes, chosen for their selective actions on certain impurities, may be used. The choice of a solute is dictated by the need that it be but slightly soluble in, harmless to, or readily removable from the charge substance. Short zone length l and short interzone spacing d which are desirable in zone refining are readily attained with the temperature gradient technique. The method can be used to remove insoluble particles, such as eutectic, from an alloy. By heating it above the eutectic temperature in a temperature gradient, the particles will be caused to form dot zones which will migrate to the hottest surface.

Miscellaneous Fabrication Techniques: By advancing into a block a wire zone extending entirely through the block and then blowing out the molten material, an extremely fine hole can be produced. By heating a plated wire by I^2R heat and simultaneously cooling it, a radial temperature gradient will be set up which can cause the plated material, if properly chosen, to migrate to the wire axis. In general, a surface layer can be caused to move to the interior or to another part of the surface of a solid body.

Summary

The simplicity of the temperature gradient idea, the variety of its possible applications, and the fact that it does not appear to have been exploited, lead to the conclusion that it will be utilized in several fields of technology. While it has been discussed here in somewhat idealized fashion, sufficient experimentation has been done to demonstrate the validity of the basic ideas.

Acknowledgment

The author wishes to thank D. Dorsi for much painstaking and fruitful experimental assistance, E. E. Thomas for informative microscopic work, A. J. Goss, C. D. Thurmond, F. L. Vogel, and J. H. Wernick for helpful criticism of the manuscript.

Discussion of this paper, if any, will appear in JOURNAL OF METALS, May 1956, and in AIME Metals Branch *Transactions*, Vol. **206**, 1956.

References

[1] W. G. Pfann: Principles of Zone-Melting. *Trans.* AIME (1952) **194**, p. 747; JOURNAL OF METALS (July 1952).

[2] W. G. Pfann and K. M. Olsen: Purification and Prevention of Segregation in Germanium Single Crystals. *Physical Review* (1953) **89**, p. 322.

[3] W. G. Pfann: Redistribution of Solutes by Formation and Solidification of a Molten Zone. *Trans.* AIME (1954) **200**, p. 294; JOURNAL OF METALS (February 1954).

[4] W. G. Pfann: Continuous Multistage Separation by Zone-Melting. *Trans.* AIME (1955) **203**, p. 297; JOURNAL OF METALS (February 1955).

[5] R. Law, C. W. Mueller, J. I. Pankove, and L. D. Armstrong: A Developmental Germanium P-N-P Transistor. *Proceedings* IRE (1952) **40**, p. 1352.

[6] G. L. Pearson and B. Sawyer: Silicon P-N Junction Alloy Diodes. *Proceedings* IRE (1952) **40**, p. 1348.

[7] E. Buehler and A. C. Walker: Growing Quartz Crystals. *Scientific Monthly* (1949) **69**, p. 148.

[8] H. Reiss: Private communication.

[9] W. Jost: *Diffusion in Solids, Liquids, and Gases.* (1952) New York. Academic Press.

[10] J. H. Wernick: To be published.

Correction

In the May 1955 issue: TP 4001E. Discussion by J. F. Brown and B. J. Connolly of *475°C (885°F) Embrittlement in Stainless Steels* by A J. Lena and M. F. Hawkes. On pp. 691 and 692 of the text and on p. 692 in the title of Table IV and the captions for Figs. 16 and 17, the alloy composition should read "18 pct Cr-10 pct Ni-3 pct Mo-0.5 pct Ti," not "18 pct Mo-10 pct Ti Cr-Ni" as printed.

Phase Equilibria in the System FeO-Fe_2O_3-SiO_2

by Arnulf Muan

Liquidus data are presented for mixtures in the ternary system FeO-Fe_2O_3-SiO_2 in equilibrium with a gas phase with O_2 pressures ranging from $10^{-10.4}$ to 1 atm. Data obtained are combined with previously published data to construct lines of equal O_2 pressures and lines of equal CO_2/H_2 mixing ratios along the liquidus surface. Courses of crystallization of selected mixtures under conditions of constant total composition, constant O_2 pressures, and constant CO_2/H_2 mixing ratios are discussed.

PHASE equilibrium studies of silicate systems where iron is one component are complicated by the fact that iron readily occurs in three different states of oxidation: Fe^{0}, Fe^{2+}, and Fe^{3+}. Success or failure in work with iron silicate systems is to a large extent dependent on control of the oxidation state of iron and all investigations therefore must be carried out under carefully controlled atmospheric conditions. Silicate systems containing only strongly electropositive metals (like Na^{+}, Ca^{2+}, Mg^{2+}, etc.) can, for simplicity, be treated as *condensed systems*, that is, the gas phase can be neglected and the phase relationships discussed in terms of the phase rule written in the well known simplified form $P + F = C + 1$. In the case of iron silicate systems, however, the composition of the condensed phases varies with the gas composition, and a complete picture of phase relationships can be obtained only by varying the gas composition over a wide range.

In order to understand the phase relationships in the more complicated multicomponent silicate systems with iron oxide as one of the constituents, a knowledge of the ternary system FeO-Fe_xO_y-SiO_2 is essential, since it constitutes a bounding portion of all such systems. It was with this in mind that the present study was undertaken.

Previous Work

A considerable amount of work has been done on various aspects of the chemistry and metallurgy of systems containing silica and iron oxides. The two bounding binary systems FeO-Fe_xO_y and FeO-SiO_2* have been worked out in detail, but no complete investigation of the phase relationships of the ternary system FeO-Fe_xO_y-SiO_2 has been reported.

Darken and Gurry[1, 2] investigated phase relationships for the system FeO-Fe_2O_3, including a study of the variation in the composition of liquid and solid phases as a function of temperature and O_2 pressure. Bowen and Schairer[3] adapted the quenching technique to the study of iron silicate systems under reducing conditions, making the runs in iron crucibles in an inert atmosphere. The first system to be studied with this technique was FeO-SiO_2.

The first attempt to obtain information on phase relationships of iron oxide-SiO_2 mixtures at different O_2 pressures was made by Greig.[4] Darken[5] determined the melting points of iron oxide on solid silica under various atmospheric conditions. Darken did not determine experimentally the composition of the melts at liquidus temperatures but discussed very ably the principles involved in applying the phase rule to the system.

In a recent study Schuhmann, Powell, and Michal[6] determined experimentally the liquidus surface of a portion of the ternary system and combined the new information with data in the literature to construct a phase diagram. Their method was briefly as follows:

Homogeneous mixtures with various contents of SiO_2, FeO, and Fe_2O_3 were made up by melting together stock mixtures in various proportions. Samples of the homogeneous mixtures, the compositions of which were determined by chemical analysis, were then heated in platinum crucibles in an inert atmosphere until equilibrium among the condensed phases was achieved. The samples were quenched to room temperature and the phases present determined by microscopic examination. Assuming that no change in composition takes place during the equilibration run in inert atmosphere, the liquidus surface can be determined, but no information is obtained regarding the partial pressures of O_2 of the gas phase in equilibrium with the condensed phases.

The author's method, to be described in the next section, permitted the location of points at the liquidus surface as well as a calculation of the corresponding partial pressures of O_2.

Experimental Method

General Procedure: The standard quenching technique was adapted for a study under controlled variable atmospheric conditions. Premelted mixtures of silica and iron oxides in platinum envelopes were held at constant temperature under chosen atmospheric conditions until equilibrium was reached among solid, liquid, and gas phases. The sample was then quenched to room temperature, the phases present identified, and, for the most significant runs, the composition was determined by chemical analysis. The corresponding partial pressure of O_2 was calculated from known equilibrium constants of the gas reactions occuring in the furnace atmosphere.

Materials: Starting materials were oxides of commercially highest available purity; cp silicic acid was dehydrated by heating to 1350°C for 6 hr and cp Fe_2O_3 was dried at 400°C for the same length of time. Samples of 10 g were made up by mixing

* The system FeO-SiO_2 can be pictured as a binary system only when the small but inevitable amount of trivalent iron in the melt is neglected.

A. MUAN, Member AIME, is Research Associate, College of Mineral Industries, The Pennsylvania State University, University Park, Pa.

Discussion of this paper, TP 3985CD, may be sent, 2 copies, to AIME by Nov. 1, 1955. Manuscript, July 26, 1954. Chicago Meeting, February 1955.

these materials in required proportions and grinding under alcohol for 30 min. Each mixture was fired twice in a gas-air furnace at about 1650°C for 1 hr. The platinum crucibles containing the mixtures were essentially saturated with iron under the conditions prevailing in the furnace, so that the loss of iron oxide to platinum could be kept at a minimum. These mixtures, after grinding to −60 mesh, were used for the equilibration runs in the quench furnace. In order to make sure that equilibrium was achieved in the quench runs, the final state was approached from both sides of the equilibrium FeO/Fe_2O_3 ratio. For this purpose, some preliminary runs were made in which a portion of the material from the gas furnace was melted subsequently in iron crucibles in a nitrogen atmosphere. When these mixtures, containing essentially all the iron in the ferrous state, were used as starting material for the quench runs, the same results were obtained as given previously.

Control of Atmosphere: The method used for controlling O_2 pressures was very similar to that used by Darken and Gurry.[1,2] The O_2 pressure was controlled in the range from $10^{-10.2}$ to 1 atm in the following ways: Runs were made at 1 atm O_2 by leading commercial tank oxygen through the furnace. Runs at 0.21 atm O_2 were made in the open furnace with air circulating through. Lower O_2 pressures were obtained by mixing CO_2 and H_2 in various proportions. CO_2 and H_2 react upon heating according to the *water gas* equation

$$CO_2 + H_2 = CO + H_2O.$$

Data for the equilibrium constant

$$K_1 = \frac{p_{CO} \times p_{H_2O}}{p_{CO_2} \times p_{H_2}}$$

of this reaction are available in the literature. The partial pressure of O_2 in the mixture can be calculated by combining the foregoing equilibrium equation with the equilibrium equation

$$K_2 = \frac{p_{CO}^2 \times p_{O_2}}{p_{CO_2}}$$

for the reaction

$$2CO_2 = 2CO + O_2$$

the equilibrium constant of which is also available in the literature. Numerical values of the constants K_1 and K_2 used for calculations in the present study are:[1] K_1 = 2.08, 2.49, 2.905, and 3.32 at 1100°, 1200°, 1300°, and 1400°C, respectively. K_2 = 3.98×10^{-20}, 1.122×10^{-15}, 2.06×10^{-12}, and 2.65×10^{-9} at 1100°, 1200°, 1300°, and 1400°C, respectively.

The gases used were of highest commercial quality with reported compositions 99.956 pct CO_2, 0.044 pct H_2O, and approximately 99.8 pct H_2 and 0.2 pct H_2O, respectively. Both gases were dried with $CaSO_4$ (Drierite) before going to the gas mixer. The rate of flow of each of the two gases was measured separately by two capillary flow meters with bleeder tubes on both ends of the capillaries to maintain a constant pressure drop. A series of mutually interchangeable capillaries of different openings was at hand, so that a wide range of mixing ratios could be obtained with manometer readings of convenient magnitude. A third manometer was inserted in the line to measure the rate of flow of gas through the furnace. The flow was adjusted to approximately 0.15 cu ft per hr, corresponding to a linear flow rate of approximately 1 cm per sec through the furnace tube.

The flow meters were calibrated individually with the various capillaries, using a standard wet test meter. The method was checked in preliminary experiments with conventional gas analysis techniques (CO_2 absorbed in a 30 pct solution of KOH and H_2 burned with O_2).

Furnace: The furnace used for the quenching experiments was a vertical platinum-wound tube furnace of standard design as far as heating element and insulation were concerned. In order to obtain reliable control of the atmospheric conditions during the runs, some modifications of the standard quenching arrangements were introduced. A gas-tight high temperature refractory porcelain tube was inserted inside the heating element and protruded above and below the furnace. The top of the tube was sealed by a water-cooled brass head with a rubber gasket. The brass head had a central bore through which a refractory protection tube could be inserted and clamped in gas-tight connection. Two identical interchangeable protection tubes were used, one for the thermocouple wires and one for the platinum quench wires supporting the envelopes with the charges. The thermocouple was never kept in the furnace simultaneously with the charges. Before and after each equilibration experiment, which was carried out with the usual quenching technique, the thermocouple tube was inserted through the brass head bore and the temperature measured. The lower end of the furnace tube was closed by a closed cup device for quenching in mercury. This device could be replaced by a copper block in which samples for analysis were quenched. The gas mixture was introduced into the furnace from below and escaped at the top through a wash bottle containing H_2SO_4. In this way a pressure slightly in excess of atmospheric was maintained within the furnace, corresponding to the head of the H_2SO_4 in the wash bottle, approximately 5 mm Hg. The main advantage of this arrangement is that leaks or irregularities in the gas mixture line or in the furnace immediately show up.

Temperature Control and Measurement: Temperatures were measured before and after each run with a Pt—Pt-10 pct Rh thermocouple which was frequently calibrated at melting points defined as follows: Au, 1063°C; $CaMgSi_2O_6$, 1391.5°C; $CaSiO_3$, 1544°C. Literature values for temperatures on the Geophysical Laboratory scale are used without correction up to 1550°C, the upper limit of the original scale. Temperatures above 1550°C are adjusted to the 1948 International Scale by use of the correction data of Corruccini[3] and of Sosman.[4]

The furnace temperature was controlled by a second thermocouple inserted close to the heating element and connected through compensating lead wires to a Celectray controller. The temperature gradient at the hot spot did not exceed 1° over 1 in. at 1450°C.

Identification of Phases: The phases present were determined by examination under the microscope, using both transmitted light and reflected light. The identity of the phases was further confirmed by X-ray techniques using Fe-radiation with a Norelco X-ray spectrometer unit. The X-ray technique could not be used as a means to determine liquidus temperatures, since the melts, with some exceptions, were exceedingly fluid and gave rise to dendritic *quench crystals* even with the fastest quenching of small samples in mercury. In polished sections, there

was no difficulty in distinguishing primary magnetite and primary wüstite from corresponding crystals formed during quenching. Tridymite was easily identified both in transmitted light as well as in reflected light, whereas fayalite was best recognized in transmitted light. Some difficulty was experienced in distinguishing primary from quench-formed fayalite, but the former were in all cases much larger and better developed than the latter.

Table I. Composition of Liquid at Various Temperatures and O_2 Pressures

Temperature, °C	Mixing Ratio, $CO_2:H_2$	P_{O_2}, Atm	Final Composition by Analysis, Wt Pct		
			FeO	Fe_2O_3	SiO_2
1201	3.5	10^{-10}	66.6	12.1	21.3
1198	3.5	10^{-10}	65.8	10.6	23.6
1198	3.5	10^{-10}	62.9	9.0	28.1
1200	3.5	10^{-10}	59.0	6.6	34.4
1200	10.1	10^{-9}	60.4	15.5	24.1
1199	10.1	10^{-9}	58.4	14.0	27.6
1198	10.1	10^{-9}	56.0	10.0	34.0
1301	2.8	10^{-9}	68.2	13.5	18.3
1296	2.8	10^{-9}	67.0	11.3	21.7
1298	2.8	10^{-9}	62.8	8.9	28.3
1298	2.8	10^{-9}	58.7	8.0	33.3
1298	7.5	10^{-8}	63.4	19.1	17.5
1300	7.5	10^{-8}	61.0	17.4	21.6
1303	7.5	10^{-8}	60.0	12.2	27.8
1299	7.5	10^{-8}	56.5	9.3	34.2
1299	23.6	10^{-7}	56.0	21.8	22.2
1301	23.6	10^{-7}	55.0	17.0	34.0
1306	23.6	10^{-7}	53.1	13.9	34.0
1403	20.2	10^{-6}	59.0	32.0	9.0
1404	20.2	10^{-6}	56.8	21.4	21.8
1399	20.2	10^{-6}	53.4	18.2	28.4
1401	20.2	10^{-6}	52.0	13.1	34.9
1398	65	10^{-6}	48.9	28.7	22.4
1401	65	10^{-6}	48.8	23.0	28.2
1400	65	10^{-6}	46.9	18.6	34.5

Method of Chemical Analysis: Due to reaction between the platinum envelopes and the melts, it was necessary to determine by chemical analyses the total amount of iron oxides as well as the ratio FeO/Fe_2O_3 for critical runs. No analysis for platinum in the melts was made, but Darken and Gurry[7] found that negligible amounts of platinum dissolved in iron oxide melts under conditions similar to the present. The loss of iron due to alloying with the platinum envelope, which increases with decreasing O_2 pressures, did not prevent equilibrium from being reached in the melts under study. It was found that the platinum envelopes were saturated with iron with respect to the melts after a period of 2 to 5 hr, whereas the FeO/Fe_2O_3 equilibrium in the melt is established in 1 to 2 hr. In order to make sure that equilibrium was achieved, the runs were kept in the furnace for a period of 8 to 12 hr.

Before analysis, the samples were crushed in a Plattner mortar to pass a 100 mesh screen. For the determination of divalent iron, 0.1 to 0.2 g samples were heated to boiling in 20 ml 1:3 H_2SO_4 in a covered platinum crucible. When steam evolved, 5 ml HF was added and the solution allowed to boil slowly for 5 to 10 min. The crucible was then plunged into a 600 ml beaker containing 5 pct H_2SO_4 saturated with boric acid, and the solution was titrated with 0.05-normal $KMnO_4$. Total iron content was determined by dissolving 0.1 to 0.2 g samples in 20 ml 1:3 H_2SO_4 and 5 ml HF in a large platinum dish and heating on a hot plate until all HF was driven off. The dish was cooled, the contents diluted and reduced by running it through a Jones' reductor, and then titrated with 0.05-normal $KMnO_4$. The trivalent iron was calculated as the difference between total iron and divalent iron.

Two uncertainty factors are involved in the analyses: In a large number of cases it was found difficult to separate the samples from the thin platinum foil of the envelopes. Careful grinding and screening of the samples helped considerably, but traces of platinum remained in a number of samples. This undissolved platinum was filtered off, dried, weighed, and subtracted from the original weight of the sample. Since the platinum contained some unknown amount of iron picked up from the sample during the run, this introduces an uncertainty in the analytical results. As previously mentioned, it was practically impossible to prevent dendritic crystals from forming even with the fastest quenching. This process could conceivably, at the same time, change to some extent the ratio between divalent and trivalent iron. In a series of preliminary tests, however, it was established that rate of quenching did not significantly affect composition as long as the samples were quenched in the equilibrium atmosphere. Similarly, Darken and Gurry found[7] that the effect of rate of quenching on composition was slight in their experiments at low oxygen pressures. Since it is difficult to remove all traces of mercury from a sample quenched in this medium, quenching the samples for analysis in a copper block attached to the bottom of the furnace tube was preferred.

Results

As pointed out previously, the composition of the condensed phases is a function of the gas composition in the system under study. Thereby one variable in addition to those dealt with in most *dry* ternary silicate systems is introduced. This complicating factor has to be taken into account when the plan of attack is made up for obtaining the necessary data to construct the diagram, and it has to be kept in mind in presenting the results.

Although the determination of liquidus temperatures for different compositions within the ternary system was the primary object of this investigation, it was thought desirable first to obtain more information regarding the ratios between FeO and Fe_2O_3 in homogeneous melts above the liquidus temperature as a function of temperature and O_2 pressure. With such data at hand, it is possible to attain a desired composition in the system $FeO-Fe_2O_3-SiO_2$, and the phase studies can be made in a systematic manner. A study was therefore made of the composition of melts in equilibrium with gas phase at O_2 pressures of 10^{-10} to 10^{-6} atm at 1200°, 1300°, and 1400°C. The results of these experiments are given in Table I and illustrated in Figs. 1, 2, and 3. In each of the diagrams, a light line encloses the area in which all compositions are one homogeneous liquid at the temperature represented by the diagram. Circles represent composition of mixtures studied and heavy lines are O_2 isobars. At these temperatures, experiments were not run at lower O_2 pressures than those shown because the increasingly high escaping tendency of iron made difficult the attainment of equilibrium. These curves, combined with data available in the literature, give a reasonably complete picture of the composition of the melts as a function of temperature and O_2 pressure and serve as a guide for the main part of the investigation, the phase equilibrium studies.

In ordinary dry phase diagram work, the procedure consists in keeping all independent variables constant except one, namely, the temperature. In other words, the total pressure is kept constant, the total composition is kept constant, and the change in phase assemblages caused by a change in temperature is observed. In the present system, how-

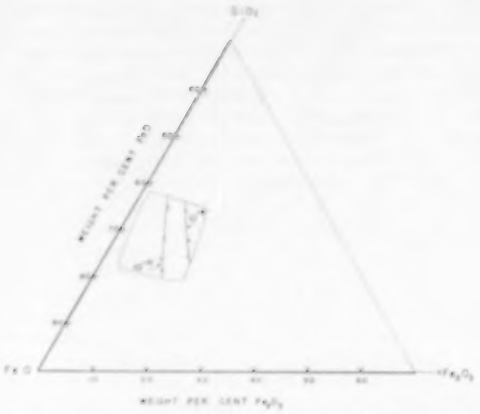

Fig. 1—Diagram of a part of the system FeO-Fe_2O_3-SiO_2 is shown to illustrate relationship of liquid and gas compositions in equilibrium at 1200°C. Compositions in the area enclosed by the light line are completely liquid at 1200°C. Circles represent the compositions, as shown by analysis, of liquids in equilibrium with a gas phase at O_2 pressures of 10^{-10} and 10^{-5} atm. Heavy lines approximately passing through the circles are O_2 isobars.

Fig. 2—Diagram of a part of the system FeO-Fe_2O_3-SiO_2 is given to illustrate relationship of liquid and gas compositions in equilibrium at 1300°C. Compositions in the area enclosed by the light line are completely liquid at 1300°C. Circles represent the compositions, as shown by analysis, of liquids in equilibrium with a gas phase at O_2 pressures of 10^{-6}, 10^{-4}, and 10^{-1} atm. Heavy lines approximately passing through the circles are O_2 isobars.

ever, the situation is more complicated because the ratio FeO/Fe_2O_3, and thus the total composition of a mixture, varies with temperature, partial pressure of O_2, and silica content. At temperatures above the liquidus where only one phase is present, the silica content remains constant for a chosen starting mixture, neglecting the slight change in composition caused by removal of iron by the platinum of the envelope. The ideal procedure would then be, when approaching the liquidus surface from the high temperature side (one liquid phase), to change the O_2 pressure in steps together with the stepwise change in temperature in such a way that the composition of the liquid remains constant. When working in an open system, this would require a detailed knowledge of the variation in composition of the melt as a function of temperature and O_2 pressure and, even with such information at hand, the

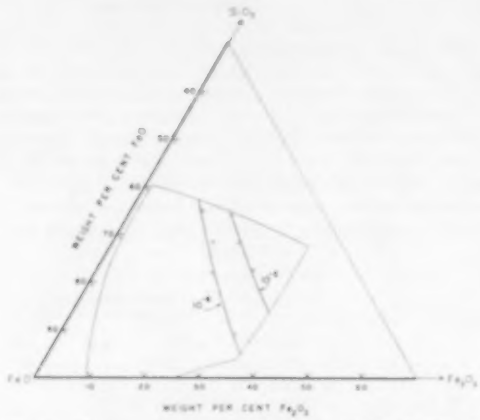

Fig. 3—Diagram of a part of the system FeO-Fe_2O_3-SiO_2 is shown to illustrate relationship of liquid and gas compositions in equilibrium at 1400°C. Compositions in the area enclosed by the light line are completely liquid at 1400°C. Circles represent the compositions, as shown by analysis, of liquids in equilibrium with a gas phase at O_2 pressures of 10^{-4} and 10^{-1} atm. Heavy lines approximately passing through the circles are O_2 isobars.

method would be very impractical. When working in a closed system and also in an open system with inert atmosphere and charges of high FeO/Fe_2O_3 ratio, the constancy of total composition is theoretically closely obtained. However, no crucible material has been found which does not react with the iron-silicate melt and, therefore, the ideal condition of constancy of composition is not realized in practice.

The second possible procedure is to keep the O_2 pressure constant while lowering the temperature. This method is the one actually used in the case of runs in air or at 1 atm O_2.

At low O_2 pressures, where the desired atmosphere was obtained by mixing CO_2 and H_2, the same procedure would be possible but not very practical, since the mixing ratio of the two gases would have to be adjusted every time the temperature is changed. In the case of runs made at low O_2 pressures, it was therefore found more practical to keep the CO_2/H_2 ratio constant at all temperatures for each mixture. The determination of the temperatures along the boundary curves silica-fayalite and fayalite-wüstite is most easily accomplished when, during crystallization of the solid phases, the composition of the liquid moves along a path perpendicular to the boundary curve. This is approximately the case when mixing ratio CO_2/H_2 is kept constant but not when O_2 pressure is kept constant. For these reasons, all of the quenching experiments for a particular mixture were made at constant ratio CO_2/H_2.

The results of the quenching experiments are given in Table II and drawn in Fig. 4, the phase diagram constructed by combining data of the present investigation with data published by various other investigators. The join FeO-Fe_2O_3 was constructed from data of Darken and Gurry.[1, 2] The construction of the boundary curves iron-wüstite, iron-fayalite, and iron-silica was based mainly on the data of Bowen and Schairer[3] for the system FeO-SiO_2. In the low silica portion of the boundary curve iron-wüstite, the agreement among data of Bowen and Schairer[3] and those of Darken and Gurry,[1, 2] and of Ensio and Schuhmann[5] is not very good. In the

Table II. Results of Quenching Experiments

Mixing Ratio, CO_2/H_2	Temperature of Quench Run, °C	Phases Present*	Temperature of Run for Analysis, °C	Calculated P_{O_2}, Atm, at Liquidus Temperature	Final Composition by Analysis, Wt Pct		
					FeO	Fe_2O_3	SiO_2
1.10	1336	Liq.	1330	$10^{-0.8}$	77.6	13.1	9.3
	1305	Wüs. + Liq.					
1.61	1350	Liq.	1347	$10^{-0.1}$	75.3	16.5	8.2
	1332	Wüs. + Liq.					
5.10	1362	Liq.	1355	$10^{-7.8}$	67.7	25.0	7.3
	1349	Wüs. (tr) + Liq.					
	1345	Wüs. + Liq.					
10.6	1387	Liq.	1382	$10^{-6.8}$	62.9	29.4	6.7
	1369	Wüs. + Liq.					
1.68	1304	Liq.	1291	$10^{-0.8}$	75.7	10.9	13.4
	1261	Wüs. + Liq.	1308	$10^{-6.0}$	70.0	17.4	12.6
2.45	1311	Liq.					
	1301	Wüs. + Liq.					
7.41	1304	Liq.	1288	$10^{-6.1}$	65.2	21.9	13.9
	1281	Wüs. (tr) + Liq.					
	1270	Wüs.					
15.7	1336	Liq.	1335	$10^{-7.0}$	61.3	27.0	11.7
	1328	Magn. (tr) + Liq.					
	1304	Magn. + Liq.					
1.72	1247	Liq.	1241	$10^{-10.5}$	72.0	10.0	18.0
	1221	Wüs. + Liq.					
	1174	Wüs. + Liq.					
	1165	Wüs. + Fa.					
2.61	1255	Liq.	1257	$10^{-6.7}$	69.3	13.8	16.9
	1247	Wüs. (tr) + Liq.					
	1243	Wüs. + Liq.					
	1173	Wüs. + Liq.					
	1158	Wüs. + Fa.					
14.1	1301	Liq.	1297	$10^{-7.0}$	60.6	23.9	16.5
	1275	Magn. + Liq.					
4.12	1206	Liq.	1208	$10^{-6.9}$	67.3	12.0	20.7
	1193	Wüs. + Liq.					
	1167	Wüs. + Liq.					
	1161	Wüs. + Fa.					
6.92	1201	Liq.	1205	$10^{-6.8}$	64.6	16.5	19.9
	1186	Wüs. + Liq.					
	1151	Wüs. + Liq.					
	1143	Wüs. + Fa.					
2.18	1181	Liq.	1181	$10^{-10.0}$	88.0	7.9	24.1
	1174	Fa. + Liq.					
5.61	1164	Liq.	1169	$10^{-10.1}$	66.7	11.4	22.9
	1157	Fa. + Liq.					
13.1	1206	Liq.	1204	$10^{-6.7}$	60.2	16.1	23.7
	1191	Magn. + Liq.					
	1153	Magn. + Liq.					
	1142	Magn. + Fa.					
22.9	1302	Liq.	1296	$10^{-7.0}$	55.2	22.7	22.1
	1280	Magn. + Liq.					
3.96	1179	Liq.	1183	$10^{-10.2}$	64.0	8.4	27.6
	1169	Fa. + Liq.					
8.26	1156	Liq.	1162	$10^{-6.9}$	61.2	12.1	26.7
	1148	Fa. + Liq.					
58.0	1331	Liq.	1326	$10^{-6.1}$	49.1	25.6	25.3
	1283	Magn. + Liq.					
3.42	1176	Liq.	1180	$10^{-10.0}$	60.2	5.4	34.4
	1169	Fa. + Liq.					
9.11	1156	Liq.	1168	$10^{-6.7}$	57.6	9.0	33.4
	1152	Fa. + Liq.					
29.6	1186	Liq.	1193	$10^{-6.3}$	53.0	13.8	33.2
	1181	Magn. + Liq.					
86.4	1312	Liq.	1309	$10^{-6.4}$	46.8	31.1	38.1
	1288	Magn. + Trid.					
14.3	1252	Liq.	1244	$10^{-6.3}$	54.4	9.7	35.9
	1201	Trid. + Liq.					
	1147	Trid. + Liq.					
	1142	Trid. + Fa.					
31.2	1247	Liq.	1251	$10^{-7.4}$	52.1	13.8	38.1
	1233	Trid. + Liq.					
	1187	Trid. + Liq.					
	1171	Trid. + Magn.					
51.6	1364	Liq.	1348	$10^{-6.9}$	49.4	15.2	35.4
	1302	Trid. + Liq.					
76.2	1408	Liq.	1411	$10^{-6.2}$	47.0	18.7	34.3
	1379	Trid. + Liq.					
	1302	Trid. + Liq.					
	1271	Trid. + Magn.					
51.6	1513	Liq.	1488	$10^{-6.0}$	46.7	16.1	37.2
	1472	Trid. + Liq.					
Air	1472	Liq.	1474	$10^{-6.7}$	21.8	65.9	13.3
	1461	Magn. + Liq.					
	1450	Magn. + Trid.					
Air	1464	Trid. (tr) + Liq.	1483	$10^{-6.7}$	23.3	55.6	21.2
	1455	Trid. + Magn.					
P_{O_2} = 1 atm	1464	Liq.	1466	10^{0}	17.8	69.3	12.9
	1457	Magn. + Liq.					
	1450	Magn. + Trid.					
P_{O_2} = 1 atm	1464	Liq.	1473	10^{0}	17.7	67.1	15.2
	1458	Magn. (tr) + Liq.					
	1456	Magn. + Liq.					
	1454	Magn. + Trid.					

* Abbreviations in the table have the following meanings: Liq. is liquid, Wüs. is crystals of wüstite, Magn. is crystals of magnetite, Fa. is crystals of fayalite, Trid. is crystals of tridymite, and tr is trace.

present paper, the curve in this region was drawn as a smooth curve in better agreement with phase principles than was the case in the original paper of Bowen and Schairer. Since the data of Bowen and Schairer were used for compositions and temperatures at the boundary curves for higher silica contents, their value for the incongruent melting point of wüstite (1380°C) and composition of liquid at this point (11.5 wt pct Fe_2O_3) were used rather than the values of Darken and Gurry. The bound-

aries for the two liquid region were drawn in accordance with Greig's[4] data.

The liquidus surface of the Fe_xO_y-SiO_2 side of the diagram can not be determined experimentally with the author's technique, since O_2 pressures higher than 1 atm would be required. Although the exact locations of the boundary curves in this region are unknown, the phase relationships probably are similar to those indicated by dashed boundary curves.

No data are available for locating the boundary curve between molten iron and silicate liquid (or liquids) with increasing silica content and increasing liquidus temperatures—the extreme left-hand side of the diagram. In Fig. 4 the boundary curves therefore are discontinued before they reach the FeO-SiO_2 join.

The diagrams in Figs. 5 and 6 were constructed in order to illustrate the relationship between the compositions of liquid and gas phases in equilibrium at liquidus temperatures. Light dash-dot lines in Fig. 5 are lines of equal O_2 pressures for points on liquidus surface and light dash-double-dot lines in Fig. 6 are lines of equal CO_2/H_2 mixing ratios. These curves were constructed by combining data summarized in Tables I and II with those in the literature. For compositions along the join FeO-Fe_2O_3, the data of Darken and Gurry[1, 2] were used and for melts in equilibrium with metallic iron those of Ensio and Schuhmann.[3] Compositions of liquids in equilibrium with air and 1 atm O_2 at 1600°C were taken from Gurry and Darken.[2] Larson and Chipman[11] determined FeO/Fe_2O_3 ratios at O_2 pressure of 10^{-6} atm and 1550°C.

Fig. 7 is constructed in order to show the relationship between compositions of liquid and crystalline phases. Heavy lines are boundary curves and medium dash lines are fractionation curves.† Of the crystalline phases occurring in this system, silica and fayalite are assumed to be essentially constant in composition, corresponding to the chemical formulas SiO_2 and $2FeO \cdot SiO_2$, respectively. In the primary fields of silica and fayalite, therefore, the fractionation curves are straight lines. The variations in compositions of wüstite and magnetite as a function of temperature and O_2 pressure were determined by Darken and Gurry.[1, 2] The data of these authors were combined with data obtained in the present investigation to construct fractionation curves in the wüstite and magnetite fields as shown in Fig. 7. The composition of the crystalline phase in equilibrium with a liquid is represented by the point of intersection of the FeO-Fe_2O_3 join and the tangent to the fractionation curve at the point representing the liquid composition.

† Fractionation curves are curves drawn to illustrate relationship of composition of liquid and crystalline phases in equilibrium. The curves are constructed from conjugation lines in such a way that the conjugation lines are tangent to the fractionation curves. (A conjugation line joins the composition of a liquid with the composition of the solid with which it is in equilibrium.)

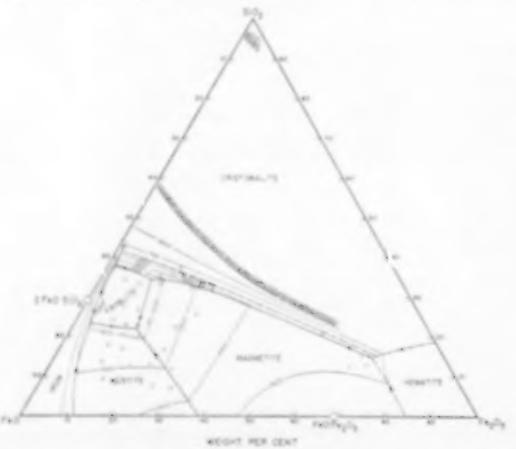

Fig. 4—Phase equilibrium diagram is presented for the system FeO-Fe_2O_3-SiO_2. Circles represent compositions, as shown by analysis, of mixtures at liquidus temperatures. Light lines are liquidus isotherms at 100°C intervals and heavy lines are boundary curves, with arrows pointing in the directions of falling temperatures. The tridymite-cristobalite boundary curve is dashed. Medium lines with stippling on one side indicate limit of two liquid region.

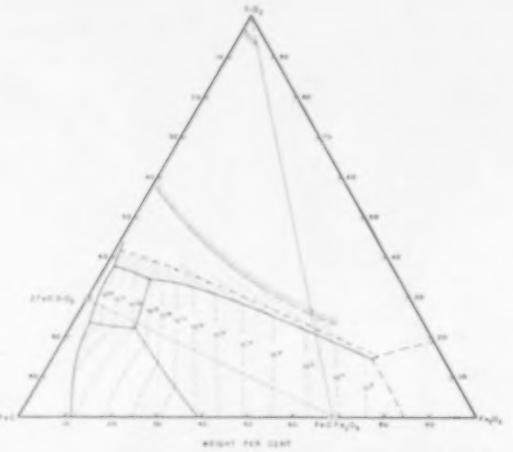

Fig. 5—Phase equilibrium diagram is shown for the system FeO-Fe_2O_3-SiO_2. Heavy lines are boundary curves and dash-dot lines are lines of equal O_2 pressures for points on liquidus surface. Lines with stippling on one side indicate limit of two liquid region.

Paths of Crystallization

In ordinary *dry* ternary silicate systems, the paths of crystallization under equilibrium conditions are determined unambiguously from the changes in composition of liquid and crystalline phases accompanying a change in temperature. In other words, curves representing paths of crystallization can be constructed from a knowledge of the liquidus surface and fractionation curves. In a series of papers from the Geophysical Laboratory (for example, those describing the systems CaO-Al_2O_3-SiO_2,[12] CaO-FeO-SiO_2,[13] MgO-FeO-SiO_2,[14] and $CaSiO_3$-$Ca_2MgSi_2O_7$-$Ca_2Al_2SiO_7$[15]), classic descriptions may be found of crystallization phenomena in such systems. For the system FeO-Fe_2O_3-SiO_2, however, in addition to the changes in composition of the condensed phases, variation in composition of the gas phase during the crystallization process must be taken into consideration. Consequently, crystallization under equilibrium conditions in this case is described in terms of three variables in addition to temperature, namely, the composition of the liquid, crystalline, and gas phases. A representation of all these variables in a single diagram would result in a confusingly large number of lines. For this reason, the different variables are shown in separate diagrams. The phase diagram in Fig. 4 shows the liquidus surface with isotherms and thus gives the relationship between temperature and composition of liquid. Fig. 5 is a representation of liquidus surface and O_2 isobars,

thus relating liquid composition to partial pressure of O_2 in the gas phase in equilibrium with liquid. Similarly, the fractionation curves in Fig. 7 illustrate the relationship between compositions of liquid and crystalline phases in equilibrium.

On the basis of these diagrams, it is possible to derive the paths of crystallization under various conditions. The relationships can best be discussed in terms of three different idealized cases, namely, 1—the total composition of the condensed phases remains constant, 2—the O_2 pressure is kept constant, and 3—the CO_2/H_2 mixing ratio is kept constant.

Throughout the following discussion, it is assumed that perfect equilibrium always exists among gas, liquid and crystalline phases, and that heat is continually removed from the mixtures.

Constant Total Composition of Condensed Phases—The derivation of paths of crystallization under conditions of constant total composition of condensed phases involves mainly principles well known from ordinary dry silicate systems.[12-13] The curves representing paths of equilibrium crystallization are constructed from the fractionation curves on the basis of postulating constant total composition of condensed phases. The only additional complication in the present case arises from the fact that the O_2 pressure must change continuously during crystallization in order to maintain equilibrium among crystalline, liquid, and gas phases while the total composition of the condensed phases remains constant. The relationships can be explained by considering the paths of crystallization of typical mixtures.

Fig. 8 shows an enlarged portion of the ternary system FeO-Fe_2O_3-SiO_2, including the primary fields of fayalite and wüstite. Heavy lines are boundary curves. Medium dash lines are fractionation curves, medium solid lines are equilibrium crystallization curves, and medium dash-cross lines are conjugation lines.‡ Light solid lines are liquidus isotherms at 50°C intervals and light dash-dot lines are O_2 isobars. Light dash lines are auxiliary construction lines. The straight line from the fayalite composition ($2FeO \cdot SiO_2$) through point *b* on the boundary curve fayalite-magnetite is part of a straight line joining the composition points $2FeO \cdot SiO_2$ and $FeO \cdot Fe_2O_3$.

‡ Conjugation lines are indicated by their end points in cases where they fall very close to other lines.

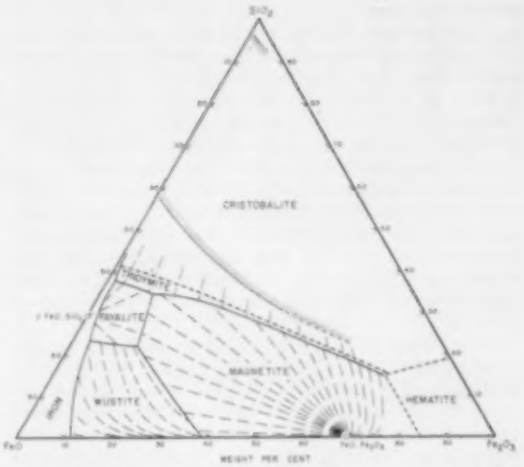

Fig. 7—Diagram of the system FeO-Fe_2O_3-SiO_2 is presented to illustrate relationship of compositions of liquid and crystalline phases in equilibrium. Heavy lines are boundary curves and medium dash lines are fractionation curves. Lines with stippling on one side indicate limit of two liquid region.

As an example of paths of crystallization in fields where the primary crystals have constant composition, three mixtures located at *A*, *B*, and *C* in the fayalite field are considered.

In mixture *A* crystals of fayalite start separating out at approximately 1180°C, and the liquid composition changes along the straight line *A*-*a* away from the fayalite composition. At point *a*, approximately 1145°C, magnetite begins to crystallize together with fayalite, and the liquid composition moves along the boundary curve fayalite-magnetite until at 1140°C the liquid, now of composition *X*,

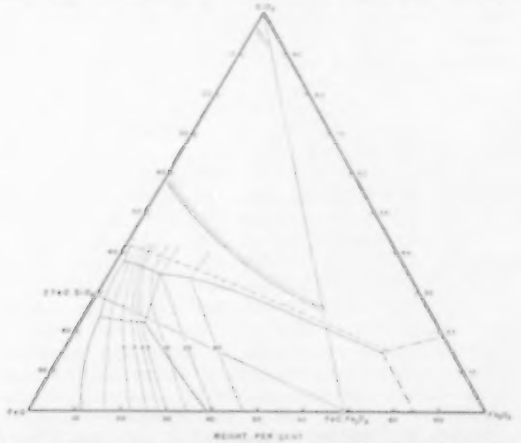

Fig. 6—Phase equilibrium diagram is presented for the system FeO-Fe_2O_3-SiO_2. Heavy lines are boundary curves and dash-double-dot lines are lines of equal CO_2/H_2 mixing ratios for points on liquidus surface. Lines with stippling on one side indicate limit of two liquid region.

Fig. 8—Diagram of a part of the system FeO-Fe_2O_3-SiO_2 is shown to illustrate paths of equilibrium crystallization under conditions of constant total composition of condensed phases. Heavy lines are boundary curves. Medium dash lines are fractionation curves, dash-cross lines are conjugation lines, and medium solid lines are equilibrium crystallization curves. Light solid lines are liquidus isotherms at 50°C intervals, light dash-dot lines are O_2 isobars for points on liquidus surface, and light dash lines are auxiliary construction lines.

disappears, the final product being a mixture of fayalite, magnetite, and tridymite. During this process the O_2 pressure of the gas phase changes continuously from approximately 10^{-11} atm at point *A* through $10^{-8.3}$ atm at point *a* to $10^{-8.5}$ atm at *X*.

In mixture *B* fayalite starts separating out at approximately 1180°C, and the liquid composition moves along the straight line *B-b*. When point *b* is reached, at approximately 1150°C, magnetite precipitates together with fayalite and the liquid disappears. The final product in this case therefore is a mixture of fayalite and magnetite. During this process, the O_2 pressure changes continuously from approximately 10^{-11} atm at point *B* to $10^{-8.5}$ atm at point *b*.

In mixture *C* fayalite begins to separate at approximately 1195°C, and the liquid composition changes along the straight line *C-c* away from the fayalite composition. At point *c*, approximately 1170°C, wüstite of composition *c*" starts crystallizing together with fayalite, the wüstite composition being determined by the tangent to the fractionation curve at this point (i.e., conjugation line *c-c*"). With wüstite of continuously changing composition and fayalite crystallizing out together, the liquid composition moves along the boundary curve wüstite-fayalite. The liquid disappears at point *c*' where the composition of wüstite (*c*"') determined by conjugation line *c-c*"', falls on the extension of the straight line from $2FeO \cdot SiO_2$ through *C*. The crystallization process takes place at continuously varying O_2 pressures, from approximately $10^{-10.4}$ atm at point *C* to $10^{-10.9}$ atm at point *c*'.

Mixture *D* is chosen to illustrate paths of crystallization in the field of wüstite. At approximately 1370°C wüstite starts separating out and the liquid composition moves along the equilibrium crystallization curve *D-d* (medium solid line). The composition of the wüstite in equilibrium with liquid, determined by the tangent to the fractionation curve through the points representing liquid composition, changes continuously from *d*" (31 wt pct Fe_2O_3) to *d*"' (28 wt pct Fe_2O_3). Fayalite starts separating out together with wüstite from the liquid at point *d*, and the liquid composition moves along the boundary curve wüstite-fayalite toward *d*'. From the point *d* where the boundary curve is reached, a reversal occurs in the direction of change in composition of wüstite, the Fe_2O_3 content increasing as the liquid composition moves along the boundary curve. The liquid disappears at point *d*', the end product being a mixture of fayalite and wüstite. The composition *d*"" of wüstite at this point, determined by the conjugation line *d-d*"", falls on the extension of the straight line from $2FeO \cdot SiO_2$ through point *D*. During the crystallization process, the O_2 pressure changes continuously. It first decreases along the curved path *D-d* from approximately 10^{-8} atm at *D* to $10^{-10.5}$ atm at *d*. From here on, with fayalite and wüstite coprecipitating, the change in O_2 pressure reverses itself, increasing to approximately $10^{-10.4}$ atm at point *d*'. The increase in O_2 pressure is necessary to keep the total composition constant during the increased *extraction* of FeO from the melt by the crystallization out of fayalite.

Fig. 9 shows an enlarged portion of the ternary system in the neighborhood of the magnetite composition. The various lines have the same meaning as in Fig. 8. As examples of paths of crystallization in the primary field of magnetite, three mixtures *E*, *F*, and *G* are considered. In mixture *E* magnetite starts separating out at approximately 1530°C, the first crystals to appear having a composition *e*", corresponding to approximately 76 wt pct Fe_2O_3. With liquid composition moving along the curved path *E-e* (medium solid line), the magnetite composition changes continuously from *e*" to *e*"'. At point *e* tridymite starts separating out together with magnetite, and the liquid composition moves to the right along the boundary curve magnetite-tridymite. The liquid disappears at point *e*', where the composition of magnetite, determined by the conjugation line *e*'-*e*"', falls on the extension of the straight line connecting the SiO_2 corner of the ternary diagram with point *E*. The end product therefore is a mixture of magnetite and tridymite. The O_2 pressure, which at point *E* is approximately 1 atm, decreases slightly while the liquid composition moves along the curved line *E-e* in the magnetite field. At point *e* the change in O_2 pressure reverses itself, slightly increasing pressure being necessary to maintain total composition of condensed phases constant with magnetite and tridymite crystallizing out together.

In mixture *F* magnetite of composition *f*' (72 wt pct Fe_2O_3) starts separating out at approximately 1570°C. With equilibrium cooling, the liquid composition changes along the curved line *F-f* (medium solid line) while the magnetite in equilibrium with the melt varies in composition continuously from *f*' to *f*"', *f*" being determined by the conjugation line *f-f*"'. This conjugation line has a direction pointing to the SiO_2 corner of the triangle representing the ternary system, and the liquid therefore must disappear at point *f*. The end product is a mixture of magnetite and tridymite. During the crystallization process, the O_2 pressure changes continuously from approximately $10^{-6.6}$ atm at point *F* to $10^{-7.0}$ atm at point *f*. The directions of the conjugation lines give information regarding the slope of the boundary curve magnetite-tridymite. By quenching experiments, no detectable difference in temperature was

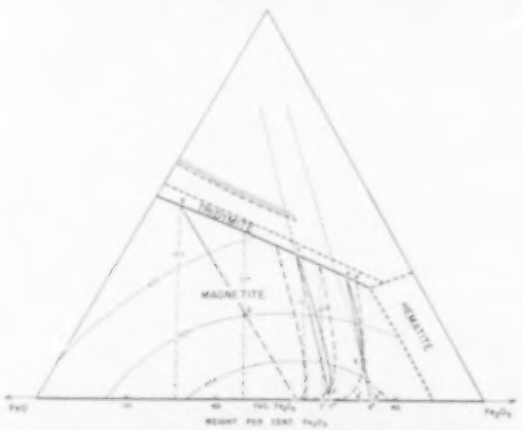

Fig. 9—Diagram of a part of the system FeO-Fe_2O_3-SiO_2 is presented to illustrate paths of equilibrium crystallization for mixtures in the magnetite field under conditions of constant total composition of condensed phases. Heavy lines are boundary curves. Medium dash lines are fractionation curves, medium dash-cross lines are conjugation lines, and medium solid lines are equilibrium crystallization curves. Light solid lines are liquidus isotherms at 50°C intervals, light dash-dot lines are O_2 isobars for points on liquidus surface, and light dash lines are auxiliary construction lines. Line with stippling on one side indicates limit of two liquid region.

found for points on the boundary curve in air and at 1 atm O_2 pressure, indicating that the boundary curve is extremely flat in this region. The construction of conjugation lines shows that a maximum must exist at point *f*. The temperature of this maximum on the tridymite-magnetite boundary curve is approximately 1456°C, and the following phases coexist in equilibrium: tridymite, magnetite with a composition corresponding to 73 wt pct Fe_2O_3, a liquid of composition 19 wt pct SiO_2, 59 wt pct Fe_2O_3, 22 wt pct FeO, and a gas phase with partial pressure of O_2 of approximately 0.1 atm. The slope of the boundary curve tridymite-magnetite thus established, together with the known decomposition temperature of Fe_2O_3 at 1 atm O_2, indicates the approximate location of the ternary invariant point tridymite-magnetite-hematite-liquid-gas, which was not obtained experimentally. The decomposition temperature of Fe_2O_3 at 1 atm O_2 was determined in the present investigation to 1453±3°C, as compared to 1452±5°C reported by Greig et al.[10] and 1457±2°C by Darken and Gurry.[2] Because the temperature of decomposition of hematite to magnetite increases with increasing O_2 pressure, while the liquidus temperature along the boundary curve magnetite-tridymite decreases when O_2 pressure is increased from 1 atm, hematite must be the stable phase of iron oxide in equilibrium with liquid of composition on the boundary curve magnetite-tridymite slightly to the right of the point where the 1 atm O_2 isobar (Fig. 5) intersects this boundary curve. From this it can be inferred that the aforementioned invariant point must be located at approximately 1455°C, with a liquid composition of approximately 15 wt pct SiO_2, 16 wt pct FeO, and 69 wt pct Fe_2O_3, and a partial O_2 pressure of the gas phase only slightly higher than 1 atm.

In mixture *G* magnetite of composition $FeO \cdot Fe_2O_3$ starts separating out at about 1500°C, and with continued cooling the liquid moves along the straight line *G-g* away from the magnetite composition. At point *g* tridymite starts crystallizing out together with magnetite, and the liquid composition moves along the boundary curve magnetite-tridymite. The rest of the crystallization path is not shown in Fig. 9 but can be followed in Figs. 4 and 5. The liquid composition moves all the way down to invariant point *X*, where the liquid disappears, leaving as end product a mixture of magnetite, tridymite, and fayalite. During this process the O_2 pressure changes continuously from about 10^{-4} atm at point *G*, through 10^{-6} atm at point *g*, to $10^{-6.6}$ atm at point *X*.

The O_2 Pressure is Kept Constant—This condition gives rise to paths of crystallization which are less familiar but in many respects simpler than the case just considered. The whole theory of paths of crystallization in ordinary *dry* silicate systems is based on the assumption of constant total composition, a fact which is not always fully appreciated. As soon as this requirement is not fulfilled, the concept of composition triangles is not applicable and the construction of equilibrium crystallization curves from fractionation curves can not be carried out. In the present case, therefore, new criteria must be established from which the paths of crystallization can be derived.

Since the composition of the liquid is unambiguously determined by silica content, temperature, and O_2 pressure, it follows that in all cases during crystallization at constant O_2 pressure the liquid composition must follow the isobars along the liquidus surface. In other words, the isobars at the same time become the curves of equilibrium crystallization. This relationship holds regardless of the nature of the crystalline phases separating out, whether they be of constant composition like SiO_2 and $2FeO \cdot SiO_2$, or of varying composition like magnetite and wüstite. When a boundary curve is reached, a new crystalline phase appears, and one of the previous phases must disappear, either the liquid or the primary crystalline phase. The liquid phase disappears in all cases where the point of intersection of the isobar and the boundary curve is a temperature minimum point on the isobar. If the point of intersection is not a minimum, then either the liquid or the primary crystalline phase disappears, depending on the location of the starting mixture. For the purpose of illustrating more clearly the principles involved, the paths of crystallization of a few selected mixtures are considered. In order to simplify this discussion, a new term is introduced, namely isosilica lines. These are lines having a constant Si/Fe ratio. As pointed out previously, it is assumed that no reaction takes place between the iron silicate melt and the crucible material. This means that the silica content of the condensed phases is constant. The only change in total composition of the condensed phases taking place is an addition or a subtraction of oxygen, in other words, a variation in the ratio FeO/Fe_2O_3. The situation is more easily understood by keeping in mind that the system under consideration is part of the ternary system Fe-Si-O. The only way the total composition of the condensed phases can change is by exchanging oxygen with the gas phase. In other words, still referring to the ternary system Fe-Si-O, the Fe/Si ratio remains constant, whereas the oxygen content varies. The total composition of the condensed phases for a chosen mixture must therefore always remain on a straight line through the O-corner of the triangle representing the system. The lines in the $FeO-Fe_2O_3-SiO_2$ diagram describing this situation, the isosilica lines, are of course also straight lines which can easily be constructed. They are almost parallel to the $FeO-Fe_2O_3$ join when the diagram is plotted on a weight percentage basis. The usefulness of the isosilica lines is evidenced by the fact that regardless of what is done to a mixture of chosen starting composition, the total composition of the condensed phases is always represented by a point somewhere on the isosilica line through the point of original composition. In other words, the total composition, so to speak, slides back and forth on the isosilica line. One of the isosilica lines is of special importance for the derivation of paths of crystallization, namely, the isosilica line through the fayalite ($2FeO \cdot SiO_2$) composition. At low O_2 pressures, the paths of crystallization differ, depending on whether the starting mixture is located above or below this line.

The paths of crystallization are discussed with reference to Figs. 10 and 11. In these diagrams heavy lines are boundary curves. Light dash-dot lines are O_2 isobars at liquidus temperatures and at the same time equilibrium crystallization curves. Light dash-cross lines are isosilica lines and light dash lines, auxiliary construction lines. The isobars through invariant points *X* and *Y*, corresponding to O_2 pressures of approximately $10^{-6.6}$ and $10^{-0.6}$ atm, respectively, as well as the isobar corresponding to 1 atm O_2, are drawn as medium dash-dot lines. The following discussion is limited to the area between the 1 atm O_2 isobar and the field of metallic iron. The $10^{-6.6}$ and $10^{-0.6}$ atm isobars divide this portion

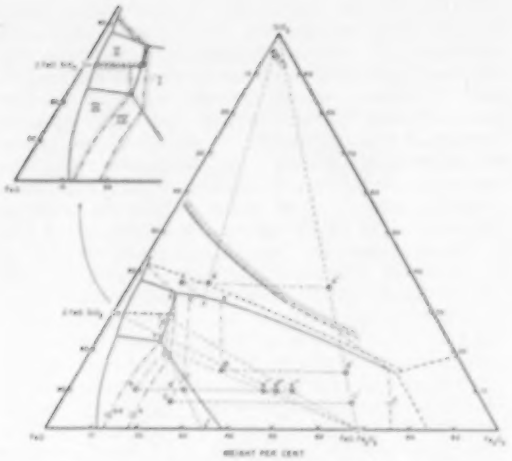

Fig. 10—Diagram of the system FeO-Fe_2O_3-SiO_2 is shown to illustrate paths of equilibrium crystallization at constant O_2 pressures. Heavy lines are boundary curves. Light dash-dot lines are O_2 isobars for points on liquidus surface and at the same time equilibrium crystallization curves. The isobars corresponding to O_2 pressures of 1, $10^{-0.5}$, and $10^{-4.0}$ atm are drawn as medium dash-dot lines. Light dash-cross lines are isosilica lines. The isosilica line through the fayalite ($2FeO \cdot SiO_2$) composition is drawn as a medium dash-cross line. Light dash lines are auxiliary construction lines. Outlines of areas I, II, III, and IV referred to in the text are indicated by different shadings for a part of the system drawn separately to the side of the main diagram. Lines with stippling on one side indicate limit of two liquid region.

of the diagram vertically into three sections to be discussed separately. The dash-cross straight line through the fayalite ($2FeO \cdot SiO_2$) composition is the isosilica line through this point. This line, similarly, divides the diagram horizontally into two sections, separating mixtures above and below the line. On the basis of these subdivisions, four different areas will be considered, the boundaries of which are shaded differently in Fig. 10. The area labeled I includes all mixtures located between the 1 atm and $10^{-0.5}$ atm isobars. Area II includes mixtures located above the $2FeO \cdot SiO_2$ isosilica line and to the left of the $10^{-4.0}$ atm isobar. In areas III and IV the mixtures are located below the $2FeO \cdot SiO_2$ isosilica line in both cases, but the O_2 pressures are different. Mixtures in area III are equilibrated at O_2 pressures below $10^{-4.0}$ atm, whereas the O_2 pressures in area IV are between $10^{-4.0}$ and $10^{-0.5}$ atm.

Mixtures Located in Area I, Fig. 10: In mixture *A*, when equilibrated at an O_2 pressure of 10^{-1} atm, tridymite starts separating out at about 1400°C and the liquid composition moves along the 10^{-1} atm isobar until the boundary curve tridymite-magnetite is reached at point *a*. Since *a* is the lowest point on the liquidus surface at the chosen O_2 pressure, as heat is withdrawn, the liquid phase disappears, and the end product is a mixture of tridymite and magnetite. The total composition of the condensed phases, which was *A* at the liquidus temperature, changes continuously along the isosilica line through *A*. It is represented by point *A'* when the liquid composition reaches the boundary tridymite-magnetite, and at the end is represented by point *A"*, the point of intersection between the isosilica line through *A* and the straight line joining the silica (SiO_2) and magnetite ($FeO \cdot Fe_2O_3$) compositions.

A mixture represented by point *B* in the primary field of magnetite behaves similarly. Magnetite starts separating out at about 1370°C and, with decreasing temperature and equilibrium maintained, the liquid composition moves along the 10^{-4} atm isobar until the boundary curve magnetite-tridymite is reached. Here the liquid phase disappears, leaving as an end product a mixture of tridymite and magnetite. During this process the total composition of the condensed phases moves along the isosilica line from *B* to *B'*.

In mixture *C* wüstite starts separating out at about 1350°C, and as heat is withdrawn, the liquid composition moves along the wüstite liquidus surface following the 10^{-4} atm isobar. The wüstite composition changes continuously in a way which can be derived from the fractionation curves. These curves are not drawn in Fig. 10, in order to avoid the confusion caused by too many lines. The relationships can, however, be derived easily by comparing Figs. 5, 10, and 7. When the liquid composition reaches point *c*, wüstite disappears and magnetite starts separating out with temperature remaining constant. When the last trace of wüstite disappears, the liquid composition starts moving along the magnetite liquidus surface following the 10^{-4} atm isobar, with magnetite continuously separating out. When the boundary curve magnetite-tridymite is reached, at point *c'*, the liquid disappears, leaving as end product a mixture of magnetite and tridymite. The total composition during this process changes along the isosilica line from *C* to *C"*.

From these considerations, it appears that all iron oxide-silica mixtures, when equilibrated at O_2 pressures between $10^{-4.0}$ and 1 atm, give as end product a mixture of magnetite and tridymite at a temperature infinitesimally below the solidus.

Mixtures Located in Area II, Fig. 11: For a point *D* in the tridymite field, tridymite crystallizes out; and, as heat is withdrawn, the liquid composition moves along the 10^{-10} atm isobar until the boundary curve tridymite-fayalite is reached, at which point the liquid phase disappears.

A point *E* in the fayalite field behaves similarly; fayalite crystallizes out and the liquid composition during equilibrium crystallization moves along the 10^{-11} atm isobar until the boundary fayalite-tridymite is reached, where the liquid phase disappears.

For point *F* in the magnetite field, magnetite separates out and the liquid moves along the $10^{-9.1}$ atm isobar until the isobar intersects the boundary curve magnetite-fayalite at point *f*. As heat is withdrawn, magnetite disappears with temperature remaining constant. When no magnetite is left, the temperature decreases; and, with fayalite crystallizing out, the liquid follows the $10^{-9.1}$ atm isobar along the fayalite liquidus surface until the boundary fayalite-tridymite is reached, where the liquid phase disappears. The total composition, which at the liquidus temperature is *F*, moves first to the right on the isosilica line reaching the minimum FeO/Fe_2O_3 ratio at *F'* when the liquid composition reaches the boundary magnetite-fayalite at *f*. With fayalite starting to crystallize at this point, the change in total composition reverses itself, the point representing total composition moving to the left along the isosilica line until at the solidus temperature the total composition is represented by point *F"*, the intersection between the isosilica line and the FeO-SiO_2 join.

From these considerations it appears that all mixtures above the isosilica line through the $2FeO \cdot SiO_2$ composition, when equilibrated at O_2 pressures below approximately $10^{-4.0}$ and above $10^{-10.6}$ atm, give as an end product a mixture of fayalite and tridymite.

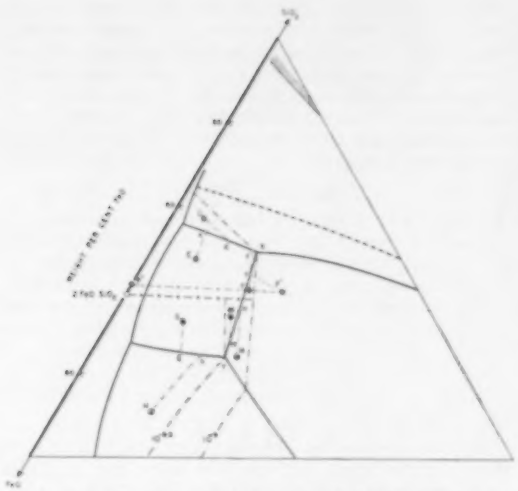

Fig. 11—Diagram of a part of the system FeO-Fe_2O_3-SiO_2 is presented to illustrate paths of equilibrium crystallization at constant O_2 pressures. Heavy lines are boundary curves. Light dash-dot lines are O_2 isobars for points on liquidus surface and at the same time equilibrium crystallization curves. The isobars corresponding to O_2 pressures of 1, $10^{-0.6}$, and $10^{-0.8}$ atm are drawn as medium dash-dot lines. Light dash-cross lines are isosilica lines. The isosilica line through the fayalite ($2FeO \cdot SiO_2$) composition is drawn as a medium dash-cross line. Light dash lines are auxiliary construction lines. Line with stippling on one side indicates limit of two liquid region.

Mixtures Located in Area III: In mixture G, Fig. 11, fayalite is the first crystalline phase to appear, and with decreasing temperature the liquid composition follows the 10^{-11} atm isobar until the boundary curve fayalite-wüstite is reached at point g. Here the liquid disappears, leaving as end product a mixture of fayalite and wüstite.

In mixture H wüstite of continuously varying composition crystallizes out, and the liquid composition moves along the corresponding isobar until at point h the liquid disappears, the end product being a mixture of fayalite and wüstite. Similarly, all mixtures below the isosilica line through $2FeO \cdot SiO_2$, when equilibrated at O_2 pressures below $10^{-8.8}$ and above $10^{-10.5}$ atm, crystallize completely to a mixture of wüstite and fayalite.

Mixtures Located in Area IV: In mixture M, Fig. 11, fayalite is the first crystalline phase to appear, and the liquid composition moves along the $10^{-8.8}$ atm isobar until the magnetite-fayalite boundary is reached. Here the liquid disappears and the end product consists of a fayalite and magnetite mixture.

In mixture N magnetite separates out as a primary phase, and the liquid composition moves along the $10^{-9.5}$ atm isobar until the boundary curve magnetite-fayalite is reached. Here the last liquid disappears and the end product is a mixture of magnetite and fayalite.

In mixture K, Fig. 10, wüstite is the primary phase. With wüstite of continuously varying composition crystallizing out, as heat is withdrawn, the liquid composition moves along the corresponding $10^{-8.8}$ atm isobar until at point k the boundary curve wüstite-magnetite is reached. Here wüstite disappears and magnetite starts forming, with temperature remaining constant. When the last traces of wüstite disappear, the temperature decreases, and with magnetite crystallizing out the liquid composition follows the isobar along the magnetite liquidus surface. When the boundary curve magnetite-fayalite is reached at point k', the last liquid disappears, leaving as end product a mixture of magnetite and fayalite. The total composition, which is represented by point K at the liquidus temperature, changes along the isosilica line through K during the crystallization process. When the liquid composition reaches point k, the total composition is K', the point of intersection of the isosilica line with the conjugation line through k (point K' is found by using fractionation curves from Fig. 7 together with Fig. 10). The liquid composition remains constant at k until the wüstite has disappeared completely, with total composition steadily changing to the right along the isosilica line until point K'' is reached. With magnetite separating out and the liquid composition starting to move along the $10^{-9.5}$ atm isobar in the primary field of magnetite, the total composition moves further along the isosilica line until point K''' is reached when the liquid reaches point k'. At this point fayalite starts crystallizing out together with magnetite, and the change in total composition is reversed. It now changes from K''' toward K'''', K'''' being the point of intersection between the isosilica line through K and the straight line joining $2FeO \cdot SiO_2$ and $FeO \cdot Fe_2O_3$.

Similarly, all other mixtures located below the isosilica line through $2FeO \cdot SiO_2$, when equilibrated at O_2 pressures between $10^{-8.8}$ and $10^{-9.5}$ atm, give as end product a mixture of magnetite and fayalite.

Mixing Ratio CO_2/H_2 is Kept Constant—This condition gives rise to paths of crystallization which can be derived in a manner completely analogous to the case just considered. The discussion is a repetition of the foregoing, with lines of equal CO_2/H_2 mixing ratios taking the place of the O_2 isobars. The diagram can be divided into four sections in analogy with the foregoing, the vertical

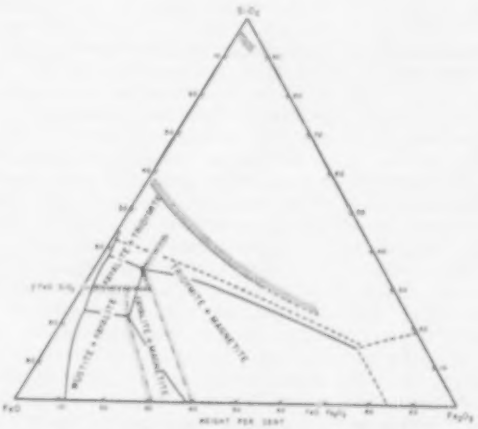

Fig. 12—Diagram of the system FeO-Fe_2O_3-SiO_2 is shown to illustrate phase assemblages at temperatures infinitesimally below solidus, under conditions of constant CO_2/H_2 mixing ratios. Heavy lines are boundary curves. Medium dash-double-dot lines are lines of equal CO_2/H_2 mixing ratios of 6.5 and 19, for points on liquidus surface. The medium dash-cross line is the isosilica line through the fayalite ($2FeO \cdot SiO_2$) composition. Outlines of four areas are indicated by different shadings. Within each area, all mixtures give the same end product at a temperature infinitesimally below the solidus. Lines with stippling on one side indicate limit of two liquid region.

subdivisions this time being based on the lines of equal CO_2/H_2 ratios through invariant points *X* and *Y*, corresponding to CO_2/H_2 ratios of about 19 and 6.5, respectively. The results are summarized in Fig. 12, showing the phase assemblages at temperatures infinitesimally below the solidus temperatures.

Summary

The ternary system FeO-Fe_2O_3-SiO_2 deviates from ordinary *dry* silicate systems in that the composition of the condensed phases is dependent on the partial O_2 pressure of the gas phase. Liquidus data were obtained at O_2 pressures ranging from $10^{-10.8}$ to 1 atm. In this part of the system there are two ternary invariant points: At one invariant point (*X* in Figs. 8, 10, and 11), the following phases coexist in equilibrium at 1140°C: tridymite (SiO_2), fayalite ($2FeO \cdot SiO_2$), magnetite ($FeO \cdot Fe_2O_3$), a liquid with composition 35 wt pct SiO_2, 11 wt pct Fe_2O_3, and 54 wt pct FeO, and a gas phase with partial O_2 pressure of 10^{-9} atm. At the other invariant point (*Y* in Figs. 8, 10, and 11), the following phases coexist in equilibrium at 1150°C: fayalite ($2FeO \cdot SiO_2$), magnetite ($FeO \cdot Fe_2O_3$), wüstite with a composition corresponding to 35 wt pct Fe_2O_3, a liquid with composition 22 wt pct SiO_2, 14 wt pct Fe_2O_3, and 64 wt pct FeO, and a gas phase with partial O_2 pressure of $10^{-8.8}$ atm. The ternary invariant point where tridymite (SiO_2), magnetite, hematite, liquid, and gas are in equilibrium was not determined experimentally but is inferred to be located at a temperature of approximately 1455°C, with liquid composition approximately 15 wt pct SiO_2, 69 wt pct Fe_2O_3, 16 wt pct FeO, and a partial O_2 pressure of the gas slightly higher than 1 atm.

Along the boundary curve tridymite-magnetite, a maximum point exists at a temperature of 1456°C with the following phases coexisting in equilibrium: tridymite (SiO_2), magnetite with a composition corresponding to 73 wt pct Fe_2O_3, a liquid of composition 19 wt pct SiO_2, 59 wt pct Fe_2O_3, 22 wt pct FeO, and a gas phase with partial pressure of O_2 of approximately 0.1 atm.

Isobars along the liquidus surface, corresponding to partial pressures of O_2 (Fig. 5), illustrate the marked change in phase relationships with change in atmospheric conditions. The lowest temperature at which liquid can exist under equilibrium conditions in an iron oxide-silica mixture is approximately 1455°C at 1 atm O_2 pressure. With O_2 pressure decreasing to 10^{-1} atm, the lowest temperature of liquid existence is essentially the same. With further decrease in O_2 pressure, liquid is present at rapidly decreasing temperatures, reaching a minimum of 1140°C at 10^{-9} atm O_2 for mixtures above the $2FeO \cdot SiO_2$ isosilica line and a minimum of 1150°C at $10^{-8.8}$ atm O_2 for mixtures below the $2FeO \cdot SiO_2$ isosilica line. With further decrease in O_2 pressure, the lowest temperature of liquid existence increases somewhat, until metallic iron appears as a phase at O_2 pressures between 10^{-12} and 10^{-13} atm.

The paths of crystallization for mixtures within this system are complicated, but the relationships can be deduced for chosen idealized conditions, which in practical industrial processes are never realized but often approached. In a closed system, the total composition of the condensed phases remains essentially constant, and the equilibrium crystallization paths can be deduced from well established principles of *dry* silicate systems. In the primary fields of tridymite and fayalite the crystallization curves are straight lines, whereas in the fields of magnetite and wüstite the liquid composition during crystallization follows curved lines. In an open system under constant O_2 pressure, the O_2 isobars along the liquidus surface are the paths of equilibrium crystallization. During this crystallization process, the total composition of the condensed phases changes along lines of equal Si/Fe ratios.

Acknowledgments

The studies described in this paper are part of a research program conducted in the College of Mineral Industries on phase equilibria in steel plant refractories systems, sponsored by the American Iron and Steel Inst. The author is indebted to E. F. Osborn and M. L. Keith for constructive suggestions during the course of the work and for critical reading of the manuscript. Contribution No. 53-77 from the College of Mineral Industries, The Pennsylvania State University.

Discussion of this paper, if any, will appear in JOURNAL OF METALS, November 1956, and in AIME Metals Branch *Transactions*, Vol. **206**, 1956.

References

[1] L. S. Darken and R. W. Gurry: The System Iron-Oxygen. I. The Wüstite Field and Related Equilibria. *Journal* Amer. Chemical Soc. (1945) **67**, p. 1398.

[2] L. S. Darken and R. W. Gurry: The System Iron-Oxygen. II. Equilibrium and Thermodynamics of Liquid Oxide and Other Phases. *Journal* Amer. Chemical Soc. (1946) **68**, p. 798.

[3] N. L. Bowen and J. F. Schairer: The System FeO-SiO_2. *Amer. Journal of Science* (1932) **24**, p. 177.

[4] J. W. Greig: On Liquid Immiscibility in the System FeO-Fe_2O_3-Al_2O_3-SiO_2. *Amer. Journal of Science* (1927) **14**, p. 473.

[5] L. S. Darken: Melting Points of Iron Oxides on Silica; Phase Equilibria in the System Fe-Si-O as a Function of Gas Composition and Temperature. *Journal* Amer. Chemical Soc. (1948) **70**, p. 2046.

[6] R. Schuhmann, Jr., R. G. Powell, and E. J. Michal: Constitution of the FeO-Fe_2O_3-SiO_2 System at Slagmaking Temperatures. *Trans.* AIME (1953) **197**, p. 1097; JOURNAL OF METALS (September 1953).

[7] R. J. Corruccini: Differences Between the International Scales of 1948 and 1927. *Journal of Research* National Bureau of Standards (1949) **43**, p. 133.

[8] R. B. Sosman: Temperature Scales and Silicate Research. *Amer. Journal of Science* (1952) Bowen Vol., p. 517.

[9] P. J. Ensio and R. Schuhmann, Jr.: Thermodynamics of Iron Silicate Slags: Slags Saturated with Gamma Iron. *Trans.* AIME (1951) **191**, p. 401; JOURNAL OF METALS (May 1951).

[10] R. W. Gurry and L. S. Darken: The Composition of CaO-FeO-Fe_2O_3 and MnO-FeO-Fe_2O_3 Melts at Several Oxygen Pressures in the Vicinity of 1600°. *Journal* Amer. Chemical Soc. (1950) **72**, p. 3906.

[11] H. Larson and J. Chipman: Oxygen Activity in Iron Oxide Slags. *Trans.* AIME (1953) **197**, p. 1089; JOURNAL OF METALS (September 1953).

[12] G. A. Rankin and F. E. Wright: The Ternary System CaO-Al_2O_3-SiO_2. *Amer. Journal of Science* (1915) **39**, p. 1.

[13] N. L. Bowen, J. F. Schairer, and E. Posnjak: The System FeO-CaO-SiO_2. *Amer. Journal of Science* (1933) **26**, p. 193.

[14] N. L. Bowen and J. F. Schairer: The System MgO-FeO-SiO_2. *Amer. Journal of Science* (1935) **29**, p. 151.

[15] E. F. Osborn and J. F. Schairer: The Ternary System Pseudowollastonite-Akermanite-Gehlenite. *Amer. Journal of Science* (1941) **239**, p. 715.

[16] J. W. Greig, E. Posnjak, H. E. Merwin, and R. B. Sosman: Equilibrium Relationships of Fe_2O_3, Fe_3O_4, and Oxygen. *Amer. Journal of Science* (1935) **30**, p. 268.

AIME OFFICERS:
President—H. DeWitt Smith
Vice-Presidents—T. B. Counselman, W. A. Dean, Harold Decker, L. E. Elkins, A. B. Kinzel, W. W. Mein, Jr.
President-Elect—C. E. Reistle, Jr.
Treasurer—G. F. Moulton
AIME STAFF:
Secretary—Ernest Kirkendall
Secretary Emeritus—E. H. Robie
Ass't. Secretaries—J. B. Alford, H. N. Appleton, E. J. Kennedy, Jr.
Field Secretary & Ass't. Secy—R. E. O'Brien
Ass't. Treasurer—P. J. Apol

aime NEWS

IMD Fall Meeting Features

Symposiums on Nuclear Metallurgy, Titanium, and High-Temperature Alloys

THIS year the Philadelphia Fall Meeting of the Institute of Metals Div., October 17 to 19, has several feature attractions. Of special interest are a Symposium on Nuclear Metallurgy, a Symposium on Titanium, and a Symposium on High-Temperature Alloys.

The Symposium on Nuclear Metallurgy is scheduled for Monday, October 17. Problems in nuclear energy lie principally in the field of materials. Afternoon and evening sessions are planned to help AIME members keep abreast of the most recent important developments in nuclear metallurgy.

The Fourth Annual Titanium Symposium will be held Tuesday, October 18. The present status of titanium development and its fabrication and use will be the subject of panel discussions, with Dept. of Defense officials participating.

A Joint Symposium on High Temperature Alloys will be conducted by the AIME Institute of Metals Div. and the Metals Engineering Div. of ASME on Wednesday, October 19. Separate sessions will review materials for use up to 1250°F, and for use above 1250°F.

Registration for the meeting will start Sunday at 3 pm in the mezzanine of the Adelphia Hotel. Monday registration will be from 8 am to 5 pm in the William Penn Room. The desks will also be open from 9 am to 5 pm on Tuesday and Wednesday. Member registration is $2.00, while the charge to nonmembers is $4.00. AIME student associates will not be charged for registration. Fee to non AIME students is $1.00.

The Annual IMD Fall Dinner will be held Tuesday, 7 pm, in the Crystal Room. The speaker of the evening is to be Dr. Froelich Rainey, director, the University Museum, University of Pennsylvania. His subject is to be *Speculation of an Archeologist on World History*. The pre-dinner cocktail party will be with the compliments of the Philadelphia Section. Dinner dress is informal.

SUNDAY, OCTOBER 16

3:00 to 9:00 pm
Registration

1:30 pm
IMD Program Committee Meeting
W. J. Harris, Jr., Chairman

4:30 pm
IMD Publications Committee Meeting
W. R. Hibbard, Jr., Chairman

MONDAY, OCTOBER 17

8:00 am to 5:00 pm
Registration

9:00 am to 12:00 m
Research in Progress
Paul Gordon and B. S. Lement, Chairmen

Abstracts of papers will not be published but will be available in mimeographed form at the registration desk during the meeting.

9:00 am to 12:00 m

Research Summaries—Deformation (I)

Howard Scott and G. A. Timmons, Chairmen

Internal Friction in Zirconium: W. J. Bratina, Ontario Research Foundation and W. C. Winegard, University of Toronto.

Creep of Polycrystalline Tin: J. E. Breen and J. Weertman, Naval Research Laboratory.

Interaction of Precipitation and Creep in Magnesium-Aluminum Alloys: C. S. Roberts, Dow Chemical Co.

Tensile Deformation of Germanium Single Crystals: R. P. Carreker, Jr., General Electric Co.

Tensile Deformation of Molybdenum as a Function of Temperature and Strain Rate: R. P. Carreker, Jr. and R. W. Guard, General Electric Co.

Mechanism of Plastic Flow in Titanium at Low and High Temperatures: F. D. Rosi, RCA Laboratories, F. C. Perkins and L. L. Seigle, Sylvania Electric Products, Inc.

Strain Rate Effects in Tungsten: J. H. Bechtold, Westinghouse Electric Corp.

Effects of Oxygen, Nitrogen, and Carbon on the Ductility of Cast Molybdenum: L. E. Olds and G. W. P. Rengstorff, Battelle Memorial Institute.

Strain-Induced Porosity and Hydrogen Embrittlement in Zirconium: F. Forscher, Westinghouse Electric Corp.

2:00 to 5:00 pm

Seminar on Recrystallization and Grain Growth

Bruce Chalmers and J. E. Burke, Chairmen

Recrystallization Textures of a Cold-Rolled Aluminum Single Crystal: Y. C. Liu, New York University and W. R. Hibbard, Jr., General Electric Co.

Primary Recrystallization Textures in Cold-Rolled Silicon-Iron Crystals: C. G. Dunn, General Electric Co. and P. K. Koh, Allegheny Ludlum Steel Corp.

Preferred Orientations in Rolled and Annealed Titanium: J. H. Keeler and A. H. Geisler, General Electric Co.

Measurement of Grain Growth Rates in Recrystallization: C. D. Graham, Jr., General Electric Co. and R. W. Cahn, University of Birmingham, England.

Grain Growth Rates and Orientation Relationships in the Recrystallization of Aluminum Single Crystals: C. D. Graham, Jr., General Electric Co. and R. W. Cahn, University of Birmingham, England.

2:00 to 5:00 pm

Symposium on Nuclear Metallurgy

Nuclear energy—probable future source for commercial power—has many unsolved problems. These problems lie principally in the field of materials. Hence, metallurgy is of fundamental importance to the success of atomic energy efforts. To help AIME members keep abreast of recent important developments in nuclear metallurgy, two meetings on this subject have been scheduled for afternoon and evening sessions. It is planned to have preprints of the papers available at the meetings for sale at a nominal charge. Following the presentation and discussion of papers at the evening session, there will be a social hour at which beer and soft drinks will be provided. A charge of $1.00 for those attending this session will be made to cover the cost of refreshments and hotel service.

J. H. Frye, Jr., Chairman

D. H. Gurinsky and A. R. Kaufmann, Assistant Chairmen

Plutonium Metal: E. R. Jette, Los Alamos Scientific Laboratory

Physical Metallurgy of Thorium: H. A. Wilhelm and B. A. Rogers, Iowa State College

Physical Metallurgy of Uranium: F. G. Foote, Argonne National Laboratory

4:30 pm

Membership Committee Meeting

David Swan, Chairman

8:00 pm

Symposium on Nuclear Metallurgy

J. H. Frye, Jr., Chairman

D. H. Gurinsky and A. R. Kaufmann, Assistant Chairmen

Power Reactors: A. M. Weinberg, Oak Ridge National Laboratory

Intermission

Problems in Materials for Atomic Power: J. B. Howe, North American Aviation, Inc.

TUESDAY, OCTOBER 18

9:00 am to 5:00 pm

Registration

9:00 am to 12:00 m

Seminar on Deformation (II)

Robert Maddin and F. L. Vogel, Jr., Chairmen

Effects of Alloying Elements on Plastic Deformation in Aluminum Single Crystals: E. E. Underwood and L. L. Marsh, Battelle Memorial Institute.

Tensile Creep of High Purity Aluminum: R. W. Guard and W. R. Hibbard, Jr., General Electric Co.

Creep of Copper at Intermediate Temperatures: T. E. Tietz and J. E. Dorn, University of California.

Creep-Rupture by Vacancy Condensation: E. S. Machlin, Columbia University.

Cleavage Steps on Zinc Monocrystals—Their Origins and Patterns: J. J. Gilman, General Electric Co.

On the Collapse of Dislocation Loops During Annealing: Jack Washburn, University of California.

9:00 am to 12:00 m

Symposium on Titanium

L. Schapiro, Chairman

J. H. Jackson and L. S. Busch, Assistant Chairmen

Keynote Address: H. H. Kellogg, Chairman, Titanium Advisory Committee, Dept. of Defense.

Present Status of Titanium Development: D. J. McPherson, Armour Research Foundation

Panelists:

S. A. Herres, Titanium Metals Corp. of America
L. S. Busch, Mallory-Sharon Titanium Corp.
V. W. Whitmer, Republic Steel Corp.
D. W. Kaufmann, Rem-Cru Titanium Corp.
Harold Margolin, New York University

Status of Titanium Fabrication and Use (a Report of the Dept. of Defense, Titanium Steering Committee): J. H. Garrett, Office Assistant Secretary of Defense

Panelists:

Lt. Col. L. W. Herway, U. S. Air Force
J. J. Harwood, Office of Naval Research
N. L. Reed, Watertown Arsenal
C. B. Voldrich, Battelle Memorial Institute

2:00 to 5:00 pm

Symposium on Titanium

L. Schapiro, Chairman

J. H. Jackson and L. S. Busch, Assistant Chairmen

The Background for Practical Heat Treatment of Various Titanium Alloy Types: P. D. Frost, Battelle Memorial Institute

Panelists:
W. L. Finlay, Rem-Cru Titanium Corp.
B. Molander, North American Aviation
S. Abkowitz, Watertown Arsenal
William Rostoker, Armour Research Foundation
H. J. Middendorp, Materials Laboratories, Wright-Patterson Air Force Base

Future Use Pattern for Titanium: Col. B. S. Mesick, Retired, Arthur D. Little, Inc.

Panelists:
L. Schapiro, Douglas Aircraft Corp.
C. W. Alesh, Consolidated Vultee Aircraft Corp.
R. Thielemann, Pratt & Whitney Aircraft Corp.
A. T. Mociun, North American Aviation Corp.
V. Kudryk, Chemical Construction Co.

2:00 to 5:00 pm

Research Summaries—Diffusion and Related Phenomena

C. E. Birchenall and A. S. Nowick, Chairmen

Diffusion of Nitrogen in Iron: P. E. Busby and Cyril Wells, Carnegie Institute of Technology and D. P. Hart, Pittsburgh Plate Glass Co.

Diffusion in Liquid Lead: S. J. Rothman, Argonne National Laboratory and L. D. Hall, Stamford Research Institute.

Self-Diffusion in Solid Nickel: R. E. Hoffman, F. W. Pikus, and R. A. Ward, General Electric Co.

Diffusion and Marker Movements in Beta Brass: U. S. Landergren, SKF Industries, Inc., C. E. Birchenall, Princeton University and R. F. Mehl, Carnegie Institute of Technology.

Self-Diffusion in Single and Polycrystals of Zinc at Low Temperatures: F. E. Jaumot, Jr., and R. L. Smith, Franklin Institute.

Some Studies of Al-Cu and Al-Zr Solid State Bonding: Samuel Storcheim, Sylvania Electric Products, Inc.

On the Rate of Sintering: Gerhard Bockstiegel, Sintermetallwerk Krebsoge Smett, Germany.

Temperature Gradient Zone Melting: W. G. Pfann, Bell Telephone Laboratories, Inc.

Thermodynamic Properties of Solid Iron-Gold Alloys: L. L. Seigle, Sylvania Electric Products, Inc.

A Search for Oxidation-Resistant Alloys of Molybdenum: G. W. P. Rengstorff, Battelle Memorial Institute.

4:30 pm

Nuclear Metallurgy Committee Meeting

J. H. Frye, Jr., Chairman

WEDNESDAY, OCTOBER 19

9:00 am to 5:00 pm

Registration

9:00 to 10:30 am

Research Summaries—Constitution and General Metallurgy

D. J. Blickwede and David Swan, Chairmen

Titanium-Rich Corner of the Ti-Al-V System: J. J. Rausch and F. A. Crossley, Armour Research Foundation and H. D. Kessler, Titanium Metals Corp. of America

Titanium-Molybdenum-Oxygen System: P. A. Farrar, L. P. Stone, and Harold Margolin, New York University

Thorium-Columbium and Thorium-Titanium Alloy Systems: O. N. Carlson, J. M. Dickerson, H. E. Lunt, and H. A. Wilhelm, Iowa State College

System Zirconium-Nitrogen: R. F. Domagala, D. J. McPherson, and M. Hansen, Armour Research Foundation

Fabrication of Powdered Thorium: W. W. Beaver, K. G. Wikle, and J. G. Klein, Brush Beryllium Co.

Metallographic Identification of Nonmetallic Inclusions in Uranium: R. F. Dickerson, A. F. Gerds, and D. A. Vaughan, Battelle Memorial Institute

9:00 to 10:30 am

Joint Symposium on High-Temperature Alloys Institute of Metals Div., AIME and Metals Engineering Div., ASME

W. R. Hibbard, Jr., Institute of Metals Div., AIME and J. J. B. Rutherford, Metals Engineering Div., ASME, Chairmen

Materials for Use up to 1250°F

Alloy Design of Material up to 1250°F: University of Michigan.

Stability of Alloy Steels: A. B. Wilder, E. F. Ketterer, and D. B. Collyer, National Tube Div., U. S. Steel Corp.

12:00 m

IMD Executive Committee Luncheon Meeting

J. S. Smart, Jr., Chairman

2:00 to 5:00 pm

Joint Symposium on High-Temperature Alloys Institute of Metals Div., AIME and Metals Engineering Div., ASME

W. R. Hibbard, Jr., Institute of Metals Div., AIME and J. J. B. Rutherford, Metals Engineering Div., ASME, Chairmen

a. Materials for Use up to 1250°F

Some Practical Aspects of High-Temperature Design Below 1250°F: E. C. Chapman, Combustion Engineering, Inc.

b. Materials for Use Above 1250°F

Principles of Design and Development of Alloys for Use Above 1250°F: N. J. Grant, Massachusetts Institute of Technology.

Over 6 Million Flying Hours Later: A. W. F. Green, General Motors Corp.

2:00 to 5:00 pm

Research Summaries—Phase Transformations

M. E. Nicholson and W. G. Pfann, Chairmen

High-Speed Quenching Dilatometer: F. E. Martin and R. H. Raring, Naval Research Laboratory.

Heat Treatment and Mechanical Properties of Titanium-Iron Alloys: F. C. Holden, H. R. Ogden, and R. I. Jaffee, Battelle Memorial Institute.

Effect of Carbon on Some Properties of Ti-Mo Alloys: D. W. Levinson, W. Rostoker, and A. Yamamoto, Armour Research Foundation.

Hardenability of Titanium Alloys Calculated From Composition: A Preliminary Examination: L. D. Jaffe, California Institute of Technology.

Preliminary Examination of the Quenching of Titanium Alloys: L. D. Jaffe, California Institute of Technology.

Sigma Nucleation Times in Stainless Steels: G. F. Tisinai, J. K. Stanley, and C. H. Samans, Standard Oil Co. (Indiana).

Evidence for Solidification of a Metastable Phase in Fe-Ni Alloys: R. E. Cech, General Electric Co.

Heterogeneous Nucleation of the Martensite Transformation: R. E. Cech and D. Turnbull, General Electric Co.

Effects of Alloying Elements on the Electrical Properties of Manganin Type Alloys: D. D. Pollock and D. I. Finch, Leeds & Northrup Co.

475°C Embrittlement of Chromized Coatings on Low Carbon Steel: W. L. Chu, General Electric Co.

Rocky Mountain Minerals Conference Offers Choice Of Seven Field Trips

Members of the Rocky Mountain Minerals Conference committee are shown together before the meeting. First row, left to right: Glen A. Burt, Secretary, Utah Local Section; Norman Weiss, co-chairman, Rocky Mountain Minerals Conference; Neil Plummer, Vice Chairman, Utah Local Section; J. M. Ehrhorn, Chairman, Utah Local Section; and R. C. Cole, co-chairman, Rocky Mountain Minerals Conference. Second row, left to right: C. P. Mott, chairman, meeting rooms and equipment committee; Raymond Thompson, chairman, extractive metallurgy, nonferrous; I. K. Hearn, co-chairman, cocktail buffet committee; S. I. Bowditch, chairman, mining and geology committee; V. L. Stevens, publicity chairman; and W. F. Rappold, chairman, industrial minerals. Third row, left to right: I. G. Pickering, chairman, hotel reservations; R. E. O'Brien, Field Secretary, AIME; K. A. Lehner, co-chairman, entertainment committee; and E. K. Olson, co-chairman, field trips.

The Second Annual Rocky Mountain Minerals Conference will take place in Salt Lake City at the Hotel Newhouse on October 6 to 8 with the Utah Section of AIME as host. The Minerals Beneficiation Div., holding its fall meeting simultaneously, is represented by a generous number of milling papers distributed through the 3-day meeting. Each of the five sessions will cover a wide range of professional interest.

Registration will start Wednesday afternoon, October 5, and technical sessions will be held morning and afternoon on Thursday and Friday and on Saturday morning. Seven field trips are planned for Saturday afternoon.

This year's program includes papers on geology, mining, minerals beneficiation, extractive metallurgy, and education. Commodity-wise, there are papers on uranium, coal, iron and steel, industrial minerals, base metals, tungsten, and rare metals.

R. W. Lawson is chairman of luncheon arrangements; Grant Schaunburg, co-chairman, field trips; Ewald Kipp, co-chairman, cocktail buffet committee; Max DuBois, co-chairman, entertainment committee; and Leonard Tofft, chairman, ferrous metallurgy.

Officers of the Utah Section, host for the conference, are Jack M. Ehrhorn, Chairman, and Neil Plummer, Vice Chairman. Responsible for conference arrangements are Norman Weiss and R. C. Cole, general co-chairmen. Mrs. Max Kennard, Chairman of the Women's Auxiliary AIME, Utah Section, will supervise the arrangements for the ladies' activities.

For the ladies there will be coffee at the Newhouse from 9 to 11 am on Thursday, and luncheon and fashion show on Friday are also planned for them. Ladies are invited to attend the two luncheons, and the Scotch Breakfast. There will also be the Thursday evening cocktail party and the Saturday night dinner-dance.

Of first importance is the well-balanced technical program comprising 16 papers and a symposium. On Thursday noon Governor J. Bracken Lee of Utah will be guest of honor at the Welcoming Luncheon, and on the following day MBD will hear William W. Mein, Jr., Vice President and Director of the Institute at its regular fall luncheon.

Envelopes containing program, pre-registration form, application for housing, and return envelope were mailed during August to all Metals Branch and Mining Branch members of the 11 Western States, Minnesota and South Dakota, and to MBD members in all states. Prompt replies are requested by the Committee.

Technical Sessions and Field Trips

Thursday am, October 6

Uranium Occurences West of the Colorado Plateau: Ernest E. Thurlow, manager, Salt Lake Exploration Branch, AEC.

Geneva Works Water Supply and Water Treating System: Earl H. Pierce, power and fuel engineer, Columbia-Geneva steel div. U. S. Steel Corp.

Control Engineering in Minerals Beneficiation: Carl M. Marquardt, Industrial Physics & Electronics Co.

Chemical Refining of Tungsten: Blair Burwell, Jr., Salt Lake Tungsten Co.

Thursday pm, October 6

Rare Metals: M. H. Kline, vice president, Rare Metals Corp. of America.

Production of Phosphoric Acid and High Strength Phosphate, Fertilizers from Western Phosphate Rock: R. J. McNally, assistant manager, sulphuric acid dept., American Smelting & Refining Co.

Quantitative Approach to Bulk Material Handling Problems: Andrew W. Jenike.

Rod Mills and Ball Mills at the Hayden Plant of Kennecott Copper Corp.: Milling Staff, Kennecott Copper Corp.

Friday am, October 7

Beneficiation of Utex Ores: Clement K. Chase, chief metallurgist, Utex Exploration Co.

Underground Mining of Phosphates: D. L. King, general manager, San Francisco Chemical Co.

Forty-two Inch Vibrating Rod and Ball Mills: F. E. Briber, Jr.

Engineering Education in the Mineral Industry: John R. Lewis, head, dept. of metallurgical engineering, University of Utah.

Friday pm, October 7

Award Paper—University of Utah Student.

Uranium Mining Methods: J. Fred Johnson.

Approaches to the Problem of Coking Western Coals: John D. Price, superintendent of by-product coke plant, Colorado Fuel & Iron Co.

Crushing and Milling at Pend Oreille East Mill: J. C. Crampton, mill superintendent, Pend Oreille Mines & Metals.

Saturday am, October 8

Symposium—"Greater Cooperation Among Geologists, Mining Engineering, and Metallurgists for Metallurgical Planning."
W. R. Landwehr—Moderator
M. B. Kildale and Kenyon Richard, Geologists
A. G. Kirkland and J. C. Landenberger, Jr., Mining Engineers
Bruce Clemmer and Frank McQuiston, Metallurgists
Reno H. Sales—Summary

Seven Field Trips

Geneva Works of the Columbia-Geneva steel div., U. S. Steel Corp. near Provo, about 35 miles south of Salt Lake City. A visit to largest integrated mill in West.

Bingham and Lark trip to view world's largest copper mines and the surface plant of one of the largest lead-zinc mines in the U. S.

Magna and Arthur Mills, a tour of the two 50,000-tons per day concentrators of the Kennecott Copper Corp.

Garfield Smelter and Refinery trip includes American Smelting & Refining Co.'s copper smelter, world's largest, as well as the new Kennecott copper refinery.

Western Phosphates plant at Garfield is owned by AS&R, Kennecott, and Stauffer Chemical Corp. in partnership. Capacity is 90,000 tons of triple super-phosphate per year.

Vitro Uranium mill located 10 miles south of Salt Lake City will be toured except for classified areas.

Kennecott Research and Engineering Center, a modern center equipped for pilot plant flotation studies, and pyro and hydrometallurgical testing.

Reinartz NOHC Scholarship Awarded

Donald McFarlane, 18-year old son of a Cleveland brickmason, is the first recipient of the Leo F. Reinartz AIME NOHC Scholarship in metallurgy at the Carnegie Institute of Technology. Mr. McFarlane was selected from a group of candidates submitted by the Carnegie Tech admissions committee. The AIME NOHC scholarship committee consisted of H. G. Grim, C. E. Carr, and A. W. Thornton.

He was in the upper 10 pct of his class at the James Ford Rhodes High School in Cleveland and was active in student affairs. The award amounts to $500.

Progress Report On Engineering Building

One representative from each of the five societies concerned, consisting of four current presidents and one past president, met on July 25 to expedite united action with regard to the new engineering building. They agreed on eight recommendations to be made to their governing bodies as follows:

(1) That the majority and minority reports dated April 3 and 4 of the Committee of the Five Presidents be received, and that this committee now be discharged with thanks.

(2) That a Special Task Committee of 15 persons be created by the appointment of three representatives of each society with all voting in such Task Committee to be by each society as a unit.

(3) That the representatives on this Special Task Committee should be: (a) unbiased, and (b) not an employee of a society.

(4) That the Special Task Committee be charged with the duty of recommending a specific site for the Engineering Societies Center, based upon a review and comprehensive additional study of feasible locations.

(5) That the Special Task Committee be empowered to select its own chairman and to employ a secretary, and to engage independent unbiased professional consultants to investigate the problem and to report its findings with recommendations to the Committee.

(6) That the Special Task Committee report simultaneously to the governing boards of the five societies as soon as possible but not later than Feb. 1, 1956.

(7) That the sum of $15,000 be appropriated by each of the five societies to finance the activities of the Special Task Committee. Any unexpended funds from this appropriation are to revert equally to the societies.

(8) That the societies express their appreciation of the interest and substantial offers of assistance that have been received from various groups.

Signed by Wm. Roy Glidden, ASCE; H. DeWitt Smith, AIME; D. W. R. Morgan, ASME; Elgin B. Robertson, AIEE; and Barnett F. Dodge, AIChE.

The AIME Executive Committee subsequently named the following as the three representatives of the AIME on the Task Committee; Harold Decker, Vice-President AIME, president of the Houston Oil Co. of Texas, Houston; H. DeWitt Smith, President AIME, consulting engineer, New York City; and Clyde Williams, a past President of the AIME, director of Battelle Memorial Institute, Columbus, Ohio. All the recommendations as above stated have been approved by the AIME Directors by a mail vote.

Compile Calendar Of Engineering Meetings

A current project of Engineers Joint Council is the quarterly compilation of a calendar of all meetings of interest to engineers that have been scheduled for the next five years. Routine local section meetings will not be included. The intention is to avoid duplication of work by individual societies, to provide a clearing house of information, and to avoid conflicts in meeting scheduling. As soon as a date has been decided upon for a meeting, information should immediately be sent to the Secretary of EJC, 29 W. 39th St., New York 18, for inclusion in the calendar. First issue of the calendar is scheduled for October 1955.

Sept. 15, 1955 is the deadline for the Institute of Metals Div. papers for the 1956 New York Annual Meeting and the deadline for all Iron & Steel Div., and Extractive Metallurgy Div. papers to be preprinted. Papers received by this deadline but requiring revision may not be processed in time to permit scheduling for this meeting.

Personals

Sidney G. Roberts recently joined the Kaiser Aluminum & Chemical Corp., Spokane, Wash., as a research metallurgist in the dept. of metallurgical research. He had been associated with the Chrysler Corp., as a metallurgical project engineer.

Eric C. Bell is associated with the Avro Aircraft Ltd., Malton, Ont., Canada. He had been with A. V. Roe Canada Ltd., Toronto.

Charles V. Klimas, U. S. Steel Corp., has transferred from the Duquesne, Pa. office to Pittsburgh, Pa.

B. H. Alexander is manager of semiconductor operations, CBS-Hytron, Lowell, Mass. He had been manager of engineering, Sylvania Electric Products, Woburn, Mass.

D. G. Schaffert has resigned as assistant melting superintendent, Copperweld Steel Co., Warren, Ohio, to accept the position of assistant to works manager, Northeastern Steel Corp., Bridgeport, Conn.

S. G. Salamy has resigned as technical assistant to the chief metallurgist, King Island Scheelite (1947) Ltd., to accept the position of iron ore research officer, Broken Hill Co. Ltd., Melbourne, Australia.

R. Allen Crosby has joined the Aerojet-General Corp., Azusa, Calif. Mr. Crosby had been associated with the U. S. Steel Corp., South Works, Chicago.

Royal B. Jackman has joined Northrup Aircraft, Inc., as chief, engineering laboratories. He recently resigned as research director for the R. T. Collier Corp.

James W. Volk has been named sales manager, steel fabricating div., Michiana Products Corp., Michigan City, Mich.

George W. Taylor has been appointed chemical research engineer, special applications dept., Permutit Co., New York.

H. Sturgis Potter and **Arlington A. Britton, Jr.,** have been elected to the board of directors, Carpenter Steel Co., Reading, Pa. **Carl B. Post,** head of the metallurgical and research depts., has been promoted to vice president in charge of metallurgy.

Ralph E. Forsman has been appointed to the sales staff of Basic Refractories, Inc., Cleveland. Mr. Forsman will be located at the Philadelphia office.

William L. Walsh was elected president of Quebec Iron & Titanium Corp., New York, N. Y.

Robert H. Kaltenhauser, John E. Mosser, Jr., and **David L. Raymer** have joined the technical staff of the Allegheny Ludlum Steel Corp., research laboratory, Brackenridge, Pa.

J. Paul Maddox has been appointed special representative of the refractory specialties div., Mexico Refractories Co., Mexico, Mo. Mr. Maddox was formerly vice president in charge of the Laclede Arch Co., a Chicago div. of Laclede-Christy Co.

Frederick C. Kroft has been appointed general superintendent of manufacturing for Haynes Stellite Co., New York, N. Y.

G. L. McMillin was appointed vice president, steel foundry, Canadian Car & Foundry Co., Ltd. He was formerly assistant vice president, steel foundry.

J. M. Buchanan has been named assistant superintendent, zinc dept., Consolidated Mining & Smelting Co., Trail, B. C.

W. W. Sebald, president, Armco Steel Corp., Middletown, and **William M. Akin,** president, Laclede Steel Co., St. Louis, have been elected vice presidents of the American Iron & Steel Institute.

David Swan has been appointed director of research, metals research laboratories, Electro Metallurgical Co., Niagara Falls. Mr. Swan has been with UCC since 1946.

Leonard C. Schmidt was elected to the board of directors, Worcester Pressed Steel Co.

Walter K. Zwicker and **Donald J. Hansen** have joined the staff of Electro Metallurgical Co., metals research laboratories, Niagara Falls.

Fred L. Shanklin has been appointed vice president and general manager, ore div., Union Carbide & Carbon Corp. Mr. Shanklin has been with UCC since 1934.

John D. Harper, works manager, smelting plant, Aluminum Co. of America, Rockdale, Texas, has been named assistant general manager of the company's smelting div

Jack C. Bokros has joined North American Aviation, Inc., Long Beach, Calif. Mr. Bokros is a research engineer in the nuclear engineering and mfg. div.

J. Gordon Parr has accepted the position of associate professor of metallurgy at the University of Alberta, Edmonton. He had been on the staff of the dept. of mining and metallurgy, University of British Columbia, Vancouver.

Cecil J. Bier has resigned from the atomic energy div. of Sylvania Electric Products, Inc. He is now employed in the materials engineering section of the Knolls atomic power laboratory, General Electric Co., Schenectady.

John F. Pollack, Jones & Laughlin Steel Corp., Pittsburgh, has been named superintendent, open hearth dept. Mr. Pollack had been assistant to the superintendent, open hearth and Bessemer.

Denis L. Ramball is with the Crucible Steel Co. of America, Syracuse.

Joseph Rosenblatt, president of Eimco Corp., Salt Lake City, was named a Knight of the Legion of Honor by the Republic of France. The award was made for contributions to the mining industry.

N. K. Chen is located at the research laboratories of Westinghouse Electric Corp., East Pittsburgh. He had been on the staff at Johns Hopkins University, Baltimore.

Donald Keith Magnus has joined the Westinghouse atomic power div., Pittsburgh. He had been associated with the Chase Brass & Copper Co., Waterbury, Conn.

James B. Russell recently accepted a position with the Nichols Wire & Aluminum Co., Davenport, Iowa, as metallurgical engineer, development. Mr. Russell had been a research metallurgist, dept. of metallurgical research Kaiser Aluminum & Chemical Corp., Spokane.

L. W. Cashdollar, metallurgical engineer, Pittsburgh Metallurgical Co., has been transferred from Pittsburgh to Cleveland.

E. W. Engle is manager, Fansteel Metallurgical Corp., North Chicago. He had been in the Carboloy dept., General Electric Co., Detroit.

J. J. Martin, vice president in charge of operations, Colorado Fuel & Iron Corp., was awarded the Alumni Assn. service award by Lehigh University.

Murilo de Oliveira Marcondes is technical director for the Cia. Paulista de Laminacao, Sao Paulo, Brazil.

Charles A. Bittmann has joined Pacific Semiconductor, Inc., Topanga, Calif. Mr. Bittmann has been with the Hughes Aircraft Co., Venice, Calif.

Robert A. Lenhart, General Electric Co., Schenectady, is now mill metallurgist for the company at Leechburg, Pa.

Leory W. Davis recently accepted the position as manager of the forging div., Harvey Machine Co., Inc., Torrance, Calif. He was previously associated with the Kaiser Aluminum & Chemical Corp.

Carl F. Allison has retired after 42 years of continuous service with Jones & Laughlin Steel Corp., Pittsburgh. **George M. Dreher** has been appointed supervisor, chemical services, succeeding Mr. Allison.

B. D. Thomas, David C. Minton, Jr., and **John S. Crout** have been appointed vice presidents at Battelle Memorial Institute, Columbus.

Frank P. Shonkwiler has been named manager of basic sales by Harbison-Walker Refractories Co., Pittsburgh. Mr. Shonkwiler was formerly a member of the Chicago district sales staff. He has been associated with the firm since 1943.

Samuel L. Hoyt, metallurgical consultant, Columbus, Ohio was recently awarded the honorary Sc.D. degree from the South Dakota School of Mines and Technology.

Thomas E. Ban has been appointed director of research, McDowell Co., Inc., Cleveland. Prior to joining McDowell, Mr. Ban was associated with Cleveland Cliffs Iron Co.

Cyril Stanley Smith has been granted leave from his position as director of the Institute for the Study of Metals, University of Chicago. He will be engaged in research on the history of science, in London.

Michael A. Kuryla has been named assistant manager of the Lima, Peru div., Cerro de Pasco Corp.

John W. DeLind, Jr., has resigned as chairman of the board, Borg-Warner International Corp. and has retired from executive duties.

A. E. Lee, Jr., American Metal Co., Ltd., New York, is now located at the Blackwell Zinc Co., Inc., Blackwell, Okla.

John E. McNamara has joined the Motorola Research Laboratory, Phoenix, Ariz. Mr. McNamara had been associated with the Bell Telephone Laboratories, Allentown, Pa.

John Dasher has resigned from the metals group, Chemical Construction Corp., New York. He has joined the central research laboratory, Crucible Steel Co. of America, Pittsburgh.

Clare A. Best, formerly chief chemist for National Lead Co., titanium alloy mfg. div., Niagara Falls, N. Y., has been appointed director of quality control. **Karl W. Traub** has been chief chemist succeeding Mr. Best.

William Bohrer is sales engineer at the Cleveland office of the Wheelco Instruments div., Barber-Colman Co., Rockford, Ill.

Oliver F. Senn has been appointed chairman of the chemistry dept., Stanford Research Institute, Stanford, Calif. He was formerly assistant chairman of the dept.

Alexander H. Reynolds, Jr., controller, Leeds & Northrup Co., has been elected treasurer of the company.

W. B. Caldwell has retired as president of the Calumet Steel and Franklin Steel divs., Borg-Warner Corp., Chicago. **Howard J. David** was elected to succeed him.

Robert A. Lannoye, John F. Langkau, Roger Gilbert, Jr., Bruce M. Lane, Eugene F. Riebling, and **Neal Griffing** have joined the staff of Electro Metallurgical Co., metals research laboratory, Niagara Falls, N. Y.

E. H. Hughes, manager of the sales order dept., Timken Roller Bearing Co., has been named to the newly created post of assistant to the sales director. Mr. Hughes has been with the firm since 1938.

Charles E. Lapple and **Rudolf H. Thielemann** have joined the chemical and metallurgical engineering section, Stanford Research Institute, physical sciences div. Mr. Lapple was formerly associate professor of chemical engineering, Ohio State University and Mr. Thielemann, development metallurgist for Pratt & Whitney Aircraft.

Necrology

Date of Election	Name	Date of Death
1930	Marcel Dupont	July 24, 1955
1940	H. E. Hall	July 8, 1956
1911	Morris F. Lacroix	July 29, 1955
1941	Martin C. Messner	May 31, 1955
1920	Harry A. Townsend	June 11, 1955
1916	H. Y. Walker	July 2, 1955

Proposed for Membership

— Metals Branch AIME —

Total AIME membership on July 31, 1955 was 22,073; in addition 1918 Student Associates were enrolled.

ADMISSIONS COMMITTEE

P. D. Wilson, Chairman; F. A. Ayer, Vice-Chairman; A. C. Brinker, R. H. Dickson, T. D. Jones, F. T. Hanson, Sidney Rolle, O. B. J. Fraser, F. T. Sisco, Frank T. Weems, R. L. Ziegfield, R. B. Caples, F. W. McQuiston, Jr., A. R. Lytle, H. R. Wheeler, L. P. Warriner, J. H. Scaff.

The Institute desires to extend its privileges to every person to whom it can be of service, but does not desire as members persons who are unqualified. Institute members are urged to review this list as soon as possible and immediately to inform the Secretary's office if names of people are found who are known to be unqualified for AIME membership.

In the following list C/S means change of status; R, reinstatement; M, member; J, Junior Member; A, Associate Member; S, Student Associate.

Arizona
Phoenix—Murdock, Don J. (A)
Michigan
Belleville—Porter, Vernon L. (A)
Midland—Pearsall, George W. (J)
Minnesota
Virginia—Porter, Edward F. (M) (R. C/S—J-M)
New Jersey
Westfield—Lord, Robert L. (J) (R. C/S—S-J)
New York
Lewiston—Brown, Charles M. (M)
Lewiston Heights—Brown, Raymond G. (M)
New York—Minkler, Ward W. (M) (R. C/S—J-M)
New York—Shearman, Robert W. (M)
Niagara Falls—Johnson, Gene J. (J)
Niagara Falls—Pochon, Max A. (M)
Pennsylvania
Beaver Falls—Henderson, Charles D. (M)
Hatboro—Clash, Frederick H., Jr. (A)
New Kensington—Milliken, Spencer R. (M)
Pittsburgh—Titzel, John M. (A)
Washington
Vancouver—Wilson, Charles R. (J)
Argentina
Rosario—Werner, Hans R. (A)
Canada
Cobalt, Ont.—Seger, Claude A. Jr. (M) (R. C/S—S-M)
Germany
Mulheim-Ruhr—Schinn, Rudolf (M)
West Germany
Dortmund—Mathur, Indra N. (J)

Superior
BLAST FURNACE
COPPER CASTINGS
Hot Blast Valves and Valve Seats
Blast Furnace Tuyeres, Licensed Manufacturers of all Leading Designs
SMEETH-HARWOOD COMPANY
3124 Vincennes Ave., Chicago 20, Ill.
In Canada—The William Kennedy & Sons, Ltd., Owen Sound, Ontario
Blast Furnace Copper Castings—also Brass and Bronze Mill Castings

STRESS RUPTURE LIFE INCREASED OVER 300% BY VACUUM MELTING

in high temperature alloys for jet turbine blading

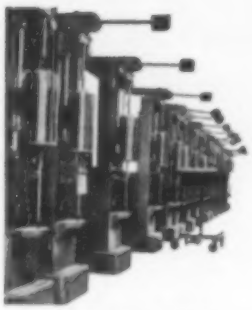

To speed the vital work of testing, UTICA maintains a battery of 72 stress rupture machines, a few of which are shown above.

In the Metals Division at UTICA twenty-eight consecutive heats of UTICA vacuum melted Waspaloy were compared with the same number of heats made by standard mill practice. Test conditions were—1500°F, 32,500 psi. Stress rupture life of the vacuum melts proved to be at least *three times* that of the air melts.

UTICA's facilities for quality control are unexcelled. The electronic machine above records the chemical content of specimens tested while the melt is in progress.

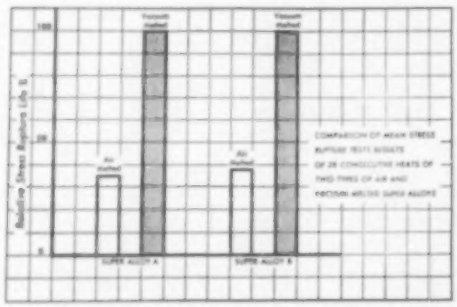

The Metals Division at UTICA is one of the largest producers of these high temperature alloys. The meeting of very rigid specifications has become routine, even on a high production basis. Uniformity is maintained within extremely small tolerances from melt to melt and among the ingots within a melt.

The Metals Division at UTICA invites inquiries from prospective customers. Through refinements in technique, costs are constantly being reduced—and the Division is glad to work closely in assisting the customer in his metallurgical problems.

For the full story of UTICA *Metals Division vacuum melting, send for this brochure.*

Offer of our facilities is subject to priority of national defense orders.

*UTICA TRADE MARK

Utica Metals Division

U DI MET ALLOYS

UTICA DROP FORGE AND TOOL CORP., UTICA, N. Y.

Advertisers' Index

Air Reduction Co., Inc. — *
G. M. Basford

Ajax Engineering Corp. — *
Eldridge, Inc.

American Bridge Div., U. S. Steel Corp. — 937
Batten, Barton, Durstine & Osborn, Inc.

American Machine & Metals Inc. — *
The L. W. Ramsey Adv. Agency

Bailey Co., Wm. M. — Fourth Cover
Walker & Downing

Basic Refractories Inc. — *
The Griswold-Eshleman Co.

Bell Telephone Labs. — *
N. W. Ayer & Son, Inc.

Bradley Mining Co. — *

Braun & Co., C. F. — *
The McCarty Co.

Buehler Ltd. — *
Kreicker & Meloan, Inc.

Consolidated Vacuum Corp. — *
Charles L. Rumrill & Co., Inc.

Dow Chemical Co. — *
MacManus, John & Adams, Inc.

Electro Met. Div., Union Carbide & Carbon Corp. — Third Cover
J. M. Mathes, Inc.

Ferro Engineering Co. — *
C. A. Reece Ind. Publicity

General Electric Co., X-Ray Dept. — 941
Klau, Van Pietersom-Dunlap Assoc.

Great Lakes Carbon Corp. — *
Davis, Parsons & Strohmeier, Inc.

Harbison-Walker Refractories Co. — *
Walker & Downing

Hevi Duty Electric Co. — *
Camm, Costigan, Inc.

International Nickel Co. — 942
Marschalk & Pratt

Leitz, Inc., E. — *
L. W. Frohlich & Co., Inc.

Molybdenum Corp. of America — 934
Smith, Taylor & Jenkins, Inc.

Morgan Construction Co. — 935
Davis Press, Inc., The

North American Philips Co. — 931
Anders Assoc. Adv.

Pittsburgh Lectromelt Furnace Corp. — *
The Griswold-Eshleman Co.

Ramtite Co., The — *
Marsteller, Rickard, Gebhardt and Reed Inc.

Smooth-Harwood Co. — 983
Allbright Associates Adv.

Stokes Machine Co., F. J. — *
John Mather Lupton Co., Inc.

Swindell-Dressler Corp. — *
Walker & Downing

Titanium Alloy Mfg. Div. — 933
Comstock & Co.

United States Graphite Co., The — Second Cover
Price, Tanner & Willox, Inc.

U. S. Steel Corp. — 929
Columbia-Geneva Steel Div.
Tennessee Coal & Iron Div.
U. S. Steel Supply Div.
U. S. Steel Export Co.
Batten, Barton, Durstine & Osborn, Inc.

Utica Drop Forge and Tool Corp. — 984
Wilson, Haight, Welch & Grover, Inc.

Wyman-Gordon Co. — 936
John W. Odlin Co., Inc.

* Previous issue.

USE

"ELECTROMET"

Trade-Mark

SILICOMANGANESE

for fast, easy ***ladle*** *additions . . .*

combination alloy dissolves fast and reduces chilling of the steel

Check these Advantages

COMBINATION ALLOY

In making steel, silicon and manganese are much more effective in combination than when used separately. ELECTROMET silicomanganese is designed for the simultaneous addition of silicon and manganese in the correct proportion.

FAST SOLUBILITY

Because of the concentration of active elements in ELECTROMET silicomanganese, less time is required for solution in molten steel than when equivalent amounts of silicon and manganese are used separately in the form of ferrosilicon and ferromanganese.

LESS CHILL

The weight of silicomanganese is less than the weight of equivalent amounts of ferrosilicon and ferromanganese. The chilling effect is less with the lower weight of the silicomanganese addition.

LOW CARBON CONTENT

When ELECTROMET silicomanganese is added in the ladle, the low carbon content of the alloy allows the melt to be tapped at a higher carbon level with a saving in furnace time.

DEOXIDIZER FOR SEMI-KILLED STEELS

ELECTROMET silicomanganese is particularly effective as a ladle addition for the deoxidation of semi-killed steels.

METALLURGICAL SERVICE AVAILABLE

Our metallurgists will be glad to assist you in the application of ELECTROMET silicomanganese to your specific requirements. For further information, please get in touch with the nearest ELECTROMET office.

ELECTRO METALLURGICAL COMPANY

A Division of Union Carbide and Carbon Corporation

30 East 42nd Street UCC New York 17, N. Y.

OFFICES: Birmingham • Chicago • Cleveland • Detroit
Houston • Los Angeles • New York • Pittsburgh • San Francisco

In Canada: Electro Metallurgical Company, Division of Union Carbide Canada Limited, Welland, Ontario

The term "Electromet" is a registered trade-mark of Union Carbide and Carbon Corporation.

SINTERING PLANT

Bailey PUG MILLS

This was the first Bailey Pug Mill, installed in 1930. It still operates efficiently today, and even the original bearings still are in service.

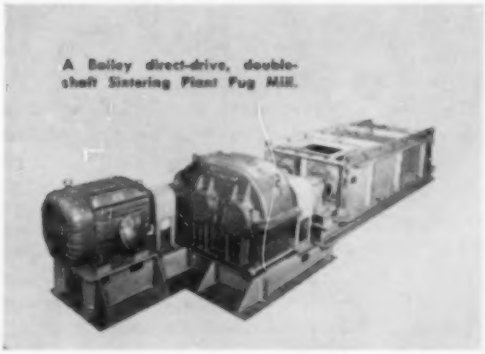

A Bailey direct-drive, double-shaft Sintering Plant Pug Mill.

These mills are built for continuous service and for the low-cost processing of greater tonnages of more uniform sintered products. Bailey Pug Mills have capacities ranging from 100 to 400 tons per hour. They are made in single and double shaft models, with direct or rope drives. *Write for bulletin.*

REPRESENTATIVE BAILEY PUG MILLS USERS	Number of Mills
Bethlehem Steel Company	5
Jones & Laughlin Steel Corporation	2
United States Steel Corporation	13
Youngstown Sheet & Tube Company	3

WILLIAM M. Bailey COMPANY
ENGINEERS
LEADERSHIP THROUGH QUALITY

1221 BANKSVILLE ROAD PITTSBURGH 16, PA

Journal of METALS

SEPTEMBER 1955

VOL. 7, NO. 9, IN TWO SECTIONS — SECTION TWO

TRANSACTIONS SECTION

Ordering and Magnetic Heat Treatment of the 50 Pct Fe-50 Pct Co Alloy — R. C. Hall, G. P. Conard, and J. F. Libsch — 985

Further Observations on Yield in Single Crystals of Iron — H. W. Paxton and I. J. Beer — 989

Diffusion of Co^{60} and Fe^{55} in Cobalt — H. W. Mead and C. E. Birchenall — 994

Grain Boundary Diffusion of Nickel into Copper — S. Yukawa and M. J. Sinnott — 996

Bainite Reaction in a Plain Carbon Steel — H. I. Aaronson and C. Wells — 1002

Diffusion of Zinc and Copper in Alpha and Beta Brasses — R. Resnick and R. W. Balluffi — 1004

Thermal Conductivity of Vanadium and Certain Vanadium Alloys — J. L. Weeks and K. F. Smith — 1010

Kinetics and Mechanism of the Oxidation of Molybdenum — M. Simnad and A. Spilners — 1011

Contribution to Mathematics of Zone Melting — L. Burris, Jr., C. H. Stockman, and I. G. Dillon — 1017

Instability of a Smooth Solid-Liquid Interface During Solidification — D. Walton, W. A. Tiller, J. W. Rutter, and W. C. Winegard — 1023

Some Aspects of Slip in Germanium — R. G. Treuting — 1027

Bauschinger Effect in Creep and Tensile Tests on Copper — J. D. Lubahn — 1031

Zirconium-Columbium Diagram — B. A. Rogers and D. F. Atkins — 1034

Lineage Structure in Aluminum Single Crystals — A. Kelly and C. T. Wei — 1041

Microcalorimetric Investigation of Recrystallization of Copper — P. Gordon — 1043

Method of Determining the Diffusivity of Gas in Metal: Oxygen in Chromium — D. Caplan and A. A. Burr — 1052

Relationship Between Recovery and Recrystallization in Superpurity Aluminum — E. C. W. Perryman — 1053

On the Casting, Rolling, and Annealing Textures of Chromium — W. H. Smith — 1064

Copyrighted by American Institute of Mining and Metallurgical Engineers, Inc., 1955
Printed in U.S.A.

Ordering and Magnetic Heat Treatment of The 50 Pct Fe-50 Pct Co Alloy

by R. C. Hall, G. P. Conard, and J. F. Libsch

The 50 pct Fe-50 pct Co alloy undergoes a transformation from disorder to an ordered structure of the CsCl type reportedly in the vicinity of 732°C. During this process, the coercive force goes through a maximum, apparently as a result of strains associated with the coherent nucleation and growth reaction. This magnetic alloy also shows a marked increase in the ratio of residual to saturation induction, which is associated with annealing to a high degree of order with the continuous application of a magnetic field. The increase in ratio can be explained on the basis of a decrease in 90° domain boundaries and, perhaps, by an increase in anisotropy resulting from lattice distortion.

THE 50 pct Fe-50 pct Co alloy undergoes a disorder-order transformation which has been reported to occur in the vicinity of 732°C.[1, 2] The ordered structure is the CsCl type.[1] This magnetic alloy also shows a marked increase in the ratio of residual to saturation induction as a result of heat treatment in a magnetic field, sometimes called a response to magnetic anneal.[3-6] The purpose of this investigation was to study the course of the ordering reaction, the nature of the response to heat treatment in a magnetic field, and the relation, if any, between ordering and the response.

Procedure

The method of approach in this investigation was to produce an initial structure as completely disordered as possible and then gradually to order the alloy by isothermal anneals at various temperatures under different conditions of the applied magnetic field. Magnetic, magnetostriction, and X-ray analyses were of primary importance in determining the property and structural changes resulting from the isothermal anneals.

Rings of the 50 pct Fe-50 pct Co alloy were prepared from the elemental powders by a powder metallurgy technique, further details of which may be found in ref. 7. The initial structure was produced by annealing the specimens for ½ hr at 1000°C, cooling to and holding for ½ hr at 900°C (in the α range above the ordering temperature), and water quenching. Isothermal anneals were performed at 600°, 675°, 720°, and 740°C. For example, rings were heated to 600°C, held for a predetermined period of time, and cooled by natural cooling at a rate slightly slower than an air cool (average of 20° to 25°C per min). The tests (magnetic, etc.) were made after each heat treatment. All high temperature treatments were performed in a purified hydrogen atmosphere. The treatments at the various temperatures were carried out under one or more conditions of an applied field including 1—no field, 2—field of 20 oersteds applied on cooling only, and 3—field of 20 oersteds applied continuously during heating, holding, and cooling.

Magnetic measurements were made using the standard Rowland ring technique[8] with a maximum field strength of 100 oersteds. The magnetization curve, induction at 100 oersteds (B_s), residual induction (B_r), and coercive force (H_c) were determined. All magnetic analysis data were based on an average of the results from three rings. A strain gage technique[9] was used for the measurement of magnetostriction. The X-ray determination of the relative amount of ordered phase present was made on the ring specimen used for magnetic measurement. This was done by the back-reflection method using a rotating specimen (because of the large grain size) with unfiltered CoKα radiation and a 7 hr exposure time. Intensity measurements of the ordered line (300) were made by comparing visually the films so obtained with standard films prepared by exposing for different lengths of time a specimen given a long time anneal (high degree of order).

Results

In all instances the *saturation induction* (induction at 100 oersteds) was found to increase slightly with annealing time. This effect was small and appears to be the increase in saturation induction to be expected on ordering.[10-12]

The residual induction behavior was markedly influenced by the field condition during annealing. Figs. 1, 2. For the condition of no applied field, the ratio of residual to saturation induction remained essentially constant for short annealing times but showed a significant increase at longer times. With increasing annealing temperature, less time was required to produce this increase in the ratio. In the case of the 600°C anneals, the increase did not occur until approximately 20 hr, Fig. 1, while on annealing at 740°C the increase was immediate, Fig. 2. Slight decreases in the ratio may be observed at 100 hr for specimens treated at 720°C and at 1 hr for those treated at 740°C.

Specimens annealed in a field of 20 oersteds showed a residual to saturation induction ratio consistently higher than that for the specimens annealed without the field. The first anneal with the field (¼ hr) caused an abrupt increase in the ratio at all temperatures; thereafter, the increase in the ratio was generally similar for specimens annealed

R. C. HALL, Junior Member AIME, formerly Graduate Student, Lehigh University, is associated with Materials Engineering, Westinghouse Electric Corp., East Pittsburgh, Pa., G. P. CONARD, and J. F. LIBSCH, Members AIME, are Assistant Professor of Metallurgy and Director, Magnetic Materials Laboratory, and Professor of Metallurgy, respectively, Lehigh University, Bethlehem.

Discussion of this paper, TP 4047E, may be sent, 2 copies, to AIME by Nov. 1, 1955. Manuscript, Sept. 15, 1954. Chicago Meeting, February 1955.

This paper is based on a portion of a thesis by R. C. Hall submitted, in partial fulfillment of the requirements for the degree of Doctor of Philosophy, to the Graduate Faculty, Lehigh University.

The Transactions papers appearing in the Journal of Metals during 1955 will subsequently appear in AIME Transactions Volume 203, and may be permanently referenced to that volume.

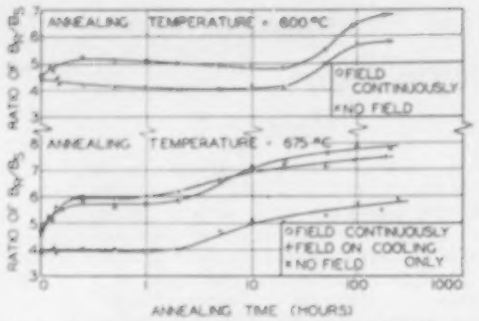

Fig. 1—Influence of annealing time at 600° and 675°C on the ratio of the residual induction, B_r, to the saturation induction, B_s. Average of three rings.

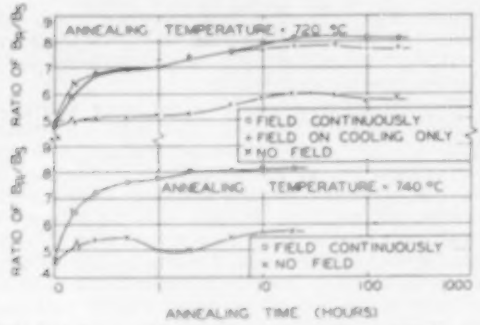

Fig. 2—Influence of annealing time at 720° and 740°C on the ratio of the residual induction, B_r, to the saturation induction, B_s. Average of three rings.

with or without the field. After long annealing times, the ratio for specimens annealed with the field applied continuously increased to slightly greater values than for those with the field applied on cooling only.

The coercive force, Fig. 3, like the ratio of residual to saturation induction, is a structure sensitive property but was found to be essentially independent of the magnetic field condition during annealing. With the 600°C series, a high peak in coercive force was observed at 100 hr, which was the time of the sharp increase in ratio of residual to saturation induction, Fig. 1. For the 675° and 720°C treatments, the peak was at 10 hr. This time was approximately at the middle of the increase in ratio. In the series annealed at 740°C, the peak appeared to be at ¼ to ½ hr but was not pronounced. With progressively higher temperatures of heat treatment, the peak values of coercive force decreased linearly with temperature, Fig. 4, in the range of temperatures studied.

Interesting results were derived from the magnetization curve by plotting the induction value at a field strength of one oersted as a function of annealing time, Fig. 5. With the exception of the 740°C series, the induction values decreased at a time corresponding closely to the peak value of coercive force for the particular annealing temperature.

Representative linear magnetostriction values at a constant induction of 17,500 gauss are shown in Figs. 6 and 7. As the magnetostriction equipment was constructed to measure magnetostriction at given field strength rather than at given induction, these values were determined by selecting the field strength for the desired induction from the magnet-

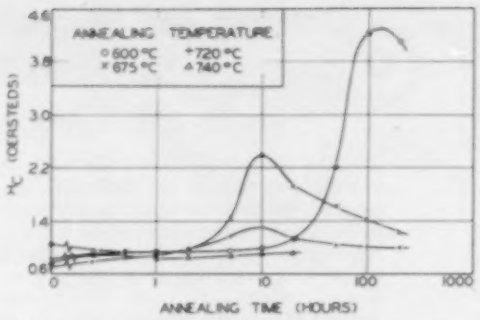

Fig. 3—Influence of annealing time at various temperatures on coercive force, H_c. Field applied continuously; average of three rings.

ization curve for each specimen and then determining the magnetostriction for this field strength from the values of magnetostriction vs field strength. As this process requires a double graphical interpolation, slight errors may have been introduced in the magnetostriction values.

In general, it is seen that the magnetostriction was greater for the condition of no applied field. For the specimens annealed without the field, Fig. 6, the magnetostriction values showed a tendency to decrease in the range of ¼ to 1 hr annealing time, increased to a maximum (quite abruptly for most temperatures) at approximately 1 hr, and then decreased at longer times. For all specimens there appeared to be a second maximum at considerably longer times.

In the case of specimens annealed with the field applied continuously, Fig. 7, the magnetostriction appeared to decrease more noticeably at short times; increased to an apparent maximum in the vicinity of the time for the start of increase in coercive force, Fig. 3; then seemed to decrease regularly.

The intensity of the ordered line, an indication of the amount of ordered phase present, is shown in Table I. No ordered line was detected in the solution treated condition. Since the intensity appeared to be a function only of the temperature and time of anneal, the results are given as averages of different field conditions. The intensities generally increased with increasing time and temperature of anneal. A smoothed plot of these data is shown in Fig. 8. From a comparison of Fig. 8 and Figs. 1 and 2, it appears that the variation in the intensity of the ordered line or amount of the ordered phase with time is similar to that observed for the ratio of residual to saturation induction of specimens annealed with the field.

Discussion of the Course of the Ordering Process

Two types of long range ordering processes have been postulated in the literature. The first is an interchange or rearrangement of atomic positions by means of thermal agitation[20] and the second is the nucleation and growth of an ordered phase from a disordered phase.[21-23] It has been suggested that both mechanisms may operate in the same system.[24-26] The results obtained in this investigation appear to be explained best on the basis of a nucleation and growth reaction, with perhaps a local atomic rearrangement superimposed.

Considering the coercive force, several investigators have postulated that peak values may be obtained as a result of strains introduced by the ordering re-

action.[10,12,13,15,19,20-27] In the 50 pct Fe-50 pct Co alloy the coercive force behavior appears to result from strains associated with the coherent growth of the ordered phase. At low temperatures such as 600°C, initial ordering by atomic interchange, if it does occur, could only take place to a small extent, thus a comparatively large degree of disregistry between the two phases would exist during nucleation and growth. High strains and a high coercive force peak result. At higher temperatures local rearrangement could produce a higher degree of initial ordering. The resulting smaller degree of disregistry between the two phases during nucleation and growth may account for the lower coercive force peak. This lower value of coercive force may, however, also be attributed to the easier loss of coherency or relief of strains at higher temperatures. At higher degrees of order, coherency is gradually lost, the strains decrease, and the coercive force decreases. The direct relation between the peak coercive force value and the annealing temperature seems to confirm the general picture presented. In addition, the low values of induction on the magnetization curve appearing with the coercive force peaks at 600°, 675°, and 720°C may be associated with the strained structure.

Considering the magnetostriction data, decreases in the values may be associated with the formation of more 180° domain boundaries as a result of the applied field[28-30] and with the relief of quenching strains.[31] Increases in the magnetostriction may be attributed to ordering,[11, 13, 32-34] while the exact effect of coherency strains is uncertain but apparently influential.

The data on the intensity of the ordered line are in general in accord with this picture of the ordering process. The increase in intensity of the ordered line even after very short time anneals may result from the existence of a degree of short range order in the quenched alloy.[23, 25-28, 35-37] This might facilitate rapid attainment of a certain degree of long range order by atomic rearrangement. The subsequent increase in the intensity of the ordered line with time may be primarily associated with the nucleation and growth process.

Discussion of the Response to Magnetic Anneal

The attainment of maximum values in the ratio of residual to saturation induction in the 50 pct Fe-50 pct Co alloy appears to depend on two conditions. First, a high degree of long range order seems to be necessary to give the maximum ratio in this alloy, although in the permalloy system this may not be the case.[38, 39] Second, a magnetic field must be applied continuously during the annealing in the order range, since the presence of the field throughout the annealing cycle yields a slightly higher ratio after long time anneals than during cooling only.

It is apparent from Figs. 1 and 2 that the ordering process, even in the absence of a magnetic field, has a significant influence on the ratio of residual to saturation induction, although the increase in ratio does not appear to be consistently related to either the degree of order, the change in saturation induction, or the magnetostriction change. The increase in ratio does appear to correspond to the initial changes in coercive force. The fact that the increase in the ratio of residual to saturation induction does not disappear as the coercive force decreases suggests that the relation is an indirect one. It appears possible that ordering in the 50 pct Fe-50 pct Co alloy is associated with the development of magnetic anisotropy both as a result of the ordered structure per se and as a result of deformation caused by the coherency stresses during formation of the ordered phase. Such anisotropy might be expected to interfere with the ease of movement of domain boundaries (particularly 90° boundaries) and thus to increase the ratio of residual to saturation induction.

The primary influence of the magnetic field during heat treatment is to increase the ratio of residual to saturation induction at the shortest annealing times, the actual increase depending significantly upon the annealing temperature. At longer annealing times, the influence of the field as measured by the increment of improvement in the ratio of residual to saturation induction remains essentially con-

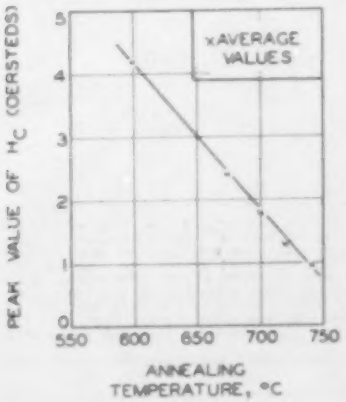

Fig. 4—Influence of annealing temperature on peak value of coercive force, H_c.

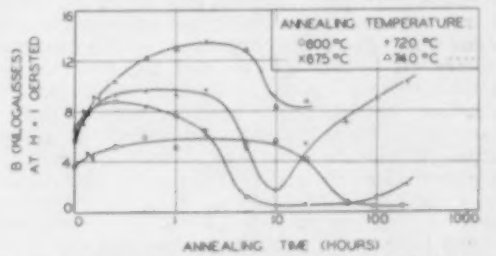

Fig. 5—Influence of annealing time at various temperatures on the magnetic induction, B, at a field strength, H, of 1 oersted. Field applied continuously; average of three rings.

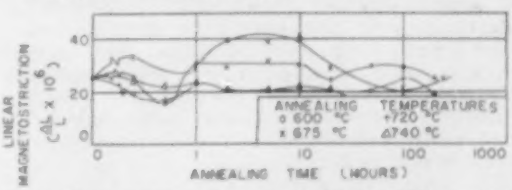

Fig. 6—Linear magnetostriction at induction of 17,500 gauss for specimens annealed without a field vs annealing time.

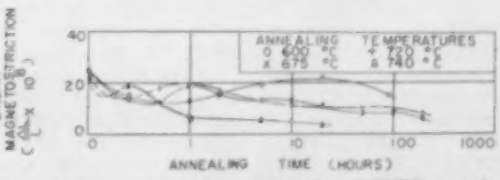

Fig. 7—Linear magnetostriction at induction of 17,500 gauss for specimens annealed in a 20 oersted field vs annealing time.

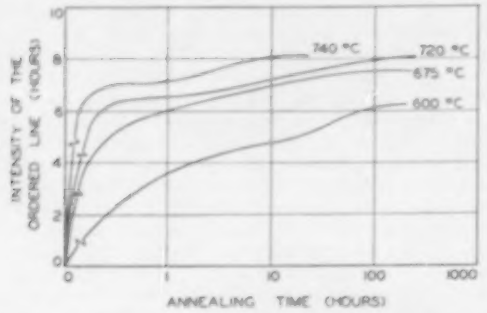

Fig. 8—Influence of annealing time at various temperatures on the intensity of the ordered line, in terms of equivalent exposure time in hours of a nearly fully ordered specimen.

stant. It therefore appears that the improvement caused by the presence of the field is additive to that associated with the ordering by nucleation and growth.

The presence of the magnetic field should produce a structure with fewer 90° domain boundaries. If, in addition, the magnetic field causes a further increase in magnetic anisotropy by deformation from magnetostrictive stresses at the annealing temperature, the improvement in the ratio of residual to saturation induction might be expected.

For the 675° and the 720°C heat treatments, the increase in ratio was slightly greater with a field applied continuously than with the field applied on cooling only at extended annealing times. This does not appear to result from an increase of rate of ordering in the presence of the field,[6, 7] since the coercive force peaks and the changes in the induction on the magnetization curve occurred after the same time of annealing regardless of the field conditions. It further appears that this result is not attributable to insufficient time at temperature to produce the maximum decrease of 90° domain boundaries when the field was applied on cooling only. This explanation was refuted by annealing specimens for 180 hr at 675°C with the field applied on cooling only, followed by 1 hr at 675°C with the field applied continuously. These specimens were found to have the same magnetic properties at the end of 181 hr as at the end of the 180 hr of annealing. The results might be explained, however, by assuming that the field has a slight effect on the orientation or shape of the ordered phase.[6, 7, 8] The development of the ordered phase by nucleation and growth (with the field applied continuously) in a preferred direction or with shape anisotropy could cause an increase in the ratio. The specimens treated with the field applied on cooling only would not be effected by this and would parallel those treated with no field.

Relation Between Ordering and Response to Magnetic Anneal

Unfortunately, the data do not lead to a definite conclusion regarding the interrelation between the magnetic field influence and the ordering process. Since the influence of the magnetic field is apparent for the shortest annealing times and lowest annealing temperature (600°C) before any high degree of order is established, it might appear that crystal order is not essential to the improvement in ratio caused by the magnetic field. Furthermore, since the increment of improvement in the residual to saturation induction ratio caused by the magnetic field appears almost constant for various annealing times (the curves representing the ratios obtained with and without the field are essentially parallel after ¼ hr), it appears that changes in the degree of order through nucleation and growth do not noticeably influence the contribution made by the field. On the other hand, it can be argued that, as some degree of crystal order was always present after the first anneal, the data presented do not answer the question as to whether there is any direct relation between ordering by local rearrangement or short range order and a response to annealing in a magnetic field.

In any event, it appears on the basis of this study that the presence of crystal order is desirable for a maximum ratio of residual to saturation induction on heat treatment in a magnetic field.

Conclusions

Several general conclusions may be drawn concerning the isothermal ordering and magnetic annealing of the 50 pct Fe-50 pct Co alloy:

1—During the ordering process, the coercive force goes through a maximum. This is apparently the result of strains associated with the coherent nucleation and growth reaction. The maximum value is inversely proportional to the temperature of the ordering anneal in the range of temperatures studied.

2—The maximum increase in the ratio of residual to saturation induction from the solution treated condition is associated with annealing to a high degree of order with the continuous application of a magnetic field. These two effects appear to be additive.

3—The increase in ratio associated with the presence of the external field might be explained on the basis of: A—a decrease in 90° domain boundaries resulting from the applied magnetic field and, perhaps, B—an increase in anisotropy as a result of lattice distortion established at the annealing temperature by magnetostriction, and possibly other effects, and retained upon cooling.

4—A further slight increase in the ratio might result from the ordered phase being caused to de-

Table I. Influence of Annealing Time at Various Temperatures on the Intensity of the Ordered Line

Annealing Time, Hr	Intensity of the Ordered Line,* at Various Annealing Temperatures			
	600°C†	675°C‡	720°C‡	740°C†
0	0	0	0	0
¼	2	2	6 1/2	7
½	2	5½	7 1/8	7
1	3½	6¼	6 1/2	6½
2	4¼	7⅛	6	7
5	4½	6⅝	7	6¾
10	4¾	7⅛	7 1/8	8¼
20	5	7	7 5/8	7⅞
50	5¾	8	7 5/8	—
85	6¼	—	—	—
100	—	7⅛	7 1/2	—
180	6	—	—	—
200	—	7⅛	8 1/8	—

* Intensity measurements of the ordered line (300) were made by comparing visually the diffraction patterns obtained on each specimen, using a constant exposure time of 7 hr, with a set of standard patterns previously prepared by exposing a nearly fully ordered specimen for different lengths of time. The values of intensity given for various annealing treatments are thus the equivalent exposure time in hours for a nearly fully ordered specimen.

† Average of two series: no field and field continuously.

‡ Average of two series: field on cooling only and field continuously.

§ Average of three series: no field, field on cooling only, and field continuously.

velop by the field in a preferred direction or with shape anisotropy.

Acknowledgments

The authors wish to express their gratitude to E. Both and the Signal Corps of the U.S. Army at Fort Monmouth for advice and support of these investigations.

Discussion of this paper, if any, will appear in JOURNAL OF METALS, May 1956, and in AIME Metals Branch *Transactions*, Vol. **206**, 1956.

References

[1] W. C. Ellis and E. S. Greiner: *Trans.* ASM (1941) **29**, p. 415.
[2] C. G. Shull and S. Siegel: *Physical Review* (1949) **75**, p. 1008.
[3] E. G. Zukas: Ph. D. Dissertation, Lehigh University (1952).
[4] J. F. Libsch, E. Both, G. W. Beckman, D. Warren, and R. J. Franklin: *Trans.* AIME (1950) **188**, p. 287; JOURNAL OF METALS (February 1950).
[5] J. F. Dillinger and R. M. Bozorth: *Physics* (1935) **6**, p. 279.
[6] A. H. Geisler, J. P. Martin, E. Both and J. H. Crede: *Trans.* AIME (1953) **197**, p. 813; JOURNAL OF METALS (June 1953).
[7] R. C. Hall: Ph. D Dissertation, Lehigh University, (1954); *University Microfilms*, Ann Arbor, Mich.
[8] R. M. Bozorth: *Ferromagnetism.* (1951) p. 843. New York. D. Van Nostrand Co.
[9] E. Costello: Fourth, Fifth, Sixth, and Seventh Quarterly Progress Reports. *Improved Magnetic Materials.* U. S. Army Signal Corps Contract No. DA-36-039-SC-61 with Lehigh University (October 1951-1952).
[10] E. M. Grabbe: *Physical Review* (1940) **57**, p. 728.
[11] J. E. Goldman: Discussion of ref. 22. *Phase Transformations in Solids.* (1951) p. 384. New York. John Wiley and Sons.
[12] J. E. Goldman: *Journal of Applied Physics* (1949) **20**, p. 1131.
[13] J. E. Goldman and R. Smoluchowski: *Physical Review* (1949) **75**, p. 310.
[14] W. L. Bragg and E. J. Williams: *Proceedings* Royal Soc. (1934) **145A**, p. 699.
[15] A. H. Geisler: Discussion of ref. 37. *Trans.* ASM (1953) **45**, p. 1051.
[16] A. H. Geisler: *Trans.* ASM (1951) **43**, p. 70.
[17] F. E. Jaumot, Jr. and C. H. Sutcliffe: *Acta Metallurgica* (1954) **2**, p. 63.
[18] J. B. Newkirk, A. H. Geisler, D. L. Martin, and R. Smoluchowski: *Trans.* AIME (1950) **188**, p. 1249; JOURNAL OF METALS (October 1950).
[19] R. A. Oriani and T. S. Jones: *Acta Metallurgica* (1953) **1**, p. 243.
[20] S. Siegel: *Journal of Chemical Physics* (1940) **8**, p. 860.
[21] N. W. Lord: *Journal of Chemical Physics* (1953) **21**, p. 692.
[22] S. Siegel: Order-Disorder Transitions in Metal Alloys. *Phase Transformations in Solids.* (1951) p. 366. New York. John Wiley and Sons.
[23] C. Sykes and H. Evans: *Journal* Inst. of Metals (1936) **58**, p. 255.
[24] P. A. Flinn, B. L. Averbach, and M. Cohen: *Acta Metallurgica* (1953) **1**, p. 664.
[25] H. Lipson, D. Shoenberg, and G. V. Stupart: *Journal* Inst. of Metals (1941) **67**, p. 333.
[26] D. L. Martin and A. H. Geisler: *Trans.* ASM (1952) **44**, p. 461.
[27] R. J. Wakelin and E. L. Yates: *Proceedings* Physical Soc., London (1953) **66B**, p. 221.
[28] E. A. Nesbitt: *Journal of Applied Physics* (1950) **21**, p. 879.
[29] K. Hoselitz and M. McCaig: *Proceedings* Physical Soc., London (1949) **62B**, p. 163.
[30] H. J. Williams, R. M. Bozorth, and H. Christensen: *Physical Review* (1941) **59**, p. 1005.
[31] J. E. Goldman: *Trans.* ASM (1946) **37**, p. 212.
[32] J. E. Goldman and R. Smoluchowski: *Physical Review* (1949) **75**, p. 140.
[33] J. E. Goldman: *Le Journal De Physique et Le Radium* (1951) **12**, p. 471.
[34] J. E. Goldman: *Physical Review* (1949) **76**, p. 471.
[35] J. M. Cowley: *Journal of Applied Physics* (1950) **21**, p. 24.
[36] G. R. Piercy and E. R. Morgan: *Canadian Journal of Physics* (1953) **31**, p. 529.
[37] F. N. Rhines and J. B. Newkirk: *Trans.* ASM (1953) **45**, p. 1029.
[38] S. Kaya: *Reviews of Modern Physics* (1953) **25**, p. 49.
[39] S. Chikazumi: *Journal* Physical Soc., Japan (1950) **5**, p. 327.
[40] S. Chikazumi: *Physical Review* (1952) **85**, p. 918.
[41] R. W. Fountain et al.: Fifth Quarterly Progress Report. *Improved Magnetic Materials.* U. S. Army Signal Corps Contract DA-36-039-SC-61 with Lehigh University (Jan. 15, 1952).
[42] M. McCaig: *Journal of Applied Physics* (1953) **24**, p. 366.

Further Observations on Yield in Single Crystals of Iron

by H. W. Paxton and I. J. Bear

Studies have been made of the method of propagation of yield in iron single crystals in the range of 205° to 295°K by microscopic and X-ray techniques. The results show yielding in two stages, of which the second corresponds closely to the Lüders extension in polycrystalline iron.

H. W. PAXTON, Junior Member AIME, formerly associated with Dept. of Physical and Theoretical Metallurgy, University of Birmingham, Birmingham, England, is associated with Dept. of Metallurgy, Carnegie Institute of Technology, Pittsburgh, and I. J. BEAR, formerly associated with Dept. of Physical and Theoretical Metallurgy, University of Birmingham, is associated with Commonwealth Scientific and Industrial Research Organization, Victoria, Australia.

Discussion of this paper, TP 3921E, may be sent, 2 copies, to AIME by Nov. 1, 1955. Manuscript, Aug. 9, 1954. Chicago Meeting, February 1955.

IRREGULAR macroscopic markings on the polished surface of a polycrystalline mild steel test piece during the lower yield extension were first observed by Lüders.[1] The lower yield stress was not very constant. Sylvestrowicz and Hall[2] showed that it was possible to obtain a constant lower yield stress by using a specimen in the form of a moderately flexible thin strip; the macroscopic markings in this case then appeared as a band of deformation (Lüders' band) which propagated steadily from one or occasionally

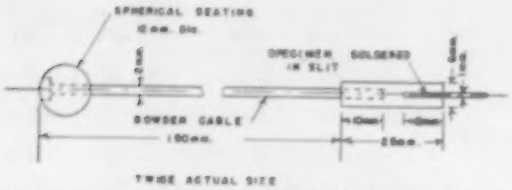

Fig. 1—Diagram of grips used to attach specimen to straining shackles.

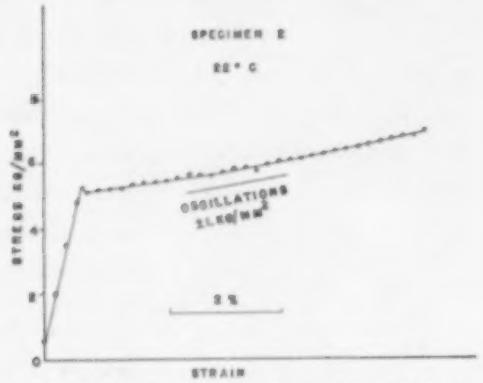

Fig. 2—Specimen 2 (see Fig. 5), electropolished surface, extended at 22°C.

both of the grips. The shear behind the band front was constant and equal to the magnitude of the lower yield strain. When the band or bands had completely covered the specimen, the stress-strain curve began to show work hardening.

The purpose of the experiments described subsequently was to investigate metallographically the corresponding behavior in single crystals of α-iron and in addition to examine some of the crystallographic aspects of the yield process.

Experimental Details

The lower yield extension in single crystals of iron at room temperature is small, about 0.5 pct. However, it has been shown by Churchman and Cottrell[3] and Paxton and Churchman[4] that at about −70°C the magnitude of the lower yield extension in crystals grown from Swedish Armco iron is increased to about 3 pct. These crystals were round and thus not very suitable for metallographic examination.

For the present work, crystals with a rectangular cross-section about 3x1 mm and of lengths up to 25 cm were prepared by a strain-anneal method previously described.[5] The material was Armco iron supplied by The British Iron and Steel Research Assn. with the analysis given in Table I.

An interesting observation was made during the preparation of these crystals. In general, round iron crystals grown by the strain-anneal method have a film of surface grains which must be etched away

Table I. Analysis of Armco Iron

Element	Pct
C	0.027
Si	0.02
Mn	0.05
S	0.028
Ni	0.072
O	0.01

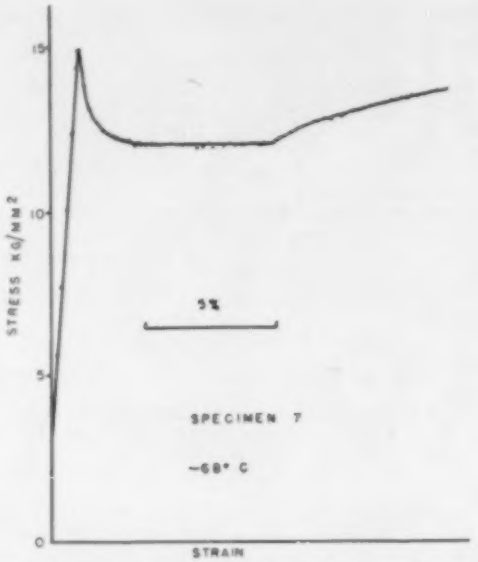

Fig. 3—Specimen 7, electropolished surface extended at −68°C.

to display the single crystal underneath. The present strip crystals had no such layer. Crystals grown by Mouflard and Lacombe[6] from nondecarburized strip also showed no surface grains, though those of Holden and Hollomon[7] from decarburized strip contained a surface film of such grains about 0.01 in. thick.

A small number of included grains of about the same size as that of the original grains were distributed throughout the volume of each crystal. Presumably these are grains of such orientations that they are not readily absorbed, i.e., those of closely similar orientations and those nearly in twin relationship. In none of the experiments was there any evidence that these grains caused spurious effects other than slight stress concentrations which enabled yield to begin occasionally at these grains.

Since the crystals were decarburized before being grown, about 0.003 pct carbon was reintroduced before testing in order to bring out the yield phenomenon.[3] Specimens were soft soldered axially into close-fitting slots in steel end pieces, as shown in Fig. 1. These end pieces were attached to spherical seatings on the straining shackles by flexible Bowden cable. The crystals were extended at a strain rate of 10^{-4} per sec in a Polanyi-type hard beam testing machine. Temperatures between 0° and −70°C were attained by a bath of alcohol and solid carbon dioxide. Variation of temperature during a test was ±1°C.

The specimens were usually tested with one or other of three surface conditions: 1—the as-grown surface, after etching with a saturated solution of ammonium persulphate to reveal crystal boundaries; 2—a surface given a standard metallographic treatment, finishing with British Iron and Steel Research Assn. ferrous polishing cream on a Selvyt pad; and 3—an electropolished surface. The crystal was first polished metallographically to 400 grade Carborundum paper and then about 50 to 100 μ of metal was removed by electropolishing in a bath of perchloric and acetic acid. The microhardness of a typical surface given this treatment was Vpn 74 (a mean of 20 readings) against a Vpn of 116 for a different

section of the same crystal given the standard metallographic treatment.

It has been shown previously[7] that at room temperature the condition of the crystal surface can affect the distribution of slip lines markedly. On a surface of type 2, the slip lines are well defined and spaced about 20 μ apart; on a type 3 surface they are difficult to resolve and have a maximum spacing of about 2 μ.

Table II. Experimental Data on Iron Crystal Specimens

Specimen No.	Temperature, °C	Lower Yield Point Extension, Pct	Surface Condition
1	20	½	Electropolished
2	20	½	Electropolished
3	−45	6	Electropolished
4*	−45	2	Electropolished
5	−68	15	Electropolished
6	−68	13	Electropolished
7	−68	7½	Electropolished
8	−68	5	As grown, etched, oxidized
9	−68	14½	Electropolished
10	−68	8½	Electropolished
11	−68	7	Electropolished
12*	−68	5	Electropolished
13	−68	7	Mechanically polished

* Showed slip on two systems.

The increase in upper yield stress and the lower yield extension of annealed single crystals as the temperature is lowered is well shown by the typical stress-strain curves shown in Figs. 2, 3, and 4. For these experiments, three specimens were cut from a single crystal, indicated as 2, 7, 8 in Fig. 5, so as to have identical orientations with respect to the tensile axes. Specimen 2, shown in Fig. 2, was electropolished and extended at 22°C. A very slight upper yield point was observed, followed by a steady rate of work hardening. Specimen 7, shown in Fig. 3, was also electropolished, but extended at −68°C. The lower yield stress is increased to 12.6 kg per mm² and the lower yield extension is 7½ pct, equivalent to a glide strain[8] of about 15 pct. Specimen 8, shown in Fig. 4, after etching the as-grown surface, was oxidized by treatment in steam for 30 min before straining. While the lower yield stress was almost identical with that of specimen 7, i.e., 12.7 kg per mm², the lower yield extension was reduced to less than 5 pct, showing that the magnitude of the lower yield extension thus depends on both temperature and surface condition.

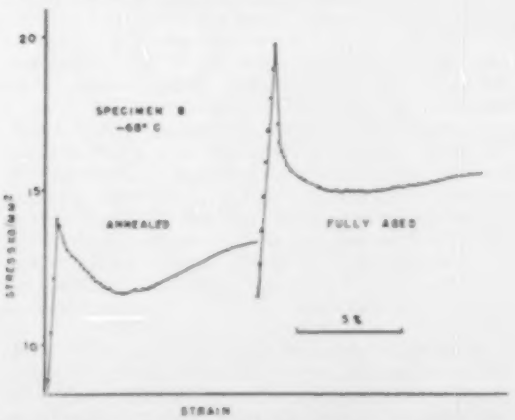

Fig. 4—Specimen 8, surface etched in saturated ammonium persulphate, then heated in steam for 30 min, extended at −68°C.

Several repeat experiments established that the very large lower yield extensions were a characteristic of electropolished crystals of rectangular cross-section strained at temperatures around −68°C.

Specimen 13, of different orientation to 2, 7, and 8, which had a mechanically polished surface, also showed a fairly large lower yield extension. Unfortunately, no other crystal could be used to prepare two specimens of identical orientation to make a direct comparison between mechanically polished and electropolished surfaces. Microscopic examination of the progress of yield indicated no differences in mechanism. Table II shows that there is a dependence of lower yield-point extension on orientation, but the physical basis of this is not clear.

Two specimens with electropolished surfaces were strained at −45°C and showed very similar behavior to those extended at −68°C. The lower yield stress was somewhat less, about 7.5 kg per mm². The lower yield extension was about 6 pct for specimen 3 which showed a single set of slip lines and about 2 pct for specimen 4 which slipped on two well marked systems.

Because of these large extensions at the yield point, it was quite possible to stop the test at intervals and examine the specimen metallographically and with X-rays. Aging the specimen after interrupting the lower yield extension caused a large upper yield point to return with a subsequent load drop to the same lower yield stress as before. The same behavior has been observed in polycrystalline iron by Sylvestrowicz and Hall.[9] A typical interrupted stress-strain curve is shown in Fig. 6.

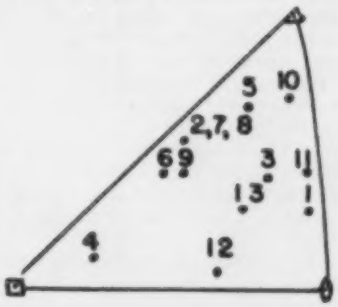

Fig. 5—Orientations of the crystals tested.

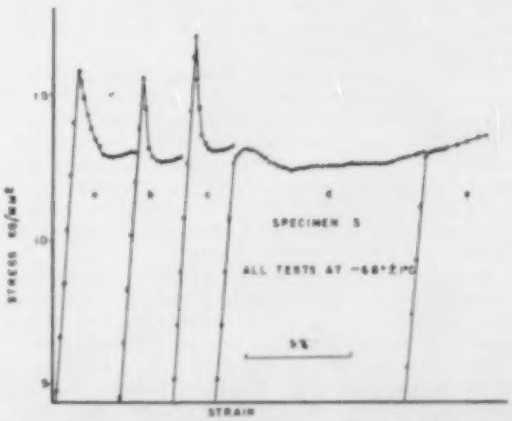

Fig. 6—Interrupted stress-strain curve on specimen 5. Between *a* and *b* and *b* and *c*, the specimen was removed from the machine and fully aged. After *c* and *d*, the specimen was unloaded, but not allowed time to age.

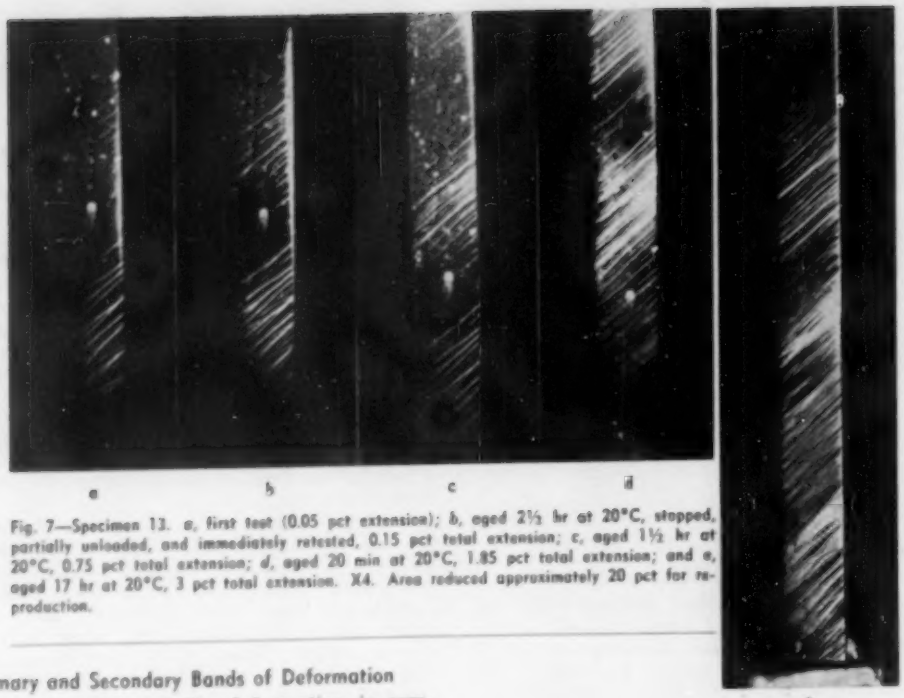

a b c d e

Fig. 7—Specimen 13. *a*, first test (0.05 pct extension); *b*, aged 2½ hr at 20°C, stopped, partially unloaded, and immediately retested, 0.15 pct total extension; *c*, aged 1½ hr at 20°C, 0.75 pct total extension; *d*, aged 20 min at 20°C, 1.85 pct total extension; and *e*, aged 17 hr at 20°C, 3 pct total extension. X4. Area reduced approximately 20 pct for reproduction.

Primary and Secondary Bands of Deformation

The metallography of the deformation is complicated and varies slightly from specimen to specimen. However, a general picture can be given. In the very early stages of deformation, before the upper yield point is reached, "primary bands" of slip appear at intervals of 20 to 50 μ. These primary bands usually form first at the grips, the most obvious stress concentrators, although one case was noted in which they began in the center of the specimen. As might be expected, this specimen showed a very high upper yield point. With further deformation the primary bands propagate along the specimen as shown for specimen 13 in the series of pictures in Fig. 7.

In addition to the propagation of the primary bands, a second deformation front passes through the specimen and corresponds to the passage of a Lüders' band through a polycrystalline specimen, i.e., after the passage of the front, the full lower yield extension has taken place in the material.

As the second band passes through them, the areas between the primary bands fill in with slip lines of apparently identical type to those in the primary bands. The specimen thus necks down and a measurement of reduction of area shows that the lower yield extension is complete in these portions. When the second deformation front has passed completely through the specimen, work hardening begins to be shown on the stress-strain curve.

Usually more than one second deformation front occurs in the specimen. Typically one starts at each grip and occasionally a third begins in parts of the specimen remote from the grips and propagates in both directions. The essential picture is not altered by this complication, and the whole deformation still takes place at very nearly constant lower yield stress.

This will be seen from the stress-strain curve of specimen 13, as shown in Fig. 8. It will be observed that a pronounced upper yield point is present (curves b and c), whereas the specimen shows some plastic deformation after an extension of about 0.05 pct (curve *a*) in which it was not stressed to the upper yield point. It is a characteristic of single crystals of iron to show some plastic deformation before yielding. This is presumably due to lack of straightness in the specimen, and to slight nonaxiality of testing, since specimens which have been given a preliminary stressing just below the upper yield point followed by an aging treatment show no detectable plastic deformation before yielding[5] in a subsequent test.

Each of the primary bands at −70°C consists of three or four approximately parallel sets of slip lines with a spacing of about 2 μ. The slip lines are not continuous along their length as viewed in the optical microscope, and each short length is conveniently referred to as a slip packet.

The primary bands do not appear to form on any specific plane. Indeed they are often not parallel and branch occasionally, as shown in Fig. 7a and b. They usually start at one edge of the crystal and spread across with increasing strain. It seems likely that they are essentially a delineation of lines of stress concentration in the specimens—complex near the grips because of bending and more uniform towards the center of the specimen. They are usually approximately parallel to the trace of the plane of maximum resolved shear stress although deviations from this trace on the polished surface of up to 10° are common. Each primary band always contains more than one row of slip packets even when separated by as much as 1 mm from its nearest neighbor.

At room temperature and −15°C, it is difficult to resolve slip lines in the primary bands, although these bands can be seen quite readily with the naked eye or at very low magnifications. They form all over the specimen at very small strains (0.1 pct) and are just as branched and noncrystallographic

as are the bands formed at −68°C, which may not cover the entire specimen until strains of order 4 pct have been reached. No experiments were carried out above room temperature.

The advance of the primary bands in front of the main deformation means that the band front is not sharp. This has also been observed in coarse grained polycrystalline iron by Hall.[20] The band front is sharp to within a single grain diameter in fine grained material.

X-Ray Examination

The yield process also can be conveniently followed by X-ray Laue back-reflection photographs. Fig. 9 shows the position of the tensile axis of crystals 5 and 6. Both these crystals were electropolished and extended at −68°C. Specimen 5 showed *ideal* behavior in that a single second deformation front moved progressively through the crystal from one grip; specimen 6 had more than one interface leading to reduction of area in three different places.

The stereogram shows the position of: T_1, the original axis; T_2, the axis in a section showing only primary bands (i.e., no reduction of area); and T_3, the axis in a position through which the secondary band has passed. Both specimens deformed by single slip, as can be predicted from the position of T_1. T_2 is almost coincident with T_1, while T_3 is rotated considerably along the great circle joining T_1 with the operative [111] slip direction.

The lattice rotation can be calculated from the well known expression[6]

$$1 + \epsilon = \frac{\sin \lambda_2}{\sin \lambda_1}$$

where λ_2 is the angle between T_2 and [111], λ_1 is the angle between T_3 and [111], and ϵ is the strain.

The slip plane is here taken as the plane of maximum resolved shear stress. With specimen 5, the rotation corresponds to 13±3 pct lower yield extension if ±1° is allowed as the error in angles. The actual extension was about 15 pct which is as good agreement as can be expected. For specimen 6, the calculated value of the lower yield extension from the lattice rotation was 12.5±2.5 pct. The experimental value was 13 pct.

The photographs obtained for T_1 and T_2 showed round spots with no asterism; T_3 showed slight intensity maxima in the spots. The spots obtained on the film for T_3 showed considerable asterism and nonuniform intensity.

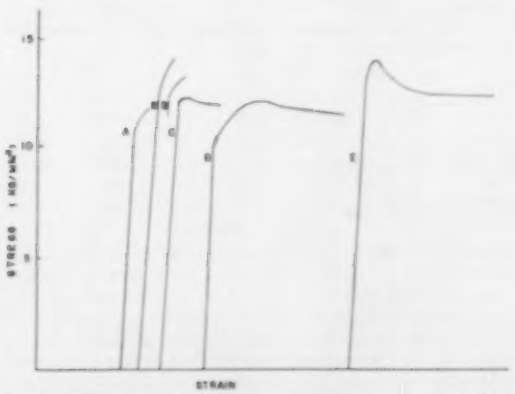

Fig. 8—Specimen 13 strained to various amounts as shown, corresponding to interruptions shown in Fig. 7.

Dislocation Loops

The nature of the slip bands produced at −70°C is interesting. Each of the slip packets, presumably coming from a single Frank-Read source[21] of dislocation loops, is about 10 to 20 μ long if it appears on a face corresponding to the outcrop of mainly the edge component of the loops and of a length several hundred microns where screw components appear on the surface of the crystals.

Thus there is the picture of long narrow dislocation loops first predicted by Mott[22] and recently also demonstrated by Chen and Pond[23] in aluminum single crystals by cine-camera studies. The reason for these is presumed to be that, when the screw component of a loop cuts intersecting screw dislocations, a trail of vacancies or interstitial atoms is left (depending on the sign) and thus a considerable amount of energy is required to continue motion of the screw. When an edge dislocation cuts other dislocations, however, only a single *jog* (a displacement of part of the dislocation line by an amount equal to the Burgers' vector of the intersecting dislocation) is formed and the extra energy needed for movement to continue is not very great. Thus edge components of the loops should be considerably more mobile, and if approximately round loops are formed at the Frank-Read sources, they rapidly become extended in the direction of the Burgers' vector of the loop.

Discussion

The period of low work hardening after the upper yield point is similar in some ways to the period of easy glide observed in high purity single crystals of aluminum,[16-18] gold,[17] silver,[17] and the hexagonal-close-packed metals.[18] It is possible that the yield elongation and the period of easy glide are both manifestations of some deformation process about which nothing is yet known. The metallography of easy glide does not appear to have been sufficiently closely studied to indicate whether deformation propagates as in the yield process or whether the density of slip bands in any given part of the specimen increases fairly steadily.

The idea that work hardening is produced by deformation bands has been proposed by Honeycombe[19]

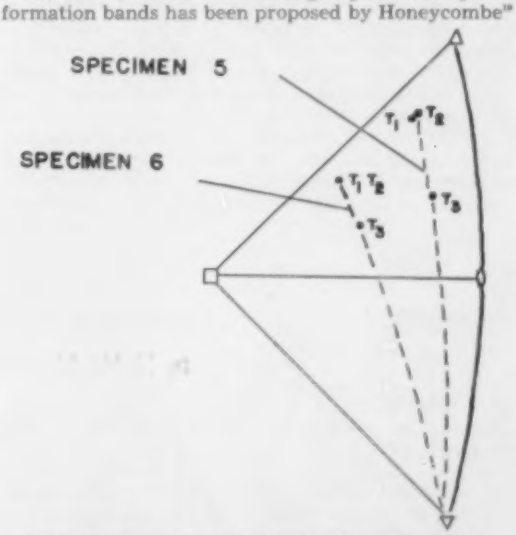

Fig. 9—Showing position of initial tensile axis T_1, position after passage of the primary bands T_2, and position after passage of the secondary band T_3.

and others. In this work these could not be observed metallographically on a section which has been traversed by the secondary band, although asterism is noted in the back-reflection Laue patterns. It has been shown that deformation bands cause asterism, but the converse does not appear to be necessarily true. No asterism or deformation bands were noted in Honeycombe's cadmium crystals or Lücke and Lange's aluminum crystals during the easy glide period.

The work of Holden and Kunz[25] on specimens deformed entirely at room temperature is similar in many respects to the present work. However, their observations of the sharpness of the yield point being affected by orientation at 25°C did not appear to be true at −68°C, although not as wide a range of orientations is represented here. All specimens tested in the authors' work at the lower temperature showed a well defined sharp upper yield point. Thus, no correlation could be observed between slip distance and shape of the stress-strain curve.

Their observation of very localized flow during early stages of the yield process is confirmed by the present work; it was more clearly visible in this study at the lower temperature, since the slip distance on the electropolished surfaces used appeared to be considerably greater than at room temperature. Insufficient metallographic work has been done on decarburized crystals to compare results. No figures are available in Holden and Kunz' paper to enable exact comparison of lower yield extensions, although in one of their crystals the load was still dropping at 4 pct strain; hence the magnitudes are roughly equal.

Conclusions

The results of experimental data presented in this paper can be summarized as follows:

1—The lower yield extension in single crystals of iron is similar in many ways to that in polycrystalline iron. It depends markedly on temperature and on the surface condition of the specimen and to some extent on the orientation of the specimen relative to the tensile axis.

2—Deformation takes place in two distinct stages here termed primary and second bands. Primary bands form before the upper yield point and extend along the specimen causing little total deformation. The secondary bands correspond closely to Lüders' bands in polycrystalline iron and are responsible for the great majority of the extension.

3—The secondary bands cause marked asterism and a lattice rotation consistent with the observed macroscopic deformation.

4—The dislocation loops which are formed are approximately rectangular in shape, as predicted by theory.

5—The relation, if any, between yielding and easy glide is not yet clear.

Acknowledgments

The authors wish to express their sincere gratitude to A. H. Cottrell and F. R. N. Nabarro for many helpful discussions, to the late Professor D. Hanson who created the opportunities for this work to be performed, and to their colleagues, especially G. W. Ardley and M. J. Dumbleton, who provided much timely help and criticism.

Discussion of this paper, if any, will appear in JOURNAL OF METALS, May 1956, and in AIME Metals Branch *Transactions*, Vol. **206**, 1956.

References

[1] W. Lüders: *Dinglers Polytechnical Journal* (1860) **155**, p. 18.
[2] W. Sylvestrowicz and E. O. Hall: *Proceedings* Physical Society (1951) **B64**, p. 495.
[3] A. T. Churchman and A. H. Cottrell: *Nature* (1951) **167**, p. 943.
[4] H. W. Paxton and A. T. Churchman: *Acta Metallurgica* (1953) **1**, p. 473.
[5] M. Mouflard and P. Lacombe: *Revue de Metallurgie* (1952) **49**, p. 140.
[6] A. N. Holden and J. H. Hollomon: *Trans.* AIME (1949) **185**, p. 179; JOURNAL OF METALS (February 1949).
[7] H. W. Paxton, M. A. Adams, and T. B. Massalski: *Philosophical Magazine* (1952) **43**, p. 257.
[8] E. Schmid and W. Boas: *Kristallplastizitat.* (1933) p. 58. Berlin. Springer.
[9] H. W. Paxton: *Journal of Applied Physics* (1953) **24**, p. 104.
[10] E. O. Hall: *Proceedings* Physical Society (1951) **B64**, p. 742.
[11] F. C. Frank and W. T. Read: *Physical Review* (1950) **79**, p. 722.
[12] N. F. Mott: *Proceedings* Physical Society (1949) **B64**, p. 729.
[13] N. K. Chen and R. B. Pond: *Trans.* AIME (1952) **194**, p. 1085; JOURNAL OF METALS (October 1952).
[14] G. Masing and J. Raffelsieper: *Ztsch. für Metallkunde* (1950) **41**, p. 65.
[15] K. Lücke and H. Lange: *Ztsch. für Metallkunde* (1952) **43**, p. 55.
[16] H. W. Paxton and A. H. Cottrell: *Acta Metallurgica* (1954) **2**, p. 3.
[17] E. N. da C. Andrade and C. Henderson: *Phil. Trans.* Royal Society (1951) **A244**, p. 177.
[18] E. Schmid and W. Boas: *Kristallplastizitat.* (1933) p. 125. Berlin. Springer.
[19] R. W. K. Honeycombe: *Journal* Institute of Metals (1951) **80**, p. 415.
[20] A. N. Holden and F. W. Kunz: *Acta Metallurgica* (1953) **1**, p. 495.

Technical Note

Diffusion of Co^{60} and Fe^{55} in Cobalt

by H. W. Mead and C. E. Birchenall

SELF-DIFFUSION of cobalt has been investigated by Ruder and Birchenall,[1, 2] Nix and Jaumot,[3] and Gruzin.[4] The results for a given temperature differ by a factor of about six in the extreme cases with no really close agreement between any two sets of data. The first two groups of investigators employed the decrease of surface activity method. Since Ruder and Birchenall have shown that the values obtained from this method are sensitive to the surface preparation, it seemed desirable to perform a few check experiments by a method not open to this objection.

H. W. MEAD, Junior Member AIME, is Technical Officer, Metals Div., Imperial Chemical Industries Ltd., London, England, and C. E. BIRCHENALL, Member AIME, is Associate Professor of Chemistry, Princeton University, Princeton, N. J.

TN 2806. Manuscript, Mar. 2, 1955.

The cobalt used in this investigation was the same as that employed by Ruder and Birchenall, containing 99.9+ pct Co. Disks of cobalt, 1 in. diam and 1/8 to 1/16 in. thick, were ground through 4/0 emery paper on one face each. Half of the disks were electroplated with either Co^{60} or Fe^{59}. Co^{60} was plated from a cobalt sulphate solution made slightly alkaline with ammonia. Fe^{59} was plated from ferrous oxalate solution. Welding and annealing techniques were similar to those described elsewhere.[5] Each active disk was welded in an atmosphere of argon to an inactive disk. Diffusion anneals were performed in tube furnaces controlled within ±2°C in an atmosphere of hydrogen. The specimens were packed in cobalt chips inside an iron crucible. After diffusion thin layers were machined from the specimen. Chips for the determination of Co^{60} activity were dissolved in acid and diluted with water to give a total solution volume of 250 ml. A liquid jacketed counter with an annular volume of 35 ml was filled three times with the solution and allowed to drain. The fourth charge was counted. The time to give 4096 counts was recorded and corrected for background activity. All counting rates were less than 1000 counts per min. However, the somewhat larger than usual statistical counting error probably affected the diffusion coefficient very little. Cobalt chips for the determination of Fe^{59} were dissolved. To the solution, 10 mg of inactive iron were added in the form of ferric chloride. The iron was precipitated as hydroxide, filtered, washed, and again dissolved and precipitated. The filtered precipitate was redissolved and plated onto blanks from ferrous oxalate solution.[6] The samples were counted with an X-ray sensitive tube. The time for 12,288 counts was recorded and corrected for background and coincidence losses. All results were normalized to constant sample weight. Diffusion coefficients were calculated by the method of Johnson,[4] and the results are given in Table I. The cobalt self-diffusion measurements from all available sources are compared in Fig. 1.

In their studies of iron self-diffusion in wüstite, Carter and Richardson[7] have shown that the formation of surface crystallites during deposition of the radioactive tracer or during the early stages of the diffusion anneal may lead to very low results. Crystallites which were observed on the surface of cobalt specimens under conditions similar to those employed by Ruder and Birchenall[1] for self-diffusion measurements on electropolished specimens may account for their very low values. Their other results[2] on etched specimens agree reasonably well with the extrapolation of the present data. This agreement seems to support Carter and Richardson's belief that Ruder and Birchenall[1] gave too much weight to the effect of surface roughness in explaining the differences in diffusion coefficients obtained on surfaces polished in different ways. If it is accepted that the results on electropolished samples are low due to activity bound at the surface during diffusion, the proportion bound is fairly constant from one sample to another. This suggests that the surface crystallites may have formed by the hydrogen reduction of an oxide film of nearly constant thickness left by the electropolishing procedure.

Table I. Diffusion Coefficients for Co^{60} and Fe^{59} in Cobalt

Time of Anneal, Sec	Temperature, °C	1/T, °K⁻¹	Diffusion Coefficients, Sq Cm per Sec	
			for Co^{60}	for Fe^{59}
2.568×10^{6}	1104	7.38×10^{-4}	1.29×10^{-11}	2.47×10^{-11}
6.048×10^{5}	1211	6.73×10^{-4}	9.96×10^{-11}	1.34×10^{-10}
3.348×10^{5}	1303	6.32×10^{-4}	—	4.58×10^{-10}
8.730×10^{4}	1406	5.86×10^{-4}	1.28×10^{-9}	—

Fig. 1—Cobalt self-diffusion measurements are compared. Open circle represents present work; closed circle, Ruder and Birchenall;[2] triangle, Ruder and Birchenall;[1] plus, Nix and Jaumot;[3] and cross, Gruzin.[4]

While the results of Nix and Jaumot[3] may be affected by surface hold-up, the exponential absorption curves they reported for Co^{60} radiations may also be a source of error. Berkowitz[8] reports new measurements on the absorption of Co^{60} radiations which are similar to those of Ruder and Birchenall.[1]

Gruzin's[4] procedure should have revealed any surface hold-up in his specimens. The fact that his results are appreciably higher than those reported here may be due to the impurities contained in his 98.4 pct Co.

The present results yield the following equation for self-diffusion in 99.9+ pct Co

$$D = 0.83\, e(-67{,}700/RT) \text{ sq cm per sec.}$$

The activation energy is close to that reported by Nix and Jaumot.[3]

The diffusion of iron in dilute solution in this cobalt may be represented by

$$D = 0.21\, e(-62{,}700/RT) \text{ sq cm per sec.}$$

Acknowledgments

This work was carried out in the Metals Research Laboratory, Carnegie Institute of Technology, Pittsburgh, under the sponsorship of the Office of Naval Research. The radioactive isotopes of iron and cobalt were obtained from the Oak Ridge National Laboratory under authorization from the Isotopes Div., AEC.

References

[1] R. C. Ruder and C. E. Birchenall: *Trans.* AIME (1951) **191**, p. 142; JOURNAL OF METALS (February 1951).

[2] R. C. Ruder and C. E. Birchenall: Unpublished results. See R. C. Ruder: Doctorate Thesis, Carnegie Institute of Technology (1950).

[3] F. C. Nix and F. E. Jaumot: *Physical Review* (1951) **82**, p. 72.

[4] P. L. Gruzin: *Doklady Akad. Nauk SSSR* (1952) **86**, p. 289.

[5] H. W. Mead and C. E. Birchenall: To be published.

[6] W. A. Johnson: *Trans.* AIME (1941) **143**, p. 107.

[7] R. E. Carter and F. D. Richardson: *Trans.* AIME (1954) **200**, p. 1244; JOURNAL OF METALS (November 1954).

[8] A. E. Berkowitz: *Journal of Applied Physics* (1955) **26**, p. 403.

Grain Boundary Diffusion of Nickel into Copper

by S. Yukawa and M. J. Sinnott

A high resolution autoradiographic study of the diffusion of a nickel isotope (Ni^{63}) into copper in the temperature range of 650° to 925°C, with particular emphasis on grain boundary diffusion, has been made. The extent of grain boundary diffusion is a function of the grain boundary angle and the diffusion temperature. The ratios of the grain boundary diffusion coefficient to the lattice diffusion coefficient ranges from 10^4 to 10^5. The activation energy for grain boundary diffusion decreases with increasing grain boundary angle.

STUDIES and reviews[1-4] of metallic diffusion have indicated that grain boundary diffusion is a common phenomenon but quantitative studies of the many variables involved are not numerous. The present work was concerned with determining the influence of the crystallographic orientation of the grain boundaries and the temperature on the extent of boundary diffusion of nickel into copper. The study involved essentially three steps: 1—the production of grain boundaries of known crystallographic orientation, 2—the determination of the extent of diffusion into the boundaries, and 3—the analysis of the resulting data in terms of the usual diffusion concepts.

The grain boundaries investigated approximated the simple tilt variety having 1° of freedom. They were produced by controlling the solidification from a melt of Cuprovac (a high purity vacuum-melted copper obtained from Vacuum Metals Corp.) of a pair of seed crystals so that the bicrystals of copper produced had a common <100> axis. By rotating one seed crystal relative to the other, a simple tilt boundary was produced. The angle of rotation between the two crystals is the grain boundary angle θ, or what is sometimes termed the *misfit angle*. In all, some 16 boundaries ranging from 2° to 72° in 5° to 10° steps were investigated. The crystallographic orientations were measured with the use of both X-ray and optical goniometric techniques. The <100> axes in the crystals were found to be parallel within 2° to 3° with the exception of one crystal (θ = 12°) in which the axes were 6° from being parallel. All bicrystals showed evidences of subgrain structures. Laue analyses showed that these subgrains differed in orientation up to a maximum of 2°. Because of these variations, and some curvature in the boundaries, the grain boundary angles listed are actually average values and deviate from the 1° of freedom boundaries.

The stripping film technique of high resolution autoradiography was used to detect the diffusion of the nickel isotope into the grain boundaries of the bicrystals of copper. Kodak experimental permeable stripping film with an emulsion layer 5 μ thick

S. YUKAWA, Junior Member AIME, formerly Graduate Student, University of Michigan, is Engineer, Steam Turbine Div., Materials and Process Laboratory, General Electric Co., Schenectady, and M. J. SINNOTT, Member AIME, is Associate Professor of Metallurgical Engineering, University of Michigan, Ann Arbor, Mich.

Discussion of this paper, TP 4053E, may be sent, 2 copies, to AIME by Nov. 1, 1955. Manuscript, Aug. 30, 1954. Chicago Meeting, February 1955.

This paper is based on a thesis by S. Yukawa submitted, in partial fulfillment of the requirements for the degree of Doctor of Philosophy, to the Rackham School of Graduate Studies, University of Michigan.

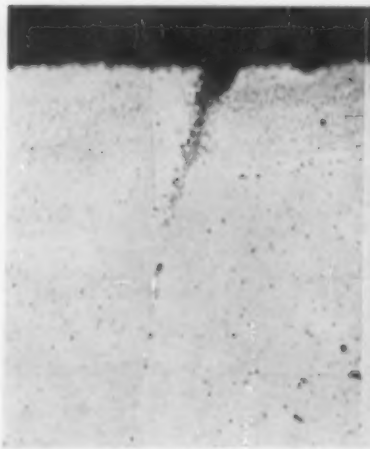

Fig. 1—Autoradiograph shows grain boundary diffusion of nickel into copper. Sample was diffused for 120 hr at 650°C. X500. Area reduced approx. 30 pct for reproduction.

Fig. 2—Autoradiograph shows boundary diffusion of nickel into copper after diffusion for 144 hr at 650°C. Θ = 15°. X500. Area reduced approx. 30 pct for reproduction.

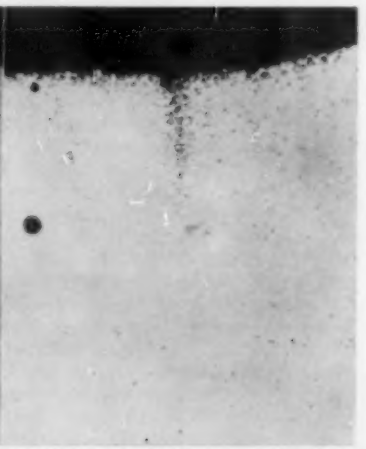

Fig. 3—Autoradiograph shows boundary diffusion of nickel into copper after diffusion for 144 hr at 650°C. Θ = 31°. X500. Area reduced approx. 30 pct for reproduction.

Fig. 4—Autoradiograph shows boundary diffusion of nickel into copper after diffusion for 144 hr at 650°C. $\theta = 45°$. X500. Area reduced approx. 30 pct for reproduction.

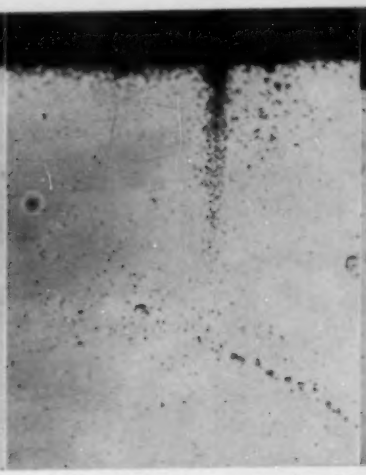

Fig. 5—Autoradiograph shows boundary diffusion of nickel into copper after diffusion for 144 hr at 650°C. $\theta = 66°$. X500. Area reduced approx. 30 pct for reproduction.

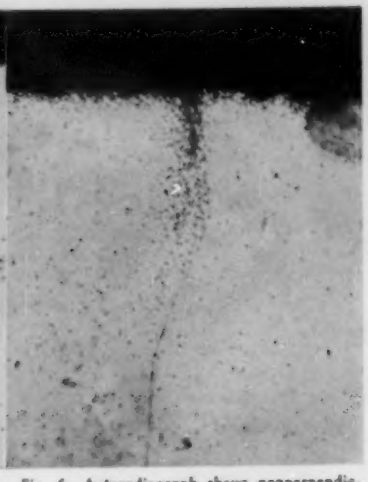

Fig. 6—Autoradiograph shows nonperpendicular grain boundary diffusion. Sample was diffused 144 hr at 650°C. $\theta = 31°$. X500. Area reduced approx. 30 pct for reproduction.

was used in all the studies. In practice, this film is placed in contact with the metal surface to be examined after first coating the surface with a protective film. It is exposed and processed intact with the metallographic surface so that in examining the microstructure the investigator looks through the photographic film and can obtain a direct correlation between the microstructure and the photographic emulsion. Fig. 1 is such an autoradiograph of a polycrystalline copper surface plated with radioactive nickel and diffused at 650°C for 120 hr. Note the penetration of the nickel into one boundary but not into the adjacent one.

The diffusion data obtained were analyzed using Fick's laws as simplified by Fisher,[5] and the more exact solution of Whipple,[6] for the special case of grain boundary diffusion. The procedures used are discussed later.

Experimental Procedure

The copper bicrystals, 1 in. wide, ¾ in. thick, and 5 in. long were sectioned perpendicular to the growth direction, the 5 in. length, into slices approximately ⅛ in. thick using a thin silicon-carbide cutoff wheel. These slices were then heavily etched in HNO_3 to remove any disturbed metal which might recrystallize on the subsequent anneal. An anneal at 1090°C for 2 or 3 days was used to stabilize the grain boundaries. After this treatment, one of the flat surfaces, perpendicular to the grain boundary, was metallographically polished and then electropolished in order to obtain a flat strain-free surface. A circular area, ⅜ in. diam, was plated with purified high activity Ni^{63} isotope over the intersection of the grain boundary with the surface. The isotope was obtained from the Oak Ridge National Laboratory as $NiCl_2$ in HCl solution. It was purified and plated from an aqueous-ammoniacal sulphate solution to give a smooth, continuous, and adherent plate 1 to 2 μ thick.

The plated diffusion specimens were sealed in vacuum in Vycor capsules and placed in a tubular muffle furnace maintained at the desired diffusion temperature. Temperatures were measured with chromel-alumel thermocouples attached to the Vycor capsules and the maximum temperature variation which occurred during diffusion was ±3°C. Diffusion temperatures of 650°, 750°, 800°, 825°, and 915°C for times of from 10 to 144 hr were used.

After diffusion, the samples were sectioned perpendicular to the diffusion interface and the plane of the grain boundary, mounted, and prepared for metallographic examination. Electropolishing could not be used due to the rounding of the specimen edges, so polishing was carried out with silicon-carbide papers and powders with the final polishing being accomplished with Linde A and B powders. Alternate etching and polishing were used to remove the cold worked surface. After the final polishing, the sample was etched in a 20 pct ammonium persulphate-water mixture. The etched surface was then coated with a layer of Vinylite resin 1 μ thick to prevent reaction between the copper and the stripping film. The stripping film was then placed on the specimen and exposed for a period of five days. After exposure, the emulsion was developed, stopped, fixed, washed, and dried with the emulsion in situ on the specimen. Figs. 2 through 5 are typical autoradiographs obtained by this technique on four different grain boundaries given diffusion treatment at 650°C for 144 hr.

For the measurement of the depths of diffusion of the nickel into the copper, a calibrated eyepiece grid was used in conjunction with a Bausch and Lomb research metallograph which permitted measurements to be made to within 3 μ which is the degree of uncertainty of the end point of the diffusion penetration. The outer edge of the nickel electroplate was used for a base line and the original thickness of the electroplate was subtracted from the measurement of both lattice and boundary penetration to obtain penetration measurements. The end point of penetration for both lattice and boundary diffusion was taken to be the point where the density of the developed silver grains became equal to the background, or fog density, of the emulsion. Since the exposure time was kept constant for all specimens, this means that penetration measurements were made to some constant value of nickel concentration.

While it is possible to calculate approximately the minimum concentration of radioactivity required for an observed autoradiographic effect, it was felt

Table I. Depth of Nickel Penetration into Copper Along Bicrystal Grain Boundaries and in the Lattice*

Temperature, °C	Time, Hr	Specimen†	Penetration Along Boundaries of Indicated Misfit Angle, in 10^{-4} Cm														
			0‡	2	12	15	23	25	28	31	39	45	50	52	61	63	66	72
650	144	*A*, cut No. 1																
		1st ARG	10	10	20	28	63	63	102	102	87	108	80	94	78	66	90	63
		2nd ARG	10	10	20	—	60	113	88	95	106	175	97	88	107	88	135	75
		A, cut No. 2																
		1st ARG	10	10	44	60	100	—	—	106	100	102	124	63	—	103	100	72
		2nd ARG	10	10	—	60	85	97	90	66	113	180	104	91	—	70	88	75
		B, 1st ARG	10	—	—	—	—	—	—	—	138	—	146	121	—	—	—	—
		2nd ARG	10	—	—	—	—	—	—	—	120	—	150	116	—	—	—	—
700	10.25	1st ARG	12	—	—	32	—	—	—	—	74	—	86	—	—	—	—	—
		2nd ARG	12	—	—	31	—	—	—	—	71	—	77	—	—	—	—	—
750	41.3	Cut No. 1																
		1st ARG	25	25	31	49	82	83	90	86	114	162	77	108	—	70	83	43
		2nd ARG	25	—	31	—	49	—	—	112	—	130	—	—	—	77	—	—
		Cut No. 2																
		1st ARG	25	25	40	52	68	74	92	106	70	130	111	100	—	102	80	46
		2nd ARG	25	—	40	—	61	102	—	123	—	138	61	—	—	105	—	—
750	116.8	1st ARG	43	—	—	83	—	—	—	—	—	—	188	—	—	—	—	—
		2nd ARG	43	—	—	88	—	—	—	—	—	—	168	—	—	—	—	—
800	13	1st ARG	28	—	36	—	63	61	—	70	108	100	100	80	—	58	61	40
		2nd ARG	28	—	—	—	67	68	—	77	105	86	—	83	—	—	58	—
825	84	1st ARG	108	—	—	—	115	133	130	147	132	181	145	130	132	130	130	—
915	27	1st ARG	200	—‖	—‖	—‖	—‖	—‖	—‖	—‖	—‖	—‖	—‖	—‖	—‖	—‖	—‖	—‖

* Measured autoradiographically from the Ni-Cu interface.
† ARG stands for autoradiograph.
‡ Value from lattice diffusion measurement.
‖ Grain boundary does not meet interface perpendicularly.
§ Absence of value indicates no measurable difference from lattice diffusion.

that a more reliable determination should be made by preparing a series of alloys of varying radioactive nickel concentrations. Accordingly, alloys of nominal composition of 0.1, 0.01, and 0.001 wt pct of radioactive nickel were made up and autoradiographed. The results of this work indicated that the end point detectable above the background was 0.005 wt pct. The activity of the surface of the alloys was also measured with a windowless gas flow counter and these measurements were used to compute the approximate number of β particles emitted from a sample containing 0.005 pct Ni. The value obtained compared favorably with the value given by Towe[8] as being necessary to give a density of 0.5 above fog on Kodak autoradiographic plates.

Results

The extent of nickel penetration for both lattice and boundary diffusion for the various times and temperatures investigated are given in Table I. In some cases the diffusion specimens were sectioned at two different places; these are designated as the first and second cuts. Check specimens were also made on the 650°C diffusion series; the two sets of measurements for this temperature have been designated as specimens *A* and *B*. On many surfaces, two sets of autoradiographs were made; the second set was made by repolishing, etching, and autoradiographing. Measurements of this type are identified as the first and second autoradiographs.

In examining the autoradiographs, it was noticed that in several specimens the bicrystals did not meet the diffusion interface perpendicularly. Autoradiographs of specimens in which this occurred always showed evidences of a high concentration of nickel in the concave side of the curvature. This is believed to be due to boundary migration occurring during the diffusion process although, if this occurred, the migration is in the opposite direction to the one expected. Fig. 6 is an illustration of this type of autoradiograph. Penetration measurements made on such boundaries are indicated in the table and in nearly all such cases these measurements are inconsistent with the data from boundaries perpendicular to the surface.

Figs. 7 through 9 are plots of the penetration data to show the variation of the depth of penetration as a function of the grain boundary, or misfit, angle.

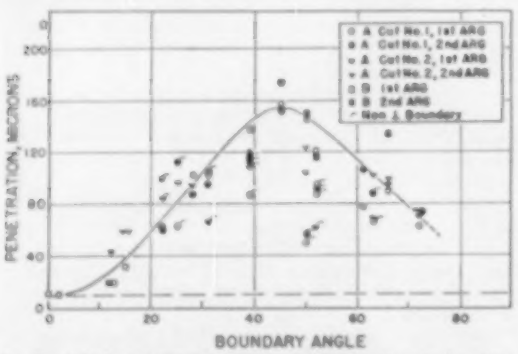

Fig. 7—Nickel penetration is given as a function of grain boundary angle. Samples were diffused for 144 hr at 650°C.

Analysis and Discussion of Data

Using Fick's law of diffusion and assuming that the diffusion coefficient is independent of concentration, the following solution is obtained for a boundary condition such that the interface concentration of the diffusing material remains essentially constant at some value c_0

$$c/c_0 = erf\, c\left[\frac{Z_l}{2(D_l t)^{0.5}}\right] \qquad [1]$$

where Z_l denotes the depth of lattice penetration for concentration c, t is time, and D_l is the diffusion

Table II. Summary of Calculations for the Lattice Diffusion Coefficients for the Diffusion of Nickel in Copper

Temperature, °C	$10^4/T$, °K	Penetration, 10^{-4} Cm	Diffusion Time, 10^5 Sec	Lattice Diffusion Coefficient, Sq Cm per Sec
650	10.52	10	51.9	5.96×10^{-14}
750	9.77	25	14.9	1.28×10^{-12}
800	9.38	28	4.68	5.1×10^{-13}
825	9.11	108	30.2	1.17×10^{-11}
915	8.42	200	9.73	1.25×10^{-10}

constant. From this equation it can be seen that, if penetration measurements are made to some fixed value of concentration c, the argument of *erf* c must always be a constant. For a given temperature, D_l is a constant and therefore the depth of the lattice penetration at some fixed concentration will be proportional to the square root of the diffusion time.

For penetration along a high diffusivity grain boundary, Fisher's mathematical treatment can be used, but the assumptions and approximations involved should be noted. Fisher's equation is

$$c = c_0 \exp - [(4D_l/\pi t)^{0.5} Z_b/(\delta D_b)^{0.5}]\ erf\ c\ [X/2(D_l t)^{0.5}] \quad [2]$$

where Z_b is the depth of penetration along the grain boundary and X is the lateral distance from the grain boundary of width δ. The value of δ is arbitrary and assumed to be temperature independent. D_b is the grain boundary diffusion coefficient. The concentration of the diffusing material in the grain boundary is the same expression with the *erf* c term omitted as follows

$$c = c_0 \exp [-(4D_l/\pi t)^{0.5} Z_b/(\delta D_b)^{0.5}]. \quad [3]$$

The main assumption involved in this expression is that a quasi-steady state is approached in the grain boundary region. For any given temperature, D_l and D_b will be constant. From Eq. 3 it follows that the depth of boundary penetration at some fixed concentration will vary as the one-fourth power of time if Fisher's treatment is valid.

Data for examining the time dependence of the depth of diffusion for both lattice and boundary are to be found in the results obtained on the 750°C diffusion specimens. The depths of penetration into the lattice and along grain boundaries for several boundary angles are shown plotted against the one-half power of the diffusion time in Fig. 10 and the one-fourth power of the diffusion time in Fig. 11. It can be seen that the penetration data for lattice diffusion and for a small angle boundary ($\theta = 15°$) fit the one-half power relation very well, while the penetration data for the larger angle boundaries ($\theta = 39°$ and $50°$) appear to fit the one-fourth power relation more closely, especially for the shorter diffusion times. It would seem that Fisher's treatment of grain boundary diffusion is satisfactory for the large angle boundaries and relatively short diffusion times but not for small angle boundaries. The better agreement is to be expected at the large angle boundaries, since Fisher assumed that the grain boundary diffusion rate was very much greater than the lattice diffusion rate and this assumption is more

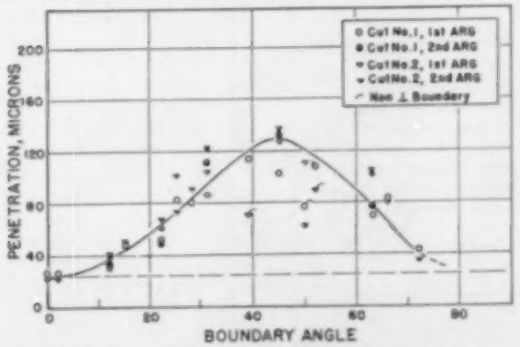

Fig. 8—Nickel penetration is given as a function of grain boundary angle. Samples were diffused for 41.3 hr at 750°C.

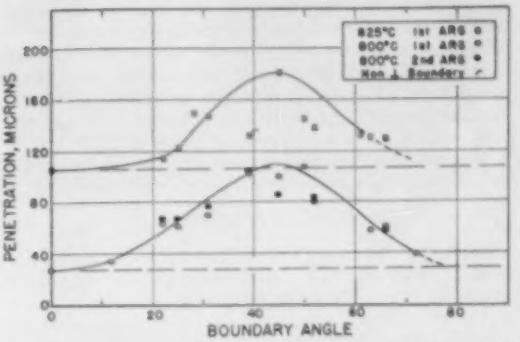

Fig. 9—Nickel penetration is given as a function of grain boundary angle. Samples were diffused for 13 hr at 800°C and 84 hr at 825°C.

valid as the degree of misfit in the boundary increases.

The observed proportionality of the depth of lattice diffusion to the square root of diffusion time does not necessarily validate the assumption of a diffusion coefficient being independent of concentration, as implied in the Eq. 1.

In regard to lattice diffusion, it can be seen from Eq. 1 that the lattice diffusion coefficient can be calculated if the diffusion time and depth, at which the concentration ratio c/c_0 exists, are known. It will be assumed that the interface concentration of the nickel remains essentially constant at 100 pct in all of the specimens at the various diffusion temperatures. This assumption is probably more valid at the

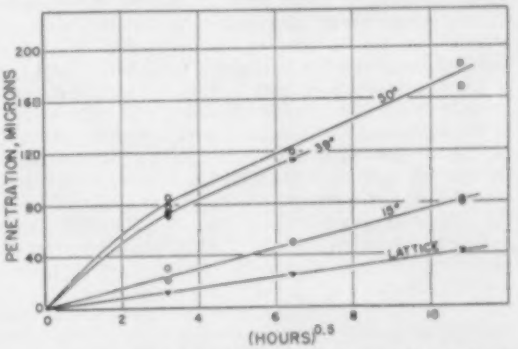

Fig. 10—Penetration of nickel along copper bicrystal boundaries of several boundary angles is given as a function of the one-half power of the diffusion time at 750°C.

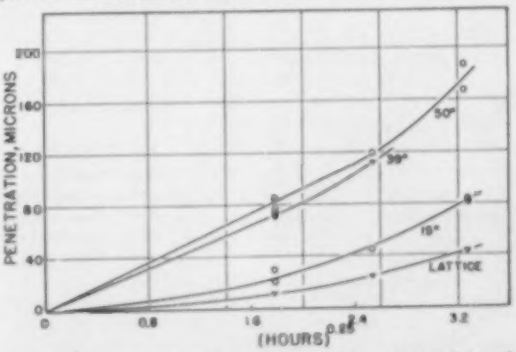

Fig. 11—Penetration of nickel along copper bicrystal boundaries of several boundary angles is given as a function of the one-fourth power of the diffusion time at 750°C.

lower temperatures than at the higher temperatures. Since the sensitivity experiments had established that the concentration of nickel at the autoradiographically determined penetration end point is 0.005 wt pct, the ratio of c/c_s is then 0.00005 and the lattice diffusion coefficients can be calculated. The results are summarized in Table II.

The diffusion coefficients are usually related to the diffusion temperature by the Arrhenius equation

$$\text{Log } D = \text{Log } A - Q/2.303RT. \qquad [5]$$

The plot of the data fitted to this equation is given in Fig. 12. From this, the activation energy for lattice diffusion is calculated as 64.8 kcal per g mol. This is a higher value than those previously reported for this system but the present investigation was carried out at lower temperatures and over a more extensive range of temperatures than any used previously. Table III lists comparative data from other investigators.

Table III. Comparison of Lattice Diffusion Coefficients for the Diffusion of Nickel into Copper Obtained by Various Investigators

Investigator	Diffusion Coefficient at 915°C, Sq Cm per Sec	Activation Energy, Kcal per G Mol
Present work	1.25×10^{-10}	64.8
Thomas and Birchenall,[7] 0 pct Ni	1.7×10^{-10}	54.0
da Silva and Mehl,[8] 5 pct Ni	1.5×10^{-10}	42.0
Grube and Jedele,[9] extrapolated to 0 pct Ni	2.3×10^{-10}	34.4

Since the ratio c/c_s is known and the lattice diffusion coefficients have been calculated, the results of the penetration measurements on the various boundaries can be used to calculate δD_b. By arbitrarily assuming that the grain boundary width, δ, is 5A, the grain boundary diffusion coefficients can be calculated. The results of these calculations are given in Table IV. In making these calculations, the values for the depth of penetration were taken from the curves of Figs. 7 through 10. The value for the lattice diffusion constant at 650°C was adjusted to fit the linear relationship of Fig. 12. The difference between this value and the actual value determined experimentally is within the range of the experimental error.

The ratios of the grain boundary diffusion coefficient to the lattice diffusion coefficient for the various boundaries are given in Table IV. It will be noted that they are of the order of 10^4 to 10^6 and are a function of the grain boundary angle. Fig. 13 is a plot of grain boundary diffusion coefficient as a function of the grain boundary angle. A log plot has been used to show more clearly the low angle boundary data.

The fact that Fisher's expression for grain boundary diffusion did not appear to be entirely valid for the low angle boundaries explains the anomalous behavior of the 825°C data of Fig. 13. For this same reason, the grain boundary coefficients for boundaries less than 20° cannot be considered reliable, particularly at the higher diffusion temperatures.

Whipple[5] considered the mathematics of grain

Table IV. Summary of Calculations of the Grain Boundary Diffusion Coefficients of Nickel in Copper Analyzed According to Fisher's Equation

Misfit Angle, Degrees	Penetration, 10^{-4} Cm	δD_b, 10^{-17} Cm Cm per Sec	Boundary Diffusion Coefficient, D_b, 10^{-10} Sq Cm per Sec	$\left(\frac{D_b}{D_l}\right)\times10^4$
	Diffusion Temperature, 650°C (1200°F)*			
10	22	1.59	3.17	0.76
20	60	11.78	23.6	5.62
30	100	36.1	72.3	17.2
40	145	68.6	137	32.6
45	154	77.4	155	36.8
50	147	70.7	141	33.6
60	115	43.3	86.6	20.8
70	78	19.9	39.8	9.1
	Diffusion Temperature, 750°C (1380°F)†			
10	35	4.16	0.83	0.65
20	87	11.04	2.21	1.73
30	90	27.4	5.48	4.28
40	121	49.7	9.94	7.75
45	130	57.1	11.4	8.9
50	120	48.8	9.75	7.62
60	90	27.4	5.48	4.28
70	46	7.8	1.56	1.22
	Diffusion Temperature, 800°C (1470°F)‡			
10	32	1.23	2.45	0.48
20	53	3.37	6.75	1.32
30	80	7.67	15.3	3.01
40	104	13.0	26	5.1
45	110	14.5	29	5.68
50	104	13	26	5.1
60	74	6.56	13.1	2.55
70	44	2.13	4.27	0.84
	Diffusion Temperature, 825°C (1517°F)§			
10	108	8.35	1.67	1.43
20	114	9.27	1.86	1.58
30	144	14.8	2.97	2.54
40	154	22.1	4.43	3.78
45	180	23.1	4.62	3.95
50	172	21.2	4.24	3.62
60	133	12.5	2.49	2.13
70	113	9.11	1.83	1.56

* For diffusion temperature of 650°C, $c/c_0 = 0.00005$, $D_l = 4.2\times10^{-14}$ sq cm per sec, and $t = 51.9\times10^4$ sec.
† For diffusion temperature of 750°C, $c/c_0 = 0.00005$, $D_l = 1.28\times10^{-12}$ sq cm per sec, and $t = 14.9\times10^4$ sec.
‡ For diffusion temperature of 800°C, $c/c_0 = 0.00005$, $D_l = 5.1\times10^{-12}$ sq cm per sec, and $t = 4.68\times10^4$ sec.
§ For diffusion temperature of 825°C, $c/c_0 = 0.00005$, $D_l = 1.17\times10^{-11}$ sq cm per sec, and $t = 30.2\times10^4$ sec.

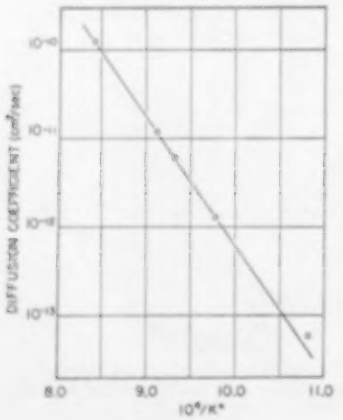

Fig. 12—Lattice diffusion coefficients of nickel in copper are given as a function of the reciprocal absolute temperature.

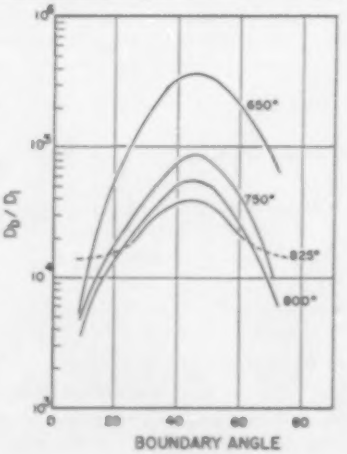

Fig. 13—Curves illustrate the influence of grain boundary angle on the ratio of grain boundary diffusion coefficient to lattice diffusion coefficient at various temperatures.

boundary diffusion and gives an equation that is an exact expression derived without the simplifying assumptions made by Fisher. A simplified form of this expression is given as follows

$$c/c_o = 1.159\,\beta^{4/5}\,\eta^{-6/5}\exp[-0.476\,\beta^{-4/5}\,\eta^{4/5} + 0.398\,\beta^{-4/5}\,\eta^{8/5}\,(1-\beta\,\xi) + \cdots] \qquad [6]$$

where

$$\eta = \frac{Z}{(D_1 t)}\,0.5$$

$$\xi = \frac{X}{(D_1 t)}\,0.5$$

$$\Delta = \frac{D_b}{D_1}$$

$$\beta = \left[\frac{\delta}{2(D_1 t)}\,0.5\right](\Delta - 1)\cdot$$

This may be used if $1 << \eta << \Delta^5/\beta$ and ξ is small. Calculations were made using Eq. 6 and the values obtained were in approximate agreement with Fisher's equation. Whipple's values are larger by a factor of 2 to 5 with the largest difference occurring at the low misfit boundaries. Table V lists the ratio of the coefficients calculated by the two equations and it shows that the ratio is fairly constant for the high angle boundaries. It is difficult to decide which of the two equations is the more correct in view of the fact that no exact estimate of the width of a grain boundary can be made at the present time. Since there is little basis for selecting one in preference to the other, the results calculated by Fisher's equation will be considered for further discussion.

It should be noted that the failure to detect grain boundary diffusion at 915°C does not necessarily mean that the boundary diffusion coefficient is equal to the lattice diffusion coefficient. For example, if under the conditions used at 915°C the boundary penetration is 1 μ more than the lattice penetration, then the ratio of the two coefficients, using either Fisher's or Whipple's equation, will be of the order of 10^4, although it is doubtful if either of the two equations apply. Such small differences in the depth of penetration are beyond the limit of resolution of the techniques used in this investigation. This means then that very refined measurements and a more exact mathematical analysis will be required to evaluate accurately the amount of grain boundary diffusion that occurs at high temperatures as well as penetration that occurs in low angle boundaries at all temperatures.

The temperature dependence of the grain boundary diffusion coefficients can be correlated by the Arrhenius equation similar to that used for lattice diffusion. Fig. 14 shows the logarithms of the diffusion coefficients for the various boundaries plotted against the reciprocal absolute temperature. The correlation is good for the large angle boundaries over the entire temperature range but the low angle boundaries show deviations at the higher temperatures. This deviation is probably due to the inadequacy of the mathematical analysis, as discussed previously.

From the slopes of Fig. 14, the activation energy for grain boundary diffusion can be calculated as a function of the grain boundary angle. These are shown graphically in Fig. 15. Although the results are not conclusive, it appears that the activation energy is markedly dependent on the grain boundary angle at low angles and less so at higher angles. A rapid decrease occurs up to $\theta = 20°$ with no further change occurring for larger values of θ. The dependence of the activation energy on θ resembles closely the dependence of the interfacial energy of a grain boundary on θ which increases to $\theta = 25°$, then remains fairly constant. Such an interrelationship is reasonable, since both energies are a measure of the binding forces between atoms in the grain boundary region of a metal.

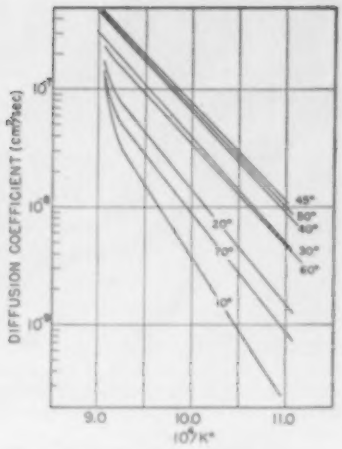

Fig. 14—Grain boundary diffusion coefficients are given as a function of the reciprocal absolute temperature.

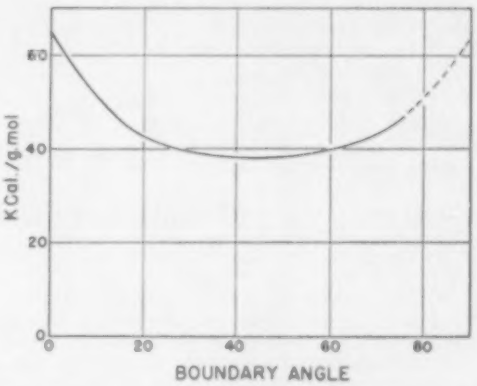

Fig. 15—Activation energy for grain boundary diffusion of nickel into copper is given as a function of grain boundary angle.

Conclusions

The extent of nickel penetration along the grain boundaries of copper is dependent upon the degree of crystallographic misfit between the grains forming the boundary, with the maximum penetration occurring at the point of maximum misfit.

The ratio of grain boundary diffusion coefficients to lattice diffusion coefficients at low concentrations of nickel is of the order of 10^4 to 10^5 for the tempera-

Table V. Comparison of Grain Boundary Diffusion Coefficients for the Diffusion of Nickel in Copper Calculated by Whipple and Fisher's Equations

Temperature, °C	Ratio of D_b (Whipple) to D_b (Fisher) for the Indicated Values of θ							
	10°	20°	30°	40°	45°	50°	60°	70°
650	2.04	2.21	2.33	2.25	2.19	1.68	2.18	2.27
750	2.36	2.13	2.48	2.24	2.24	2.24	2.48	2.58
800	2.98	2.22	2.89	2.53	2.53	2.53	2.98	4.08
825	3.96	3.56	3.75	3.49	3.47	3.43	4.07	3.96

ture range of 650° to 825°C and for grain boundary angles of from 10° to 70°.

The activation energy for grain boundary diffusion of nickel into copper decreases with increasing boundary angle and varies from 64.8 kcal per g mol for 0° misfit (pure lattice diffusion) to 38.5 kcal per g mol at maximum misfit.

The available mathematical solutions for the calculation of grain boundary coefficients are satisfactory for high angle boundaries but are only approximations for low angle boundaries.

Acknowledgments

The authors acknowledge the support of this investigation by the General Electric Co. through a Gerard Swope Fellowship, the U. S. Army Ordnance Corps for support through a project on the Application of Autoradiography to Metallurgical Problems, and the Michigan Memorial Phoenix Project for laboratory and technical assistance in working with radioactive materials.

Discussion of this paper, if any, will appear in JOURNAL OF METALS, May 1956, and in AIME Metals Branch *Transactions*, Vol. **206**, 1956.

References

[1] A. D. Le Claire: Diffusion in Metals. *Progress in Metal Physics*. (1953) **IV**. New York. Interscience Publishers Inc.

[2] R. Flanagan and R. Smoluchowski: Grain Boundary Diffusion of Zinc in Copper. *Journal of Applied Physics* (1952) **23**, p. 245.

[3] D. Turnbull and R. E. Hoffman: The Effect of Relative Crystal and Boundary Orientations on Grain Boundary Diffusion Rates. *Acta Metallurgica* (1954) **2**, pp. 184-187.

[4] J. C. Fisher: Calculation of Diffusion Penetration Curves for Surface and Grain Boundary Diffusion. *Journal of Applied Physics* (1951) **22**, pp. 74-77.

[5] R. T. P. Whipple: Calculation of the Shape of the Concentration Contour in Grain Boundary Diffusion. *Report No. AERE-T/R-1026* Atomic Energy Research Establishment, Harwell, England (1952).

[6] G. C. Towe: Wet Process Autoradiography Applied to Metallurgical Studies. Ph.D. Thesis, University of Michigan (1953).

[7] D. E. Thomas and C. E. Birchenall: Concentration Dependence of Diffusion Coefficients in Metallic Solid Solutions. *Trans.* AIME (1952) **194**, pp. 867-873; JOURNAL OF METALS (August 1952).

[8] L. C. C. da Silva and R. F. Mehl: Interface and Marker Movements in Diffusion in Solid Solutions of Metals. *Trans.* AIME (1951) **191**, pp. 155-173.

[9] G. Grube and A. Jedele: Diffusion of Metals in the Solid State. *Ztsch. für Elektrochemie* (1932) **38**, pp. 799-807.

Technical Note

Bainite Reaction in a Plain Carbon Steel

by H. I. Aaronson and C. Wells

THIS is a preliminary report on a detailed metallographic investigation of the bainite reaction in a plain carbon hypoeutectoid steel. In view of the current interest in the bainite reaction and of the controversies which still exist about even the basic phenomenology of this mode of transformation, it was considered desirable to present a summary of the more important results obtained to date prior to the completion of this investigation.

The steel used contained 0.29 pct C, 0.76 pct Mn, 0.25 pct Si, 0.005 pct P, and 0.007 pct S. The alloy was homogenized for 48 hr at 1250°C. Individual specimens were then austenitized for 30 min at 1300°C and isothermally transformed for various times at temperatures above and within the bainite region, ranging from 775° through 500°C at intervals of 25°C. These specimens were carefully examined on a research metallograph; a few specimens of especial interest were also studied electron microscopically.[1]

Bainite may be defined as the aggregate structure resulting from the precipitation of carbides from supersaturated ferrite which formed by nucleation and diffusion-limited growth. Two groups of experimental observations made during the present study provide support for this mechanism of the bainite reaction: 1—at 625°C, partial conversion of proeutectoid ferrite to bainite began after more than 99 pct of the austenite had decomposed and 2—the precipitation of bainitic carbides occurred only within the ferrite phase.

The proeutectoid ferrite and the bainite reactions in the steel studied were found to be morphologically continuous. Following the classification scheme of Mehl and Dube,[2] three principal morphologies of proeutectoid ferrite were identified in the temperature region (625° to 550°C) in which the two reactions blend—grain boundary allotriomorphs,* Widmanstaetten side plates, and intragranular plates. Carbide precipitation converted these morphologies into their bainitic equivalents with increasing isothermal reaction time. Conversion took place more rapidly as the reaction temperature was reduced. The replacement of supersaturated ferrite by bainite, however, did not occur uniformly even within individual austenite grains and was noticeably incomplete at higher transformation temperatures, e.g., 625° to 575°C. The ferritic and bainitic forms of a given morphology thus were frequently found to coexist, often inextricably intermixed, in a given specimen.

* Grain boundary allotriomorphs are crystals which nucleate at and grow preferentially along matrix grain boundaries.

At 625° and 600°C, the conversion of ferrite to bainite was clearly seen to have occurred entirely by the nucleation of carbides at ferrite/ferrite boundaries, as shown in Fig. 1. The nature of the loci at which carbides formed at lower temperatures was often difficult to ascertain with a light microscope, although the alignment in rows of many of the carbides, illustrated in Fig. 2, suggested that nucleation had again occurred at grain boundaries or subboundaries within the ferrite. Application of the electron microscope confirmed this deduction for bainitic structures formed at these temperatures, as shown in Fig. 3. The dense black appearance of bainite formed at very low reaction temperatures in higher carbon steels[3] indicates, however, that isolated lattice defects within ferrite crystals prob-

H. I. AARONSON, Junior Member AIME, and C. WELLS, Member AIME, are Research Metallurgist and Principal Research Metallurgist, respectively, Metals Research Laboratory, Carnegie Institute of Technology, Pittsburgh.

TN 285E. Manuscript, Apr. 11, 1955.

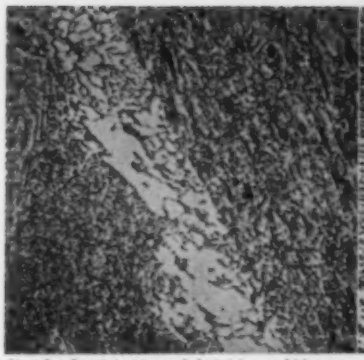

Fig. 1—Precipitation of bainitic carbides at ferrite/ferrite boundaries within impinged grain boundary allotriomorphs. Background is partially spheroidized pearlite. Reacted for 3½ hr at 625°C. Specimen etched in 2 pct nital. X1000. Area reduced approx. 25 pct for reproduction.

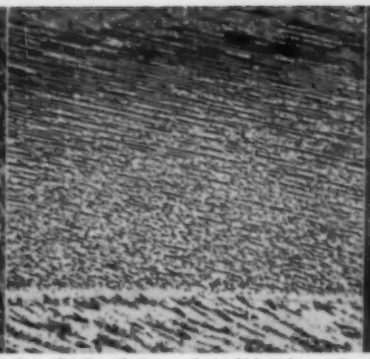

Fig. 2—Distribution of carbides in grain boundary allotriomorphs and in Widmanstaetten side plates. Reacted for 4 sec at 525°C. Specimen etched in 2 pct nital. X1000. Area reduced approx. 25 pct for reproduction.

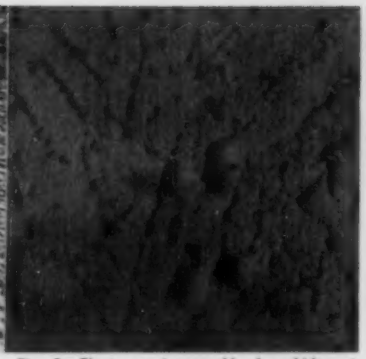

Fig. 3—Electron micrograph[1] of carbides at ferrite/ferrite boundaries. (The four large "humps" near the center of the field are ferrite; an effect of orientation upon etching rates is presumably responsible for the unusual appearance of these crystals.) Reacted 7 sec at 550°C. Polystyrene-silica replication, chromium shadowing used. Specimen etched in 2 pct nital. X4250, enlarged to X8500. Area reduced approx. 25 pct for reproduction.

ably become important nucleation sites for carbides under such circumstances. Carbide precipitation at austenite/ferrite boundaries was not observed in any specimen studied so far, in disagreement with the results of Hultgren.[4, 5]

Utilizing the data of C. S. Smith,[6] the observation that carbides nucleate only at ferrite/ferrite boundaries may be explained by the decrease (approximately 7 pct) in the specific interfacial energy of the nucleus/nucleation site interface which accompanies carbide precipitation at these boundaries as compared with the large increase (approximately 31 pct) in the specific energy of this interface which would result if carbides were to nucleate at austenite/ferrite boundaries. Current nucleation theory considers that rates of nucleation are very markedly dependent upon the interfacial energy of the nucleus. The energy relationships described accordingly require effectively zero rates of carbide nucleation at austenite/ferrite interfaces, as is experimentally observed.

The morphology, growth rates, and relative distribution of ferrite crystals, as well as the availability of nucleation sites within and between these crystals, have been found to affect rates of conversion to bainite. Rows of grain boundary allotriomorphs normally contained the lowest densities of carbides, while groups of Widmanstaetten side plates generally exhibited the highest carbide densities. Fig. 2 shows a typical example of the unequal levels of carbide precipitation in these morphologies. Carbides formed in intermediate numbers within intragranular plates at early stages of reaction. As transformation of the austenite approached completion, however, extensive carbide precipitation occurred at the boundaries between impinging intragranular plates at temperatures as high as 575°C.

It has been reported that the pearlite and bainite reactions overlap in time over appreciable ranges of temperature in several plain carbon and alloy steels.[7, 8] The two reactions were also found to occur simultaneously in the steel used in this investigation. It was observed, however, that the pearlite reaction participated significantly in the final stages of transformation only when the average density of carbides within the ferrite formed earlier was small, e.g., at 600°C and, to a lesser extent, at 575°C. When extensive precipitation of bainitic carbides occurred, as at 550°C and below, the pearlite reaction was essentially confined to the earlier stages of transformation. Decomposition of the austenite at these lower temperatures was entirely completed by the bainite reaction to within the limits of detection of the metallographic method. No period of stasis in the formation of bainite was observed at any reaction temperature studied, in marked contrast to the behavior of the bainite reaction in many alloy steels.[8, 9]

Britton and coworkers[10] have made a brief study of the bainite reaction in an 0.66 pct C, 0.85 pct Mn steel and have found the basic conclusions discussed previously to be applicable to this alloy.

Acknowledgments

The investigation was initially supported by the Aeronautical Research Laboratory of the Wright Air Development Center. It is being continued under the sponsorship of the Office of Naval Research. Reproduction in whole or in part is permitted for the purposes of the U. S. Government.

References

[1] Electron micrographs were made by Mrs. A. Revere, Consulting Electronmicroscopist, Washington, D. C., in support of this investigation.

[2] R. F. Mehl and C. A. Dube: *Phase Transformation in Solids.* (1951) p. 545. New York. John Wiley and Sons.

[3] A. B. Greninger and A. R. Troiano: *Trans.* ASM (1940) **28**, p. 537.

[4] A. Hultgren: *Trans.* ASM (1947) **39**, p. 915.

[5] A. Hultgren et al.: *Jernkontorets Annaler* (1951) **135**, p. 403.

[6] C. S. Smith: *Trans.* AIME (1948) **175**, p. 15; METALS TECHNOLOGY (June 1948).

[7] E. S. Davenport and E. C. Bain: *Trans.* AIME (1930) **90**, p. 117.

[8] E. P. Klier and T. Lyman: *Trans.* AIME (1944) **158**, p. 394; METALS TECHNOLOGY (June 1944).

[9] T. Lyman and A. R. Troiano: *Trans.* ASM (1946) **37**, p. 402.

[10] W. H. Britton, G. M. Pound, and H. I. Aaronson: Unpublished research, Metals Research Laboratory, Carnegie Institute of Technology (1955).

Diffusion of Zinc and Copper in Alpha and Beta Brasses

by R. Resnick and R. W. Balluffi

NUMEROUS investigations of chemical diffusion in α brass have been made and the results are collected in several places.[1-4] This work has been mainly concerned with the determination of the chemical diffusivity as a function of composition and temperature. In 1947 Smigelskas and Kirkendall[5] showed that zinc and copper diffuse at different rates in face-centered-cubic brass, and since then, a number of efforts have been made to determine the intrinsic diffusivities of zinc and copper in this alloy.[1, 6-9] Horne and Mehl[9] in particular have recently determined the intrinsic diffusivities as functions of temperature and composition using sandwich-type couples and inert markers. Inman et al.[8] also have determined the intrinsic diffusivities in homogeneous alloys using tracer techniques. When the present work was started, no information of this type was available. Consequently, measurements of the intrinsic diffusivities were made as a function of temperature at a constant composition of 28 atomic pct Zn with vapor-solid diffusion couples where the zinc was diffused into the diffusion couple from the vapor phase. The application of these couples to the study of diffusion in α brass has been described previously.[6, 7] The temperature dependence of the intrinsic diffusivities was found to follow the relation $D_i = A_i \exp(-H_i/RT)$ and the values of H_{Zn} and H_{Cu} were found to be closely the same. It is emphasized, however, that the chemical diffusivity ($D = N_1D_2 + N_2D_1$) is a composite diffusivity and does not necessarily follow this exponential form. It is usually found to do so within experimental error for substitutional alloys because the heats of activation of the intrinsic diffusivities generally are not greatly different.[10]

Also, at the onset of this work, there was no information available concerning possible unequal diffusion rates of individual components and the existence of a Kirkendall effect in alloys with other than face-centered-cubic structures. Since then, two reports indicating a Kirkendall effect in body-centered-cubic β brass have appeared. Landergren and Mehl[11] have published a note describing Kirkendall diffusion experiments with sandwich-type couples. Inman et al.[8] also find a Kirkendall effect in this alloy using the tracer technique.

In the present work, several aspects of the Kirkendall effect in β brass were further investigated using vapor-solid couples. Two different couples were used, one in which the zinc was diffused into the specimen from the vapor phase and the other in which the zinc was diffused out of the specimen into the vapor phase. Briefly, the existence of a Kirkendall effect is confirmed and it is found that $D_{Zn}/D_{Cu} \cong 3$ at about the 46 atomic pct composition in this alloy at 600°, 700°, and 800°C. As a result of the unequal diffusion rates of zinc and copper, volume changes occur and subgrain formation is observed in the diffusion zone. In addition, significant porosity is produced by the precipitation of supersaturated vacancies. Diffusion in this alloy is therefore outwardly similar to diffusion in α brass where these effects are also observed.

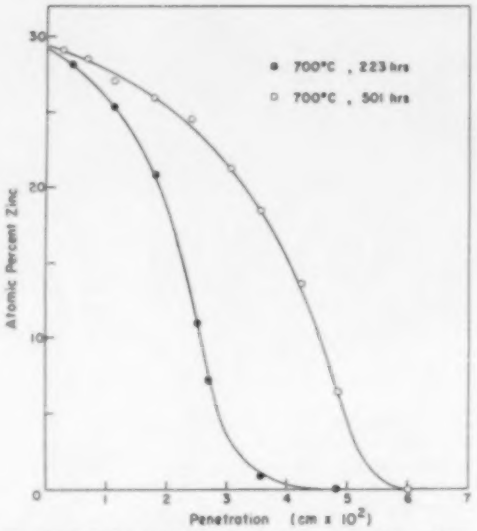

Fig. 1—Diffusion-penetration curves are given for α brass vapor-solid couples at 700°C.

α Brass

Experimental Methods—The use of vapor-solid couples in studying diffusion in α brass has been described in previous articles.[6, 7] The method briefly consists of sealing a copper specimen with Kirkendall markers initially placed on its surface in an evacuated quartz capsule along with a large zinc source of fine α brass chips and then diffusing the zinc into the specimen through the vapor phase. The zinc concentration at the specimen surface rises rapidly enough to a value near that of the α brass source so that the surface concentration may be regarded as constant during diffusion. Under these boundary conditions, values of the chemical diffusivity may be obtained by applying the Boltzmann-Matano analysis to the concentration penetration curve, and the intrinsic diffusivities may be obtained from Darken's[5] equations when the velocity of marker movement is known.

The diffusion specimens were made from OFHC copper in the form of disks 3.2 cm diam and 0.5 cm thick with faces surface-ground parallel to within ±0.001 cm. Markers in the form of fine alumina particles <0.0002 cm diam were placed on the specimen surface. These specimens were then sealed in quartz capsules along with enough α brass chips of a 30.0 atomic pct Zn composition to keep the source concentration from decreasing by more than 0.3 atomic pct Zn as a result of the loss of zinc to the specimen during diffusion. The quartz capsules which were initially evacuated to a pressure of

R. RESNICK, Junior Member AIME, is associated with Atomic Energy Div., Sylvania Electric Products Inc., Bayside, N. Y., and R. W. BALLUFFI, Junior Member AIME, formerly associated with Sylvania Electric Products Inc., is Assistant Professor, Dept. of Mining and Metallurgy, University of Illinois, Urbana, Ill.

Discussion of this paper, TP 4059E, may be sent, 2 copies, to AIME by Nov. 1, 1955. Manuscript, July 1, 1954. Chicago Meeting, February 1955.

Table I. Compilation of Intrinsic Diffusivity Data for α Brass

Reference	Temperature, °C	Time, Hr	Marker Composition, Atomic Pct Zn	Marker Movement, Cm x10⁸	D_{Zn}/D_{Cu}	Intrinsic Diffusivities at 28 Atomic Pct Calculated from Diffusivity Ratios and D Values from Fig. 3	
						D_{Cu}, Sq Cm per Sec x10⁸	D_{Zn}, Sq Cm per Sec x10⁸
Present work	700	223	29.1	4.5	5.7	0.19	1.1
Present work	700	501	29.3	8.0	5.9	0.22	1.3
Present work	800	39.5	28.6	6.5	5.0	1.4	7.0
6	850	68.	27.0	9.	5.2	3.8	20.
Present Work	860	23.5	28.3	6.4	5.3	4.3	23.
6	890	150.	27.0	15.	5.8	9.7	56.
6	890	187	27.0	16.	5.7	9.3	53.
6	890	39.3	28.0	12.0	5.3	9.8	52.
Present work	910	2.0	28.1	3.6	4.7	9.1	43.

about 0.1μ Hg were then uniformly heated for various times at 700°, 800°, 860°, and 910°C.

After diffusion, the buried markers were found by polishing into one side of the disk until all edge effects were removed and the depth of burying below the surface was measured. Concentration-penetration curves were then obtained by chemical analysis of parallel slices machined from the diffusion zone. The slices were analyzed for copper content by the electrolytic method and the zinc concentration was obtained by difference.

Results—A summary of the diffusion runs that were made is given in Table I. Two typical diffusion curves at 700°C are shown in Fig. 1. The Kirkendall marker data are given in Table I along with the ratio of the intrinsic diffusivities calculated from the ratio of the amounts of zinc and copper diffused past the markers. Corresponding data at 850° and 890°C from previously published work[6, 7] are also included. Values of the chemical diffusivity as a function of concentration were next obtained from the diffusion curves by applying the Boltzmann-Matano analysis and are shown in Fig. 2. Included in this figure are values at 890°C which were taken from previous work.[7] Values of log D vs $1/T$ are plotted in the conventional manner in Fig. 3 for different concentration levels. The intrinsic diffusivities of copper and zinc were then calculated for different temperatures at the average marker concentration of 28 atomic pct Zn from values of the chemical diffusivity ($D = N_{Zn} D_{Cu} + N_{Cu} D_{Zn}$) at this concentration and the ratios of the diffusivities. These results are given in Table I and are plotted vs $1/T$ in Fig. 4. Assigning the observed diffusivity ratios in Table I to the average marker composition of 28 atomic pct in this manner is permissible, since the ratios are insensitive to small variations of zinc concentration within the accuracy of the present experiments. All the diffusivities appear to vary with temperature according to the usual form

$$D = A \cdot \exp\left(\frac{-H}{RT}\right) \qquad [1]$$

for the chemical diffusivity, or

$$D_i = A_i \cdot \exp\left(\frac{-H_i}{RT}\right) \qquad [2]$$

for the intrinsic diffusivity, and values of the constants in Eqs. 1 and 2 are presented in Table II.

Discussion—The present data are compared with values from refs. 8 and 9 in Figs. 3 and 4. Inman et al. determined the diffusivities of zinc and copper in homogeneous alloys using a tracer technique. These data have been converted to chemical diffusivities for present purposes by using Darken's equations[8] $D_i = D_i^* \left(1 + N_i \frac{d \ln \gamma_i}{d N_i}\right)$ and $D = N_1 D_2 + N_2 D_1$. The activity coefficients used were obtained from ref. 12. At the low zinc concentrations, the agreement between the present diffusivities and the values of Horne and Mehl is excellent (Fig. 3). Inman et al. determined D values at a zinc concentration <1 pct Zn and these values are approximately 50 pct smaller than the corresponding values of the present work and of Horne and Mehl. At the higher zinc contents, the present values are consistently somewhat lower than those obtained by Horne and Mehl. However, they are in rather good agreement with the values of Inman et al. Some loss of accuracy may be expected at the extremes of the composition range where the precision of the Boltzmann-Matano analysis is lower because of difficulty in determining the exact slope of the diffusion curve. In order to minimize errors in the analysis at these concentrations, a number of D determinations were made and the best smooth curve was drawn through the resulting points as seen in Fig. 2. This smoothing process was used in reanalyzing the earlier data at 890°C[7] and accounts for the approximately 25 pct difference between the presently reported intrinsic diffusivities at this temperature and the previously published values.[7]

In general, the agreement between all of these data is considerably better than the agreement among the earlier data (see, for example, ref. 2). The intrinsic diffusivity data in Fig. 4 compare in the same manner. The present values (at 28 pct Zn) and those of Inman et al. (at 27 pct Zn) seem in quite good agreement. The values of Horne and Mehl (at 25.2 pct Zn) are found to be higher when the increase of diffusivity with concentration is taken into account.

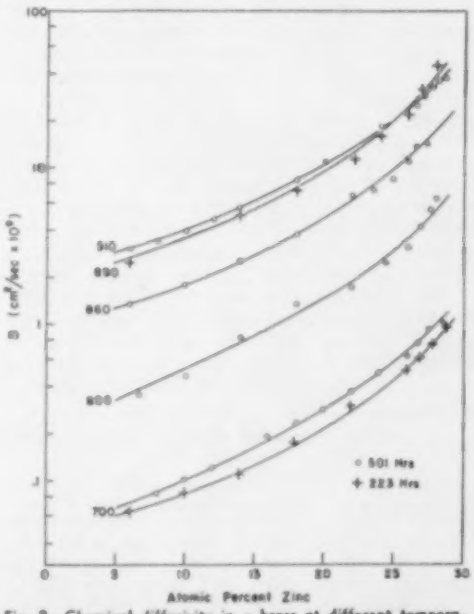

Fig. 2—Chemical diffusivity in α brass at different temperatures (°C) is shown as a function of composition. Data for the 890°C line are taken from ref. 7.

uniformly heated for various times at 600°, 700°,

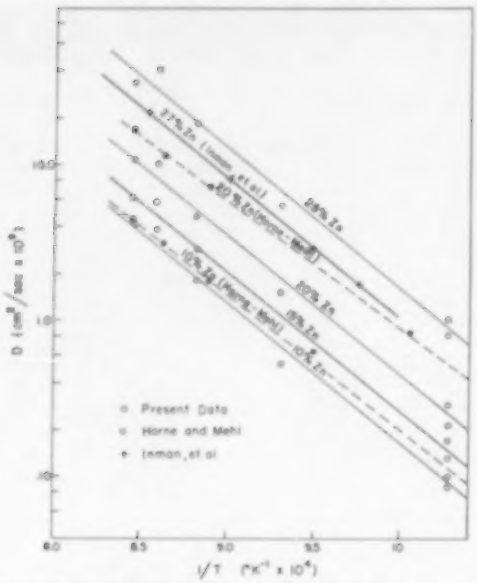

Fig. 3—Log of chemical diffusivity vs $1/T(°K)$ for α brass at different composition levels (atomic pct Zn) is shown.

Eq. 2 should apply, since D_i defines the rate of diffusion of a single component relative to the diffusing crystal and so may be described by a single atomic jump process. In contrast to the intrinsic diffusivity, the chemical diffusivity is a composite diffusivity which depends upon the intrinsic diffusion rates of both components and is given by

$$D = N_1 D_2 + N_2 D_1 = N_1 A_2 \cdot \exp\left(\frac{-H_2}{RT}\right) + N_2 A_1 \cdot \exp\left(\frac{-H_1}{RT}\right). \quad [3]$$

As LeClaire[7] has noted, this expression cannot be represented exactly by the commonly used form, Eq. 1. However, the relation Eq. 1 has been found to hold in nearly all diffusion experiments within experimental error and seems adequate for the present data (see Fig. 3). Examination of Eq. 3 indicates that Eq. 1 will hold within usual experimental error when the D_i's are of comparable magnitude if the H_i's are not too different. In the case of substitutional alloys if a simple vacancy mechanism is accepted, the heat of activation is the sum of two parts: the heat of activation to form a vacancy and the heat of activation for the vacancy-atom exchange. The heat of activation for the formation of a vacancy is estimated to be in the neighborhood of one-half the average value of H_1 and H_2 and will appear in both H_1 and H_2. Since it is also likely that the heats of activation for the movement of the two components are of the same order, H_1 and H_2 should not be expected to be greatly different. The present values for H_{Zn} and H_{Cu} which are tabulated in Table II correspond to this case.

The actual values of the constants for Eqs. 1 and 2 cannot be regarded as highly significant. The values were obtained from data extending over a relatively narrow temperature range and Nowick[16] has thoroughly discussed the problem of determining the true values of these quantities under such conditions. It is apparent however that H_{Zn} and H_{Cu} must be closely the same, since the ratio of diffusivities (see Table I) which is given by

$$\frac{D_{Zn}}{D_{Cu}} = \left(\frac{A_{Zn}}{A_{Cu}}\right) \exp\left[-(H_{Zn} - H_{Cu})\right] \quad [4]$$

shows very little systematic variation with temperature.

Nevertheless, the present heats of activation are in the neighborhood of 40,000 cal per mol which is in good agreement with the values obtained by Inman et al. at the 27 pct Zn concentration. The value of 51,000 cal per mol obtained by Inman et al. from only two determinations at the <1 pct Zn composition seems too high, since the value of H for the self-diffusion coefficient of copper is $\simeq$ 47,000 cal per mol.[16] The present data are not accurate enough to show any continuous decrease of H with increasing zinc that might be expected to partially account for the observed increase of D with zinc content. The decrease in H to a value of 30,000 cal per mol which is found by Horne and Mehl at the 30 atomic pct composition, however, seems too rapid when compared to the other results. Hino[18] in some preliminary unpublished work reports an activation energy of about 40,500 cal per mol for the diffusion of radioactive zinc in homogeneous α brass containing about 30 atomic pct Zn. It would seem on the basis of the available measurements, therefore, that the actual value of H most probably decreases with increasing zinc content from a value somewhat below that of the self-diffusion coefficient of copper to a value of approximately 40,000 cal per mol at the α brass composition.

Table II. Frequency Factors and Heats of Activation for Diffusion in α Brass

Composition, Atomic Pct Zn	Frequency Factor, Sq Cm per Sec	Heat of Activation, Cal per Mol
10	$A = 0.13$	$H = 40,800$
15	$A = 0.21$	$H = 40,800$
20	$A = 0.36$	$H = 40,800$
28	$A = 1.7$	$H = 41,300$
28	$A_{Zn} = 2.1$	$H_{Zn} = 41,200$
28	$A_{Cu} = 0.01$	$H_{Cu} = 42,700$

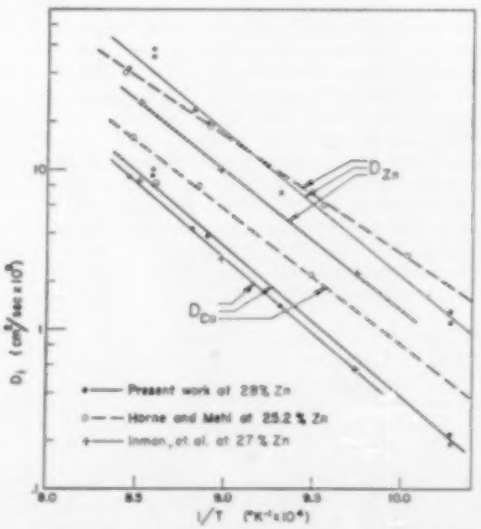

Fig. 4—Log of intrinsic diffusivity has been plotted vs $1/T(°K)$ for α brass at 28 atomic pct Zn.

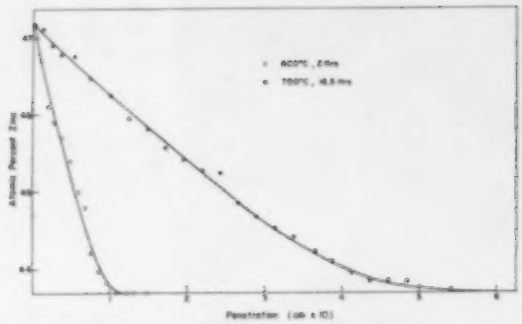

Fig. 5—Diffusion-penetration curves are given for β brass vapor-solid couples at 600° and 700°C.

It is not clear at present whether the differences in the foregoing diffusion data could be due to the different types of diffusion couples used or whether they are due to other causes. In general, it seems that techniques, such as the present one, involving chemical analysis of couples containing comparatively larger concentration differences are not suitable for the most precise determination of diffusion coefficients. Factors such as plastic deformation, nonequilibrium vacancy effects, porosity formation, and dimensional changes may be significant in certain cases. It would be interesting at this point to carry out precision diffusivity determinations, using tracer techniques in incremental couples over a wide range of temperatures.

β Brass

Two types of diffusion couples were used to study the Kirkendall effect in β brass. The first type in which zinc vapor from β brass chips was diffused into a disk specimen of a lower zinc content was similar to the type already described in the α brass experiments. This couple was used to investigate the different diffusion rates of zinc and copper and also the dimensional changes and polygonization which occurred during inward diffusion of zinc. In the second type of couple, the zinc flux was reversed and the zinc was diffused out of the specimen via the vapor phase into fine β brass chips of a lower zinc content. This couple was useful for following porosity formation and accompanying volume changes during the outward diffusion of zinc.

Intrinsic Diffusivities of Zinc and Copper—*Experimental Methods:* The couples used to investigate the intrinsic diffusivities of zinc and copper were made by sealing β brass disks containing 43 atomic pct Zn in quartz capsules along with a larger mass of loosely packed β brass chips of a 48 atomic pct composition. The capsules which were initially evacuated to a pressure of about 0.1μ Hg were then uniformly heated for various times at 600°, 700°, and 800°C. Enough chips were used so that the zinc source composition did not decrease by more than 0.5 atomic pct Zn as a result of the transfer of zinc to the disk specimen during diffusion. The disks were made 3.0 cm diam and 0.75 cm thick and were machined with faces parallel from coarse grained β brass castings which were made by directionally cooling brass melts in sealed and evacuated quartz capsules. After the machining operation, the disks from each casting were again sealed in an evacuated capsule and were homogenized at 825°C for 48 hr. These disks which had a final coarse grain size of about 1 cm were next electroplated with a 0.003 cm thick chromium plate, leaving one face exposed. The chromium plate served to prevent zinc penetration into all surfaces except the one exposed face and so reduced undesirable edge effects. This technique allowed a greater amount of zinc diffusion into the exposed face than would have been possible if all surfaces had been equally exposed and chemical analysis proved that negligible zinc penetrated the chromium layer. The markers were put on the disk surfaces before diffusion in the form of fine alumina particles <0.0002 cm diam.

After the diffusion anneal, the specimens were water quenched in order to prevent any phase transformation upon cooling. A cross-section of each diffusion zone was obtained by polishing into one side of the disk until all edge effects were removed, and the depth of burying of the markers was measured. No porosity was found anywhere in the diffusion zones of these couples. The concentration-penetration curves were obtained by chemical analysis of parallel slices machined from the diffusion zone. Marker movements were then obtained by locating the position of the original interface relative to the final surface by graphical integration and subtracting the measured depth of marker burying.

Results: The displacement of the markers is given in Table III for all runs. The markers were found to move outward with increasing time, thereby proving that zinc diffuses more rapidly than copper and establishing the existence of a Kirkendall effect. It was also immediately apparent from the results of the chemical analyses that the surface concentration did not rapidly increase to a value approaching the concentration of the zinc source during the early stages of the run as was found to be the case in α brass[7] but instead remained appreciably lower at all observed times. Two typical diffusion curves at 600° and 700°C are given in Fig. 5. The final surface composition at the end of each run is given in Table III along with the composition at the marker and the compositions of the source and original disk. The problem of maintaining the surface concentration constant during diffusion and thereby estab-

Table III. Diffusion Data for β Brass Vapor-Solid Diffusion Couples

Temperature, °C	Time, Hr	Composition of Zinc Source, Atomic Pct Zn	Base Composition of Disk, Atomic Pct Zn	Final Surface Composition, Atomic Pct Zn	Final Composition at the Markers, Atomic Pct Zn	Marker Movement, Cmx10^{5}	D_{Zn}/D_{Cu}
600	2.0	49.2	43.9	47.2	47.2	1.0	2.4
600	6.0	49.0	43.4	47.2	47.1	2.6	3.8
600	24.0	48.5	41.7	46.9	46.8	5.8	3.6
600, ref. 9	—	45.0	—	—	—	—	2.1
700	1.0	48.7	44.2	48.3	48.2	2.3	3.2
700	2.5	50.2	42.7	46.9	46.8	3.4	3.0
700	16.5	—	43.8	47.3	47.3	8.7	3.6
700, ref. 9	—	45.0	—	—	—	—	2.0
800	1.0	47.4	39.6	47.0	46.7	4.9	3.0
800, ref. 9	—	45.0	—	—	—	—	1.8

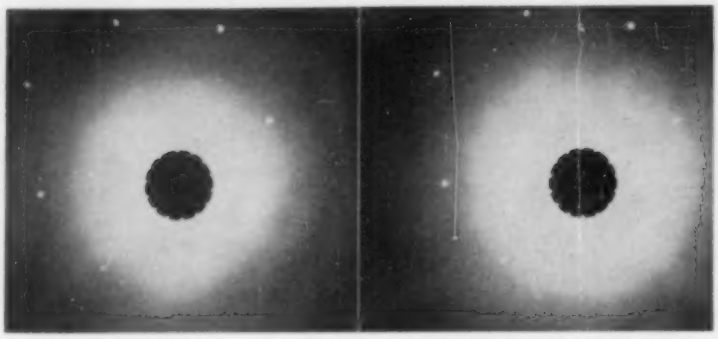

a—Photogram was taken before diffusion.

b—Photogram was taken after diffusion at 800°C for 3½ hr.

Fig. 6—Laue back-reflection X-ray photograms of volume adjacent to surface, β brass couple.

lishing constant boundary conditions has been discussed previously.[7] When the surface concentration is maintained essentially constant, the Matano analysis may be applied to the penetration curve and D values may be calculated. However, this analysis no longer applies when the surface concentration varies in an undetermined manner. Consequently, it was only possible to calculate an average value of the ratio of diffusivities (D_{Zn}/D_{Cu}) from the present data by finding the ratio of the amounts of zinc and copper diffused past the markers in each case. These latter quantities were obtained graphically from areas under the diffusion curve and are given in Table III along with corresponding values of Inman et al.[7] Since the composition range was small in these couples, these diffusivity ratios should refer to a composition of about 46 atomic pct Zn which is slightly less than the final marker concentration in each case. It is interesting to note that the ratio does not appear to vary systematically with time or temperature and must therefore be fairly insensitive to small composition changes as well. It does not seem likely that differences in composition could account for the ≈ 30 pct discrepancy between the present ratios and those of Inman et al.[7] The explanation for the low surface concentrations is not understood at present. As has been previously discussed,[7] a high diffusion rate or a low vapor pressure should increase the time required for the surface concentration to approach the concentration of the zinc source. A rough calculation based upon the penetration curves indicates that diffusion in the β phase is comparatively very rapid and that D at 800°C is about 10^{-4} sq cm per sec. This high diffusion rate which is about 10^5 times the corresponding rate in the α phase may partially account for the low surface concentration, but the fact that the surface concentration did not steadily increase with time indicates that other factors inhibiting transfer of zinc to the specimen surface must have been present.

Dimensional Changes Due to Diffusion—Previous measurements[1-7] have shown that in the case of the face-centered-cubic metals the volume changes caused by diffusion in large diffusion couples of the type usually used in diffusion studies are largely restricted to the direction of diffusion. However, in the case of thin wires or sheets, comparatively large dimensional changes may occur normal to the diffusion direction.[16] It appears that in the former case the large bulk of the usual diffusion specimen acts to restrict the volume changes to the direction of diffusion.

Measurements were made of any dimensional changes normal to the direction of diffusion in the present alloy by employing two vapor-solid couples similar to those previously described. Tungsten wires 0.075 cm diam were first welded onto each specimen face to use as gage marks. Zinc was then diffused into these 0.75 cm thick and 3.0 cm diam disks at 800°C for 1 and 2 hr. Measurements after diffusion proved that linear dimensional changes normal to the diffusion direction were less than 0.1 pct. This result therefore agrees generally with previous measurements[1-7] on face-centered-cubic metal couples and also validates the graphical integrations used in the previous section for the determinations of the position of the original interface and the ratio of diffusivities. These graphical methods, of course, depend upon a constant specimen cross-section.

Subgrain Formation During Diffusion—Extensive subgrain formation has been found to occur in the diffusion zones of several face-centered-cubic alloys.[7, 17, 18] This process appears to be a result of the volume changes and mass flow accompanying diffusion and the restraints imposed upon the mass flow by the bulk of the specimen. This phenomenon consequently was investigated in β brass by both X-ray and metallographic methods.

A vapor-solid couple with a grain size of about 1 cm and similar to those previously described was used. The surface of the well annealed disk was first carefully electropolished to a metallographic finish and a back-reflection Laue X-ray pattern was taken of the volume adjacent to the surface. The X-ray beam used was collimated to a 0.060 cm diam. The photogram shown in Fig. 6a is char-

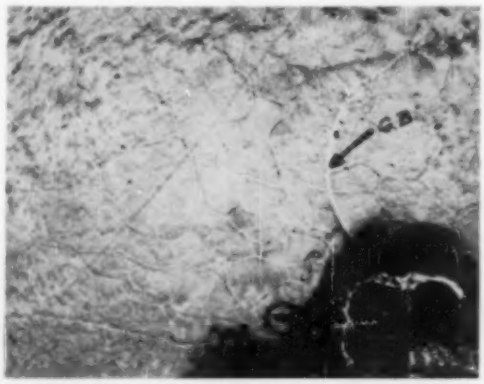

Fig. 7—Final surface of β brass disk is shown after diffusion at 800°C for 3½ hr. Arrow indicates position of high energy grain boundary. X100. Area reduced approximately 40 pct for reproduction.

[7] M. C. Inman, D. Johnston, W. L. Mercer, and R.

acteristic of the pattern of a recrystallized metal usually obtained by this technique. Zinc was then diffused into this disk for 3½ hr at 800°C and the surface was re-examined and X-rayed in exactly the same area previously used. Metallographic examination of the surface revealed the subgrain structure over the entire surface which is shown in Fig. 7. The position of a high energy grain boundary is indicated by the arrow and illustrates the difference in the surface grooves produced at the intersections of the surface with the various interfaces. The X-ray pattern after diffusion is shown in Fig. 6b. The originally single sharp spots have been broken up into a number of smaller ones in a pattern typical of a subgrain structure. The angular difference between adjacent subgrains was estimated to be of the order of 0.5° from the spread of spots in each cluster.

Porosity Formation—When α brass is heated in vacuo, the zinc diffuses outward into the vacuum more rapidly than copper diffuses inward to replace it and vacancies are therefore deposited in the alloy. These vacancies reach supersaturation and a fraction of them precipitate out in the form of observable pores.[10] The remaining vacancies are destroyed at various sinks within the specimen causing a volume contraction.

Porosity formation in β brass at 800°C was studied by diffusing zinc out of single crystal disk specimens containing 49 atomic pct Zn after sealing them in evacuated quartz capsules containing a large mass of 40 atomic pct Zn β brass chips. The disks were made 0.5 cm thick and 1.5 cm diam from single crystals which were prepared by sealing the brass in quartz capsules and employing the Bridgman method. The diffusion anneals were made at 800°C for various lengths of time and the amount of porosity formed at each stage was followed by taking density measurements using the weigh-in-air—weigh-in-water method. The results are given in Fig. 8. For purposes of comparison, the percentage of porosity has been included, which would have been obtained if all the vacancies which were left behind by the unequal fluxes of zinc and copper had precipitated as pores. These values were calculated by assuming that the atomic volumes of zinc and copper are equal and by allowing for the counterflow of copper and the small lattice parameter shrinkage caused by the loss of zinc. The counterflow of copper was assumed to be one-third as large as the outward zinc flow. These curves may be compared to other results obtained

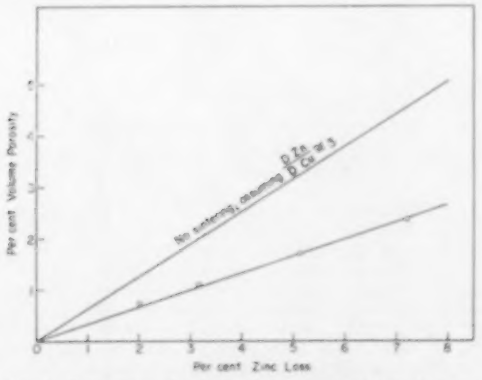

Fig. 8—Percentage of volume porosity produced in β brass during outward diffusion of zinc at 800°C is shown.

Fig. 9—Cross-section shows 50 pct Cu-50 pct Zn β brass single crystal dezincified at 800°C for 5.5 hr in the presence of 60 pct Cu-40 pct Zn β brass chips. X200. Area reduced approximately 45 pct for reproduction.

for α brass.[10] It is clear that a large fraction of vacancies precipitated as holes during zinc loss in both alloys. The porosity in the specimen diffused for 5.5 hr is shown in Fig. 9. The width of the porous region is fairly narrow, since high enough vacancy supersaturations for hole formation must have been reached only in the regions near the specimen surface. The low supersaturations reached elsewhere must have been partly a result of the relatively small concentration difference between the specimen and the brass chips. The average hole size which is considerably larger than in the case of α brass may have resulted from the small number of heterogeneous nuclei which became active in the presence of a low supersaturation and the relatively high diffusion rate of vacancies in this alloy.

Discussion—The results show that all of the phenomena presently associated with the Kirkendall effect in α brass accompany diffusion in β brass and that diffusion in this body-centered-cubic alloy is, therefore, at least outwardly, similar to diffusion in the face-centered-cubic structure. Diffusion is much more rapid, however, in the nonclose-packed body-centered-cubic phase, as seems to be the case in other systems where diffusion rates in face-centered-cubic and body-centered-cubic phases have been compared. A number of the present findings agree with the work reported by Landergren and Mehl.[11] The values of D_{Zn} and D_{Cu} calculated by Heumann[10] from data communicated by Landergren and Mehl cannot be accepted, however, since Heumann employed an improper form of Darken's equations. The fact that the diffusivity ratios reported in Table III do not show any marked variation with temperature indicates that H_{Zn} and H_{Cu} for β brass are not greatly different, see Eq. 4.

On the basis of these results, it seems that Zener's[25] ring exchange mechanism cannot be the main chemical diffusion mechanism in β brass. A discussion of the ring exchange mechanism has been recently given by LeClaire[26] where it is suggested on the basis of an interpretation of observed frequency factor values that self-diffusion occurs by a 4-ring mechanism in body-centered-cubic metals. The viewpoint that the ring mechanism may be favored in nonclose-packed structures such as β brass may be ruled out for at least chemical diffusion, since this mechanism cannot account for the observed Kirkendall phenomena.

Acknowledgments

The writers wish to acknowledge the aid of R. Bastian of Sylvania Electric Products Inc. for performing the chemical analyses and E. Weaver and

Kinetics and Mechanism of the Oxidation of Molybdenum

M. Kurtz for carrying out the metallographic phases of this work. This work was sponsored by the AEC and performed under Contract AT-30-1 GEN-367.

Discussion of this paper, if any, will appear in JOURNAL OF METALS, May 1956, and in AIME Metals Branch *Transactions*, Vol. **206**, 1956.

References

[1] L. C. C. da Silva and R. F. Mehl: *Trans.* AIME (1951) **191**, p. 155; JOURNAL OF METALS (February 1951).
[2] C. Wells: *Atom Movements.* (1951) p. 26. Cleveland. ASM.
[3] O. Kubaschewski: *Trans.* Faraday Soc. (1950) **46**, p. 713.
[4] A. D. Smigelskas and E. O. Kirkendall: *Trans.* AIME (1947) **171**, p. 130; METALS TECHNOLOGY (October 1946).
[5] L. S. Darken: *Trans.* AIME (1948) **175**, p. 184; METALS TECHNOLOGY (February 1948).
[6] R. W. Balluffi and B. H. Alexander: *Trans.* AIME (1952) **194**, p. 1315; JOURNAL OF METALS (December 1952).
[7] R. W. Balluffi and L. L. Seigle: *Journal of Applied Physics* (1954) **25**, p. 607.
[8] G. T. Horne and R. F. Mehl: *Trans.* AIME (1955) **203**, p. 88; JOURNAL OF METALS (January 1955).
[9] M. C. Inman, D. Johnston, W. L. Mercer, and R. Shuttleworth: *Proceedings* Second Radioisotope Conference, Oxford (July 19-23, 1954); *Butterworths Scientific Publications* (1954) p. 85.
[10] This point has been discussed by A. D. LeClaire: *Progress in Metal Physics.* (1949) **I**, p. 354. New York. Interscience Publishers Inc.
[11] U. S. Landergren and R. F. Mehl: JOURNAL OF METALS (1953) **5**, No. 2, p. 153.
[12] J. C. Fisher, J. H. Hollomon, and D. Turnbull: *Trans.* AIME (1948) **175**, p. 202; METALS TECHNOLOGY (February 1948).
[13] A. S. Nowick: *Journal of Applied Physics* (1951) **22**, p. 1182.
[14] A. Kuper, H. Letaw, Jr., I. Slifkin, E. Sonder, and C. T. Tomizuka: *Physical Review* (1954) **96**, p. 1224.
[15] J. Hino: Private communication, University of Illinois.
[16] R. W. Balluffi and B. H. Alexander: *Journal of Applied Physics* (1952) **23**, p. 953.
[17] R. J. Barnes: *Proceedings* Physical Soc., London (1952) **65B**, p. 512.
[18] R. W. Balluffi: *Journal of Applied Physics* (1952) **23**, p. 1407.
[19] R. W. Balluffi: *Journal of Applied Physics* (1952) **23**, p. 1237.
[20] T. Heumann: *Naturwissenschaften* (1953) **40**, p. 164.
[21] C. Zener: *Acta Crystallographica* (1950) **3**, p. 346.
[22] A. D. LeClaire: *Acta Metallurgica* (1953) **1**, p. 438.

Technical Note

Thermal Conductivity of Vanadium and Certain Vanadium Alloys

by James L. Weeks and Karl F. Smith

IN order to determine the magnitude of thermal conductivity changes resulting from alloying vanadium with titanium and a few other elements, several samples were prepared and measured. The thermal conductivity values reported herein in Table I were determined with an apparatus previously described.[1]

As in recently reported[2] determinations on uranium and uranium alloys, whose thermal conductivities are in the same range as vanadium,[3] the accuracy of the values was checked by using synthetic sapphire.[4] The error in the measurement is estimated to be ±3 pct or 0.003 cal sec^{-1} cm^{-1} °C^{-1}, whichever is larger.

The vanadium used in preparing the samples was the calcium-reduced type and was supplied by the Electro Metallurgical Co. as 99.6+ pct pure. All alloying elements used in the preparations were 99+ pct pure. A nonconsumable tungsten electrode arc furnace was used for melting the alloys and, without opening the furnace, each ingot was remelted a number of times to insure homogeneity. The samples as prepared by the Armour Research Foundation were machined from *as forged* material without annealing.

Acknowledgment

The note is based on work performed under the auspices of the AEC.

References

[1] J. L. Weeks and R. L. Seifert: Apparatus for the Measurement of the Thermal Conductivity of Solids. *Review of Scientific Instruments* (1953) **24**, pp. 1054-1057.
[2] J. L. Weeks: Thermal Conductivity of Uranium and Several Uranium Alloys. *Trans.* AIME (1955) **203**, p. 192; JOURNAL OF METALS (January 1955).
[3] C. A. Hampel: *Rare Metals Handbook.* (1954) p. 593. New York. Reinhold Publishing Corp. Thermal conductivity of vanadium is given as 0.074 cal sec^{-1} cm^{-1} °C^{-1} at 100°C.
[4] J. L. Weeks and R. L. Seifert: Note Regarding the Thermal Conductivity of Synthetic Sapphire. *Journal* Amer. Ceramic Soc. (1952) **35**, p. 15. At 70°C, K = 0.071 cal sec^{-1} cm^{-1} °C^{-1}.

Table I. Thermal Conductivity of Vanadium and Certain Vanadium Alloys

Alloying Element, Wt Pct*	Thermal Conductivity at 20°C, Cal Sec^{-1} Cm^{-1} °C^{-1}
None	0.084 4
5 Ti	0.069 9
10 Ti	0.058 2
20 Ti	0.047 1
10 Ti, 5 Al	0.031 2
40 Ti, 5 Al	0.024 6
1 Si	0.063 8
2 Si, 2.5 Zr	0.050 0

* Balance vanadium.

J. L. WEEKS and K. F. SMITH are associated with Chemistry and Metallurgy Divs., respectively, Argonne National Laboratory, Lemont, Ill.

TN 282E. Manuscript, Mar. 24, 1955.

Kinetics and Mechanism of the Oxidation of Molybdenum

by M. Simnad and Aija Spilners

The rates of formation of the different oxides on molybdenum in pure oxygen at 1 atm pressure have been determined in the temperature range 500° to 770°C. The rate of vaporization of MoO_3 is linear with time, and the energy of activation for its vaporization is 53,000 cal per mol below 650°C and 89,600 cal per mol at temperatures above 650°C. The ratio $MoO_{3(vaporizing)}/MoO_{3(surface)}$ increases in a complicated manner with time and temperature. There is a maximum in the total rate of oxidation at 600°C. At temperatures below 600°C, an activation energy of 48,900 cal per mol for the formation of total MoO_3 on molybdenum has been evaluated. The suboxide MoO_2 does not increase beyond a very small critical thickness. At temperatures above 725°C, catastrophic oxidation of an autocatalytic nature was encountered. Pronounced pitting of the metal was found to occur in the temperature range 550° to 650°C. Marker movement experiments indicate that the oxides on molybdenum grow almost entirely by diffusion of oxygen anions.

USEFUL life of molybdenum in air at elevated temperatures is limited by the unprotective nature of its oxide which begins to volatilize at moderate temperatures. Although the oxide/metal volume ratio is greater than one, the protective nature of the oxide film is very limited. Gulbransen and Hickman[1] have shown, by means of electron diffraction studies, that the oxides formed during the oxidation of molybdenum are MoO_2 and MoO_3. The dioxide is the one present next to the metal surface and the trioxide is formed by the oxidation of the dioxide. Molybdenum dioxide is a brownish-black oxide which can be reduced by hydrogen at about 500°C. Molybdenum trioxide has a colorless transparent rhombic crystal structure when sublimed, but on the metal surface it has a yellowish-white fibrous structure. It is reported to be volatile at temperatures above 500° and melts at 795°C. It is soluble in ammonia, which does not affect the dioxide or the metal.

In his extensive and classic investigations of the oxidation of metals, Gulbransen[2] has studied the formation of thin oxide films on molybdenum in the temperature range 250° to 523°C. These experiments were carried out in a vacuum microbalance, and the effect of pressure (in the range 10^{-4} to 76 mm Hg), surface preparation, concentration of inert gas in the lattice, cycling procedures in temperature, and vacuum effect were studied. The oxidation was found to follow the parabolic law from 250° to 450°C and deviations started to occur at 450°C. The rates of evaporation of a thick oxide film were also studied at temperatures of 474° to 523°C. In vacua of the order of 10^{-4} mm Hg and at elevated temperatures, an oxidation process was observed, since the oxide that formed at these low pressures consisted of MoO_2 which has a protective action to further reaction in vacua at temperatures up to 1000°C. Electron diffraction studies showed that, as the film thickened in the low temperature range, MoO_3 became predominant on the surface. Above 400°C MoO_2 was no longer observed, MoO_3 being the only oxide detected.

The failure to detect MoO_2 on the surface of the film formed at the higher temperatures does not militate against the formation of this oxide, since according to free energy data MoO_2 is stable up to much higher temperatures. At the low pressures employed, this oxide would volatilize off as soon as it was formed. Its vapor pressure is relatively high and is given by the equations[4]

$$\log p_{(mm\ Hg)} = -16{,}140\ T^{-1} - 5.53 \log T + 30.69 \quad (25°C\text{—melting point})$$

$$\log p_{(mm\ Hg)} = -14{,}560\ T^{-1} - 7.04 \log T^{-1} + 34.07 \quad (\text{melting-boiling point}).$$

Lustman[4] has reported some results on the scaling of molybdenum in air which indicate a discontinuity at the melting point of MoO_3 (795°C). Above the melting point of MoO_3, oxidation is accompanied by loss of weight, since the oxide formed flows off the surface as soon as it is formed.[5, 6] Rathenau and Meijering[7] point out that the eutectic MoO_3-MoO_2 melts at 778°C, and they ascribe the catastrophic oxidation of alloys of high molybdenum content to the formation of low melting point eutectics of MoO_2 with the oxides of the melts present. Fontana and Leslie[8] explain the same phenomenon in terms of the volatility of MoO_3, which leads to the formation of a porous scale.

Recent unpublished work by Speiser[9] on the oxidation of molybdenum in air at temperatures between 480° and 960°C shows that the rate of weight change of molybdenum is controlled by the relationship between the rates of formation and evaporation of MoO_3. They have measured the rates of evaporation of MoO_3 in air at different temperatures and estimated an activation energy of 46,900 cal. This compares with the value of 50,800 cal per mol obtained by Gulbransen for the rate of sublimation of MoO_3 into a vacuum.

M. SIMNAD, Associate Member AIME, and A. SPILNERS are associated with Metals Research Laboratory, Carnegie Institute of Technology, Pittsburgh.

Discussion of this paper, TP 4020E, may be sent, 2 copies, to AIME by Nov. 1, 1955. Manuscript, June 28, 1954. Chicago Meeting, February 1955.

a closed weighing tube as soon as they had cooled.

metal-oxide interface. At these temperatures the

The authors have studied the oxidation of molybdenum in pure oxygen at 1 atm pressure in the temperature range 500° to 770°C, since a more detailed study of the kinetics was required for an understanding of the mechanism of its oxidation at elevated temperatures and with oxide thicknesses much greater than those measured by Gulbransen. The gross weight change of a sample of molybdenum during oxidation at high temperatures and pressures is no useful criterion of the kinetics or mechanism of its oxidation. The individual oxides, namely, the MoO_3 which vaporizes off, the MoO_3 remaining on the surface, and the MoO_2 formed next to the metal, have to be estimated separately. This paper presents such measurements of the oxidation of molybdenum and includes a note on the influence of moisture in the oxygen upon the oxidation process. Marker movement studies with radioactive silver as markers have been carried out to establish the nature of the diffusing ions.

Apparatus

The design of the furnace unit and the oxygen gas train used for oxidation is shown in Fig. 1. The furnace temperature was controlled to ±2°C. The silica furnace tube, 1½ in. diam, contained an inner silica tube, ¼ in. diam, through which the oxygen was introduced in a preheated condition and flowed up past the specimen at a uniform rate. The electrolytic oxygen was passed over platinized asbestos at 450°C to remove hydrogen and then dried by passing through four cold traps immersed in dry ice-acetone mixtures. The cold traps were filled with copper turnings to break up the gas stream. Several test experiments in which liquid nitrogen was used for the cold traps made no difference to the results obtained. A flowmeter was included in the oxygen train and a flow rate of about 60 cu cm per min was used in all the experiments.

Each specimen was attached to a silica rod, 18 in. long, by a platinum hook and the silica rod was in turn attached by means of a nylon thread to a glass rod across the top of the furnace.

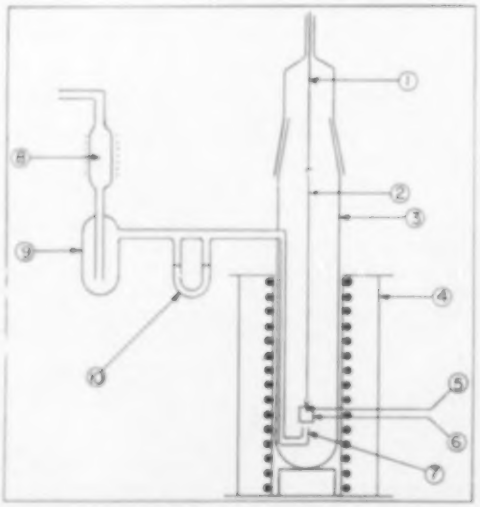

Fig. 1—Oxidation unit used for tests is shown in schematic diagram. Numbers represent: 1—nylon thread, 2—silica rod, 3—silica tube, 4—furnace, 5—platinum wire, 6—specimen, 7—coiled silica tube oxygen outlet, 8—platinized asbestos, 9—cold trap, and 10—flowmeter.

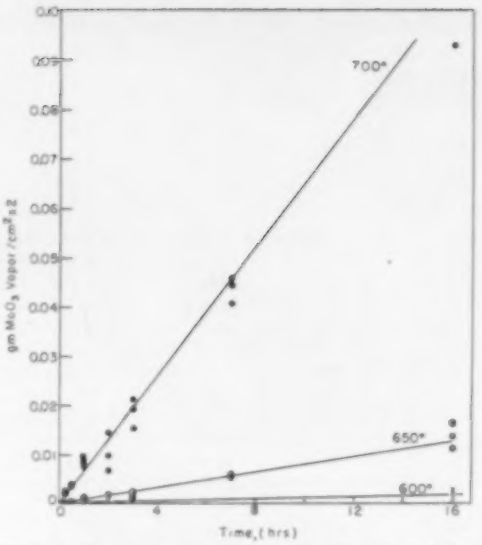

Fig. 2—Isothermal curves show the rate of formation of MoO_3 vapor below 700°C.

Experimental Procedure

The molybdenum sheet, 1 mm thick, was obtained from Westinghouse Electric Corp. and has an analysis of 99.9+ pct. The specimens were cut to 1x1.5 cm and abraded with grit paper, finishing with 4/0 paper. They were measured, degreased with acetone and alcohol, weighed, and then loaded into the furnace which had been flushed out with the pure dry oxygen. Care was taken to line up the specimen in the center of the furnace tube directly above the oxygen inlet.

At temperatures above 725°C, the phenomenon of autocatalytic oxidation took place, which resulted in the burning of the specimens and their complete disappearance within very short times. This phenomenon can be explained by the fact that the heat of formation of the oxide raises the surface temperature of the metal to above the melting point of the MoO_3, which melts and runs off the sample. Fresh metal is continuously exposed to the oxygen and the oxidation rate is catastrophic. This effect was overcome by first preoxidizing the sample at a zone in the furnace where the temperature was 725°C for a period of 10 min. It was then lowered to the zone which was at the higher temperature being studied. Preoxidation of more than 8 min duration at 725°C was sufficient to prevent burning of the samples at the higher temperatures.

Several experiments were carried out at 725°C to check the influence of moisture in the oxygen upon the rate of oxidation of molybdenum, since it has been reported that the vapor pressure of molybdenum trioxide is increased in the presence of water vapor.[9] The oxygen was bubbled in a fine stream through a column of water before entry into the furnace. No appreciable increase in the oxidation rate could be detected, and it was concluded that the effect of moisture upon the oxidation rate is negligible at these temperatures. The study of the effect of moisture was not pursued further and all experiments were carried out in dry oxygen.

A new sample was used for each time and temperature. At the end of each test, the specimens were removed from the furnace and reweighed in

a closed weighing tube as soon as they had cooled, since exposure to moist air for periods longer than a few minutes resulted in a marked increase in weight of the oxidized specimens. The MoO_3 remaining on the surface was then dissolved in ammonia and the sample again weighed. Next, the quantity of MoO_2 present on the surface was determined by reduction with hydrogen at 700°C for 2 hr. At least three specimens were used for each time and temperature.

X-ray analysis of the oxides formed on the surface of the specimens showed the presence of MoO_3 in the outer layer and MoO_2 in the inner layer.

The calculation of the amounts of the different oxides formed is as follows: Let W_1 be the original weight of the molybdenum sample, W_2 the weight of the sample after oxidation, and W_3 the weight of the sample after ammonia treatment. Then

$W_2 - W_3 =$ wt of MoO_3 remaining on metal.

Let W_4 be the weight of the sample after hydrogen treatment and W_5 the weight of molybdenum in the MoO_2 film. Then

$$W_4 - W_5 = \text{wt of O in } MoO_2 \text{ film.}$$

Let W_6 be the weight of molybdenum in $MoO_{3(vaporized)}$ and W_7 the weight of molybdenum in $MoO_{3(evaporated)}$. Let W_8 be the weight of MoO_3 which vaporized, W_9 the weight of MoO_3 on the surface, and W_{10} the weight of molybdenum oxidized. Then

$$W_6 = W_7 \times \frac{\text{mol wt } MoO_3}{\text{mol wt Mo}}$$

and

$$W_9 = W_8 \times \frac{\text{mol wt } MoO_3}{\text{mol wt Mo}}$$

and

$$W_{10} = W_1 - (W_4 - W_5).$$

It is evident from the foregoing procedure that a very large number of calculation have to be carried out for plotting the curves shown in Figs. 2 through 10. The tables on which these curves are based are not furnished because their inclusion would require an excessive amount of space.

Results and Discussion

The formation of the different oxides and the phenomena accompanying their growth will be discussed individually in the sections that follow.

Vaporized MoO_3: At temperatures above approximately 600°C, the rate of vaporization of MoO_3 becomes significant and is linear at all temperatures up to 770°C, as is expected for a zero order reaction process. The results obtained are shown in Figs. 2 and 3. The temperature dependence of the linear rate constants is shown in Fig. 4, where the logarithm of the rate constants are plotted against the reciprocals of the absolute temperatures. There is a break in the curve at about 650°C, indicating a change in activation energy at this temperature. The values for the energy of activation calculated from the two slopes are: 53,000 cal per mol for temperatures below 650°C and 89,600 cal per mol for temperatures above 650°C. This compares with the value of 50,800 cal per mol reported by Gulbransen in the range 474° to 523°C and 46,900 cal per mol found by Speiser. The change in mechanism at about 650°C is confirmed by three other phenomena:

1—The appearance and shape of the oxide on the metal changes at about 650°C. At the lower temperatures, the shape of the oxide is with re-entrant edges which show that oxidation took place at the metal-oxide interface. At these temperatures the rate of evaporation of MoO_3 is slow and most of it remains on the surface. At temperatures above 650°C, the shape of the oxide is usual for protective oxides growing on metals.

2—Pitting of the underlying metal surface and blistering of the oxide surface were clearly observed in the range of 550° to 650°C. No signs of pitting could be found at temperatures above or below this range. The number and size of these hemispherical

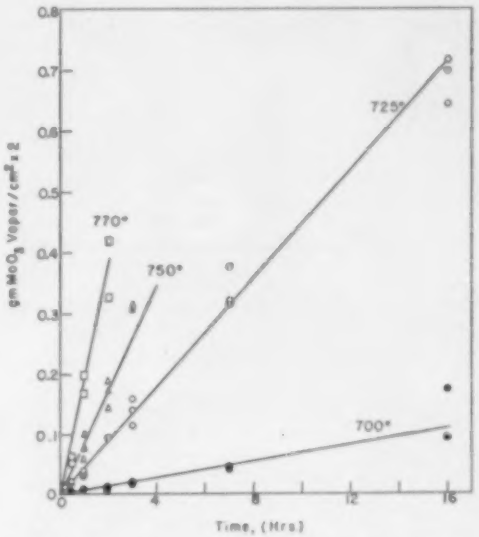

Fig. 3—Isothermal curves show the rate of formation of MoO_3 vapor above 700°C.

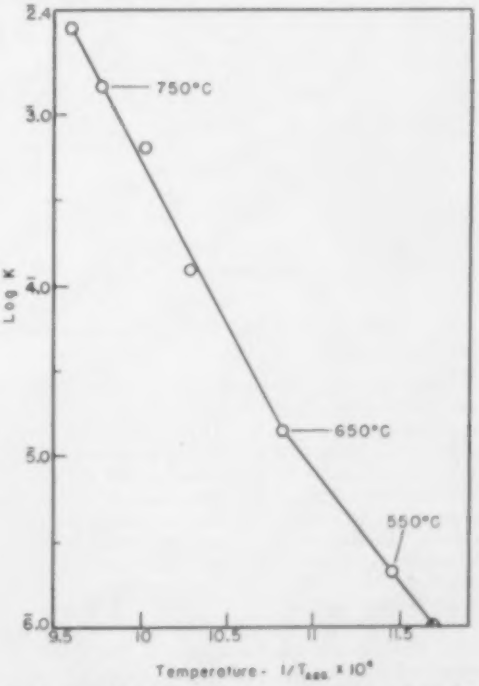

Fig. 4—Plots of the logarithm of the linear rate constants for the formation of MoO_3 vapor are given.

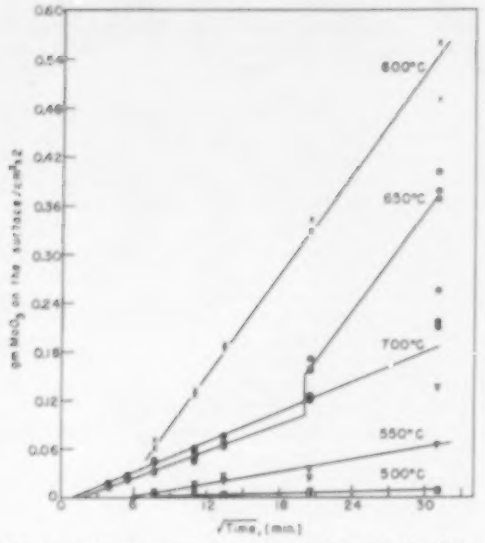

Fig. 5—Isothermal curves show the rate of growth of surface MoO_3 below 700°C.

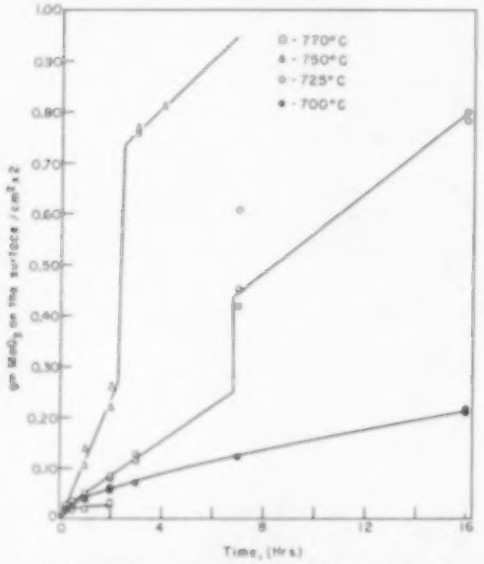

Fig. 6—Isothermal curves show the rate of growth of surface MoO_3 above 700°C.

pits increase with time and temperature. These pits are visible after about 16 hr oxidation at 550°C and after only 1 hr at 650°C. Their formation does not seem to be governed by a critical oxide thickness, since no pits could be produced at 500° or at 700°C even after formation of much thicker oxides than those required at the other temperatures for pit formation. In the pitting range the scale consists of columnar grains, and the formation of pits is ascribed here to the more rapid diffusion of oxygen at grain boundaries.

3—The rate of formation of surface MoO_3 and of total MoO_3 reaches a maximum at about 600°C, as described in the next section.

Surface MoO_3: The thickness of the MoO_3 remaining on the surface of the specimens increases with

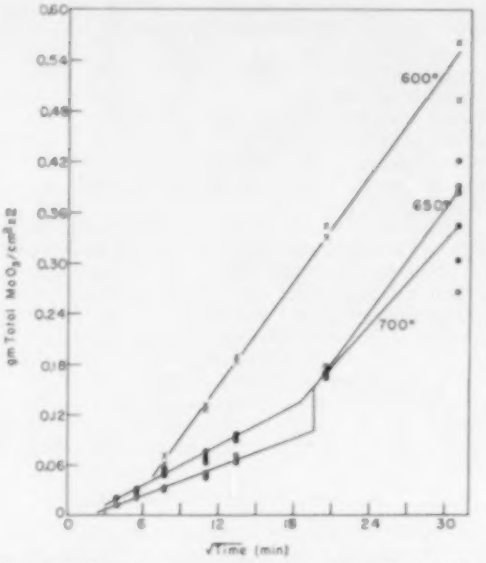

Fig. 7—Isothermal curves show the rate of growth of total MoO_3 below 700°C.

time and temperature in a manner shown in Figs. 5 and 6, which represent the plots of data for temperatures below and above 700°C, respectively. At temperatures below 700°C, the rates of growth of the oxide are parabolic and reach a maximum at 600°C. The rates at 650° and 700°C are appreciably lower than the rate at 600°C. This is an unusual phenomenon, since the oxidation rates of metals always increase with temperature. The rate at 650° is initially less than the rate at 700°C, but increases suddenly to a greater value after a critical period. This sudden increase may be related to mechanical cracking of the MoO_3 layer which occurs when a critical thickness is exceeded. The oxide is brittle at these temperatures and breaks down mechanically under the stresses set up by the increase in volume which accompanies the formation of MoO_3.

At 725° and 750°C, the rate of formation of the surface MoO_3 appears to be linear, with breaks in the curves occurring after some critical thickness has been reached. At 770°C the oxide reaches a constant thickness and does not increase further with time, since its rate of evaporation then is equal to its rate of formation.

The structure of the MoO_3 remaining on the surface consists of fibrous rhombic crystals extending across the oxide in a direction perpendicular to the metal surface.

Total MoO_3: The total amount of MoO_3 formed as a function of time is plotted in Fig. 7 for temperatures below 700°C and in Fig. 8 for temperatures above 700°C. At the lower temperatures the rates are parabolic, whereas at the higher temperatures they are linear. At temperatures below 700°C, the rate of formation of the total oxide reaches a maximum at 600°C. As in the case of the surface MoO_3, the rates at 650° and 700°C are appreciably lower than the rate at 600°C. Also, the rate at 650° is initially less than at 700°C but increases suddenly to a greater value after a critical period. There is also a break in the curve at 700°C.

At 725°, 750°, and 770°C, the rates of formation of total MoO_3 are again linear, with breaks in the

curves after a critical thickness of the oxide has been exceeded.

Since the rate of vaporization of MoO_3 is negligibly slow at temperatures below 600°C, the logarithms of the rate constants for the formation of total MoO_3 are plotted in Fig. 9 against the reciprocals of the absolute temperatures for the range below 600°C. A straight line is obtained, giving a value for the energy of activation of 48,900 cal per mol for the formation of MoO_3.

The ratio of MoO_3 vaporizing to that remaining on the metal surface is plotted in Figs. 10 and 11. The ratio $MoO_{3(vapor)}/MoO_{3(surface)}$ increases markedly with temperature, since the increase in the rate of vaporization with temperature is greater than the increase in the rate of formation of MoO_3 on the surface. There is an anomaly at 750°C, where the ratio is slightly less than at 725°. At any given temperature, the ratio appears to increase with time to a constant value, except for 770°C where the ratio continues to increase linearly and rapidly with time. At 700°C the ratio increases at a parabolic rate with time.

Suboxide MoO_2: The amount of MoO_2 formed at all the temperatures is relatively insignificant, compared to the rate of formation of MoO_3. It remains nearly constant in thickness with time and does not increase appreciably with temperature. This indicates that after a critical thickness the rate of formation of MoO_2 becomes equal to the rate at which it is oxidized to MoO_3. Fig. 12 shows the measured quantities of MoO_2 formed at 600° to 725°C. At lower temperatures, the quantity formed is negligibly small.

Marker Movements: The movement of inert markers placed at an interface across which diffusion takes place has been studied previously.[15-20] Marker movement experiments have been carried out in this study using radioactive silver as inert markers. Silver has the advantage that it neither dissolves in the metal and its oxides nor oxidizes at these temperatures. Very small amounts of the marker can be detected by means of autoradiographic methods. Thin deposits of silver were applied by wetting a silk thread in active silver nitrate solution and touching each side of the molybdenum specimens, leaving thin parallel wet marks. These were dried and the silver nitrate decomposed to silver in the preliminary heating of the sample before oxidation began. After oxidation, the MoO_3 scale remaining on the surface was easily separated from the unoxidized metal by gently tapping the edge of the specimen with a small hammer. Autoradiographs were obtained by placing the two halves of the scale and the underlying metal separately between two X-ray films for three days. The autoradiographs obtained showed that all the radioactive silver had remained on the outer surface of the MoO_3, since none could be detected either on the metal surface or on the inner surface of the MoO_2 scale.

The MoO_3 and MoO_2 grow by oxide ion diffusion, with practically no molybdenum ion participation. During oxidation, the molybdenum ions are added at the inner face and stay fixed. This finding is in accord with that of Speiser[16] who used coatings of chromic oxide as markers.

The autoradiographs of the outer surface of the MoO_3 scale showed a uniform darkening over the whole surface, which means that the original thin line of radiosilver had diffused sideways across the surface. This rapid surface diffusion of silver on MoO_3 is in marked contrast to its behavior in the

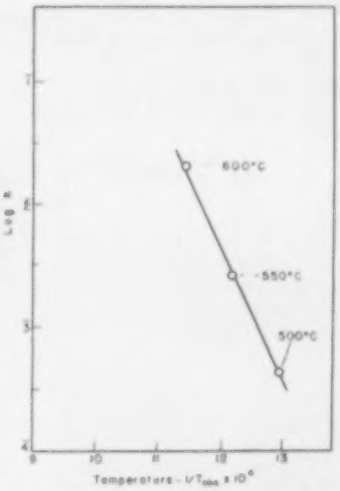

Fig. 9—Plot of the logarithm of the parabolic rate constants for the formation of total MoO_3 is given for the range below 600°C.

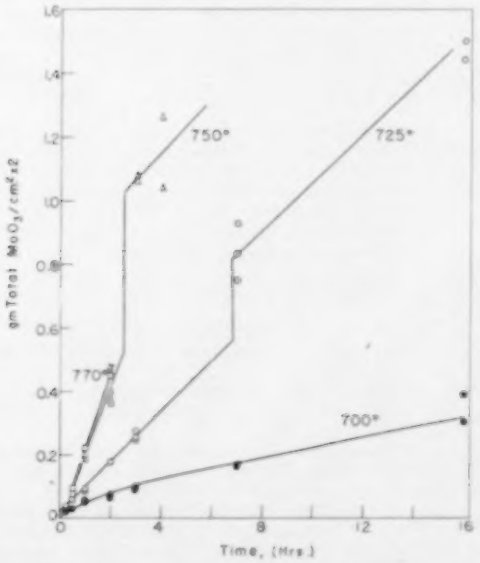

Fig. 8—Isothermal curves show the rate of growth of total MoO_3 above 700°C.

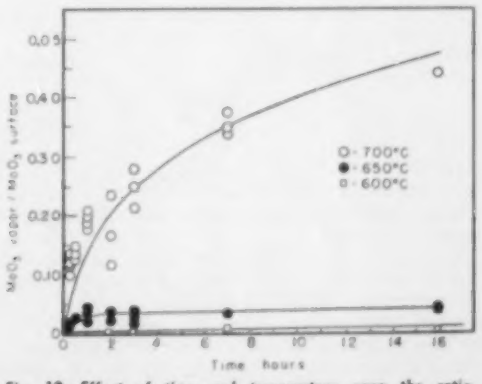

Fig. 10—Effect of time and temperature upon the ratio $MoO_{3(vapor)}/MoO_{3(surface)}$ is illustrated for the range below 700°C.

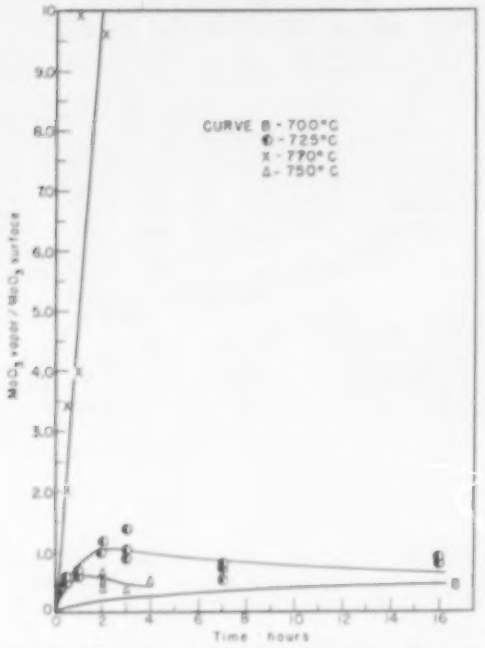

Fig. 11—Effect of time and temperature upon the ratio $MoO_{3\,vapor}/MoO_{3\,surface}$ is illustrated for the range above 700°C.

oxidation of iron, where it showed no evidence of surface diffusion at the interface between Fe and FeO.

Summary

The rates of oxidation of molybdenum in pure oxygen at 1 atm pressure have been determined with good precision over the temperature range 500° to 770°C. In addition to multilayer oxidation rates, the rates of growth of the different oxides formed, namely, the inner MoO_2 layer, the layer of MoO_3 remaining on the surface, and the MoO_3 volatilizing off, have been determined.

The rate constant is a complex function of temperature in the growth of the different oxides, since the mechanical properties of the oxides and the rates of vaporization of the MoO_3 change with temperature.

The rate of vaporization of MoO_3 is linear with time. The energy of activation is estimated to be 53,000 cal per mol for temperatures below 650°C and 89,600 cal per mol for temperatures above 650°C.

The growth of the MoO_3 remaining on the surface obeys the parabolic law below 700°C, with a maximum rate at 600° which is greater than the rates at 650° and 700°C. At 725° and 750°C, its rate of formation appears to be linear, with breaks in the curves after a critical thickness is exceeded. At 770°C the oxide does not increase beyond a critical thickness, since its rate of vaporization then equals its rate of formation.

The total amount of MoO_3 formed is again a complicated function of time and temperature. There is a maximum in the rate of oxidation at 600°C which is appreciably greater than the rates at 650° and 700°C. At temperatures below 600°C, where the rate of evaporation of MoO_3 is very low, the parabolic rate constant can be evaluated and an energy of activation of 48,900 cal per mol is calculated for the formation of MoO_2.

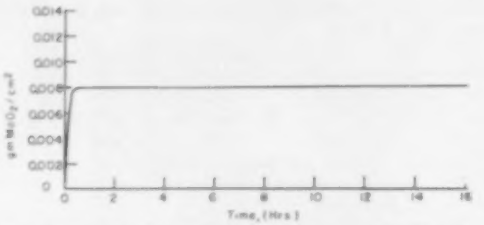

Fig. 12—Growth of MoO_3 is shown by the quantities formed at 600° to 725°C. Below this range, the quantity formed is negligible.

The ratio $MoO_{3\,vapor\,to\,gas}/MoO_{3\,surface}$ increases markedly with temperature. The ratio increases with time to a constant value, except for 700°C where it increases parabolically with time and at 770°C where it increases linearly with time.

The amount of suboxide MoO_2 formed is relatively insignificant at these temperatures and pressures and does not increase beyond a critical thickness, where its rate of formation equals the rate at which it oxidizes to MoO_3.

At temperatures above 725°C, catastrophic oxidation of an autocatalytic nature was encountered.

Pronounced pitting of the metal was found to occur in the temperature range 550° to 650°C.

Marker movement experiments, with radioactive silver as inert markers, indicate that the oxides on molybdenum grow almost entirely by diffusion of anions.

Acknowledgments

This work forms part of a research project sponsored by the Office of Naval Research. The authors would like to express their appreciation for discussions with R. F. Mehl, C. E. Birchenall, and Rudolph Speiser. Assistance was given by O. Katz in the early stage of this work.

Discussion of this paper, if any, will appear in JOURNAL OF METALS, May 1956, and in AIME Metals Branch *Transactions*, Vol. **206**, 1956.

References

[1] J. W. Hickman and E. A. Gulbransen: *Trans.* AIME (1947) **171**, p. 344; METALS TECHNOLOGY (October 1946).
[2] E. A. Gulbransen and W. S. Wysong: *Trans.* AIME (1948) **175**, p. 611; METALS TECHNOLOGY (September 1947).
[3] O. Kubaschewski and B. E. Hopkins: *Oxidation of Metals.* (1953) p. 171. New York. Academic Press Inc.
[4] B. Lustman: *Metals Progress* (1950) **57**, p. 629.
[5] O. Kubaschewski and B. E. Hopkins: *Journal* Inst. of Metals (1949) **75**, p. 403.
[6] E. Nachtigal: *Ztsch. für Metallkunde* (1952) **43**, p. 23.
[7] G. W. Rathenau and J. L. Meijering: *Metallurgia* (1950) **42**, p. 167.
[8] W. C. Leslie and M. G. Fontana: *Trans.* ASM (1949) **41**, p. 1213.
[9] R. Speiser: Private communication.
[10] T. Millner and J. Neugebauer: *Nature* (1949) **163**, p. 601.
[11] R. Speiser: Private communication.
[12] L. B. Pfeil: *Journal* Iron and Steel Inst. (1929) **119**, p. 501; (1931) **131**, p. 237.
[13] A. D. Smigelskas and E. O. Kirkendall: *Trans.* AIME (1947) **171**, p. 130; METALS TECHNOLOGY (October 1946).
[14] L. C. C. da Silva and R. F. Mehl: *Trans.* AIME (1951) **191**, p. 155; JOURNAL OF METALS (February 1951).
[15] M. H. Davies, M. T. Simnad, and C. E. Birchenall: *Trans.* AIME (1951) **191**, p. 889; JOURNAL OF METALS (October 1951).
[16] R. Speiser: Private communication.

Contribution to Mathematics of Zone Melting

by Leslie Burris, Jr., C. H. Stockman, and I. G. Dillon

Zone melting is a purification process in which separation of impurities is effected by slowly moving a narrow melted zone through a bar of solid material. Equations are presented which 1—predict the concentration profiles after successive passes of the zone and 2—give the limiting distribution of solute along the bar after an infinite number of passes of the molten zone. These equations take into account the effect of normal freezing in the last zone length. These equations were solved numerically using an electronic computer, and the concentration profiles are presented as a function of the solute distribution coefficient and the ratio of molten zone to total bar length.

ZONE MELTING is a purification process in which separation of impurities is effected by slowly moving a narrow melted zone through a bar of solid material. Separation occurs if the solid freezing from a solution at any moment has a composition different from that of the liquid from which it is freezing. Solutes which lower the freezing point will tend to remain in solution and will be moved in the direction of zone travel. Solutes which raise the freezing point will preferentially freeze out, and they will be moved in a direction opposite to that of zone travel.

After repeated unidirectional passage of a molten zone through a bar of material, impurities will be concentrated in the ends of the bar. A limiting concentration gradient will be reached in the bar after a large number of passes of the molten zone. Both the magnitude of this limiting concentration gradient and the rate of movement of solute in any pass depend on the zone length and on the equilibrium concentrations of solute in the liquid and solid phases.

The basic theory of zone melting was thoroughly covered by Pfann.[1] The purpose of this paper is to extend the theory of zone melting by presenting 1—equations which relate the concentration profiles in successive passes of the zone and 2—equations which give the limiting distribution of solute along the bar after an infinite number of passes of the molten zone. These equations take into account the effect of normal freezing* in the last zone length and are valid for all values of the distribution coefficient k, which is the ratio of equilibrium of the concentration of a given solute in the solid to the concentration of the same solute in the liquid. Analytical methods for determining the concentration profiles after any pass have been developed by Lord[2] and Reiss.[3] The method developed by Lord does not take into account normal freezing in the last zone and also becomes very complicated when the number of passes becomes large. The method developed by Reiss enables the direct calculation of the complete concentration profiles (including that in the last zone) after any pass for values of k close to unity ($0.9 < k < 1.1$). Both methods are useful and provide valuable insight into the zone melting process.

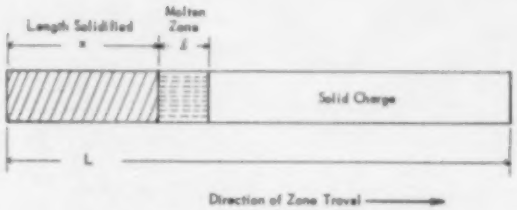

Fig. 1—Schematic diagram of zone melting.

The equations given in this article are based on the same assumptions used by Pfann. These are: 1—uniform composition in the liquid, 2—negligible diffusion in the solid, 3—constant distribution coefficient, 4—constant length of the liquid zone (except at the ends), and 5—solubility of the solute in the melt is not exceeded at any point.

Equations for Concentrations in Successive Passes

For a melted zone of length l at the left-hand end of a bar of uniform unit cross-section, the amount of solute in the liquid is

$$\int_0^l C_{n-1}(x)\,dx \qquad [1]$$

where the subscript is the number of the pass. $C_{n-1}(x)$ represents the concentration (expressed as weight per unit volume) obtained in the previous

* Normal freezing is the term applied to the freezing of a length of molten metal from one end. This occurs in the last zone length.

L. BURRIS, JR. is associated with Argonne National Laboratory, C. H. STOCKMAN, formerly on loan to Argonne National Laboratory, is associated with Nuclear Developments Group, The B. F. Goodrich Co., Brecksville, Ohio, and I. G. DILLON is associated with Argonne National Laboratory, Lemont, Ill.

Discussion of this paper, TP 4024E, may be sent, 2 copies, to AIME by Nov. 1, 1955. Manuscript, Sept. 13, 1954. Chicago Meeting, February 1955.

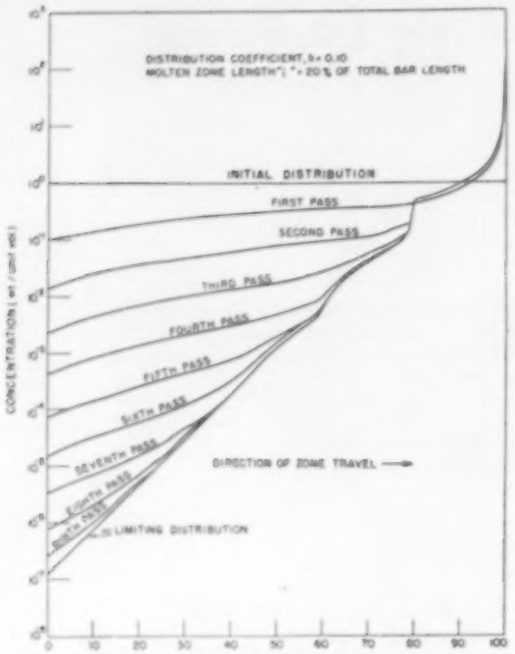

Fig. 2—Concentration profiles in a zone melted rod.

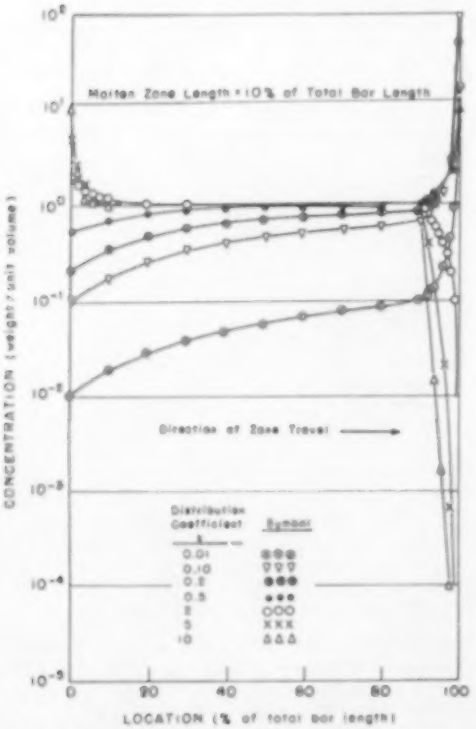

Fig. 3—Effect of k on concentration profile after one pass.

pass at a point located a distance x from the left end of the bar.

When the molten zone is moved a distance x (see Fig. 1), the net amount of solute contained in the

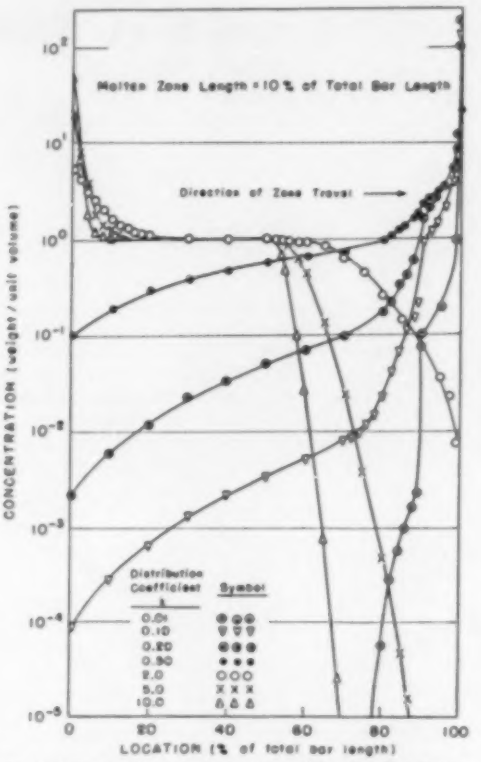

Fig. 4—Effect of k on concentration profile after five passes.

molten zone is

$$\int_0^{x+l} C_{n-1}(x)\,dx - \int_0^x C_n(x)\,dx. \qquad [2]$$

The first integral represents the total amount of solute taken up by the molten zone in moving a distance x and the second integral represents the amount of solute deposited behind the molten zone. Dividing the net amount of solute by the volume of the molten zone gives the concentration of solute in the liquid. Multiplying this concentration by k gives the concentration of solute in the solid freezing at point x. Hence

$$C_n(x) = \frac{k}{l}\left[\int_0^{x+l} C_{n-1}(x)\,dx - \int_0^x C_n(x)\,dx\right]. \qquad [3]$$

Eq. 3 holds for all of the bar except the last zone length. Because the forward end of the liquid zone reaches the end of the bar when $x = L - l$, the liquid zone gains no more solute and normal freezing begins. The term $x + l$ becomes meaningless because it refers to a point beyond the end of the bar. However, Eq. 3 becomes applicable to the last zone if it is written as

$$C_n(x) = \frac{k}{L-x}\left[\int_0^L C_{n-1}(x)\,dx - \int_0^x C_n(x)\,dx\right] \qquad [4]$$

which is applicable only for $L\text{-}l \leq x \leq L$. Eqs. 3 and 4 are the general equations for zone melting. They are applicable for all finite values of k and give concentration distributions over the entire length of the bar.

Equations for Limiting Distribution of Solutes

Eqs. 3 and 4 are suitable not only for pass by pass calculations but also for determining the ultimate

or limiting distribution. When the limiting distribution is reached, further passes produce no changes in concentrations. Consequently, $C_x = C_{x-l}$, and Eqs. 3 and 4 become

$$C(x) = \frac{k}{l}\int_{x}^{x+l} C(x)\,dx$$
$$0 \leqq x \leqq L-l \qquad [5]$$

$$C(x) = \frac{k}{L-x}\int_{x}^{L} C(x)\,dx$$
$$L-l \leqq x \leqq L. \qquad [6]$$

Solution of Equations

An analytical solution for these equations has not been found. However, numerical methods of solution have been developed using the trapezoidal rule for the integration. These numerical methods are given in the Appendix and were used in an IBM card-programmed electronic computer to obtain concentration distributions for each of ten consecutive passes for k's of 0.01, 0.1, 0.2, 0.5, 2, 5, and 10 and for molten zone lengths of 5, 10, and 20 pct of the bar length. Also, the ultimate distribution of solute along the bar was determined for each of these conditions. A uniform initial concentration of 1 (weight/unit volume) was assumed to exist in the bar. Data obtained from these theoretical calculations are presented in Figs. 2 through 11.

Fig. 2 shows the concentration profiles for ten successive passes for a k of 0.1 and an l of 0.2 and is an example of the type of information obtained. Similar data were obtained for each of the combinations of variables, but space limitations preclude showing these graphs. Instead, emphasis will be placed on discussion of the effects of changes in k and l on the concentration profiles.

In Fig. 2, reflection of the sharp concentration rise caused by normal freezing in the last zone length is evident over much of the bar length. It may be noted that nine passes produced a concentration profile very close to that of the limiting distribution. For fewer passes than the number giving the limiting distribution, the concentration profiles seem to peel off from the limiting distribution line. Thus, at the completion of the fifth pass, concentrations in the last 40 pct of the bar are essentially at the limiting concentration values, while those in the initial 60 pct of the bar are much higher than could eventually be reached. For a shorter zone length, nine passes do not produce a concentration profile close to that of the limiting distribution except in the first few zone lengths from the end of the bar toward which the zone travels, and this approach to the limiting distribution occurs only when k is less than 1.0.

Figs. 3, 4, and 5 show the first, fifth, and tenth passes with $l = 0.1$ for all the values of k used in the computations. Note that after one pass, for k greater than unity, there is a long concentration plateau on which the concentration is equal to the initial concentration. After five passes, the plateau has been considerably shortened. After ten passes, it has disappeared. If the zone length were one-twentieth the bar length, a portion of this plateau would remain even after ten passes. On the other hand, if the zone length were one-fifth the bar length, the concentration plateau would have disappeared by the completion of the fourth or fifth pass.

This effect of zone length for a k greater than one is illustrated in Fig. 6 where for a k of five the solute distribution curves are shown after one and ten

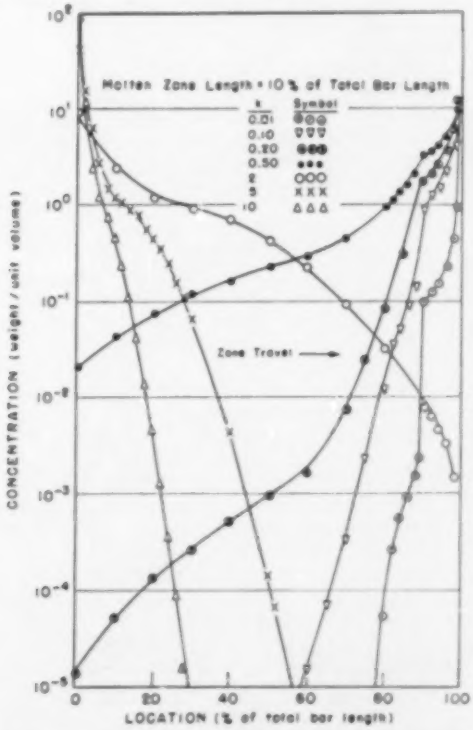

Fig. 5—Effect of k on concentration profile after ten passes.

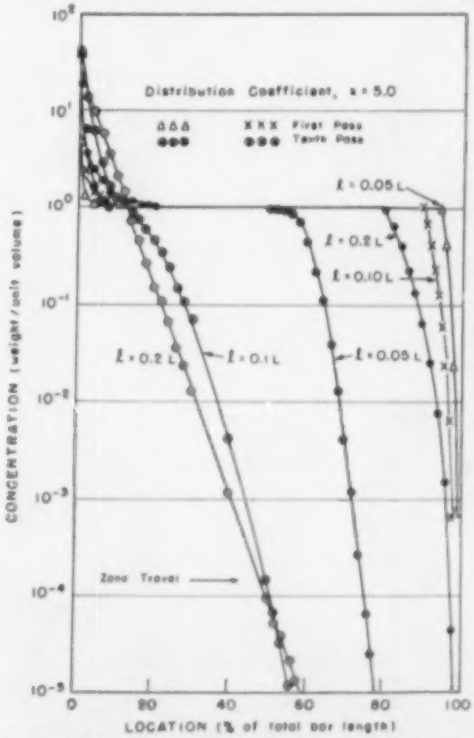

Fig. 6—Effect of zone length l on solute movement for a k greater than one.

passes for zone lengths of 5, 10, and 20 pct of the bar length. For a zone length 20 pct of the bar length, ten passes have produced the limiting concentration gradient. It should be pointed out that when k is greater than one, any molecule of solute cannot move in one pass a distance greater than the zone length. Thus, the longer the zone length, the greater is the movement of solute and the fewer the number of passes required to give the limiting concentration gradient. In the extreme, the limiting concentration is produced in one pass by normal freezing when the zone length is equal to the total bar length.

However, as shown in Fig. 7, the shorter the zone length, the steeper is the concentration gradient which results for the limiting distribution. Thus, there is merit in employing a relatively long zone length in the initial passes to effect a rapid movement of solute and a short zone length in the later passes to effect greater purification from the solute. This is illustrated in Fig. 8 in which is shown the concentration profile obtained with $k = 2.0$ by making seven passes with $l = 0.2$, followed by two passes with $l = 0.1$. This concentration profile is compared with that obtained by making ten passes with $l = 0.1$. It appears that the nine passes with two zone lengths are roughly equivalent to 12 passes, all at the shorter zone length.

The effect of zone length for k's less than one is illustrated in Fig. 9 where the first and tenth passes are shown for $k = 0.1$ and l's of 5, 10, and 20 pct of the bar length. This effect for k's less than one is less pronounced than for k's greater than one, as comparison with Fig. 6 will show. Again, the longer zone length will give more rapid solute movement and a more rapid attainment of a limiting concentration gradient than do shorter zone lengths. However, as previously pointed out, the shorter zone length produces greater eventual purification.

The fact that the tenth pass curve for $l = 0.10$ crosses that for $l = 0.05$ in Fig. 9 is a consequence of the reflection back into the bar of the effect of normal freezing in the last zone length. After several more passes, the concentration profile for $l = 0.05$ would lie entirely below that for $l = 0.10$ and eventually the limiting distribution curves shown in Fig. 7 would be approached.

Fig. 10 shows the effect of k on the limiting distribution for $l = 0.05$. Data are given in Table I from which limiting distribution lines for $l = 0.10$ and 0.20 may be constructed. The limiting distribution curves for k's of less than one are very slightly lower than those presented by Pfann[1] because of inclusion of the normal freezing effect in the last portion of the bar to freeze. The effect of normal

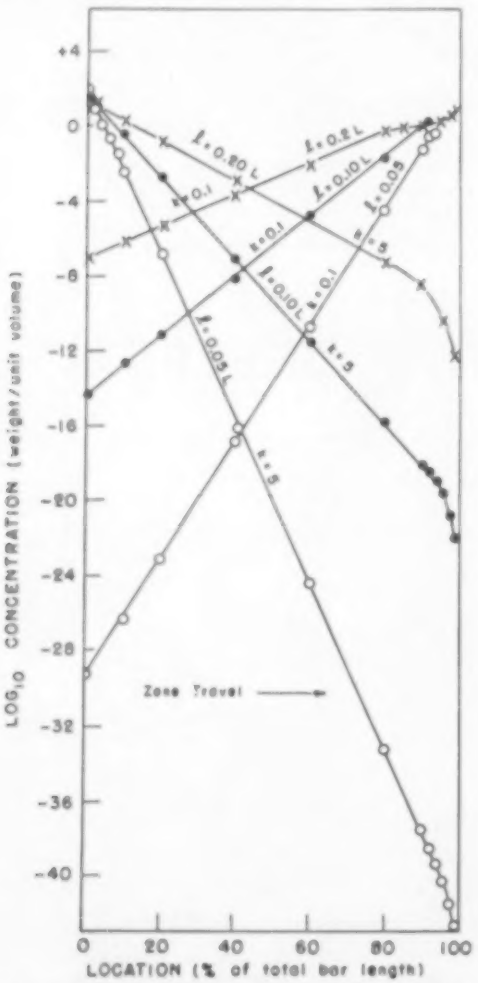

Fig. 7—Effect of zone length l on limiting distribution profile.

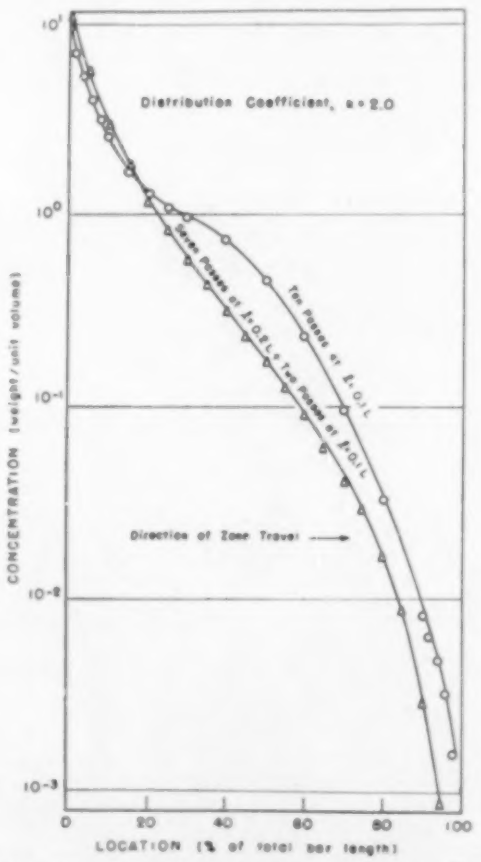

Fig. 8—Effect of changing zone lengths on concentration profiles.

Table I. Concentrations for Construction of Limiting Distribution Curves

	Starting End†		20 Pct of Bar†		30 Pct of Bar†		90 Pct of Bar†
k<1*	l = 0.10	l = 0.20	l = 0.10	l = 0.30	l = 0.10	l = 0.20	l = 0.10
0.01	2.02×10^{-67}	6.77×10^{-34}	8.03×10^{-69}	3.37×10^{-33}	1.55×10^{-33}	9.14×10^{-7}	1.00×10^{-1}
0.10	4.25×10^{-10}	1.28×10^{-6}	8.71×10^{-33}	4.50×10^{-6}	2.80×10^{-7}	1.14×10^{-6}	9.91×10^{-1}
0.20	5.30×10^{-11}	1.43×10^{-6}	1.07×10^{-9}	2.03×10^{-4}	3.04×10^{-6}	1.14×10^{-6}	1.93×10^{0}
0.50	4.43×10^{-6}	1.05×10^{-6}	5.35×10^{-4}	3.67×10^{-6}	2.19×10^{-6}	2.43×10^{-1}	2.77×10^{0}

	80 Pct of Bar†	95 Pct of Bar†		98 Pct of Bar†		99 Pct of Bar†	
k<1*	l = 0.20	l = 0.10	l = 0.20	l = 0.10	l = 0.20	l = 0.10	l = 0.20
0.01	9.93×10^{-6}	1.99×10^{-1}	1.97×10^{-1}	4.92×10^{-1}	4.83×10^{-1}	9.77×10^{-1}	9.70×10^{-1}
0.10	9.22×10^{-1}	1.85×10^{0}	1.72×10^{0}	4.22×10^{0}	3.93×10^{0}	7.87×10^{0}	7.32×10^{0}
0.20	1.67×10^{0}	3.36×10^{0}	2.90×10^{0}	6.99×10^{0}	6.04×10^{0}	1.22×10^{1}	1.05×10^{1}
0.50	2.65×10^{0}	3.34×10^{0}	3.75×10^{0}	8.44×10^{0}	5.93×10^{0}	1.19×10^{1}	8.36×10^{0}

	Starting End†		2 Pct of Bar†		5 Pct of Bar†		10 Pct of Bar†
k>1*	l = 0.10	l = 0.20	l = 0.10	l = 0.30	l = 0.10	l = 0.20	l = 0.10
2.0	1.596×10^{1}	7.97×10^{0}	1.16×10^{1}	6.80×10^{0}	7.17×10^{0}	5.35×10^{0}	3.22×10^{0}
5.0	4.97×10^{3}	2.48×10^{3}	1.80×10^{3}	1.51×10^{3}	3.93×10^{0}	7.13×10^{0}	3.11×10^{-1}
10.0	1.00×10^{6}	5.00×10^{5}	1.30×10^{5}	1.80×10^{4}	7.78×10^{0}	3.89×10^{0}	3.08×10^{-2}

	10 Pct of Bar†	50 Pct of Bar†		90 Pct of Bar†		99 Pct of Bar†	
k>1*	l = 0.20	l = 0.10	l = 0.20	l = 0.10	l = 0.20	l = 0.10	l = 0.20
2.0	3.59×10^{0}	5.37×10^{-6}	1.46×10^{-1}	8.47×10^{-6}	6.39×10^{-6}	8.47×10^{-7}	6.39×10^{-6}
5.0	2.05×10^{0}	4.74×10^{-10}	9.45×10^{-6}	1.13×10^{-61}	3.25×10^{-6}	7.07×10^{-68}	3.25×10^{-13}
10.0	3.02×10^{-1}	3.96×10^{-68}	4.05×10^{-10}	1.15×10^{-60}	1.72×10^{-10}	1.15×10^{-67}	1.72×10^{-69}

* k is distribution coefficient; in first two sections, k is less than one and in the last two sections, k is greater than one.
† Ratio of final to initial concentration at starting end and various percentages of the total bar. l is length of the molten zone.

freezing on the shape of the limiting distribution curve near the finishing end of the bar is depicted in Fig. 11. This curve shows a sharp break as the front end of the zone approaches the end of the bar. This is caused by reflection of the very steep concentration gradient at the end of the bar due to normal freezing in the last zone length.

The foregoing theoretical calculation methods give the best performance which could be realized by zone melting. How closely *k*'s realized experimentally agree with those obtained from phase diagrams will depend on the rate of zone travel and adherence to the assumptions used in the derivation. The assumption which is most difficult to realize experimentally is that of uniform concentration in the molten zone. Hayes and Chipman,[4] Tiller et al.,[5] and Wagner[6] point out the existence of a boundary layer at the solidifying interface and discuss the shape of the solute concentration gradient in this boundary layer under various conditions. The existence of such a concentration gradient will make the *k*'s realized experimentally closer to one than those obtained from phase diagrams.

Appendix: Derivation of Numerical Methods of Computation

For this derivation, the length of the bar will be considered to be unity and the bar will be divided into N equal subdivisions, each Δx in length. Furthermore, this division will be considered made in such a way that the length l of the liquid zone is an integral multiple of Δx. Hence

$$N\,\Delta x = 1 \qquad [7]$$

$$l = b\Delta x. \qquad [8]$$

In addition, let

$$C_s^i = C_s(i\Delta x) \qquad [9]$$

where i is the number of increments Δx counting from the end of the bar at which the liquid zone starts. Thus, $x = i\Delta x$.

Use of the trapezoidal role in Eq. 3 gives, at $x = 0$

$$C_s^i = \frac{k}{b}\sum_{s=i}^{s=i+b}\frac{1}{2}\left(C_{s-1}^{i-1} + C_{s-1}\right). \qquad [10]$$

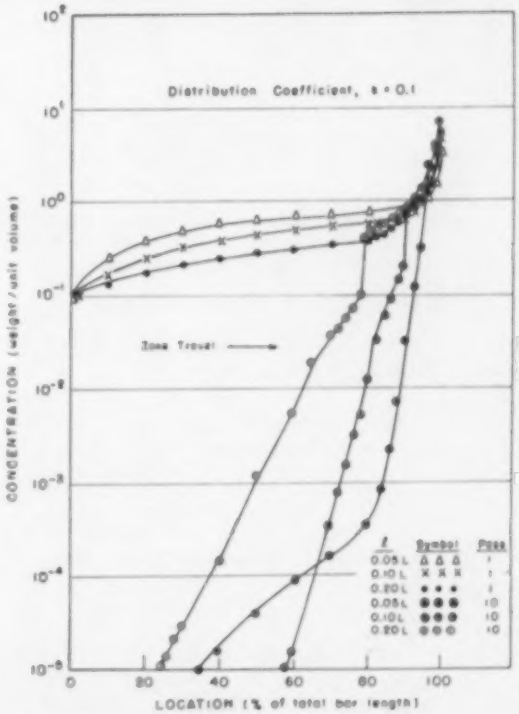

Fig. 9—Effect of zone length l on solute movement for a k less than one.

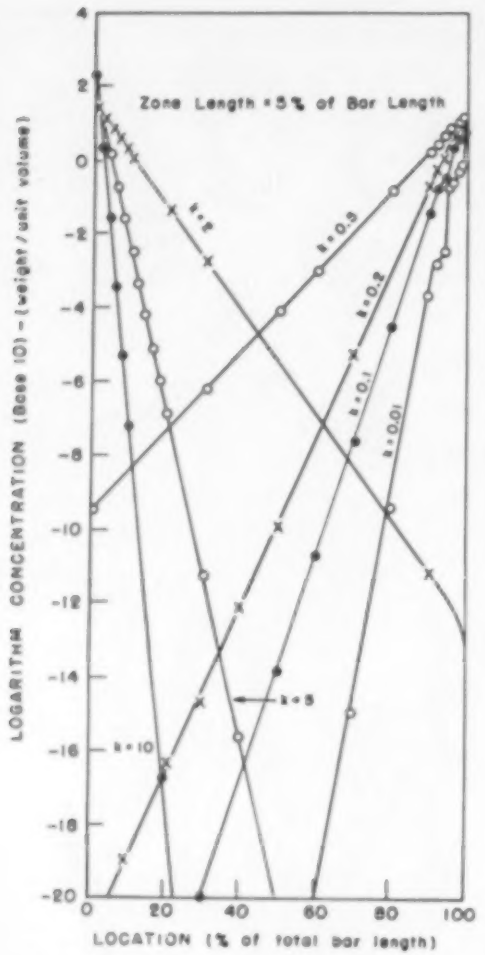
Zone Length = 5 % of Bar Length
LOGARITHM CONCENTRATION (Base 10) - (weight / unit volume)
LOCATION (% of total bar length)
k = 2
k = 0.5
k = 0.2
k = 0.1
k = 0.01
k = 5
k = 10

Fig. 10—Effect of k on limiting distribution profile.

For $0 < x \leq 1 - l$, the substitution of the trapezoidal rule in Eq. 3 reduces to

$$C_n^i = \frac{2k}{2b + k}\left(S_{n-1}^{i+b} - S_n^{i+1}\right) \qquad [11]$$

where

$$S_n^i = \sum_{j=i}^{i+b-1} \frac{1}{2}\left(C_n^{j-1} + C_n^j\right) \qquad [12]$$

$$S_n^{*i} = S_n^i - \frac{1}{2}C_n^i \qquad [13]$$

and

$$S_n^i = S_n^{i-1} + \frac{1}{2}C_n^{i-1} + \frac{1}{2}C_n^i \qquad [14]$$

$$S_n^{*i} = S_n^{*i-1} + C_n^{i-1}. \qquad [15]$$

In the last zone length, that is $1 - l \leq x \leq 1$, the trapezoidal rule is used in Eq. 4 to give

$$C_n^i = \frac{2k}{2(N-i) + k}\left(S_{n-1}^N - S_n^{*i}\right). \qquad [16]$$

Eqs. 10, 11, and 16 provide a means of calculating concentrations in successive passes. Eqs. 14 and 15 aid the computations by providing a relation between successive S^i's and S^{*i}'s in the calculations for any single pass.

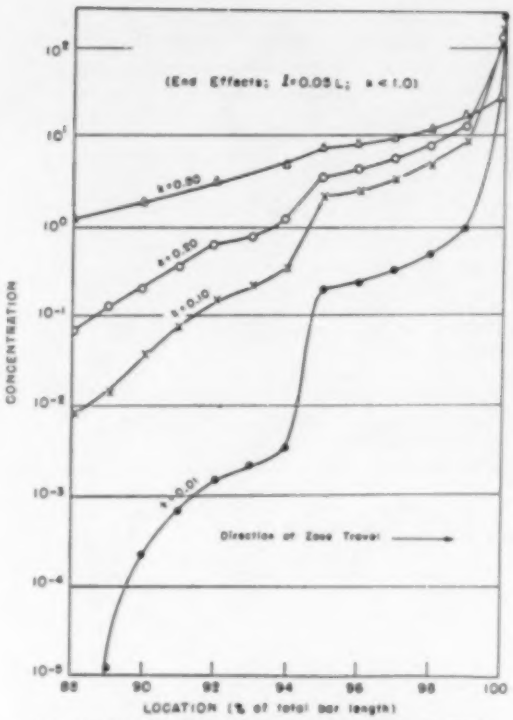

Fig. 11—Effect of normal freezing on limiting distribution.

Using the trapezoidal rule in Eq. 5 and solving for C^i gives

$$C^i = \frac{2k}{2b - k}T^i \qquad 0 \leq i < N-b \qquad [17]$$

where

$$T^i = \sum_{j=i+1}^{i+b-1} C^j + \frac{1}{2}C^{i+b} \qquad [18]$$

and

$$T^{i-1} = T^i + C^i - \frac{1}{2}C^{i+b} - \frac{1}{2}C^{i+b-1}. \qquad [19]$$

Eq. 6 has the analytical solution

$$C(x) = A(1-x)^{b-1} \qquad 1-l \leq x \leq 1 \qquad [20]$$

where A is a constant. For numerical calculations, this can be rewritten as

$$C^i = A\,(N\Delta x - i\Delta x)^{b-1} = A\,(\Delta x)^{b-1}(N-i)^{b-1} \sim (N-i)^{b-1}. \qquad [21]$$

To compute the limiting distribution, it is necessary to start at the end of the bar toward which the zone travels and work backward. Eq. 4 gives the concentration in the last zone except for a scale factor $A\,(\Delta x)^{b-1}$.

The scale factor is determined by using

$$\overline{C^i} = (N-i)^{b-1} \qquad [22]$$

for the range $N-b \leq i \leq N$. The starting values so obtained are used to continue the calculations back through the bar with Eq. 17. The proportional con-

centrations $\bar{C}$ thus obtained are integrated over the length of the bar to give the total amount of solute in the bar divided by the scale factor. Since the total amount of solute in the bar is known, the scale factor can then be determined.

When k is greater than one, the integration for the foregoing normalization can be carried out over the entire length of the bar by the trapezoidal rule. When k is less than one, however, Eq. 20 gives infinity for $x = 1.0$. This difficulty can be circumvented by integrating analytically in the last zone

$$\int_{1-t}^{1} C(x)\,dx = A\int_{1-t}^{1}(1-x)^{b-1}\,dx = -\frac{A(1-x)^b}{k}\Bigg|_{1-t}^{1} = \frac{Al^b}{k} = \frac{A(b\Delta x)^b}{k}. \quad [23]$$

Since the scale factor is $A\ (\Delta x)^{b-1}$

$$\int_{1-t}^{1} \bar{C}\ (x)\ dx = \Delta x\,\frac{b^b}{k}. \quad [24]$$

The trapezoidal rule can then be used to integrate over the remainder of the length of the bar.

When the foregoing equations are used for numerical calculations for k greater than unity, accurate results will not be obtained unless b, the number of increments of Δx in a zone length, is equal to or greater than k. Furthermore, when k is less than unity, it is better to form each T^n individually from Eq. 18 rather than to use Eq. 19.

Acknowledgments

The authors are greatly indebted to the following members of the Argonne National Laboratory, Physics Div.: Donald A. Flanders for derivations of some of the equations, Nye F. Morehouse and Jean F. Hall for assistance in coding for the IBM computer, and Esther N. Singletary and James A. Nelson for performing the actual computations on the IBM machine.

Discussion of this paper, if any, will appear in JOURNAL OF METALS, May 1956, and in AIME Metals Branch *Transactions*, Vol. **206**, 1956.

References

[1] W. G. Pfann: *Trans.* AIME (1952) **194**, pp. 747-757; JOURNAL OF METALS (July 1952).

[2] N. W. Lord: *Trans.* AIME (1953) **197**, p. 1531; JOURNAL OF METALS (November 1953).

[3] H. Reiss: *Trans.* AIME (1954) **200**, p. 1053; JOURNAL OF METALS (September 1954).

[4] A. Hayes and J. Chipman: *Trans.* AIME (1939) **135**, p. 85; METALS TECHNOLOGY (December 1938).

[5] W. A. Tiller, K. A. Jackson, J. W. Rutter, and B. Chalmers: *Acta Metallurgica* (1953) **1**, No. 4, p. 428.

[6] C. Wagner: *Trans.* AIME (1954) **200**, p. 154; JOURNAL OF METALS (February 1954).

Instability of a Smooth Solid-Liquid Interface During Solidification

by D. Walton, W. A. Tiller, J. W. Rutter, and W. C. Winegard

It is shown that the cellular substructure observed in binary alloy crystals grown from a melt of known concentration can be eliminated by the proper choice of growth conditions. For a given solute concentration, there exists a critical ratio of temperature gradient G in the melt to the rate of solidification R of the crystal, i.e., of G/R, which must be exceeded before the cellular structure can be eliminated. A secondary substructure is observed which is related to the cellular substructure.

IN crystals grown from the melt, a prismatic substructure has been observed by Buerger,[1] Pond and Kessler,[2] and Rutter and Chalmers.[3] This structure is columnar in the direction of growth and appears as a network of hexagonal cells in the plane of the solid-liquid interface.

D. WALTON, W. A. TILLER, J. W. RUTTER, and W. C. WINEGARD are associated with Dept. of Metallurgical Engineering, University of Toronto, Toronto.

Discussion of this paper, TP 4035E, may be sent, 2 copies, to AIME by Nov. 1, 1955. Manuscript, Aug. 2, 1954. Chicago Meeting, February 1955.

Rutter and Chalmers[3] have shown that this substructure occurs as a result of the presence of a layer of high impurity concentration in the melt adjacent to the solid-liquid interface. The formation of the substructure is accompanied by a redistribution of this impurity in the neighborhood of the interface. The structure can be controlled by proper adjustment of the variables in the solidification process such as a rate of solidification and the temperature gradient in the liquid.

The redistribution of solute during the solidification of metal crystals has been treated theoretically

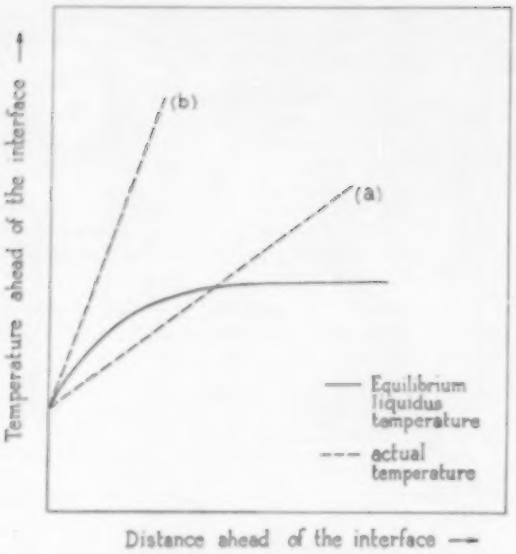

Fig. 1—Liquid is constitutionally supercooled when the actual temperature is lower than the liquidus temperature or equilibrium freezing temperature. Curve *a* demonstrates the conditions necessary for constitutional supercooling, while curve *b* illustrates the conditions necessary for the elimination of constitutional supercooling.

by Tiller et al.[4] It is shown that, in the absence of convection, the solute concentration builds up to a steady state distribution in the liquid adjacent to the advancing solid-liquid interface, given by the following equation

$$C_L = C_o\left(\frac{1-k}{k}\right) e^{-(k/D)x} + C_o \qquad [1]$$

where C_L is the solute concentration at any distance x in the liquid ahead of the interface, C_o is the initial concentration of solute in the melt, k is the ratio of concentration of solute in the solid being formed to the concentration in the liquid from which it forms (k is assumed to be constant), R is the constant rate of solidification of the crystal, and D is the diffusion coefficient of the solute in the liquid.

Wagner[5] has shown that the assumption of no mixing due to natural convection is valid for rates of solidification greater than 5 mm per min for the alloy system used in this investigation. Therefore, Eq. 1 will be valid.

The concentration at every point in the liquid ahead of the interface may be calculated from Eq. 1, and thus the equilibrium liquidus temperature T_x at each point in the liquid can be calculated from

$$T_x = T_o + m\,C_L - m\,C_o/k \qquad [2]$$

where T_o is the temperature of the interface and m is the slope of the liquidus line. The actual temperature at any point in the liquid, however, depends upon the temperature gradient G that exists in the liquid metal. It is possible, therefore, that the actual temperature may be lower than the liquidus temperature or equilibrium freezing temperature at that point. If this condition exists, as shown in Fig. 1, curve *a*, then the liquid at that point is said to be constitutionally supercooled. As discussed by Rutter and Chalmers,[6] under these conditions the plane interface may be expected to become unstable and change to the cellular form.

The initial point of instability occurs when the temperature gradient at the interface is equal to the tangent of the equilibrium temperature distribution curve at the interface, as shown in Fig. 1, curve *b*. The temperature gradient G in front of the interface may be expressed as

$$T = T_o + Gx. \qquad [3]$$

Therefore, by equating the slopes of the two curves given by Eqs. 2 and 3, it is possible to calculate the critical growth conditions for no supercooling and thus no instability of the plane interface. The critical values may be found by solving the equation

$$G/R = -\,m\,\frac{C_o}{D}\left(\frac{1-k}{k}\right) \qquad [4]$$

which results from equating the slopes of the two curves given by Eqs. 2 and 3.

The present investigation was undertaken to determine experimentally the growth conditions necessary to suppress the cellular structure at various concentrations of solute in the melt and thereby to investigate the validity of the theoretical prediction given in Eq. 4 by Tiller et al.[4]

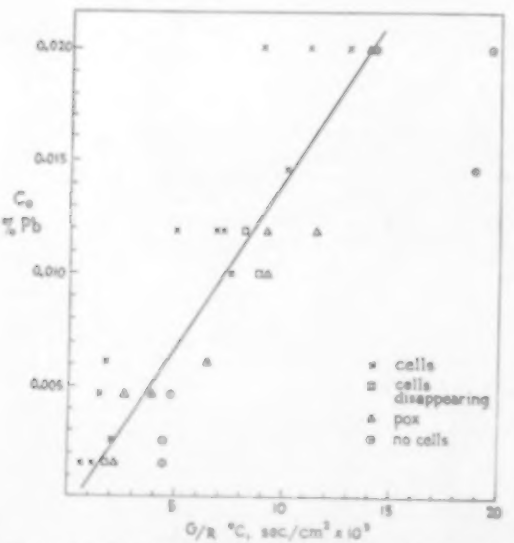

Fig. 2—Results for lead in tin, listed in Table I, are plotted as C_o vs G/R for cell formation.

Experimental Procedure

Experiments were carried out using tin as the solvent material; the tin was *zone refined* in a manner similar to that described by Pfann,[8] until the purity was estimated at better than 99.999 pct. The major solute was lead supplied by Johnson, Matthey Ltd. and was reported to be 99.998 pct pure.

The crystals with known additions of the solute were grown using the modified Bridgman technique described by Chalmers.[7] The specimens, containing a small number of crystals, were grown using various rates of solidification and different temperature gradients. The solid-liquid interface of each crystal was examined for evidence of the cellular structure by separating the liquid metal from the solid in the manner described by Elbaum.[9]

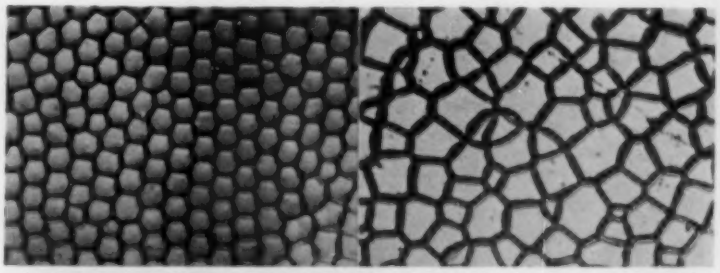

Fig. 3—Regular hexagonal cellular interface appears if specimens are produced under conditions to the extreme left of the curve in Fig. 2. X100. Area reduced approximately 40 pct for reproduction.

Fig. 4—In specimens produced under conditions to the left of, but near, curve of Fig. 2, an irregular hexagonal structure results. X140. Area reduced approximately 40 pct for reproduction.

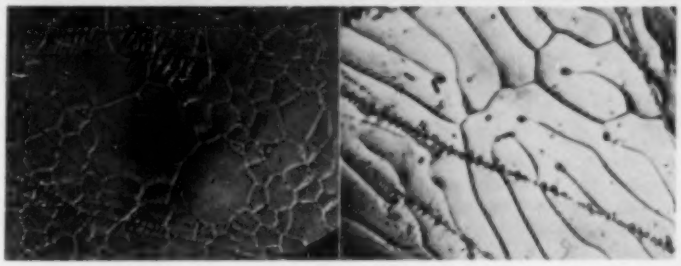

Fig. 5—Interface structure with enlarged hexagonal cells results when specimen conditions are near the curve of Fig. 2. X140. Area reduced approximately 40 pct for reproduction.

Fig. 6—Elongated hexagonal cells appear in the interface structure when specimen conditions are near the curve of Fig. 2. X140. Area reduced approximately 40 pct for reproduction.

The solidification of the crystals was controlled by moving a furnace and a cooling jacket, a fixed distance apart, down a graphite boat at a definite rate. The rate of solidification could be varied by changing the rate of movement of this heat-source—heat-sink combination along the graphite boat.

This rate was measured by putting ripples on the surface of the growing crystal at fixed time intervals. The rate of growth was found to correspond to the speed of the furnace withdrawal.

The temperature gradient was varied by changing the temperature of the furnace and the distance between the furnace and cooling jacket. The gradient was determined by using an iron-constantan thermocouple connected to a Leeds and Northrup recorder. This thermocouple was placed in the melt at the point where the interface would be when the liquid was decanted. By analyzing the time-temperature plot on the recorder, the temperature gradient at that position of the interface could be evaluated.

Table I. Results for Lead in Tin

C_o, Pct	G, °C per Cm	R, Cm per Sec	G/R	Remarks
0.0024	21	0.011	2.1×10^3	Cells
0.0024	27	0.0063	4.3	No cells
0.0060	22	0.013	1.7	Cells
0.0060	28	0.0044	6.3	Pox
0.010	32	0.0044	7.3	Cells
0.010	38	0.0044	8.7	Pox
0.010	39	0.0044	8.7	Cells, disappearing
0.015	44	0.0044	10	Cells
0.015	39	0.0032	19	No cells
0.020	44	0.0032	14	No cells
0.020	28	0.0032	8.6	Cells
0.020	43	0.0032	14	Pox
0.020	34	0.0032	11	Cells
0.020	65	0.0032	20	No cells
0.020	42	0.0032	14	Pox
0.020	40	0.0032	13	Cells
0.0015	17	0.026	0.6	Cells
0.0015	19	0.016	1.2	Cells
0.0015	23	0.013	1.8	Cells, disappearing
0.0015	23	0.011	2.1	Pox
0.0015	30	0.0068	4.3	No cells
0.0046	23	0.017	1.3	Cells
0.0046	28	0.010	2.8	Pox
0.0046	31	0.0068	4.6	No cells, growth structure
0.0046	31	0.0063	5.7	Pox
0.012	31	0.0063	4.8	Cells
0.012	42	0.0063	6.8	Cells
0.012	44	0.0063	7.0	Cells
0.012	70	0.0063	11	Pox
0.012	50	0.0063	8.0	Cells, disappearing
0.012	56	0.0063	8.9	Pox

Observations and Results

The results obtained for lead in tin are listed in Table I. If these results are plotted as C_o vs G/R, a curve is obtained as shown in Fig. 2. It may be seen that, for low solute concentrations, cells may be eliminated at low values of G/R, but for higher solute concentrations it takes a higher value of G/R in order to avoid the formation of the cellular structure. Thus, if it is desirable to eliminate the cellular structure for a given solute concentration, it is necessary to raise the G/R ratio by increasing the gradient and/or decreasing the rate of solidification.

The substructures observed on the decanted interface were different, depending upon the conditions used during the solidification process. If the specimens were produced under conditions to the extreme left of the curve in Fig. 2, then the cellular structure appeared regular and well developed, as shown in Fig. 3. When the specimens were produced under conditions to the left of, but near, the curve, the hexagonal pattern becomes irregular, as shown in Fig. 4. As the curve is approached, the cell size changes and some cells become much enlarged, Fig. 5, or elongated, as shown in Fig. 6. As the boundary is crossed, the cells disappear, as seen from Fig. 7. To the extreme right of the transition region, there are no cell boundaries present but evidence is seen of the crystallographic steplike structures investigated by Elbaum,[5] as shown in Fig. 8. At the right, but near, the curve, an inter-

Fig. 7—Cellular structure of the interface disappears as the curve of Fig. 2 is crossed. X140. Area reduced approximately 40 pct for reproduction.

Fig. 8—Interface with steplike and poxlike structures results when specimen conditions are to the extreme right of the curve in Fig. 2. X140. Area reduced approximately 40 pct for reproduction.

Fig. 9—Poxlike structure which appears when the specimen conditions are at the right, but near, the curve of Fig. 2 gives the interface a pebbly appearance. X140. Area reduced approximately 40 pct for reproduction.

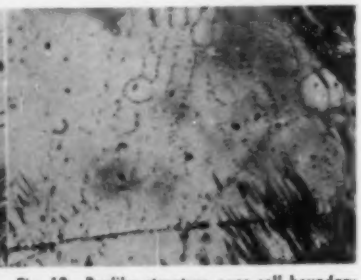

Fig. 10—Poxlike structure near cell boundary regions appears under conditions where cells begin to disappear; see Fig. 9. X140. Area reduced approximately 40 pct for reproduction.

esting structure appears, Fig. 9, which gives the interface a pebbly appearance. This poxlike structure is shown to possess the following properties:

1—It appears near the transition region.

2—The number of pox decreases as conditions move to the right of the transition region.

3—The structure depends upon crystallography, i.e., it does not appear when the steplike structure is present. This is demonstrated in Fig. 8, where two different crystal faces are present in the interface.

4—The structure does not coexist with cells.

5—The structure appears under the conditions where cells begin to disappear, as shown in Fig. 10. When the cells have disappeared, the poxlike structure exists, as shown in Fig. 9.

6—The poxlike structure consists of an irregular array of projections on the interface. The projections are much smaller than the cells.

Discussion

It appears that the *poxlike* structure is the first manifestation of the redistribution of solute in order to eliminate a small amount of constitutional supercooling. When the amount of solute is too large to be redistributed by the poxlike structure, then the cellular structure appears.

From the appearance of the curve in Fig. 2, it seems that the theoretical prediction for cell formation by Tiller et al.,[3] as given in Eq. 4, is at least qualitatively correct. If it is assumed that the equation is quantitatively correct, then it is possible to calculate a diffusion coefficient for the solute in the solvent. The values used to obtain the diffusion coefficient are obtained from the equilibrium diagram and from the experimental results; these are listed in Table II. The diffusion coefficient obtained is 2.0×10^{-4} sq cm per sec. This value is lower than the 3.68×10^{-4} sq cm per sec value given by Jost[9] for the diffusion coefficient at 500°C. However, the diffusion coefficient for 232°C can be computed by using Jost's value at 500°C and an activation energy of 1.4 kcal per mol (the activation energy of viscous flow). This calculated coefficient is 2.3×10^{-4} sq cm per sec, which is in excellent agreement with the coefficient of 2.0×10^{-4} sq cm per sec obtained by the use of Eq. 4.

Table II. Data Used to Obtain Diffusion Coefficients for Lead in Liquid Tin

Solute	k	m	C_o, R/G	D, Sq Cm per Sec
Lead	0.13	2.1	1.5×10^{-4}	2.0×10^{-4}

The fact that the diffusion coefficient as calculated from Eq. 4 appears to be correct is further proof of the validity of the theoretical work of Tiller et al.[3]

Since the transition from a plane interface to a cellular interface depends upon the concentration of solute present in the melt, this technique may be used to give a measure of the purity of any material. It is readily seen from Fig. 2 that for every C_o there is a definite G/R ratio which must be exceeded before the cellular structure can be eliminated. If, for a given system, the curve of Fig. 2 is known or can be evaluated, then it is possible to measure the composition of a true binary alloy by determining experimentally the value of G/R at which the plane interface becomes unstable. On the other hand, if the impurities present are not known, it is still possible to evaluate the purity of the material. For any alloy, a critical value of G/R can be determined experimentally. By substituting this value in Eq. 4, a concentration C_o can be calculated for assumed values of k and m. If the effects of the impurities do not cancel each other, the maximum amount of any given impurity whose k and m values are known can be estimated.

Acknowledgments

This work has been carried out in the Dept. of Metallurgical Engineering, University of Toronto, as part of the study of segregation in metals. The authors are indebted to Canadian Patents and Development Ltd., the National Research Council, Canada, and the Defence Research Board, Canada, Grant 183, for financial assistance.

Discussion of this paper, if any, will appear in JOURNAL OF METALS, May 1956, and in AIME Metals Branch *Transactions*, Vol. **206**, 1956.

References

[1] M. J. Buerger: *Ztsch. für Kristallographie* (1934) **89**, p. 242.

[2] R. B. Pond and S. W. Kessler: *Trans.* AIME (1951) **191**, p. 1156; JOURNAL OF METALS (December 1951).

[3] J. W. Rutter and B. Chalmers: *Canadian Journal of Physics* (1953) **31**, p. 15.

[4] W. A. Tiller, K. A. Jackson, J. W. Rutter, and B. Chalmers: *Acta Metallurgica* (1953) **1**, p. 428.

[5] C. Wagner: *Trans.* AIME (1954) **200**, p. 154; JOURNAL OF METALS (February 1954).

[6] W. G. Pfann: *Trans.* AIME (1952) **194**, p. 747; JOURNAL OF METALS (July 1952).

[7] B. Chalmers: *Canadian Journal of Physics* (1953) **31**, p. 132.

[8] C. Elbaum: Ph. D. Thesis, University of Toronto (1954).

[9] W. Jost: *Diffusion*. (1952) p. 479. New York. Academy Press.

Some Aspects of Slip in Germanium

by R. G. Treuting

Germanium single crystals strained in tension at 600°C slip on the {111} plane and, macroscopically at least, in the <110> direction. Deformation is inhomogeneous: various localized rotations are observed, as is a banding consistent with secondary slip banding. The structure after deformation is polygonized with a domain size of about 2×10^{-3} cm. In relaxation tests, an incubation period prior to flow is observed, of duration inversely related to temperature and applied stress. Under continuous loading, there is a sharp first yield point. A critical resolved shear stress therefore must be cited with respect both to temperature and to rate of loading. At 600°C, when loading proceeds at 2900 psi per min, it is 1310 psi. The yield point phenomenon is suggestive of Cottrell's solute atom atmosphere theory and five points of qualitative agreement with this theory are found.

PLASTICITY of germanium at elevated temperatures has been reported by Gallagher,[1] who ascribed it to slip on {111} planes and described some associated effects. Preliminary experiments with single crystals of silicon and germanium loaded as simple beams confirmed {111} as the slip plane of both materials.[2] This was demonstrated by the standard technique employing traces on two surfaces of known angle on a deformed crystal of known orientation.[3] These experiments did not fix the slip direction, since more than one glide system operated. Uniaxial tensile straining is preferred for this purpose in order to restrict slip to one predominant system and to provide an unequivocal determination of the orientation change with respect to the stress axis.

Experimental Method

Specimens were diamond-sawed from germanium crystals containing about 5×10^{-4} wt pct Sb prepared by the zone-leveling process described by Pfann and Olsen;[4] these specimens measured about 8½ in. long, 0.20 in. wide, and were of various thicknesses from 0.035 to 0.060 in. Prior to testing, a specimen was coated over 1 in. or more of length at each end with Apiezon wax, chemically polished (in a solution of 15 ml HF, 25 ml HNO_3, 15 ml CH_3COOH, and 3 to 4 drops Br_2), and dewaxed in warm xylene. A brief re-etching after scribing through a complete wax coating with vernier dividers provided gage marks at 0.200 in. intervals on the polished surface.

A specimen with grips soft soldered to the ends was passed through the furnace tube and the grips pinned to the tensile machine in series with a stress gage. The Schopper testing machine is best described by reference to the illustration on p. 107 of Schmid and Boas[5] and is operated with the pendulum arm locked, fixing the upper head. Load is applied through the screw-driven lower head, manually or by reduced speed motor.

The furnace is 2½ in. long surrounding a 4x7/16 in. ID quartz tube and was positioned about the specimen to permit free motion. The inert or reducing atmosphere required was sufficiently provided by a flow of helium introduced at the center of the furnace tube, with the tube ends loosely plugged with asbestos paper. Surface corrosion was slight.

The stress gage employs a Be-Cu strip with SR-4 units incorporated in a simple bridge network with provision for balancing and calibrating. The bridge output on loading is fed through a Leeds and Northrup dc amplifier to a Speedomax 10 mv recorder, and calibration is obtained by dead loading.

Experiments of two types have been conducted. Most have been in relaxation at constant elongation. One stress-strain curve has been taken with the machine continuously driven.

Following extension of a specimen, Laue X-ray photographs were taken to obtain the orientation change between deformed and undeformed regions, recorded on a single film by translating the specimen in a plane normal to the beam between exposures. Sequences of such multiple exposures were made on some specimens to include the entire orientation range on one film.

Slip Direction

To obtain a maximum orientation change with a single slip system, crystals of very closely <110> axial orientation were used. The classic determination of slip direction rests on establishing that direc-

R. G. TREUTING, Member AIME, is Member of the Technical Staff, Bell Telephone Laboratories Inc., Murray Hill, New Jersey.

Discussion of this paper, TP 3948E, may be sent, 2 copies, to AIME by Nov. 1, 1955. Manuscript, Aug. 31, 1954. Chicago Meeting, February 1955.

Fig. 1—Double-exposure Laue photogram shows indicated <110> zones of strained and unstrained regions intersecting in the common axis.

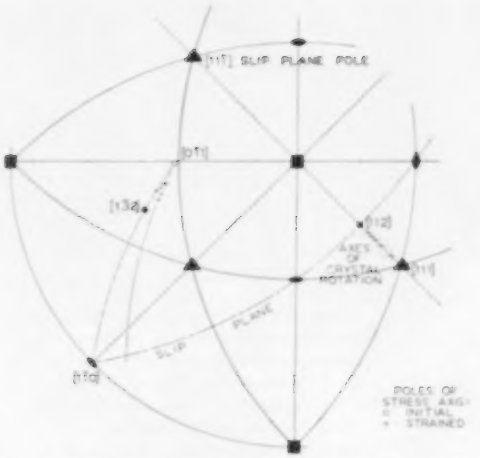

Fig. 2—Composite stereogram of five crystals shows the course of the stress axis and the axes of crystal rotation.

tion in the slip plane toward which a tensile stress axis migrates; see ref. 5, p. 84. The axis of rotation mutual to the deformed and undeformed orientations is then normal to the plane determined by stress axis and slip direction. Alternatively, workers[6] have employed the postulate that the asterism observed on Laue photographs of deformed material results from localized rotations about an axis lying in the slip plane and normal to the slip direction, the Taylor rotation.[7] In either case, any experimentally observed rotation axis should be normal to the slip direction.

In the present work, the five specimens cut parallel from the same bar were so oriented that the axis of rotation operating during deformation lay within the Laue pattern and could be well fixed, Fig. 1. In all instances, it lay essentially in a <110> zone, the axis of which was situated in the operative slip plane as determined independently from the visible slip lines. The location of the rotation axis in this zone always lies between the latter's intersection with the slip plane and its intersection with the plane normal to the stress axis, Fig. 2. This shows the location of the stress axis in five specimens at varying degrees of strain. The axes of rotation are shown between the [112] and [111] poles. (Some small variations in initial orientation due to slightly different positioning of successive specimens with respect to the X-ray beam have been eliminated by rotating to a common initial orientation. The range in orientation in each specimen is unchanged in so doing.)

The primary slip plane as determined by visible slip traces is the $(11\bar{1})$ in Fig. 2. The migration of the stress axis with increasing strain in the case of two specimens is along a great circle path directly toward the $[1\bar{1}0]$ direction in this plane. The other locations tend to define a great circle intersecting the slip plane some 7° toward $[2\bar{1}1]$ from the $[1\bar{1}0]$. All observed deviations in path from an ideal $[1\bar{1}0]$ have been in this sense.

The measured elongation of the central section of one specimen was 31.5 pct. Laue photographs of this region showed such diffuse spots due to the orientation range as to be beyond plotting, but had well developed Debye rings. A rod was therefore cut parallel to the stress axis and a rotating crystal pattern taken, Fig. 3. The pattern exemplifies a highly developed texture and indexes to a <123> rotation axis, i.e., stress axis. The location of the $[1\bar{3}2]$ pole is shown in Fig. 2. It lies on the great circle between a $[0\bar{1}1]$ initial stress axis and the $[1\bar{1}0]$ direction.

Applying the Schmid-Boas formula[8] to this case, with $[1\bar{1}0]$ as the slip direction, the calculated strain is 31.3 pct, in close agreement with the measured strain of 31.5 pct.

Banding

The elongation of Laue spots, now generally termed asterism, was observed frequently but not consistently in the photographs of deformed regions. The local rotations represented by such elongated

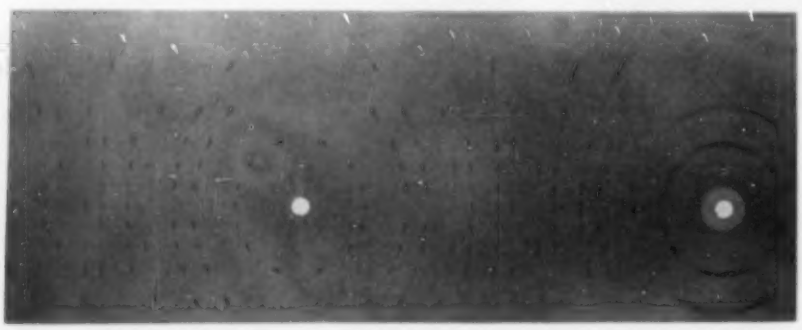

Fig. 3—Rotating crystal pattern is given for crystal extended 31.5 pct. Rotation axis is the stress axis, indexing <123>. Taken with copper radiation, nickel filter.

spots do not all have the same axis of orientation. Figs. 4a, 4b, and 4c give stereographic projections of three crystals. In the case of Fig. 4c, the direction of spot extension closely parallels a major zone. In the case of Figs. 4a and 4b, the axes of local rotations were located within a radius of perhaps 5°, with a more restricted most probable location.* The assortment of local rotations typifies the inhomogeneity of deformation found in germanium after even relatively small strains under the present conditions.

* The optimum determinations were made by plotting stereographically the zonal envelopes of the termini of the elongated spots and their zone axes. The set of great circles passing through 1—the intersection of a pair of the envelope zones and 2—the angular midpoint of the respective zone axes, then intersect at the axis common to the two orientations represented.

In the case of the crystal of Fig. 4c, the $[1\bar{2}1]$ axis of local rotation is consistent with slip on the (111) cross-slip plane in the nonprimary $[\bar{1}01]$ direction. This, however, lies also in the $(1\bar{1}1)$ conjugate slip plane. The possibility of conjugate slip is suggested by Fig. 5 and recent findings of Honeycombe.[6] Fig. 5 is an X-ray micrograph after Barrett,[7] taken on a specimen cut axially from the crystal of Fig. 4c after this had experienced a crystallographically calculated[8] resolved shear strain of 0.35 and was lightly ground smooth and chemically polished. The stress axis is horizontal, and the micrograph is a positive, i.e., lighter areas are those of greater diffracted intensity. Confirming the orientation of the specimen in situ has shown that the traces of the primary slip planes are the somewhat vague light lines roughly parallel to the dark bands, running from upper right to lower left. Honeycombe with a similar technique has found in aluminum crystals strained in tension "bands of secondary slip," the banding roughly parallel to the primary slip plane and the slip on a conjugate plane. For the original orientation of this crystal, the resolved shear stress for an axial stress σ_o is 0.43 σ_o in the primary $(11\bar{1})[1\bar{1}0]$ system and 0.39 σ_o in the conjugate $(1\bar{1}1)[\bar{1}01]$ system. These values are very close to those recorded by Honeycombe for an aluminum crystal of apparently similar orientation in which bands of secondary slip were observed.

Such bands of secondary slip and the streaking plotted in Fig. 4c suggestive of local rotations in the cross-slip plane have the $[\bar{1}01]$ direction in common. As the Laue photograph was not necessarily taken directly on a banded region, the two possibilities are not mutually exclusive and, together with the observations of the other local axes described, may all be possible inhomogeneities in the plastic deformation of germanium.

Polygonization

Reverting to Fig. 5, the alternate array of sharply defined lines disposed normal to the primary slip lines and secondary slip bands are noted. Also, in the rotating crystal pattern, Fig. 3, all the higher angle $K\alpha$ doublets are clearly resolved, although the Laue pattern for this specimen was broadly diffused. Coexistence of these aspects indicates a structure of very small volumes of strain-free material of progressively slightly different orientation, as in polygonization.[9] The finer boundaries of Fig. 5, approximately normal to the slip traces, are consistent with this.

With a magnification in Fig. 5 of X70, the average width of the delineated domain is about 0.02 mm, considerably smaller than the usually reported dimensions of a polygon. However, E. S. Greiner and P. Breidt, Jr.[10] have shown that germanium single crystals deformed 24 pct in compression at 900°C have a microstructure consisting of small volumes of linear dimensions of about 3×10^{-4} cm. The size of these domains is a function of the temperature of deformation, but in their work the size was not observed to increase perceptibly on subsequent high temperature annealing. The specimen of Fig. 5 was deformed in tension 19 pct at 600°C and held at this temperature about 2 hr.

F. L. Vogel[11] has now reported a micrographic and X-ray study on dislocations in bent germanium. His micrographs of dislocation etch pits reveal a block structure aligned normal to the slip planes at temperatures of deformation of 650°C and above. Vogel regards the array of "slightly misoriented blocks" as evidence for polygonization and gives a size of 10^{-4} cm from both optical and X-ray evidence. Thus, there is substantial agreement on the polygonized domain size among the three separate studies.

Dynamics of Flow

The dynamic behavior of germanium is quite sensitive to rate of strain. This is associated at the outset with the incubation period under stress prior to flow reported by Gallagher[1] and invariably confirmed in the present series of experiments. During the incubation period, the rate of decline of load at fixed elongation is very small. In at least one

a b c

Fig. 4—Stereographic projections (a, b, and c) are given for patterns of strained germanium crystals with axes of local rotations. In cases of elongation of Laue spots, the local rotations represented by such elongated spots do not all have the same axis.

crystal of <112> orientation studied, the load-time slope was horizontal and the incubation period terminated abruptly. In the <110> orientation, termination of incubation has been marked by a continuous transition over a few seconds to a very rapid exponential decay of stress with time. Incubation periods are given in Table I together with the applicable temperatures and initial applied stresses. An inverse relationship to temperature and to applied stress is found.

Stress-decay rates will not be given in this paper except to note that, on repeated loading to the same initial stress following relaxation to some given fraction thereof, the decay rate decreases—i.e., the time to relax the fixed fraction of stress increases. Germanium work hardens. On annealing free of load (for example, for 2 hr at 750°C after straining at 600°C), the rate of stress relaxation at 600°C is increased, but not to its initial value, and decreases as before on further straining. A part of the work hardening is recoverable, presumably in conjunction with polygonization, but restoration of the virginal mechanical properties is no more observed than is recrystallization.

The incubation period under fixed strain is paralleled by a sharp yield point under continuous loading. As the strain first increases nearly linearly in time, the required incubation period is abbreviated simultaneously with the elapsed time under load; and when yielding occurs, it is cataclysmic, with an abrupt drop in stress. Hence, a critical resolved shear stress for slip in germanium is incompletely meaningful unless the loading rate is specified. In the specimen continuously loaded, the yield point at 600°C of 3140 psi was attained in 65 sec, a loading rate of 2900 psi per min. The softness of the machine makes the strain rate inexact, but, on calibrating the machine with a test bar, an approximate rate of elongation of 0.003 in. per min was derived. Under these conditions, the resolved shear stress at yield was 1310 psi.

The abrupt yield point is followed by a strain-hardening curve of normal appearance, and the stress-strain curve as a whole is highly suggestive of the yield point phenomenon in mild steel and of the mechanism for the latter proposed by Cottrell.[10] In particular, on an immediate reloading after release of stress, the sharp first yield point is no longer evident.

Table I. Incubation Periods for Flow of Germanium in Relaxation <110> Orientation

Temperature, °C	Applied Stress, Psi	Incubation Period, Sec
600	900	185 (Approx.)
600	1330	150 (Approx.)
600	1970	80
600	2370	42
650	1340	35
600	—	Imperceptible

It is felt that the plastic behavior of germanium affords a singular opportunity for quantitative comparison with Cottrell's theory. This paper is confined to mention of five points of qualitative agreement:

1—Absence of the sharp first yield on immediate reloading is the first point.

2—The yield point is found in dilute solutions, for example, 10^{-6} to 10^{-5} wt pct C in iron. Zone-leveled

Fig. 5—X-ray micrograph taken of the crystal represented by the stereographic projection of Fig. 4c. Stress axis was horizontal. Positive print. X70. Area reduced approximately 65 pct for reproduction.

germanium is assuredly sufficiently dilute; the question is whether it is too dilute for the mechanism to apply. (The present specimens contained about $5.x10^{-6}$ wt pct Sb. Assuming a dislocation density of 10^4 per sq cm,[14] a solute concentration of the order of about 10^{-4} wt pct would be sufficient.) Since in germanium there is opportunity for both electrical and elastic interaction between dislocations and solute atoms, it is suggested that increased force may here produce the yield point at lower impurity concentrations.

3—The theory predicts a sharp dependence of yield point on temperature, which in the case of germanium follows from the temperature dependence of the incubation period.

4—The incubation period and its stress dependence are consistent with the theory and are as found in experiments of Wood and Clarke on mild steel, cited by Cottrell.[10]

5—The banding observed and local rotations described are consistent with the condition of initial yielding in regions of high stress concentration.

Summary

1—Germanium deforms by slip on the {111} plane and, on a macroscopic scale, in the <110> direction.

2—Slip in a tensile-strained single crystal is accompanied by local rotations, some of not readily rationalizable description.

3—One specific kind of local rotation observed is describable as that conforming to kinking with respect to a cross-slip plane or to secondary slip banding parallel to the primary slip plane. There is X-ray micrographic evidence of such banding.

4—Germanium polygonizes concurrently with or immediately following tensile deformation at temperatures as low as 600°C. The block domains are of linear dimensions of the order of $2x10^{-4}$ cm, essentially the same as found by other workers.

5—Germanium crystals loaded to constant stress in tension undergo an incubation period prior to any substantial plastic flow, the duration of which varies inversely with temperature and applied stress.

6—Associated with the incubation period, there is a sharp first yield point under continuous loading which is not obtained on immediate reloading, similar to mild steel.

7—On continued straining, germanium work hardens and is only partially softened by annealing,

which can result[16] in further degree of polygonization.

8—The yield point behavior is qualitatively consistent with Cottrell's solute atom atmosphere theory of the sharp yield point.

Acknowledgments

The writer is happy to acknowledge the aid of Jacqueline F. Breidt in conducting much of the experimental work; of his colleagues, E. S. Greiner, P. Breidt, Jr, and F. L. Vogel in making their own data available to him; and of W. C. Ellis, J. N. Hobstetter, and D. F. Gibbons in helpful discussions and debate.

Discussion of this paper, if any, will appear in JOURNAL OF METALS, May 1956, and in AIME Metals Branch *Transactions*, Vol. **206**, 1956.

References

[1] C. S. Gallagher: *Physical Review* (1952) **88**, 2nd series, p. 721.

[2] R. G. Treuting: *Research in Progress Report* Inst. of Metals (1952) **4**, p. 1044.

[3] C. S. Barrett: *Structure of Metals*. (1952) 2nd Ed. New York. McGraw-Hill Book Co. Inc.

[4] W. G. Pfann and K. M. Olsen: *Physical Review* (1953) **89**, p. 322.

[5] E. Schmid and W. Boas: *Kristallplastizitaet*. (1935) Berlin. J. Springer.

[6] N. K. Chen and C. H. Mathewson: *Trans.* AIME (1951) **191**, p. 653; JOURNAL OF METALS (August 1951).

[7] G. I. Taylor: *Trans.* Faraday Soc. (1928) **24**, p. 121.

[8] W. H. Honeycombe: *Journal* Inst. of Metals, London (1952) **80**, p. 49.

[9] C. S. Barrett: *Trans.* AIME (1945) **161**, p. 15; METALS TECHNOLOGY (April 1945).

[10] R. W. Cahn: *Journal* Inst. of Metals, London (1949) **76**, p. 121; *Proceedings* Physical Soc., London (1950) **63A**, p. 323.

[11] E. S. Greiner and P. Breidt, Jr.: Private communication.

[12] F. L. Vogel: *Acta Metallurgica* (1955) **3**, p. 95.

[13] A. H. Cottrell: *Dislocation and Plastic Flow in Crystals*. (1953) p. 139. Oxford. Oxford University Press.

[14] F. L. Vogel: Private communication.

Bauschinger Effect in Creep and Tensile Tests on Copper

by J. D. Lubahn

The *Bauschinger effect*, or rounding of the corner of the stress-strain curve upon reloading, represents a temporary apparent softness that is more pronounced at large strains than small and for complete unloading than for partial unloading. Interrupted creep tests on copper exhibit a similar temporary softness (high creep rate) upon reloading. The fact that the strainwise dying-out time of these effects is the same in both tensile and creep tests shows that they are related. Thus, the term *Bauschinger effect* appears to embrace behavior following partial or complete unloading and reloading in addition to behavior following reversed loading. It is suggested that the term may properly apply also to certain creep behaviors following a small load decrement.

INTERRUPTED tensile tests at low temperatures show[1] a rounding of the corner of the stress-strain curve for reloading, which indicates a temporarily low deformation resistance. In the absence of recovery, the curve soon rises to the value that would have prevailed if the test had not been interrupted. The rounding of the reloading tensile curve has sometimes been referred to[2] as the *Bauschinger effect*, although the term is more commonly applied to low deformation resistance in compression following tensile prestrain. The unusually broad usage of the term *Bauschinger effect* in ref. 1 seems justified by the obvious interconnection of the various behaviors to which it has been applied.[1] In fact, the following discussion will indicate that still broader usage might be desirable.

J. D. LUBAHN is associated with Metallurgy and Ceramics Research Dept., Research Laboratory, General Electric Co., Schenectady.

Discussion of this paper, TP 4006E, may be sent, 2 copies, to AIME by Nov. 1, 1955. Manuscript, Sept. 2, 1954. Chicago Meeting, February 1955.

The Bauschinger effect is common at room temperature but apparently disappears at higher temperatures.[4]

Interrupted creep tests and tensile tests were made on certified OFHC copper (nongaseous impurities exclusive of silver were 0.004 pct), cold drawn 84 pct to ½ in. diam, and annealed at 600° (about 0.025 mm grains) or 850°C (about 0.2 mm grains). The tests were made in standard creep or tensile machines, using an O.S. Peters microformer-type extensometer or, for the small plastic strains, a special arrangement employing General Electric magnetic gage heads.[5]

Interrupted creep tests at room temperature show[3, 4] an initial softness after reloading, manifested by an initial creep rate that is higher than that which would have prevailed if the test had not been interrupted. Fig. 1 shows some typical examples. This effect is apparently temporary (as is that in tensile tests): in four of the five tests shown, the log rate vs strain curve becomes parallel to an

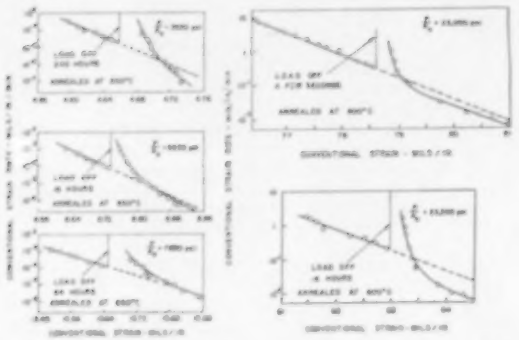

Fig. 1—Interrupted creep tests at room temperature on certified OFHC copper, cold drawn 84 pct, and annealed 1 hr at the temperature shown. See also refs. 3 and 4.

extension of the part of the curve that precedes unloading; and in the fifth test, the reloading curve appears to be approaching a parallel curve.*

* Note that the reloading curve approaches a curve which is lower than an extension of the prior curve. This tendency indicates that some strengthening has occurred while the load was off. The magnitude and significance of this strengthening are pertinent to another investigation, but not to this one, and are discussed elsewhere.

A possible relation between the temporarily low stress after interrupting a tensile test and the temporarily high rate after interrupting a creep test may be indicated by a consideration of the strain increments for dying-out of the effect. Fig. 2 shows that the strain increment required for the Bauschinger effect to die out in tensile tests on copper increases with increasing strain. This trend is indicated in Fig. 3, where the data from Fig. 2 have been summarized, as well as the results of all the interrupted creep tests from refs. 3 and 4. Fig. 3 shows that the strain increment for dying-out varies with strain in the same way for both the tensile testing effects of Fig. 2 and the creep testing effects of Fig. 1. Apparently the two effects are related to each other.

The effects described previously were obtained following complete unloading prior to reloading. The effects following partial unloading are similar but not quite as pronounced (Fig. 4). The magnitude of the effects diminishes continuously as the percentage of load removed decreases, but a pronounced

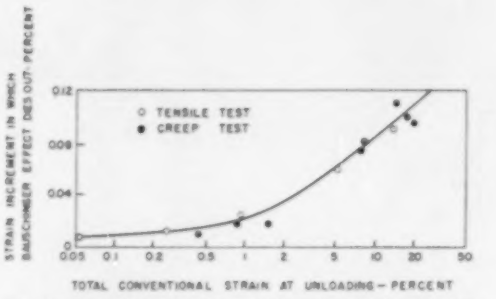

Fig. 3—Comparison of dying-out times for the Bauschinger effect in creep and tensile tests on OFHC copper.

effect still remains even when only a small fraction of the load has been removed.

The foregoing effects following partial unloading may be similar to previously observed[4] departures from *plastic ideality*† following very slight unloading. According to this earlier investigation, the elongation rate diminished with elongation much more rapidly after a load decrement than after a load increment. How rapidly the elongation rate ($\dot{\delta}$) diminishes with elongation (δ) in a constant load test may be represented by the quantity $(\partial \log_m \dot{\delta}/\partial \delta)_p$, where p is load. Fig. 5 shows a particularly striking example of this effect and Fig. 6 summarizes the results of creep test following both load increments and load decrements.

† *Plastic ideality*, as defined in ref. 4, implies that the plastic behavior depends only on the current conditions, and not on past history, such as prior temporary unloading. Thus, the Bauschinger effect constitutes a departure from plastic ideality.

The effect was apparently temporary,[4] however, because one test continuing through a much larger strain increment than the others (Fig. 7) showed an eventual decrease in the rate of diminution of creep rate. The slope eventually reached in the test of Fig. 7—the value of $(\partial \log \dot{\delta}/\partial \delta)_p$,—is shown by the filled circle in Fig. 6, which has a position near the trend line that characterizes the behavior following a load increment.

Thus, for copper, the creep characteristics following a small load decrement are similar in certain respects to those following partial or complete unloading and reloading; there is a temporarily high rate of change of the creep rate with strain. This

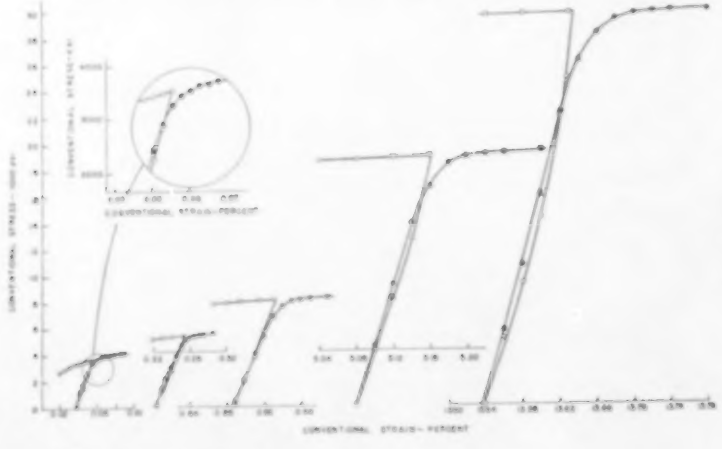

Fig. 2—Interrupted tensile test on certified OFHC copper, cold drawn 84 pct, and annealed 1 hr at 600°C.

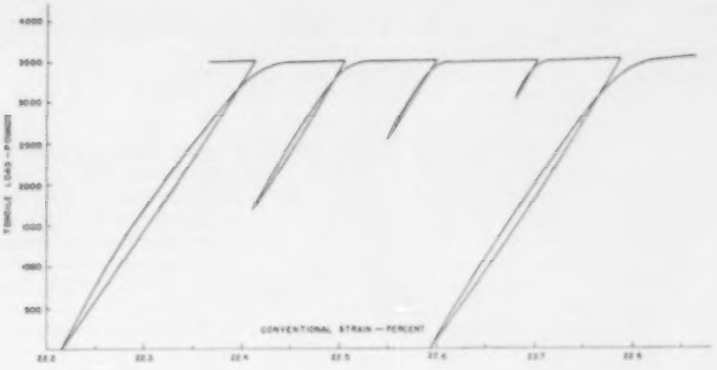

Fig. 4—Interrupted tensile test on certified OFHC copper, cold drawn 84 pct, and annealed 1 hr at 850°C. Initial diameter was 0.300 in.

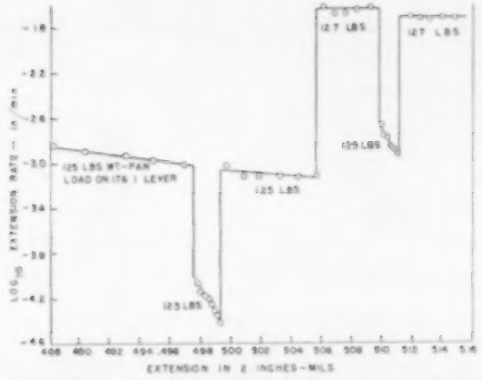

Fig. 5—Room temperature transient experiment on OFHC copper annealed at 600°C in which a small load was alternately added and removed. Initial diameter was 0.300 in. Data from Lequear and Lubahn.[4]

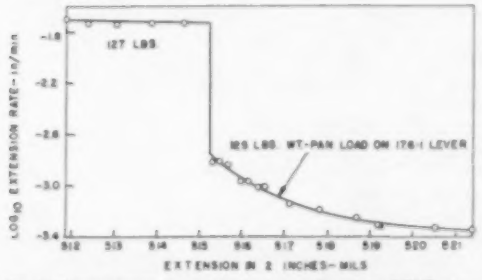

Fig. 7—Room temperature transient experiment on OFHC copper annealed at 600°C showing creep behavior following a load decrement. Initial diameter was 0.300 in. Data from Lequear and Lubahn.[4]

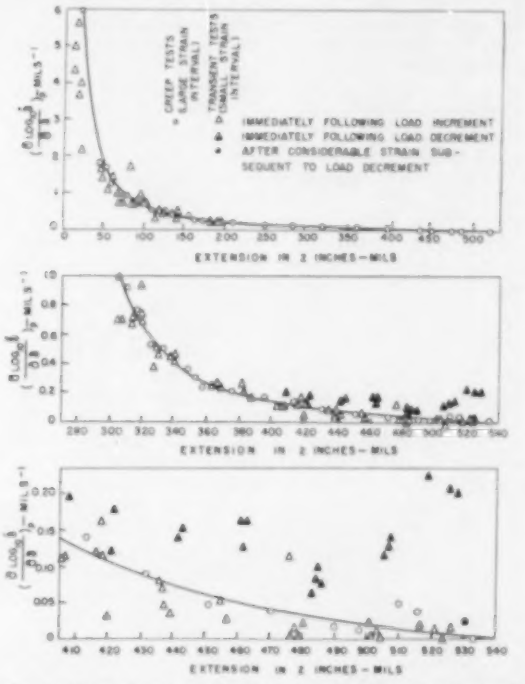
CREEP TESTS (LARGE STRAIN INTERVAL)
TRANSIENT TESTS (SMALL STRAIN INTERVAL)
IMMEDIATELY FOLLOWING LOAD INCREMENT
IMMEDIATELY FOLLOWING LOAD DECREMENT
AFTER CONSIDERABLE STRAIN SUBSEQUENT TO LOAD DECREMENT
EXTENSION IN 2 INCHES—MILS

Fig. 6—Effect of strain level on the slope of log extension rate vs extension curves from creep tests on OFHC copper annealed at 600°C. Lower curves are magnifications of upper curves. Data from Lequear and Lubahn.[4]

similarity suggests that the behaviors under the two circumstances are both manifestations of the same basic phenomenon; and perhaps, therefore, the behavior corresponding to the abnormally high filled triangles in Fig. 6 should be included as part of what is called the Bauschinger effect.

Acknowledgment

This work was performed under support of the Aeronautical Research Laboratory, Wright Air Development Center, Contract No. AF 33(038)-11773.

Discussion of this paper, if any, will appear in JOURNAL OF METALS, May 1956, and in AIME Metals Branch *Transactions*, Vol. **206**, 1956.

References

[1] J. J. Lynch, E. J. Ripling, and G. Sachs: Effect of Various Stress Histories on the Flow and Fracture Characteristics of the Aluminum Alloy 24ST. *Trans.* AIME (1948) **175**, p. 435; METALS TECHNOLOGY (January 1948).

[2] H. A. Lequear and J. D. Lubahn: Recovery and Creep in an Alloy Steel. Symposium on Strength and Ductility of Metals at Elevated Temperatures. *ASTM Special Technical Publication No. 128*. (1953) Philadelphia. ASTM.

[3] H. A. Lequear and J. D. Lubahn: Certain Departures from Plastic Ideality at Small Strains. *General Electric Research Laboratory Report RL 937* (November 1953).

[4] H. A. Lequear and J. D. Lubahn: Certain Departures from Plastic Ideality at Large Strains. To be published, ASTM. See also, *General Electric Research Laboratory Report RL 989* (December 1953).

Zirconium-Columbium Diagram

by B. A. Rogers and D. F. Atkins

The constitutional diagram presented herein is relatively simple. Complete mutual solid solubility exists for an interval below the solidus line, a continuous curve with a flat minimum near 22 pct Cb and 1740°C. Upon cooling, the solid solution breaks up, except at the columbium-rich side, from two causes: zirconium-rich alloys transform under the influence of the β-α transformation in zirconium; alloys of intermediate composition decompose into two solid solutions below 1000°C. The combined effect is the formation of a eutectoid at a temperature of 610°C and a composition of 17.5 pct Cb. The eutectoid horizontal extends from 6.5 to 87.0 pct Cb. Some age hardening effects have been observed in the zirconium-rich alloys but the positions of the solvus lines remain uncertain.

IN recent years, zirconium has been produced in much larger quantities than were available previously. Correspondingly, the incentive for studying its alloy systems has increased, as the number of recent publications on alloy systems testifies. However, only a partial diagram of the Zr-Cb system has been published and relatively few references have been made to alloys of the two metals.

Hodge[1] investigated the Zr-Cb system up to about 25 pct Cb. His data on melting points were not sufficiently numerous to distinguish with certainty between the alternatives of a narrow eutectic horizontal and a wide flat minimum in the solidus curve. Although Hodge considered his results on transformations in the solid state to be only tentative, he suggested that the eutectoid in the zirconium-rich alloys lay at about 625°C and 10 pct Cb and estimated that the solubility of columbium in zirconium at 625°C was near 6 pct.

According to Simcoe and Mudge,[2] less than 0.5 pct Cb is soluble in zirconium at 800°C. These authors observed an increased strength in both the 0.5 and 1 pct Cb alloys made with hafnium-containing zirconium. According to Keeler,[3] the strength of zirconium is increased by addition of columbium to a content of at least 3 pct. Keeler[4] also observed a maximum in hardness at about 10 atomic pct Cb and commented on the brittleness of alloys of this composition. Anderson, Hayes, Roberson, and Kroll[5] investigated the tensile properties of Zr-Cb alloys containing 5.1 and 12.9 pct Cb at room temperature and at 343°C. The 12.9 pct alloy had a high tensile strength at room temperature but also a low percentage of elongation. All alloys had high elongation at 343°C. Litton[6] measured strength and elongation values of annealed alloys containing up to 27.5 pct Cb and found low elongation values for all of the alloys of high columbium content. Some observations on the resistance of Zr-Cb alloys to corrosion in water at high temperature have been published by Lustman, De Paul, Glatter, and Thomas[7] who found that additions of columbium up to 1 pct had only a minor effect on the corrosion resistance of zirconium.

Preparation of the Alloys

Raw Material: Zirconium of a relatively good grade was available for making the alloys. It was obtained as scrap pieces that had been left over from an operation that included production by the iodide process, melting under a protecting atmosphere, and fabrication to plates. The individual pieces had hardness values of 24 to 32 RA and a typical analysis is shown in Table I.

Table I. Spectrographic Analysis of Zirconium Used in Making Zr-Cb Alloys

Element	Pct
Aluminum	<0.003
Calcium	<0.001
Chromium	<0.003
Copper	0.005
Hafnium	<0.05
Iron	<0.02
Magnesium	<0.001
Nickel	0.002
Silicon	0.014
Titanium	<0.002

The columbium also was scrap trimmed from sheets. It was furnished by the Fansteel Metallurgical Corp. and had a high ductility but its analysis was known only approximately. The metal probably contained about 0.5 pct Ta, perhaps 0.25 pct C, and a few hundredths percent each of iron, silicon, and titanium.

Melting: The alloys were melted in a tungsten-electrode copper-crucible arc furnace similar to units that have been described recently in the metallurgical journals.[8,9]

The crucible of this furnace is provided with a cavity in which a getter charge can be melted before the melting of the alloy charges. Hardness measurements on the ingots indicate that the getter charge takes up a considerable fraction of the oxygen and nitrogen from the helium atmosphere of the furnace.

The alloys used in the investigation are given with their intended compositions, hardness, and melting points in Table II.

Fabrication: All alloys of the Zr-Cb system appear to be amenable to fabrication. At least, all of the compositions listed in Table II could be reduced to wires in a rotary swaging machine. The starting material was either slabs cut from ingots and ground by hand to rough cylinders or narrow strips trimmed from sheets made by cold rolling slabs.

However, not all of the alloys could be fabricated satisfactorily by the same method. From 0 to 4 pct Cb and from 20 to 30 pct Cb or more, the alloys could be swaged cold from ¼ in. cylinders to 0.80 mm wires with only one intermediate annealing, sometimes with none. From 40 to 90 pct Cb, the alloys were difficult to swage either hot or cold but could

B. A. ROGERS, Member AIME, and D. F. ATKINS are associated with the Inst. for Atomic Research and Dept. of Chemistry, Iowa State College, Ames, Iowa.

Discussion of this paper, TP 3991E, may be sent, 2 copies, to AIME by Nov. 1, 1955. Manuscript, Aug. 9, 1954. Chicago Meeting, February 1955.

Table II. Intended Composition, Hardness, and Melting Temperature of a Series of Zr-Cb Alloys

Alloy No.	Cb, Pct	Hardness,* Rᴀ	Melting Temperature, °C: Measured Values	Melting Temperature, °C: Average
M-748	1.0	40	—	—
M-749	2.0	53	—	—
M-942	3.0	58	—	—
M-751	5.0	63	1820, 1805, 1805	1805
M-753	5.0	63	1779	
M-615	6.0	63	1749, 1789	1770
M-606	8.0	71	1790	1790
M-618	8.0	69	—	—
M-607	10	66	—	—
M-946	10	69	1779, 1774	1775
M-608	12	61	1769	1770
M-850	13	59	1765	1765
M-851	14	60	1769	1770
M-670	15	59	1758	1765
M-852	15	60	1779	
M-868	17.5	53	1733, 1749, 1743	1745
M-855	20	54	1743, 1769	1745
M-860	20	53	1743, 1743	
M-867	22.5	53	1718, 1743	1735
M-879	25	52	1743, 1750	1745
M-678	30	58	—	—
M-680	30	58	1754, 1733, 1769, 1740	1750
M-648	40	63	1790	1790
M-743	50	64	1810	1810
M-647	60	64	1851	1850
M-741	70	65	1952	1960
M-949	75	63	—	—
M-742	80	64	2085	2085
M-948	80	62	—	—
M-870	90	—	2220	2220
M-815	100	—	2435	2435

* Refers to hardness of slab cut from ingot.

be rolled cold easily. Pieces cut from the rolled strip could then be swaged cold through several dies. Alloys from 5 to 17 pct Cb required a different treatment. They were cased in air-tight steel jackets and swaged at 800° or 825°C to rods of ⅛ to 3/16 in. diam. Then, after their jackets had been stripped off, they were cleaned and put through a two-stage heat treatment under vacuum. The first stage of this treatment consisted in a heating to 900°C at a rate slow enough to ensure that the pressure did not rise above 3×10^{-4} mm Hg, holding the rods at temperature for an hour or two, and then cooling them as rapidly as possible—to a black heat in about 2 min. In the second stage, the rods, without being removed from the furnace, were reheated to about 500°C, held at temperature for 10 or 20 hr and cooled at any convenient rate, perhaps 200°C per hour. After this heat treatment, they could be swaged cold through a reduction of 50 to 80 pct in diam.

Heat Treatment of Specimens: Heat treatments were intended to bring the alloys into one of two conditions. In the first, the alloys were cooled as rapidly as possible from 900°C after having been at the temperature for 20 hr. The cooling was sufficiently effective to retain the high temperature condition in all but the zirconium-rich compositions because the transformation becomes increasingly sluggish as the columbium content rises beyond 5 pct. The second treatment included the first treatment plus subsequent heating between 500° and 600°C for periods lasting from 60 to 400 hr. It was intended to bring the low temperature phases into equilibrium.

Apparatus and Methods

The positions of the lines in the diagram were determined mainly by the measurements of four properties. These were: 1—melting point, 2—change of electrical resistance with temperature, 3—change of length with temperature, and 4—lattice parameter. Supplementary data were obtained from hardness measurements and microscopic examination.

Melting Point: The apparatus for determination of melting point was based on a method used by Pirani and Alterthum.[10] As it has been described in a report of another investigation,[11] details are not given here.

Resistance Temperature Measurements: Variation of electrical resistance with temperature can be measured with simple apparatus. The circuit used in this investigation is illustrated in Fig. 1. If the specimen and a standard resistance are connected as shown in the figure and a constant current maintained in the circuit, then the resistances are in the same ratio as the voltage drops across them.

Dimensions of the specimens differed. Diameters varied from 0.75 to 1.33 mm and lengths, before the specimen was bent to a hairpin, were 3 to 4 in.

Dilatometric Measurements: The dilatometric curves were made on an instrument developed by Dooley and Atkins.[12] As a description of the apparatus has been published, only a few of the main features need be outlined here.

The essential element of the instrument is a linear differential transformer of which the output varies according to the position of its movable core. The coils of the transformer are held in a fixed position whereas the core is mounted on a light silica push rod that rests upon the specimen and follows its change of length. Hence, the output of the transformer is a measure of the length of the specimen. An advantage of the apparatus is that specimen, specimen support, transformer, and push rod can be contained in a tight glass and silica system that may be exhausted so that the specimen is not oxidized. Furthermore, it is readily adaptable for use with automatic function plotting devices. The apparatus used in this investigation had been designed for specimens approximately ¼ in. diam by 1 in. long.

Determination of Lattice Parameters: Although the X-ray diffraction apparatus is a composite of parts from two manufacturers, the individual parts are standard items. The camera is a standard Debye-Scherrer type with a diameter of 114.6 mm. An X-ray tube with a copper cathode was used in this investigation. The filter was a sheet of nickel.

Miscellaneous Apparatus: Metallographic and hardness testing equipment is so standardized as to require no description.

Some resistance measurements on alloy wires at room temperature were made with a Kelvin bridge. Because this apparatus is designed for heavy currents, the specimens became heated slightly above

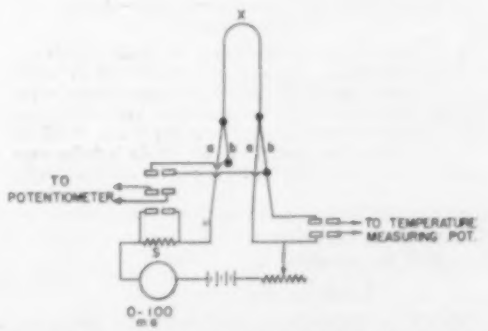

Fig. 1—Circuit used in measurements of electrical resistance. *a* represents platinum wire; *b*, Pt-Rh wire; *s*, standard 0.1000 ohm resistance; and *x*, the specimen.

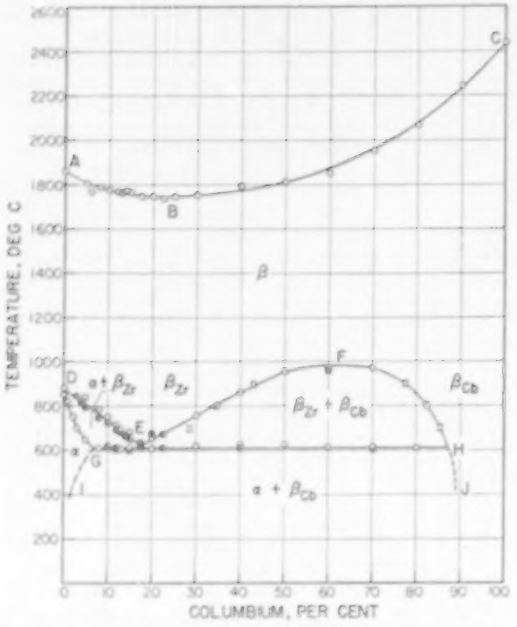

Fig. 2—Plotted data from which the Zr-Cb diagram was drawn. Open circle represents beginning of melting and also resistance temperature data; half-closed circle, dilatometric data; and square, data from X-ray patterns.

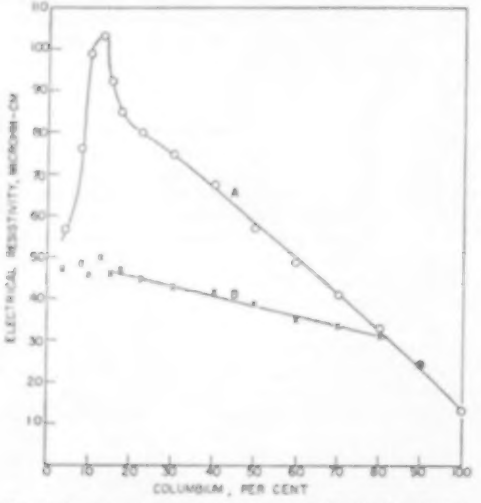

Fig. 3—Room temperature resistivity of the Zr-Cb alloys in two different conditions. Curve *A* gives resistivities of alloys cooled rapidly from 900°C. Curve *B* gives resistivities of alloys reheated after rapid cooling. Compositions from 4 to 13 pct Cb inclusive were heated at 575°C for 160 hr and 590°C for 120 hr. Compositions from 15 to 90 pct Cb inclusive were given the same treatment plus 120 additional hr at 590°C.

room temperature unless readings were taken very quickly. Frequently, measurements were interrupted so that the specimen could cool.

Results of the Investigation

General Comments on the Diagram: The results of this investigation can be described most readily from the constitutional diagram shown in Fig. 2. As suggested by the caption, the diagram is based al-

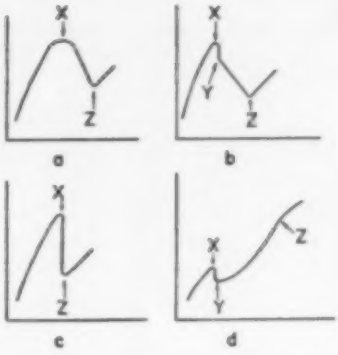

Fig. 4—Four characteristic types of electrical resistance temperature curves. a—Zirconium-rich alloys, below 6.5 pct Cb. b—Hypoeutectoid alloys, 6.5 to 17.5 pct Cb. c—Eutectoid alloy. d—Hypereutectoid alloys, 17.5 to 87 pct Cb.

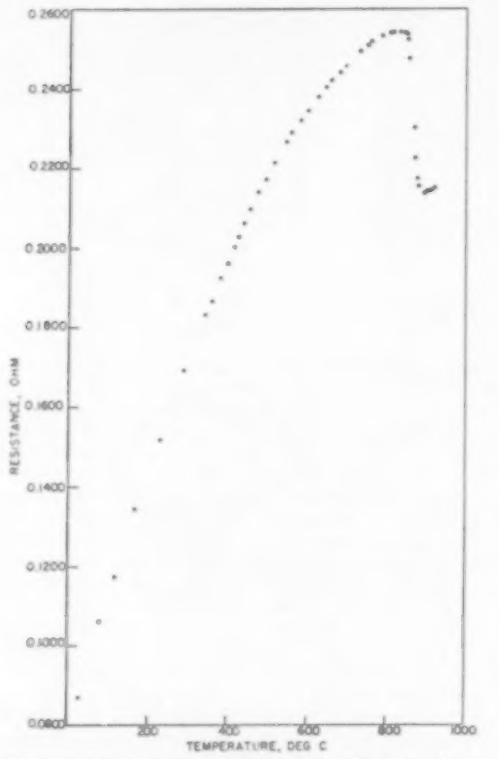

Fig. 5—Resistance temperature graph of unalloyed zirconium.

most entirely on the results obtained from dilatometric measurements, from resistance temperature graphs, and from X-ray data. Because the sluggishness of the changes in the solid alloys made thermal analysis unsatisfactory for all but the zirconium-rich alloys, the method was used very little and none of the results obtained by it have been included. Also, as considerable difficulty was encountered in obtaining properly etched surfaces, microscopic examination was of only minor value and no micrographs have been incorporated in the report.

A point to be noted is that this diagram is based on data taken with rising temperature. This restriction is the result of the sluggishness of the transformation on cooling shown by all alloys containing more than 5 pct Cb. Above 8 pct, the time required to obtain equilibrium was impractically long.

The Solidus Temperatures: Determination of the solidus points proceeded without difficulty after

early trials had indicated the need for a slow rate of heating over a temperature interval below the beginning of melting. Slow heating gave time for the specimen—cut from the button-shaped ingot—to become homogeneous. Nearly identical readings were obtained on specimens from the same ingot. The beginning of melting was signaled by the appearance of a dark spot at the bottom of the black-body hole as molten metal began seeping into it. Usually, the temperature at which the dark spot formed could be determined accurately but, in a few instances, some doubt existed as to the temperature when the spot appeared.

Corrected individual and average readings of the beginning of melting are given in Table II along with the composition and hardness of the specimen. This hardness is, of course, the hardness of the ingot.

No effort was made to determine points on the liquidus but the narrow range of melting near 20 pct Cb was observed.

Resistivity at Room Temperature: In a preliminary survey, the resistivities of the alloys in wire form were measured at room temperature with the Kelvin bridge mentioned previously. Each wire was tested in two conditions.

For the first measurement, the wire was cooled as rapidly as possible from 900°C in the manner described under the section on heat treatment. At 900°C, all of the alloys except those having columbium contents between 44 and 77 pct were in the single-phase condition. The resistivity of alloys in this interval probably was much the same whether they were cooled rapidly from 900°C or from a high temperature. At least, a 50 pct Cb alloy quenched with helium from about 1100°C had the same resistance within the limit of error of the measurements as it did after it had been cooled rapidly from 900°C in the usual manner. The results of these measurements appear as curve *A* in Fig. 3.

The wires were measured again after they had been heated to bring the α-zirconium-rich and columbium-rich phases into approximate equilibrium. That equilibrium may not have been complete was indicated by a slight decrease in resistance during the last 120 hr of a heat treatment consisting of 160 hr at 575°C plus 240 hr at 590°C. Had the heat treatments continued longer, the junction of curves *A* and *B* in Fig. 3 probably would be slightly lower than it is now placed.

Resistance Temperature Measurements: The general form of the resistance temperature graph for a Zr-Cb alloy depends upon its composition. In the four subfigures of Fig. 4, idealized characteristic graphs for four compositions are shown. Fig. 4a illustrates the type of curves for zirconium-rich alloys that do not undergo transformation at the eutectoid horizontal, that is, alloys to the left of *G* in Fig. 2. *X* and *Z* in this subfigure indicate the crossing of lines *DG* and *DE* (Fig. 2), respectively. Fig. 4b corresponds to the interval *GE*. In this figure, *X*-*Y* indicates the crossing of *GE*, and *Z* the crossing of *DE*. The curve obtained at the eutectoidal composition is depicted in Fig. 4c. Fig. 4d illustrates the type of curve that occurs in the interval *EH*, *X*-*Y* corresponds to the crossing of *EH* and *Z* to that of *EFH*.

A series of graphs plotted from simultaneous resistance and temperature measurements is presented in Figs. 5 through 9. The first graph, Fig. 5, shows the full range of measurements from room temperature to about 950°C. The remaining figures cover only the interval from a little below the eutectoid horizontal to the highest temperature necessary to include the transforming range.

Fig. 5 shows that the transformation of zirconium, even of a good grade, is likely not to be isothermal.

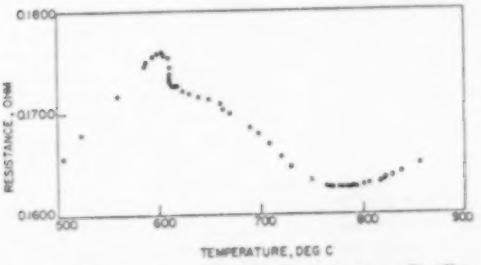

Fig. 6—Resistance temperature graph of Zr-8 pct Cb alloy.

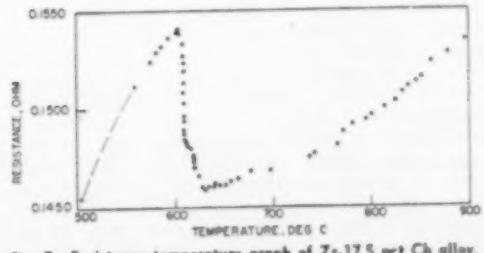

Fig. 7—Resistance temperature graph of Zr-17.5 pct Cb alloy.

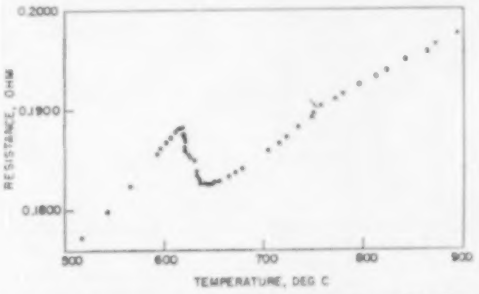

Fig. 8—Resistance temperature graph of Zr-30 pct Cb alloy.

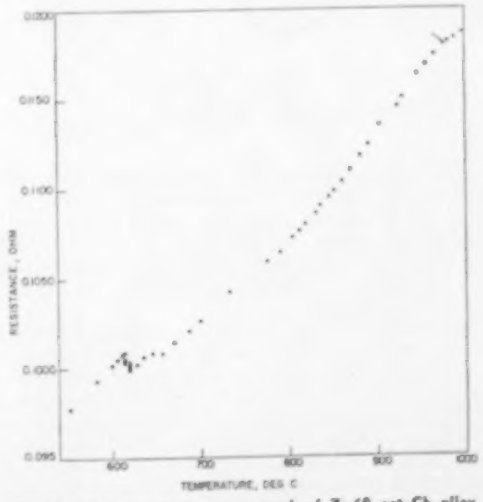

Fig. 9—Resistance temperature graph of Zr-60 pct Cb alloy.

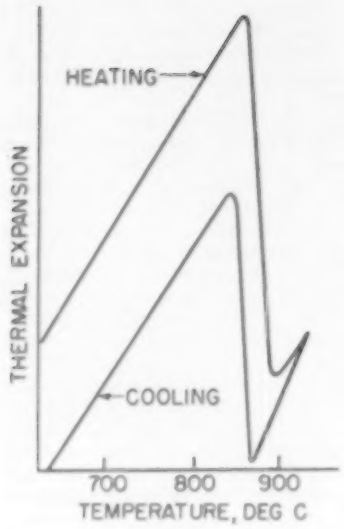

Fig. 10—Dilatometric curve of unalloyed zirconium.

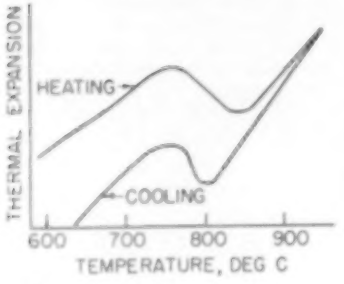

Fig. 11—Dilatometric curve of Zr-3 pct Cb alloy.

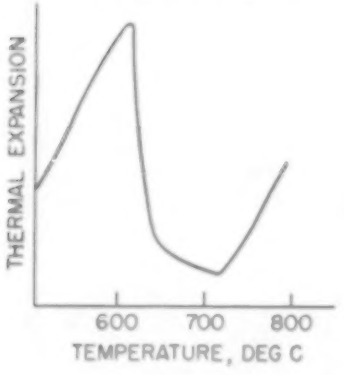

Fig. 12—Dilatometric curve of Zr-10 pct Cb alloy.

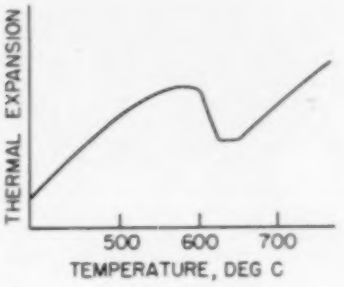

Fig. 13—Dilatometric curve of Zr-15 pct Cb alloy.

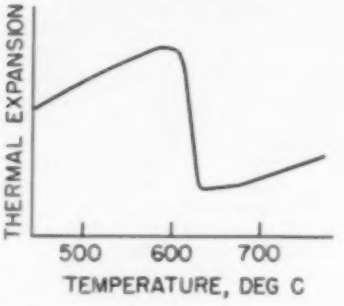

Fig. 14—Dilatometric curve of Zr-20 pct Cb alloy.

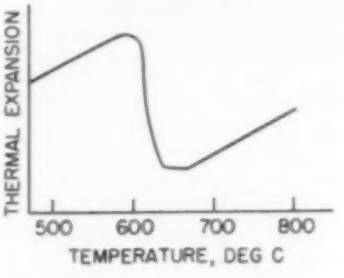

Fig. 15—Dilatometric curve of Zr-22.5 pct Cb alloy.

In this instance it extended over a range from about 850° to about 880°C. This specimen was made from stock zirconium that had not been remelted but a very similar curve was obtained on remelted metal. The unmelted metal had a hardness of about RA 28. The temperaure coefficient of resistance of the wire was 42.8 per °C at 0°C.

Not only did the specimens of unalloyed zirconium fail to transform isothermally but examination of Table III reveals that several of the zirconium-rich alloys had unreasonably high values for the crossing of *DE*. This situation may be blamed on contamination by oxygen and nitrogen but proof is not available from this investigation. Temperatures of the crossing of *DE* were not plotted in Fig. 2 for alloys containing less than 5 pct Cb. Furthermore, because of the rounded maxima of these zirconium-rich alloys, the temperature at which they cross *DG* can be fixed only approximately.

Figs. 6 through 9 include the graphs of alloys with 8 to 60 pct Cb. In them, the beginning of transformation is evident and, in most instances, occurs near 610°C. The changes in resistance as the specimen enters the β field are less definite. For example, the 8 pct Cb alloy (Fig. 6) has a wide flat portion near 780°C. This interval undoubtedly includes the crossing of the specimen from the $\alpha + \beta$ field to the β field but leaves doubt as to the temperature that should be selected as representing a point on the line *DE*. Fig. 7 shows the resistance temperature curve for the 17.5 pct Cb alloy. This alloy is very near eutectoid composition but the transformation in it is not completed until the specimen has attained a temperature of nearly 630°C. When an alloy of intermediate composition passes into the one-phase condition, a change of direction takes place in the resistance temperature graph. In Figs. 8 and 9, this temperature is marked by an arrow. For a given alloy in the intermediate range, the temperature of entering the β field appears to depend to some degree upon the prior heat treatment and upon the rate at which the temperature rises during the period of measurement. Hence, the relatively good fit of these points on the curve *EFH* (Fig. 2) and their agreement with the results of X-ray work must be regarded as fortuitous to some extent. Data on all of the alloys are presented in Table III.

Dilatometric Results: Representative dilatometric graphs obtained on unalloyed zirconium and on five alloys appear in Figs. 10 through 15. Curves for several of the zirconium-rich alloys, particularly the 4, 5, and 6 pct Cb alloys, were so rounded at the top that no reliable data could be obtained for the crossing of *DG*. In general, the temperatures that correspond to the crossing of *DE* are lower than the corresponding figures from electrical resistance measurements. In Fig. 2, the line *DE* was placed roughly in an average position between the electrical resistance and the dilatometric points. Graphs of several intermediate alloys did not give clear indications of the crossing of *EFH*. Data obtained from the figures and from other dilatometric curves are summarized in Table IV.

Data from X-Ray Patterns: Patterns from powders (filings) of the alloys have proved to be particularly helpful in the determination of the diagram. One of the first experiments was intended to confirm the evidence of the solidus curve for complete mutual solid solubility of the two components at elevated temperatures. Specimens of filings from a series of alloys were cooled rapidly from 1100°C in the way that was used for the cooling of resistance specimens. Although such cooling does not constitute quenching in the ordinary sense, it does maintain the high temperature condition in alloys that transform as sluggishly as these do. The patterns showed that the alloys had body-centered-cubic structures and that the lattice parameters varied as indicated in Fig. 16. No points appear in this graph for columbium contents below 15 pct, as the zirconium-rich alloys undergo some transformation at the rates of cooling attained.

The next step was to take patterns of a single alloy at different temperatures. Fig. 17 shows the patterns

Table III. Transformation Temperatures in Zr-Cb Alloys as Determined from Resistance Temperature Data

Alloy No.	Cb, Pct	Heat Treatment No.*	Temperature of Start of Transformation, °C	Temperature of End of Transformation, °C
—	0	6	850	880
M-748	1	2	820	915
M-749	2	2	740	865
M-942	3	7	700	870
M-753	3	5	650	840
M-618	3	5	610	780
M-607	10	5	610	750
M-608	12	2	600	720
M-850	13	2	604	695
M-852	15	4	610	685
M-868	17.5	4	609	630
M-869	20	2	608	655
M-678	30	1	618	755
M-648	40	1	624	860
M-743	50	1 (and 3)	627†	955†
M-647	60	2	612	975
M-741	70	1	614	970
M-948	80	1	610	—‡

* Heat treatments given specimens before measurements started were as follows:
1—Cooled rapidly from 900°C after 20¾ hr; heated for 160 hr at 575°C plus 240 hr at 590°C.
2—Cooled rapidly from 900°C after 20 hr; heated for 155 hr at 515°C.
3—Cooled rapidly from 900°C after 20 hr; heated for 60 hr at 550°C.
4—Cooled rapidly from 900°C after 20 hr; heated for 170 hr at 515°C.
5—Cooled rapidly from 900°C after 20 hr; heated for 120 hr at 515°C.
6—Held 8 hr at 900°C, cooled slowly to 595°C, and held for 20 hr, then cooled at 225°C per hr.
7—Cooled rapidly from 900°C after 10 hr; reheated to 580°C, held for 48 hr, cooled at 10°C per hour or slower to 250°C, then cooled in furnace.
† Average from two runs.
‡ On estimate from one point near 900°C, break is about 880° to 890°C.

Table IV. Transformation Temperatures as Determined from Dilatometric Curves

Alloy No.	Cb, Pct	Temperature of Start of Transformation, °C	Temperature of End of Transformation, °C	Hr of Preliminary Heating*
M-942	3	705	845	—
M-614	4	—†	815	—
M-606	8	607	747	—
M-607	10	616	725	160
M-608	12	612	692	18
M-850	13	609	685	20
M-851	14	605	684	20
M-852	15	600	648	160
M-868	17.5	609	625	144
M-869	20	609	675	90
M-867	22.5	609	671	96
M-648	40	613	—	190
M-647	60	—‡	981	135
M-741	70	605	—	18

* Preliminary heating was at 500°C.
† Curve rounded too much for estimate of temperature.
‡ Dilatometer improperly adjusted over this range.
Note: 5 and 6 pct Cb alloys run in a different type of dilatometer gave 795° and 785°C, respectively, for temperature of end of transformation.

of the 60 pct Cb alloy as cooled rapidly from 1100°C, as cooled rapidly from 900°C after 40 hr at temperature, and as cooled rapidly from 550°C after 116 hr at temperature. Fig. 17a has a set of lines characteristic of a body-centered-cubic metal. Patterns of this type furnished the information given in Fig. 16. In Fig. 17b, the lines were doubled, indicating that the single solid solution has decomposed into two solid solutions. Fig. 17c has a set of prominent lines, which upon analysis turn out to correspond to a close-packed-hexagonal phase with lattice parameters that differ only slightly from the parameters of α zirconium. It has a less prominent and much less numerous set of lines that correspond to a body-centered-cubic columbium-rich solid solution.

The decomposition of the solid solution was investigated next. Fig. 18 shows patterns of the 40, 60, and 75 pct Cb alloys cooled rapidly from 800°C after 48 to 87 hr at temperature. In the 40 pct alloy, Fig. 18a, the lines corresponding to the larger parameter —shorter distance from the (left) reference circle— are relatively strong. In Fig. 18b, the intensities of the two sets are roughly equal and in Fig. 18c the lines corresponding to the smaller parameter are relatively intense. Nearly identical values of lattice

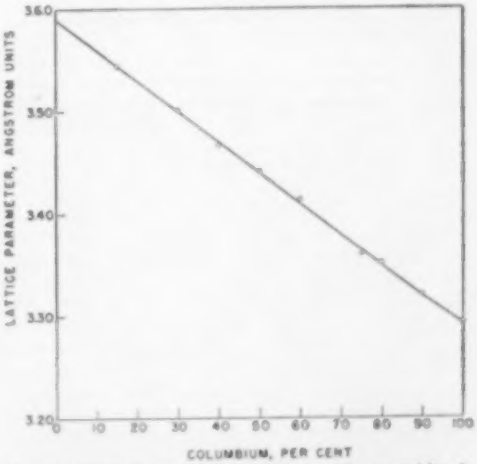

Fig. 16—Variation of lattice parameter with composition in alloys cooled rapidly from 1100°C.

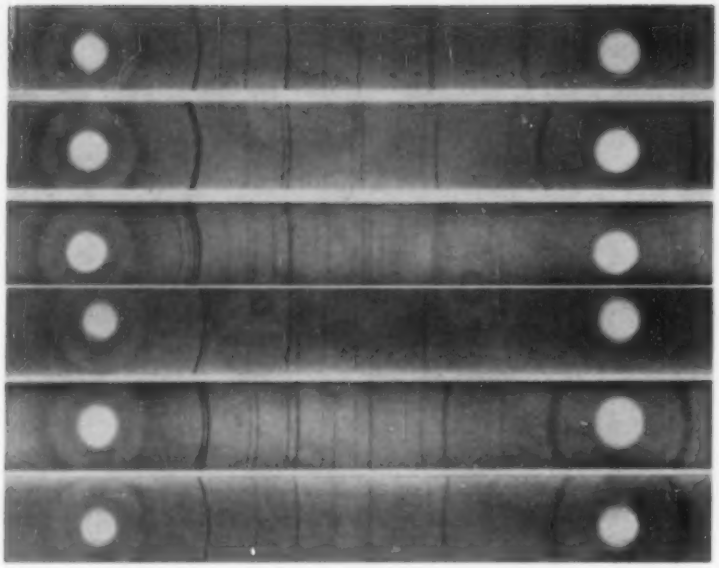

Fig. 17—Change in X-ray pattern of a 60 pct Cb alloy cooled from different temperatures.
a—Cooled from 1100°C.
b—Cooled from 900°C.
c—Cooled from 550°C.

Fig. 18—Change in intensity of X-ray diffraction lines with composition of alloys cooled from 800°C.
a—40 pct Cb alloy.
b—60 pct Cb alloy.
c—75 pct Cb alloy.

parameter are given by the inner set of lines in all three patterns and a similar situation exists with respect to the outer lines. Detailed values are presented in Table V. From the information in this table and the graph in Fig. 16, the compositions of the two body-centered-cubic phases may be calculated, disregarding variations in lattice due to temperature. Thus, from Fig. 16, it is seen that, at 800°C, the phase with the larger parameter contains 34.9 pct Cb and the other contains 82.5 pct. These points appear in the constitutional diagram of Fig. 2 as squares. Some precipitation of α phase from the β_{II} phase during rapid cooling probably is responsible for the point for 700°C being at the right of the curve (Fig. 2).

The Solvus Lines: The solvus lines *GI* and *HJ* are shown dotted because the information for placing them accurately is not available. Columbium-rich alloys are so sluggish that equilibrium is difficult to establish. Zirconium-rich alloys do show age hardening effects but, up to the present time, neither observations on age hardening nor measurements of lattice parameter have given data that permit accurate placement of the line *GI*.

Table V. Lattice Parameters of Zr-Cb Alloys Cooled Rapidly from 700°, 800°, and 900°C

Alloy No.	Cb Content, Pct	Lattice Parameter in A after Cooling from 700°C		800°C		900°C	
		β_{Zr}	β_{Cb}	β_{Zr}	β_{Cb}	β_{Zr}	β_{Cb}
M-680	30	3.506*	3.330	3.492*	3.3581	3.4851	
M-648	40	3.510*	3.332	3.490	3.342	3.4641	
M-743	50	—†	—†	—†	—†	3.469	3.349
M-647	60	3.508	3.329	3.484	3.340	3.454	3.355
M-949	75	—‡	3.334	3.484	3.340	—‡	3.346
Average parameter, A		3.506	3.331	3.487	3.341	3.461	3.351
Columbium content of phase, pct		28.0	85.5	34.0	82.5	42.5	79.0

* Weak α strontium lines present also.
† Value disregarded in average.
‡ Pattern showed only one set of lines; i.e., alloy was single phase.
§ Only one line and that in front-reflection region.

Summary

The part of the constitutional diagram of the Zr-Cb alloy system that lies above 610°C has been established with reasonable accuracy. It is relatively simple in form but time-consuming to investigate because of the sluggishness of the alloys. The positions of the solvus lines descending from the ends of the eutectoid horizontal have not been established.

Acknowledgments

The authors with to express their thanks to E. S. Hodge for making available his unpublished data. They are indebted, also, to G. E. Faulkner and R. L. Fincham for melting the alloys, to E. J. Manthos for metallographic assistance, and to R. E. Kleint for a number of preliminary experiments.

Contribution No. 366 from the Inst. for Atomic Research and Dept. of Chemistry, Iowa State College, Ames, Iowa. Work was performed in the Ames Laboratory of the Atomic Energy Commission.

Discussion of this paper, if any, will appear in JOURNAL OF METALS, May 1956, and in AIME Metals Branch *Transactions*, Vol. **206**, 1956.

References

[1] E. S. Hodge: *AEC Report No. TID-5061* (Jan. 31, 1952) pp. 461-470.
[2] C. R. Simcoe and W. L. Mudge, Jr.: *AEC Report No. WAPD-38* (Nov. 21, 1951) p. 70.
[3] J. H. Keeler: *AEC Report No. SO-2504* (Jan. 5, 1952) 21 pp.
[4] J. H. Keeler: *AEC Report No. SO-2505* (Apr. 5, 1952) 36 pp.
[5] C. T. Anderson, E. T. Hayes, A. H. Roberson, and W. J. Kroll: A Preliminary Survey of Zirconium Alloys. *Report of Investigation No. 4658* U. S. Bureau of Mines (1950) 46 pp.
[6] B. F. Litton: Ten Zirconium Alloys Evaluated. *Iron Age* (1951) **167**, No. 14, pp. 95-99; No. 15, pp. 112-114.
[7] B. Lustman, D. J. De Paul, J. Glatter, and D. E. Thomas: *AEC Report No. WAPD-MR-13* (January 1951) pp. 14-15.
[8] G. A. Geach and D. Summers-Smith: A Laboratory Arc-Melting Furnace for Melting Alloys Containing the Refractory Transition Metals. *Metallurgia* (1950) **42**, pp. 153-156.

[9] C. M. Craighead, D. W. Simmons, and L. W. Eastwood: Titanium Binary Alloys. *Trans.* AIME (1950) **188**, pp. 485-513; JOURNAL OF METALS (June 1950).

[10] M. Pirani and H. Alterthum: Über eine Methode zur Schmelzpunktbestimmung an Hochschmelzenden Metallen. *Ztsch. für Elektrochemie* (1923) **29**, pp. 5-8.

[11] J. T. Williams: Vanadium-Zirconium Alloy System. *Trans.* AIME (1955) **203**, pp. 345-350; JOURNAL OF METALS (February 1955).

[12] M. E. Dooley and D. F. Atkins: A New Electronic Vacuum Dilatometer. *AEC Report No. ISC-482* (June 17, 1954).

Technical Note

Lineage Structure in Aluminum Single Crystals

by A. Kelly and C. T. Wei

USING a recently developed X-ray method, reported by Schulz,[1] it is possible to make a rapid survey of the perfection of a single crystal at a particular surface. This technique has the advantage of allowing a large surface of a specimen to be examined by taking a single photograph and it compares well with other X-ray methods in regard to sensitivity of detection of small angle boundaries.

During the course of a survey of the perfection of large crystals of aluminum produced by a number of methods, an examination has been made of a number of single crystals produced from the melt using a soft mold (levigated alumina).[2]

Crystals grown by this method are known, from an X-ray study carried out by Noggle and Koehler,[3] to contain regions where they are highly perfect. In the present work, it has been possible to obtain photographs showing directly the distribution of low angle boundaries at a particular surface of these crystals.

Single crystals were grown from the melt using the modified Bridgman method with a speed of furnace travel of ~1 mm per min. These were about 1/10 in. thick, 1 in. wide, and several inches long. The metal was 99.99 pct pure aluminum supplied by the Aluminum Co. of America. The crystals were examined by placing them at an angle of about 25° to the X-ray beam issuing from a fine focus X-ray tube of the type described by Ehrenberg and Spear[4] and constructed by A. Kelly at the University of Illinois. A photographic film was placed so as to record the X-ray reflection from the lattice planes most nearly parallel to the crystal surface. The size of the focal spot on the X-ray tube was between 25 and 40 μ, and the distance from the X-ray tube focus to the specimen (approximately equal to the specimen to film distance) was ~15 cm. White X-radiation was used from a tungsten target with not more than 35 kv in order to reduce the penetration of the X-rays into the specimen. Exposure times were approximately 1 hr with tube currents between 150 and 250 microamp.

The type of photograph obtained from these crystals is illustrated in Fig. 1, which shows a number of overlapping reflections from the same crystal. The large uniform central reflection is traversed by sets of horizontal white and dark lines. These two sets run mainly parallel to one another. Lines of one color are wavy in nature and often branch and run together. Large areas of the crystal surface show no evidence of these lines whatsoever. The lines are interpreted as being due to low angle boundaries in the crystal, separating regions which are tilted with respect to one another. A white line is formed when the relative tilt forms a ridge at the interface and a black line is found when a valley is formed. In a number of cases, the lines stop and start within the area of the reflection and often run into the reflection from the edge, corresponding to a low angle boundary starting from the edge of the crystal.

The prominent lines run roughly parallel to the direction of growth of the crystal although narrow bands can run in a direction perpendicular to this; see Fig. 2. Although they may change their appearance slightly, the lines tend to occur in the same place in the X-ray image and to maintain their rough parallelism when the crystals are reduced in thickness by etching. Thus the low angle boundaries can occur at any depth within the crystal. The appearance of the lines is unaffected by subjecting the crystal to rapid temperature changes, such as plunging into liquid nitrogen or rapid quenching from 620°C.

From the width of the lines on the X-ray reflection, values can be found for the angular misorientation of the two parts of the crystal on either side of a boundary. The values found run from 1′ to 10′ of arc, but values of up to 20′ have sometimes been found, e.g., the widest lines on Fig. 2. These misorientations are much less than those commonly found in crystals possessing a lineage structure. When a number of black and white lines occur, running in a roughly parallel direction across the image of a crystal, the total misorientation corresponding to lines of one color is approximately equal to that corresponding to lines of the other color.

The interpretation of the lines as due to low angle boundaries has been checked in a number of ways. Photographs taken with different specimen-to-film distances distinguish lines due to low angle boundaries from effects due to surface relief of the specimen. Normal Laue back-reflection photographs, taken with the beam irradiating an area of the surface showing a number of the lines, show white lines running through each Laue spot. Black lines are difficult to see by this method. X-ray photographs were also taken, using the set-up described by Lambot et al.[5] When the beam straddles regions giving rise to lines in the Schulz pattern, split reflections are observed within the Bragg spot. The misorientations calculated from the separation of these reflections and that found from the widths of the lines on the Schulz technique patterns show good agreement. An exposure was made with Lambot technique of an area of the crystal showing no evidence of low angle

A. KELLY, formerly Research Associate, University of Illinois, is associated with Dept. of Physical Metallurgy, The University of Birmingham, Birmingham, England, and C. T. WEI is Graduate Student, Dept. of Mining and Metallurgical Engineering, University of Illinois, Urbana, Ill.

TN 270E. Manuscript, Jan. 24, 1955.

Fig. 1—X-ray image was obtained from the surface of a single crystal of high purity aluminum grown from the melt. The direction of growth is horizontal. Very strong black lines in the two reflections in corners are due to characteristic X-radiation.

boundaries. The breadth of the X-ray reflection indicated a maximum possible total misorientation of ~30' of arc. This is the same as the width of reflection obtained from parts of the crystal between the low angle boundaries and is of the same order as the sensitivity of both X-ray techniques.

The examination of a single X-ray reflection can only give information concerning misorientations about an axis parallel to the reflecting lattice planes. The boundaries detected can be of two types: tilt or twist. In the former case, displacements of the X-ray image in a direction perpendicular to the trace of the boundary on the crystal surface will be found and in the latter case the displacements will occur along the trace of the boundary. The boundaries observed are predominantly tilt boundaries. Fig. 3 illustrates a case where the absence of an appreciable twist component in the boundaries is deduced from the absence of lateral displacements occurring in the dark vertical lines due to the reflection of characteristic radiation. Twist boundaries do occur, however, and some can be seen in Fig. 2, which was obtained from part of a crystal showing a large network of boundaries throughout its volume. The boundary marked with an arrow is predominantly a twist boundary.

Some previous work has indicated that crystals of aluminum grown from the melt are less perfect than

Fig. 2—X-ray image of part of the surface of a crystal shows many boundaries. Growth direction is horizontal. The boundary marked by an arrow is predominantly a twist boundary.

Fig. 3—X-ray image of part of the surface of a crystal shows where the trace of the low angle boundaries crosses a region reflecting characteristic X-radiation.

those produced by strain-anneal methods.[6] The X-ray examinations carried out here suggest that the sole difference in perfection between crystals grown from the melt and those produced in the solid state is the presence in the former of observable low angle boundaries, showing disorientations of 1' to 20' of arc. Regions between the low angle boundaries show a perfection comparable to that shown by crystals produced by recrystallization. It is thought that the perfection of these melt-grown crystals may be due to the particular conditions of heat flow, resulting from the very low thermal conductivity of the mold rather than to its softness.[7] One crystal was grown in a hard mold of Monmouth stoneware clay which is a poor conductor of heat. This crystal was examined with both the Schulz and Lambot techniques and showed the same low angle boundary structure and perfection in regions between the low angle boundaries as was found in the other crystals. It would seem then that the important factor is the thermal conductiviy of the mold and that the mechanical properties are of less importance.

The interpretation of the majority of the low angle boundaries as being composed mainly of edge dislocations of one sign seems a straightforward one and these results indicate an approximately equal number of edge dislocations of either sign in the whole crystal. The dislocation lines run approximately parallel to the direction of growth. These facts are in qualitative accord with the views of Chalmers[8] on the mechanism of growth from the melt. However, the aluminum crystals examined here are quite perfect over large areas (see Fig. 1), and one crystal showed only one prominent boundary throughout the entire volume. It may be then that the formation of low angle boundaries is not a necessary consequence of growth from the melt.

Acknowledgments

The authors thank P. A. Beck for his encouragement in the course of this work and H. M. Otte for a helpful discussion. This work was financed by the U. S. Atomic Energy Commission under Contract No. AR(11-1)-67, Project No. 9.

References

[1] L. G. Schulz: *Trans.* AIME (1954) **200**, p. 1082; JOURNAL OF METALS (September 1954).

[2] T. S. Noggle: *Review of Scientific Instruments* (1953) **24**, p. 184.

[3] T. S. Noggle and J. S. Koehler: To be published.

[4] W. Ehrenberg and W. E. Spear: *Proceedings* Physical Soc., London (1951) 64B, p. 67.

[5] H. Lambot, L. Vassamillet, and J. Dejace: *Acta Metallurgica* (1953) **1**, p. 711.

[6] A. Guinier and J. Tennevin: *Acta Crystallographica* (1949) **2**, p. 133.

[7] P. A. Beck: Private communication.

[8] B. Chalmers: *Trans.* AIME (1954) **200**, p. 519; JOURNAL OF METALS (May 1954).

Microcalorimetric Investigation of Recrystallization of Copper

by Paul Gordon

An isothermal jacket microcalorimeter, supplemented by metallographic, microhardness, and X-ray measurements has been used to study the isothermal annealing of high purity copper after room temperature tensile deformation. The amount of stored energy released during annealing has been measured as a function of deformation in the range 10.8 to 39.5 pct elongation. The data have shown the major heat effect to be associated with recrystallization and have allowed an analysis of the recrystallization kinetics and the calculation of activation energies of recrystallization.

WHEN a metal is deformed plastically, some of the energy expended is dissipated as heat during the working process, while the remainder is stored within the metal in the form of lattice distortions and imperfections. During subsequent heating of the metal, the distortions and imperfections can be largely annealed out and the associated stored energy released as heat. It is apparent that measurements of the evolution of stored energy during such annealing may produce important information concerning the nature of the annealing mechanisms and the imperfections involved. Some excellent studies of this type have been made in the past, notably those of Taylor and Quinney,[1] Suzuki,[2] Bever and Ticknor,[3] Borelius, Berglund, and Sjöberg,[4] and Clarebrough et al.[5, 6] None of this work, however, employed isothermal techniques, with the exception of the Borelius studies[4] in which only the early annealing stages were investigated. Since isothermal measurements, as compared with heating or cooling curve, have the merits that 1—they reveal the kinetics of a process more clearly, 2—the results obtained are more easily applied to theory, and 3—most fundamental investigations of annealing using techniques other than calorimetry have been carried out isothermally, it was considered important to apply calorimetry to the study of the isothermal annealing of metals. Accordingly, an isothermal jacket calorimeter of the Borelius type,[7] supplemented by metallographic, hardness, and X-ray measurements, has been used to study the annealing of high purity copper after room temperature tensile deformation.

Experimental

The microcalorimeter has been described fully elsewhere.[8] Briefly, the specimen to be studied is placed in a constant temperature environment of virtually infinite heat capacity achieved, as shown in the drawing of Fig. 1, by means of a vapor thermostat. A high thermal resistance is provided between the sample and the environment and a sensitive differential thermopile (see Figs. 2 and 3) arranged with half its junctions in contact with, and thus at the constant temperature of, the environment, and the other half in contact with the sample. A reaction in the sample develops a small difference in temperature, ΔT, across the thermopile, which is followed by a recorder-galvanometer set-up as a function of time, t, and is converted to reaction heat per unit time, P, by the use of the equation

$$P = a\Delta T + b\frac{d\Delta T}{dt} \cdot \qquad [1]$$

The constants, a and b, in Eq. 1 are determined by a simple calibration, making use of the Peltier heat developed by a small current run through the junction of a thermocouple located in an axial hole in the specimen (Fig. 2). In its present form, the limit of sensitivity of the calorimeter is a heat flow of 0.003 cal per hr.

The copper used was the spectroscopically pure metal supplied by the American Smelting and Refining Co. in the form of ⅜ in. diam continuously cast rod, reported to be 99.999+ pct Cu. A small amount of the copper was available at the start of this work and is referred to hereafter as lot *A*. A second batch, lot *B*, was obtained later, most of the results described subsequently being for this lot. As will be seen, there is some indication that lot *A* was somewhat purer than lot *B*, but it is not known whether this difference was present in the as-received metal or arose during subsequent handling.

The two lots of copper were remelted and cast into two 1½ in. diam ingots in vacuo, using high purity graphite crucibles and molds. The ingots were upset several times to break up the large cast grains, and then rolled and swaged to rods 0.391 in. in diameter, using several intermediate anneals with about 40 pct reduction in area between anneals. The penultimate anneal was 2 hr at 350°C. X-ray examination showed no marked general preferred orientation in the resulting rods. The grain structure typical of the two rods is shown in the micrograph of Fig. 4.* It was found to be virtually impossible to get an unambiguous measure of the absolute grain size in the two annealed rods because of the profusion of annealing twins and the lack of regularity of the grain boundaries. However, counts of the number of boundaries intersected per unit length along a random line on a polished section, making a correction for the proportion of boundaries (about half) estimated to be twin boundaries, gave a figure of about 0.015 mm for the average grain diameter. The grain size of the rod from lot *A* was about 5 pct smaller than that from lot *B*.

The rods were cut into 1 ft long bars and these deformed in tension at room temperature to various total elongations in the range 10.8 to 39.5 pct. A strain rate of 1 pct per min was used. The deformed bars were then stored in a dry ice chest until such time as samples were to be cut from them. Five bars deformed as indicated in Table I were used for the subsequent tests. In all cases, all the calorimeter

* The contrasting grain shades in this micrograph (and those of Fig. 18) were obtained by depositing a sulphide film on the surface of carefully electropolished samples. This was done by a technique described by Lacombe and Mouflard[9] in which specimens are dipped in a dilute aqueous solution of ammonium sulphide. The thickness —and thus the color—of the resulting sulphide film is dependent on the orientation of the underlying metal.

P. GORDON, Member AIME, formerly associated with Institute for the Study of Metals, University of Chicago, Chicago, is Associate Professor, Dept. of Metallurgical Engineering, Illinois Institute of Technology, Chicago.

Discussion of this paper, TP 3950E, may be sent, 2 copies, to AIME by Nov. 1, 1955. Manuscript, Sept. 15, 1954. Chicago Meeting, February 1955.

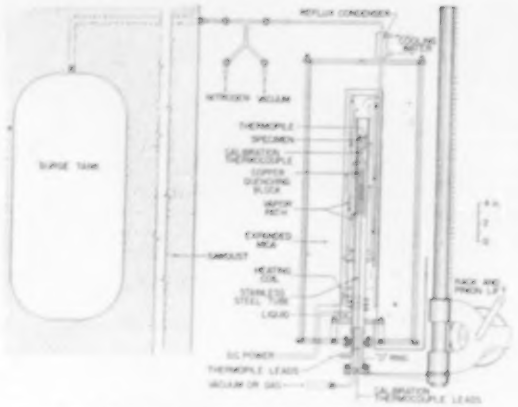

Fig. 1—General view of calorimetric apparatus.

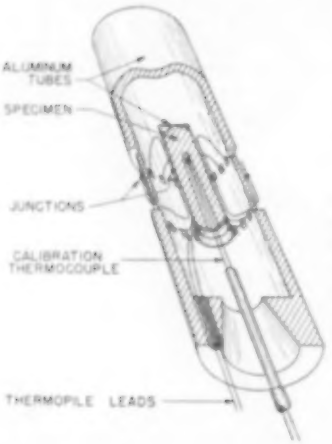

Fig. 2—Detail of thermopile, showing specimen and calibration couple.

runs and the metallographic, hardness, and X-ray observations for a given deformation were made from the same deformed bar. Though there was some inhomogeneity of deformation along a given bar as indicated by measurements of the bar diameter at various points, this inhomogeneity did not exceed about 1 pct elongation for any of the samples used. The deformational work done on the samples was calculated from the areas under the load-extension curves. These curves are shown in Fig. 5 (original cross-sectional area of bars = 0.120 sq in.). It may be seen that the stress-strain curves for the four bars from lot *B* were virtually indistinguishable from one another, while that for the bar from lot *A* deviated very slightly from the others.

The samples for the calorimeter runs were in the form of bullet-shaped pieces from 1 to 1½ in. long and ¼ to ⅜ in. diam (about 1/5 to 1/3 gram-atom of copper per sample). These samples were carefully cut and machined from the deformed bars and axial holes drilled into them to receive the supporting thermocouple shown in Fig. 2. The disturbed metal resulting from the cutting and machining was removed by etching off 0.010 in. per surface in nitric acid. All these operations were carried out at room temperature with great care being taken to avoid heating the samples. Generally, the total time the samples were at room temperature between the

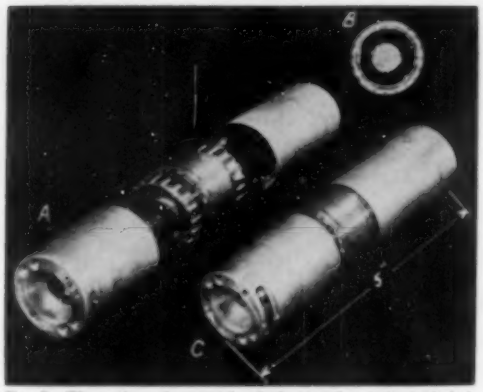

Fig. 3—Three-view photograph of thermopile. *A* is exploded view; *B*, axial view through middle section in *A*; and *C*, assembled thermopile.

tensile deformation and their insertion into the calorimeter was about 3 hr.

The calorimeter runs were carried out in the following manner: With the calorimeter at the desired annealing temperature, the sample was thoroughly cleaned, vacuum-dried, and then preheated to the calorimeter temperature (in about 2 min) by dropping it into a close-fitting hole in an aluminum block heated by a small resistance furnace. From here it was quickly transferred to the support couple, raised by a rack and pinion lift into position within the copper quenching block shown just below the thermopile in Fig. 1, held there a few seconds, and raised into place within the thermopile. The helium within the specimen chamber up to this point (to take advantage of its good thermal conductivity) was replaced with argon and the resulting thermal disturbances allowed to die down. Significant readings of the evolution of heat from the sample could generally first be obtained about 10 min after the introduction of the specimen into the preheating furnace. The reaction in the sample was followed to completion and calibration of the run by means of the Peltier heat technique, referred to previously, carried out before removal of the sample.

Results and Discussion

Heat Evolution Curves: The first calorimetric annealing experiments were carried out on samples from bar 4, lot *A*, strained to 17.7 pct elongation in tension. The evolution of heat during annealing at 160.3°, 181.3°, and 200.9°C is revealed in the curves reproduced in Fig. 6, in which the rate of evolution, *P*, in calories per gram-atom per hour is plotted as a function of annealing time. All three curves show

Fig. 4—Annealed grain structure typical of lot *A* and *B* rods just prior to tensile deformation. Ammonium sulphide etch. X150. Area reduced approximately 20 pct for reproduction.

that the stored energy is released in two overlapping stages. The first stage accounts for only a very minor portion of the total energy release (calculated from the area under the curves) and is characterized by a rate which is high at first and decreases rapidly with time. The rate of heat evolution during the second stage, on the other hand, starts low and goes through a maximum before decreasing to zero. The second-stage kinetics are typical of a nucleation and growth process and, as will be shown, this stage corresponds with recrystallization.* The first stage is presumably associated with some prerecrystallization recovery phenomenon. Since the two stages overlap, it is impossible to give a clear-cut representation of the course of the separate heat effects in the intermediate region. In Fig. 6 (and subsequently in Figs. 7 through 10) the dashed extensions toward short times of the recrystallization stage heat evolutions were drawn by assuming that, in the early phases of a nucleation and growth phenomenon, the rate of transformation is proportional to some power of the time. The positive slope sections of the second-stage curves were then extrapolated back according to this assumption, giving rise to the plotted dashed lines.

* In this paper, the term "recrystallization" will be taken to mean a process, visible under the microscope, in which a new set of grains replaces an old set by means of the motion of high angle grain boundaries. Any annealing phenomena prior to this process will be termed recovery.

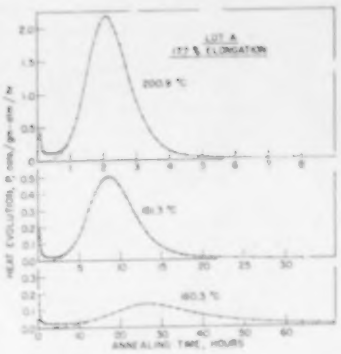

Fig. 6—Heat evolution curves for lot A, 17.7 pct elongation.

Table I. Deformation of Bars Used for Tests

Lot	Bar No.	Pct Elongation, 100ε	True Strain ε = ln(1+e)	Deformational Work Done, W, Cal per Gram-Atom
A	4	17.7	0.163	41.4
B	10	10.8	0.102	20.0
B	8	17.5	0.162	39.1
B	7	30.0	0.262	82.2
B	9	39.5	0.334	115.5

Similar studies were made on lot *B* after tensile deformations of 10.8, 17.5, 30.0, and 39.5 pct elongation. The curves of heat evolution vs time for these annealing runs are presented in Figs. 7 through 10. In Table II are listed energies in cal per gram-atom evolved during recovery, E_r, during recrystallization, E_x, and the totals, $E_T = E_x + E_r$, for each deformation and annealing temperature. The same general features are evident for all deformations and all temperatures within the range investigated. Only the quantitative aspects of the phenomena change from curve to curve. For a given deformation, the two stages occur earlier and have higher maximum rates the higher the annealing temperature, but the energies released remain constant. As the deformation is increased, the rates are greater and the times shorter for a given annealing temperature; in addition, the total energy evolved also increases.

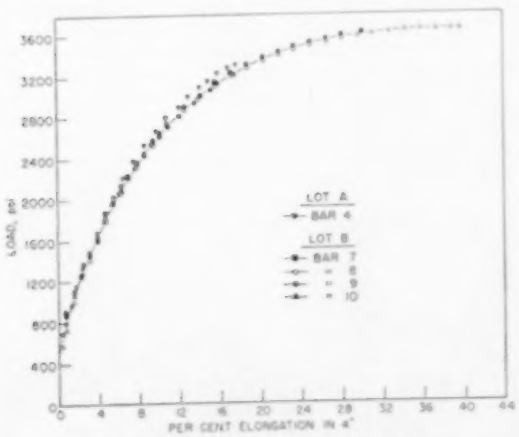

Fig. 5—Load-extension curves of test bars.

In order to calculate the total energies evolved, some estimate of the manner in which the recovery stage curves should be extrapolated back to zero time had to be made. This was done in a rough way by subtracting from the recovery stage curves the recrystallization heats indicated by the dashed lines in Figs. 6 through 10 and then attempting to fit the resulting curves to some mathematical law of behavior. Because of the early onset of recrystallization at the higher temperatures and the low rates of heat evolution during recovery at the lower temperatures, no really satisfactory fit could be found. However, the data could be made to comply roughly with equations either of the type $P \sim e^{mt}$ or $P \sim (t + t_o)^n$, where m, n, and t_o are constants, but was not good enough to determine which of the two equations was generally characteristic of the recovery process. Since the recovery energies given by the use of these equations were quite small in all cases—of the order of 0.2 cal per gram-atom as compared with from 2 to 6 cal for recrystallization—the difference between the energies obtained from either of the equations for a given run could be neglected. The values of E_r given in Table II were obtained by an extrapolation using whichever of the two equations seemed to best fit the data of the run in question. Although it is conceivable that the rates of heat evolution rise more steeply toward zero time than either of the previous two equations predict, the values of P near zero time would have to be of the order of a hundred times the highest observed rates to approximately double the recovery energies. Such high rates seem improbable. Thus, it is felt that the recovery energies given in Table II are correct, at least as to order of magnitude, and support the conclusion that for the copper used the stored energy evolved was largely associated with recrystallization.

The stored energy released during the recrystallization stage is plotted as a function of W, the work done in deformation, in Fig. 11. The ratio of E_x to W is shown also in the same figure. Points representing the values determined on both lots *A* and *B* are included in the figure, but since it was suspected that the purity of lot *A* was slightly different from that of

Table II. Energies Evolved During Annealing after Various Amounts of Deformation

Lot	Pct Elongation	Deformational Work, W, Cal per Gram-Atom	Annealing Temperature, °C	E_P, Cal per Gram-Atom	E_R, Cal per Gram-Atom	$E_T = E_P + E_R$, Cal per Gram-Atom	E_R/W, Pct	E_T/W, Pct
A	17.7 [1]	41.6	180.3	0.31	3.92	4.24	9.49	10.22
			181.3	0.18	3.51	3.69	8.47	8.84
			200.9	0.13	3.72	3.85	8.98	9.30
			Average	0.20	3.72	3.92	9.46	8.96
B	10.0	20.0	199.7	0.18	2.23	2.41	11.10	13.05
			210.2	0.36	2.29	2.64	11.40	13.20
			219.8	0.26	2.25	2.51	11.24	13.55
			Average	0.27	2.26	2.52	11.33	12.60
B	17.5	39.1	189.7	0.23	3.44	3.67	8.79	9.38
			199.7	0.20	3.60	3.80	9.20	9.71
			210.1	0.14	3.34	3.38	8.29	8.64
			Average	0.19	3.43	3.62	8.76	9.24
B	30.0	82.2	169.7	0.32	4.44	4.76	5.40	5.79
			180.5	0.28	5.06	5.34	6.15	6.50
			180.5	0.17	4.76	4.93	5.79	6.00
			189.7	0.32	4.73	4.95	5.76	6.02
			Average	0.25	4.75	5.00	5.78	6.08
B	39.5	115.5	169.7	0.18	5.83	6.01	5.05	5.20
			180.5	0.30	6.21	6.41	5.37	5.54
			Average	0.19	6.02	6.21	5.21	5.37

lot *B*, the curves are drawn only through the points for lot *B*. This procedure was adopted also for the data shown later in Figs. 12 and 17.

As indicated in Fig. 11 and Table II, the stored energy evolution associated with recrystallization increases with deformation from 2.25 cal per gram-atom when the total deformation work done is 20.0 to 6.02 cal per gram-atom when the total work is 115.5 cal per gram-atom. It is estimated that the evolved energies are known to better than ±5 pct. Within this accuracy, there was no apparent trend in the amount of stored energy released as a function of annealing temperature (within the limited temperature range studied) for a given deformation. The ratio of E_R to W, however, *decreases* with increasing deformation from about 0.12 to about 0.05 over the same deformation range. These facts are consistent with the finding that copper saturates with respect to stored energy at high deformations.[7]

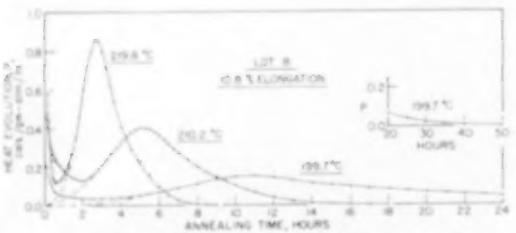

Fig. 7—Heat evolution curves for lot *B*, 10.0 pct elongation.

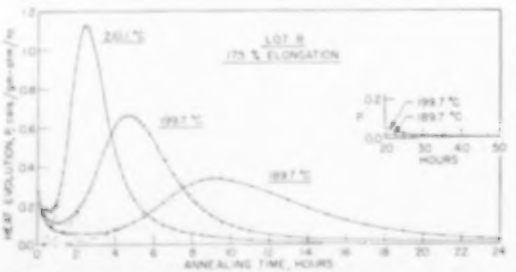

Fig. 8—Heat evolution curves for lot *B*, 17.5 pct elongation.

The shapes of the curves in Fig. 11 suggest that the region below $W = 20$ cal should be an interesting one to study, for the question arises as to whether when W decreases, E_R/W continues to rise, goes through a maximum, or vanishes abruptly at some finite value in accordance with the concept of a "critical deformation" below which recrystallization does not take place. If the recrystallization energies here determined are plotted, as in Fig. 12, against the flow stress attained during deformation, it is seen that a straight line can be drawn through the points. Whether the straight line is justified is at present still problematical, but at any rate it extrapolates to zero recrystallization stored energy at a flow stress equivalent to an elongation of about 4 pct. This could be interpreted as a critical deformation below which recrystallization will not take place. A study of this deformation range is planned for the near future. Some preliminary observations indicate that at an elongation of about 8½ pct, recrystallization is much slower than would be expected from the heat evolution curves reported here and that at about 5½ pct elongation, no recrystallization takes place at even quite high temperatures.

Isothermal Kinetics: The data of the recrystallization stage portions of the curves in Figs. 6 through 10 have been replotted in Figs. 13 and 14 as the percentage of the recrystallization heat released vs time.

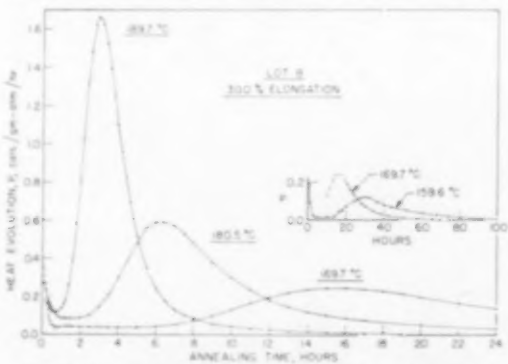

Fig. 9—Heat evolution curves for lot *B*, 30.0 pct elongation.

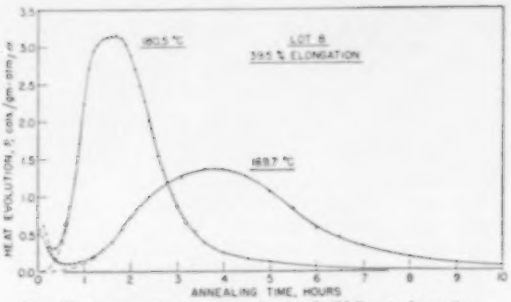

Fig. 10—Heat evolution curves for lot *B*, 39.5 pct elongation.

Such a procedure leads to the familiar sigmoidal isotherms generally found to be associated with recrystallization. The two curves shown for 30.0 pct elongation at 180.5°C give some idea of the reproducibility of the measurements. That the second-stage heat evolution actually does correspond virtually exactly with the appearance of the new microstructure during annealing was proved by making quantitative measurements of the percentage of recrystallization on annealed samples taken from the same deformed bars from which the calorimeter specimens were obtained. The annealing of these samples was carried out for appropriate periods in oil baths, the temperatures of which were controlled to within ±½°C of the corresponding temperatures used in the calorimeter. The percentage of recrystallization in the annealed samples was determined by point counting on electropolished sections employing 200 to 400 Vickers microhardness impressions per sample to distinguish between the recrystallized and unrecrystallized regions. This type of point counting was resorted to because observation under the microscope could differentiate recrystallized from unrecrystallized material only semiquantitatively due to the irregularity of the grain shapes, the complication introduced by numerous annealing twins, and the lack of any large visual difference between the recrystallized and deformed grain sizes. The microhardness measurements, on the other hand, were clearly separated into two groups of hardness, each group showing a scatter approximating a normal frequency distribution. Measurements on as-deformed samples gave hardnesses only within the higher hardness group, and, conversely, measurements on samples heated sufficiently long to give assurance of complete recrystallization showed only the softer group of readings. A further check of the validity of the microhardness point counting was made by spotting many impressions on regions in partially recrystallized samples which were clearly recognizable visually as either recrystallized or unrecrystallized. In every case the hardness fell within the appropriate hardness group. In addition, a check was made to see that recovery without recrystallization did not reduce the hardness. This was done by making microhardness readings on a sample which had been annealed for a length of time just

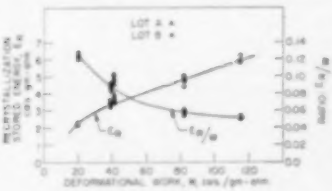

Fig. 11—Energy released during recrystallization, E_R, and the ratio E_R/W vs deformational work, W.

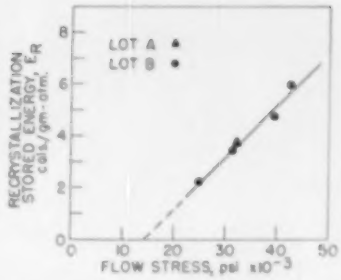

Fig. 12—Energy released during recrystallization vs flow stress.

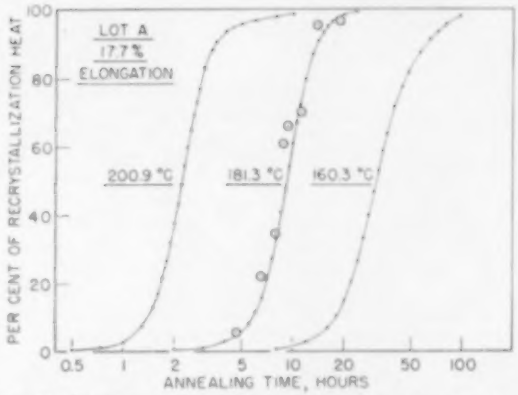

Fig. 13—Percentage of recrystallization heat vs annealing time for lot *A*. Open circle points on 181.3°C curve are microhardness determinations of percentage of recrystallization.

short of that necessary to initiate recrystallization. The measurements on this sample showed no significant difference from those on the corresponding as-deformed specimen.

Microhardness point-counting measurements were made on three sets of annealed samples corresponding respectively to the heat evolution runs for the lot *A*, 17.7 pct elongation, 181.3°C sample and the lot *B*, 10.8 pct elongation, 210.2°C and 39.5 pct elongation, 169.7°C samples. The hardness distribution-relative frequency relationships (normalized) for samples of the 10.8 pct, 210.2°C series, are shown in bar-graph form in Fig. 15. Included in this series are the hardness measurements for a completely recrystallized sample cut directly from the actual calorimeter specimen, for an as-deformed sample, and for a sample given a 1 hr anneal at 190°C in order to produce considerable recovery with no recrystallization.

The results of the microhardness percentage of recrystallization measurements are represented in Figs. 13 and 14 by the open circle points superimposed on the appropriate heat evolution curves. It is considered that these results establish beyond reasonable doubt that for all the heat curves presented, the second-stage heat effect is clearly associated with recrystallization. The displacement of any set of percentage of recrystallization points from its corresponding heat curve is small enough to be largely accounted for by a deformation error of less than 1 pct of elongation. This magnitude of deformation difference could have prevailed between samples from the same bar, as indicated previously.

It is found quite generally that recrystallization can be described as a nucleation and growth process in which the temperature dependence of the rate of nucleation and the rate of growth for a given de-

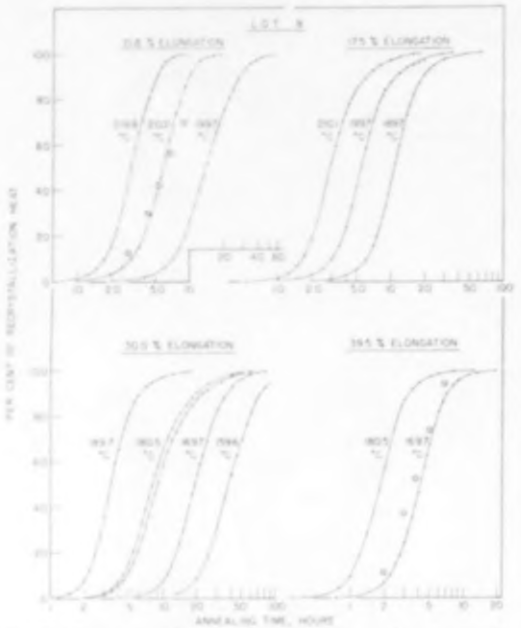

Fig. 14—Percentage of recrystallization heat vs time for lot *B*. Open circle points on 210.2°C, 10.8 pct elongation and 169.7°C, 19.5 pct elongation curves are microhardness determinations of percentage of recrystallization.

formation can be represented by Arrhenius-type equations. The rate of growth is usually found to be independent of time at a constant temperature and, as both Johnson and Mehl[10] and Avrami[11] have shown, if the further simplifying assumption is made that the rate of nucleation does not vary with time, the fraction recrystallized isothermally as as function of time can be represented by the equation

$$x_t = 1 - \exp(-Bt^k) \qquad [2]$$

where B and k are constants, and x_t is the fraction recrystallized at time t.

Eq. 2 indicates that if log $1/1-x$ is plotted against annealing time on log-log paper, a straight line should result with a slope equal to k. Plots of this kind, derived from the heat-evolution curves, are shown in Fig. 16. Each of these plots was selected as typical of the deformation represented. It is clear that Eq. 2 gives a good description of the early recrystallization stages, but that it fails in the later stages. The deviations from Eq. 2 seem to come at an earlier stage the higher the deformation, as may be seen by comparing the four curves for lot *B* in Fig. 15. Whereas at 10.8 pct elongation a straight line results up to about 65 pct recrystallization and up to 55 at 17.5 pct elongation, at 30.0 pct elongation the straight line extends only to approximately 45 pct recrystallization and at 39.5 pct elongation there is a slight curvature throughout the length of the plot.

The average values of the constant k in Eq. 2 are listed in Table III for the several deformations used. These values are estimated to be significant to about ±10 pct. According to the Johnson and Mehl[10] interpretation, k should be 4, and according to Avrami[11] from 3 to 4. The experimental values may be seen to fall within this range.

Cook and Richards[12] have proposed an alternate description of recrystallization kinetics as a first-order rate process taking place entirely within regions which have already recovered. The prerequisite recovery is also considered a first-order rate process, and an equation similar in form to Eq. 2 is derived for the fraction recrystallized vs annealing time—without reference to a nucleation and growth concept. The exponent, k, in the Cook and Richards equation, however, is 2 and thus their treatment does not fit the present experimental data.

Activation Energies: The temperature dependence of the rate of recrystallization for a given deformation can be derived from Eq. 2 and the Arrhenius equations giving the temperature dependence of the rates of nucleation and growth. The desired equation is

$$\frac{1}{t_x} = A \exp\left(-\frac{Q_x}{RT}\right) \qquad [3]$$

where t_x is the time to attain the fraction recrystallized, x, at the absolute temperature, T, A is the so-called "action" constant, and Q_x is a quantity similar to an activation energy. Using the data from the curves in Figs. 13 and 14, values of Q_x at 30, 40, 50, and 60 pct recrystallization for the several deformations were calculated and are listed in Table IV. Since no consistent trend in Q_x as a function of percentage of recrystallization was found, the values for each deformation were averaged and are listed in the last column of Table IV. A consideration of the experimental errors involved in arriving at these average Q_x's leads to the conclusion that the values for lot *B* at 17.5, 30.0, and 39.5 pct elongation may be considered to be identical, having a grand average of 30.4±1.5 kcal per gram-atom. Thus, the activation energy for recrystallization appears to be independent of deformation in the range 17.5 to 39.5 pct elongation, whereas over the same range the release of stored energy during recrystallization—which may be looked upon as the driving force—increases by a factor of almost 2 from 3.43 to 6.02 cal per gram-atom. Q_x at a deformation of 10.8 pct elongation, however, seems to be significantly greater than for the higher deformations. It would appear, therefore, that the findings of Anderson and Mehl[13] for aluminum, namely, that the activation energies for growth and, particularly, for nucleation increase rapidly at low deformations, might have a counterpart in copper at deformations of 10.8 pct elongation and below.

Table III. k Values in the Equation $x_t = 1 - \exp(-Bt^k)$

Lot	Pct Elongation	k
A	17.7	3.9
B	10.8	3.1
B	17.5	3.5
B	30.0	3.8
B	39.5	3.7

The relatively low average value of Q_x found for the lot *A* copper—26.5 kcal per gram-atom—may be explained on the basis either of a difference in purity between the two lots or a difference in their grain size before deformation. Since the best estimate of these grain sizes indicated a difference of only 5 pct, it is more probable that lower impurity content accounts for the lower activation energy. Such a conclusion is consistent with the results of Decker and Harker[14] in which the activation energy for recrystallization in spectroscopically pure copper was shown to be lower than that in OFHC copper.

In view of the fact that growth of a new structure in recrystallization involves the motion of high

angle grain boundaries, it seems possible that the atomic mechanism basic to recrystallization may be the same as that in grain boundary self-diffusion. Thus, a comparison of the activation energies of recrystallization and of grain boundary self-diffusion is of interest. Although the activation energy for grain boundary self-diffusion in copper has not been measured, the values for lattice self-diffusion in copper and for lattice and grain boundary self-diffusion in silver have been determined. These values are given in Table V. It is not unreasonable to expect from the general similarities of copper and silver that the ratio of the lattice to the grain boundary self-diffusion activation energies for copper will be about the same as that for silver. This would place the grain boundary self-diffusion activation energy of copper at approximately 21 kcal per gram-atom, a figure which is appreciably lower than the lot *B* recrystallization values listed in Table IV, but is reasonably close to the value of 26.5 kcal per gram-atom found for the lot *A* copper.

Recovery vs Recrystallization Stored Energy: The stored energy evolved during the first, or recovery, stage of the annealing process (see Table II and Figs. 6 through 10) was found to be quite small in all cases—about 0.2 ± 0.05 cal per gram-atom. This means that only from 3 to 10 pct of the total stored energy evolution during annealing after room temperature deformation was released during recovery, the remainder being associated with recrystallization. If the results of stored energy evolution measurements in deformed copper made by other investigators[2,4,5,17,18] are examined, it is found that there is

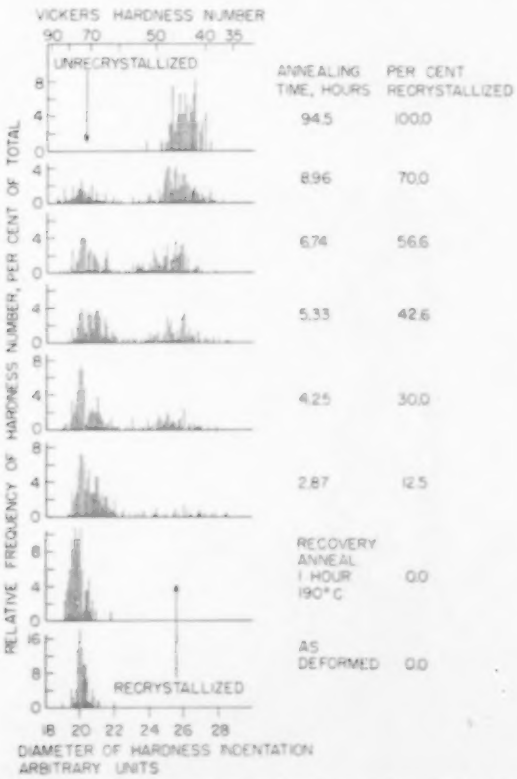

Fig. 15—Microhardness distribution charts for samples annealed at 210.2°C after 10.8 pct elongation in tension.

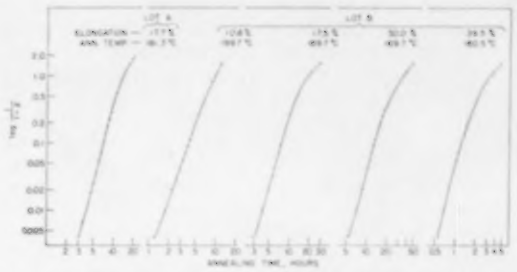

Fig. 16—Typical plots of the recrystallization parameter, log 1/1-x, vs annealing time.

little agreement on the relative importance of the recovery stage in the release of stored energy. A summary of the various investigators' findings is given in Table VI along with some of the pertinent experimental details of their work. Suzuki,[2] Kanzaki,[17] and Stansbury[18] all indicate that essentially all the stored energy was released during recovery, although Kanzaki does not show his evidence for this statement, and the Stansbury data were put forth only as preliminary results in need of further checking. The stored energy evolutions shown by Borelius[4] were measured by a technique similar to that used in the present work, and from the shape of the isothermal curves there seems little doubt that all the energy measured was recovery energy. However, the measurements were carried out at temperatures (100°C) too low to reach the recrystallization stage in the experimental times, and a comparison of the total emission of energy measured with the amount to be expected from the heavy reduction used in deformation indicates that by far most of the stored energy still remained in the metal after the annealing was stopped. Thus the measurements of Borelius should be evaluated as revealing most of the stored energy to be associated with recrystallization. Clarebrough[5] used two purities of copper; in both cases the major portion of the stored energy was released during recrystallization, the ratio E_r/E_s of recovery energy to recrystallization energy being much smaller for the purer material.

A search for the clue to the discrepancies between these investigations in evaluating the magnitude of E_r/E_s revealed only one likely possibility.

Table IV. Recrystallization Activation Energies

Lot	Pct Elongation	Pct Recrystallization	Q_R in Kcal per Gram-Atom	Average Q_R, Kcals per Gram-Atom
A	17.7	30	26.0	26.5
		40	26.4	
		50	26.6	
		60	26.6	
B	10.8	30	33.5	34.6
		40	34.4	
		50	35.2	
		60	35.3	
B	17.5	30	28.5	28.7
		40	28.5	
		50	28.6	
		60	30.5	
B	20.0	30	31.3	31.7
		40	31.6	
		50	32.0	
		60	32.1	
B	30.5	30	31.0	30.8
		40	30.5	
		50	30.8	
		60	30.8	

There seems to be a tendency for E_r/E_s to become smaller the greater the degree of purity of the metal used. Kanzaki's copper was only 99.8 pct pure, Stansbury's was described as silver-bearing, and Suzuki's was given as 99.96 pct Cu. These were the materials which gave very high values of E_r/E_s. On the other hand, the copper used in the present work was of the order of 99.999 pct pure, that of Borelius was described as the "purest available," and Clarebrough's two lots were 99.967 and 99.988 pct Cu, respectively. These materials all gave low values of E_r/E_s. A comparison of Clarebrough's two coppers is particularly suggestive in this respect, for the 99.967 pct batch gave $E_r/E_s \cong 1/3$, while the 99.988 pct batch gave $E_r/E_s \cong 1/20$. This possible effect of impurities would seem to be worthy of systematic investigation, and a series of experiments to study it is being planned.

Table V. Activation Energies for Diffusion, Kcal per Gram-Atom

Metal	Lattice	Grain Boundary
Ag	46.0[15]	20.2[15]
Cu	47.1[16]	?

Recrystallized Grain Size vs Stored Energy: Recently, Leighly, Walker, and Marx[17] have derived what they described as a phenomenological relationship between the recrystallized grain size and the stored energy released during recrystallization. The equation they give is of the form

$$G = B \exp (M/E) \qquad [4]$$

where G is the recrystallized grain diameter, B and M are constants, and E is the stored energy, the driving force, of recrystallization. Since at that time there were no correlated grain size and stored energy data available, they tested their equation by making certain assumptions as to the relationship between E and the percentage of deformation. On this basis and with some available data from the literature, they claimed a check of the equation.

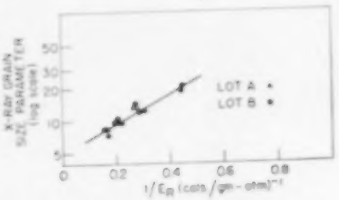

Fig. 17—Recrystallized grain-size parameter vs reciprocal of energy released during recrystallization.

Eq. 4 was derived on the assumption that the stored energy E can be considered to be distributed throughout n microscopic volume cells per unit volume of metal in a manner given by the Boltzman equation, using E/n in place of kT. The validity of this assumption is open to serious doubt because a basic requirement of Boltzman statistics is that there be a continual interchange of energy between particles as a result of thermal motion, whereas the existence of such an interchange between the n volume cells is at least highly unlikely.

In spite of this conceptual difficulty, it seemed worthwhile to check the form of Eq. 4 in view of the availability of E values from the present work. To do this required the measurement of grain sizes in the completely recrystallized calorimetric samples. Because of the difficulties mentioned before, it was not possible to get good absolute values of the desired grain sizes. However, if Eq. 4 is valid, a straight line relationship will exist not only between $1/E$ and log G, but also between $1/E$ and the logarithm of any parameter proportional to G. Such a parameter was obtained by X-ray means. Back-reflection pictures on carefully electropolished cross-sectional surfaces of the calorimetric samples were taken with a focusing technique and a diverging incident beam which allowed a proper size area of the sample to be covered to give an optimum number of spots on the (311) Debye ring. It was then assumed that the number of spots on the ring—with all the

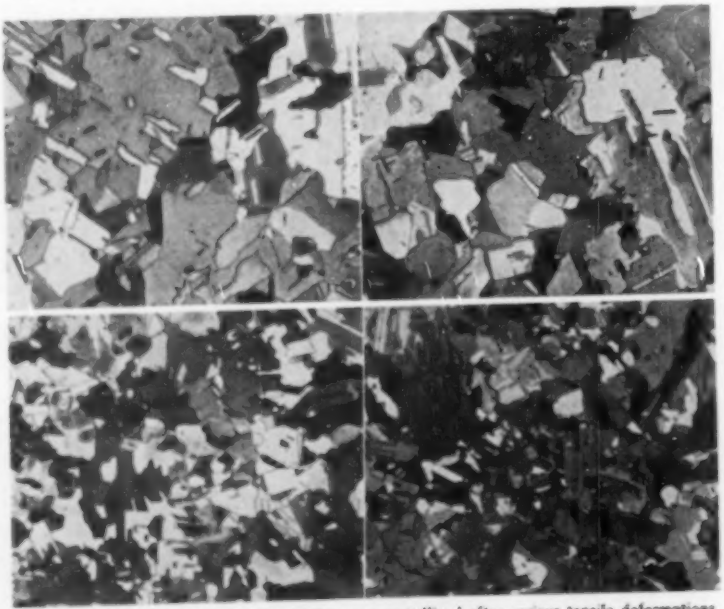

a—After 10.8 pct elongation.

b—After 17.5 pct elongation.

c—After 30.0 pct elongation.

d—After 39.5 pct elongation.

Fig. 18—Typical microstructures of samples as recrystallized after various tensile deformations. Ammonium sulphide etch.* X150. Area reduced approximately 20 pct for reproduction.

Table VI. Measurements of Stored Energy in Deformed Copper, Various Investigators

Investigator	Purity of Copper, Pct	Deformation Conditions: Type	Deformation Conditions: Temperature	Deformation Conditions: Amount	E_r/E_s	Evidence for Recrystallization
Suzuki[9]	99.96	Compression	Room	5 to 55 pct reduction in height	Very high	Hardness and yield strength correlation
Kanzaki[17]	99.8	Compression	Room	40 to 70 pct reduction in height	(>10:1)	None
Stansbury[10]	Not given	Swaging	0 to 30°C	85 pct reduction in area	Very high	Hardness correlation
Clarebrough[8]	1—99.967 2—99.988	Torsion	Room	nd/l* 0.5 to 3	1 ≅ 1/3 3 ≅ 1/20	Hardness, X-ray, metallographic, but not shown
Borelius[6]	"Purest available"	Rolling	Room	Length doubled	All recovery	None
This investigation	99.999 (nominal)	Tension	Room	10 to 40 pct elongation	1/10 to 1/30	Quantitative pct recrystallization measurements

* n = number of turns in torsion, d = specimen diameter, and l = gage length.

X-ray conditions held constant and equal areas used for all samples—was inversely proportional to the grain size. Actually, the quantity desired as G in Eq. 4 should be proportional to the number of nuclei activated during the recrystallization process, which quantity should be exclusive of the twins developed during growth. Though some of the spots on the Debye ring were reflections from twins, it appeared from metallographic examination that the number of twins per grain was roughly constant from sample to sample, and thus the presence of the twins simply introduced a proportionality factor in the relationship between the significant grain size and the stored energy. The radiation used for the X-ray pictures was cobalt $K\alpha$. With this radiation, the effective penetration distance of the incident beam into the copper samples was less than the estimated average diameter of the smallest grains examined. As a result, only the first surface layer of grains was examined and any possible nonlinearity in the grain size number of X-ray spots relationship due to absorption at different levels in the sample was eliminated.

In Fig. 17 a parameter linearly related to the reciprocal of the number of X-ray spots—and, therefore to the grain size—is plotted on semilogarithmic coordinates against the reciprocal of the stored energy released during recrystallization. For comparison purposes photographs of the various recrystallized microstructures are shown in Fig. 18. The points in Fig. 17 include data on most of the calorimetric samples recrystallized after the different deformations and at several annealing temperatures. A reasonably good straight line results. The form of Eq. 4 thus appears to be correct. In view of the remarks made previously concerning the derivation of the equation, however, the check with experiment may lack fundamental significance.

Summary

An isothermal jacket microcalorimeter supplemented by metallographic, microhardness, and X-ray measurements, has been used to study the isothermal annealing of high purity copper after room temperature tensile deformation. It has been found that the stored energy of deformation which is released during annealing is evolved in two overlapping stages. The first stage has simple relaxation kinetics and is presumably associated with recovery. The second stage has kinetics typical of a nucleation and growth process and has been shown to correspond with recrystallization. The reaction kinetics of the recrystallization stage, as revealed by the stored energy evolution, has been evaluated in terms of the equation

$$x_t = 1 - \exp(-Bt^k)$$

where x_t is the fraction transformed in time t at constant temperature and B and k are constants.

The total stored energy evolution was found to vary from 2.5 to 6.2 cal per gram-atom as the deformation was increased from 10.8 to 39.5 pct elongation. Most of this energy is released during recrystallization. The relative importance of the recovery and recrystallization stages in the stored energy evolution has been discussed.

The ratio of the stored energy evolution to the deformational work done on the sample decreased with increasing deformation from about 0.13 to 0.05 over the range studied.

Activation energies for the recrystallization stage have been calculated from the heat evolution curves and found to be essentially independent of deformation in the range 17.5 to 39.5 pct elongation. At 10.8 pct elongation, however, the value was slightly, but significantly, higher. The activation energies have been compared to those for lattice and grain boundary diffusion.

An evaluation has been given of a recently proposed phenomenological relationship between stored energy and recrystallized grain size.

Acknowledgments

This opportunity is taken to extend thanks to the staff of the Institute for the Study of Metals, at which the research reported herein was carried out, in particular Professor Cyril Stanley Smith, for many helpful discussions throughout the course of this research. Thanks are also due to Mrs. Betty Nielsen, Dr. Hsun Hu, and Messrs. Kay K. Ikeuye, and Francois d'Heurle for aid in carrying out much of the X-ray, metallographic, and metallurgical laboratory work. The research reported here was partially supported by the United States Army Office of Ordnance Research under Contract No. DA-11-022-ORD-834, Ordnance Project No. TB2-0001(382).

Discussion of this paper, if any, will appear in JOURNAL OF METALS, May 1956, and in AIME Metals Branch *Transactions*, Vol. **206**, 1956.

References

[1] G. I. Taylor and H. Quinney: The Latent Energy Remaining in a Metal after Cold Working. *Proceedings* Royal Society (1934) **A143**, p. 307.

Relationship Between Recovery and Recrystallization

[6] T. Suzuki: The Release of Energy Associated with Crystal Restoration Process in Cold-Worked Polycrystalline Copper. *Science Reports* RITU (1949) **A-1**, p. 55.
[7] M. B. Bever and L. B. Ticknor: The Energy Stored during the Cold Working of a Gold-Silver Alloy. *Acta Metallurgica* (1953) **1**, p. 116.
[8] G. Borelius, S. Berglund, and S. Sjöberg: Measurements on the Evolution of Heat During Recovery of Cold-Worked Metals. *Arkiv für Fysik* (1952) **6**, p. 143.
[9] L. M. Clarebrough, M. E. Hargreaves, D. Michell, and G. W. West: The Determination of the Energy Stored in a Metal During Plastic Deformation. *Proceedings* Royal Society (1952) **A215**, p. 507.
[10] L. M. Clarebrough, M. E. Hargreaves, and G. W. West: The Release of the Energy Stored in Deformed Nickel. *Philosophical Magazine* (1953) **44**, Ser. 7, No. 355.
[11] G. Borelius, J. Anderson, and K. Gullberg: Thermal Investigation on Constitution and Aging of Aluminum-Copper Alloys with Low Copper Content. *Handlingar* Ingeniours Vetenskaps Akademenien (The Royal Swedish Institute for Engineering Research) (1943) Nr. 169.
[12] P. Gordon: An Isothermal-jacket Microcalorimeter for Heat Effects of Long Duration. *Review of Scientific Instruments* (1954) **25**, No. 12, p. 1173.
[13] P. Lacombe and M. Mouflard: Les applications de la micrographie en couleurs par formation de pellicules minces épitaxiques à teintes d'interférence à l'étude de l'aluminium, du fer et du cuivre. *Métaux et Corrosion* (December 1953) No. 340.
[14] W. A. Johnson and R. F. Mehl: Reaction Kinetics in Processes of Nucleation and Growth. *Trans.* AIME (1939) **135**, p. 416.
[15] M. Avrami: The Kinetics of Phase Changes. *Journal of Chemical Physics* (1939) **7**, p. 1103; (1940) **8**, p. 212; (1941) **9**, p. 177.
[16] M. Cook and T. L. Richards: Observation on the Rate and Mechanism of Recrystallization in Copper. *Journal* Institute of Metals (1947) **73**, p. 1.
[17] W. A. Anderson and R. F. Mehl: Recrystallization of Aluminum in Terms of the Rate of Nucleation and the Rate of Growth. *Trans.* AIME (1945) **161**, p. 140.
[18] B. F. Decker and D. Harker: Recrystallization in Rolled Copper. *Trans.* AIME (1950) **188**, p. 887; JOURNAL OF METALS (June 1950).
[19] R. E. Hoffman and D. Turnbull: Lattice and Grain Boundary Self-Diffusion in Silver. *Journal of Applied Physics* (1951) **22**, p. 624.
[20] A. Kuper, H. Letaw, Jr., L. Slifkin, E. Sonder, and C. T. Tomizuka: Self-Diffusion in Copper. *Physical Review* (1954) **96**, No. 5, pp. 1224-1225.
[21] H. Kanzaki: On the Recovery Process of Cold-worked Metals. *Journal* Physical Society, Japan (1951) **6**, p. 90.
[22] E. E. Stansbury, G. E. Elder, and M. L. Picklesimer: Calorimetric Studies of Plastic Deformation and Phase Transformation. *Unpublished University of Tennessee Report* (March 1953).
[23] H. P. Leighly, H. L. Walker, and J. W. Marx: Recrystallization and Stored Energy. *Trans.* AIME (1953) **197**, p. 809; JOURNAL OF METALS (June 1953).

Technical Note

Method of Determining the Diffusivity of Gas in Metal: Oxygen in Chromium

by D. Caplan and A. A. Burr

IN carrying out experiments in metal-gas systems, it is often difficult to estimate how long a reaction period must be allowed for equilibration. This is especially true in systems for which the diffusion coefficient is not known. In an investigation of the Cr-O system, the necessary information was obtained in the way described subsequently.

Two pieces of chromium sheet of different thicknesses were packed in mixed powders of chromium and Cr_2O_3, and sealed into an evacuated metal capsule by welding. Austenitic stainless steel proved suitable as a capsule material up to 1350°C and molybdenum at higher temperatures. The capsule then was heated at a specific temperature for a time sufficient to saturate with oxygen the thinner but not the thicker specimen. The time is readily estimated from a preliminary experiment if a sufficient thickness differential is chosen. Under these experimental conditions, the metal sheet is exposed to a partial pressure of oxygen equal to that of the dissociation pressure of the oxide and hence can become saturated with oxygen without developing any second phase. After cooling, both samples were analyzed for oxygen by the vacuum fusion technique.

Assuming that the surface of the specimens is kept saturated with oxygen throughout the experiment, the diffusivity can be calculated by application of the appropriate solution to Fick's second law. This is most conveniently accomplished by use of a plot of mean fractional saturation $(Cm\text{-}Co)/(Cs\text{-}Co)$ vs $(Dt)^{1/2}/L$ as given by Darken,[1] where t is time, L the half-thickness of the sheet, and D the diffusion coefficient. Cm, the mean concentration at time t, is given by the oxygen percentage in the thicker specimen; Cs, the constant surface concentration, is the oxygen percentage in the thinner specimen; Co is the oxygen content of the original chromium sheet. $(Cm\text{-}Co)/(Cs\text{-}Co)$ is calculated and the corresponding $(Dt)^{1/2}/L$ is read from the graph and D thereby calculated.

By performing the experiment at two temperatures and plotting log D vs $1/T$, the D for any temperature is established. (The activation energy for diffusion may be obtained from the slope of the line.) Once D is known as a function of temperature, it is a simple matter to estimate the correct reaction time for experiments with single specimens at other temperatures by equating $(Dt)^{1/2}/L$ to its value for effective saturation. Darken[1] points out that this is approximately unity.

The solubility of oxygen in chromium, as determined from the thin samples at each temperature, proved to be approximately 0.03 pct at 1350°C and less at lower temperatures. Due to low solubility and to the known difficulties of the vacuum fusion method in this low range, the values obtained for D (5×10^{-7} sq cm per sec at 1350°C) are estimated to be correct only within an order of magnitude. Nevertheless, the method has proved useful in estimating reaction times. Its usefulness will be greater in metal-gas systems where the solubility is appreciable. A second function of the method is to permit the determination of diffusion coefficients in systems for which the conventional techniques are experimentally difficult or impossible.

D. CAPLAN and A. A. BURR, Member AIME, are associated with Dept. of Metallurgical Engineering, Rensselaer Polytechnic Institute, Troy, N. Y.
TN 284E. Manuscript, May 2, 1955.

[1] L. S. Darken: *Symposium on Atom Movements*. (1951) Cleveland. ASM.

Relationship Between Recovery and Recrystallization In Superpurity Aluminum

by E. C. W. Perryman

The recovery and recrystallization characteristics of superpurity aluminum have been investigated using electrical resistivity, X-ray line breadth, and hardness measurements for the former and the micrographic method for the latter. The three different properties recover at different rates and have different activation energies. The recrystallization results agree well with Avrami's theory and furthermore indicate that the perfect subgrains formed during recovery are not the nuclei for recrystallization.

WHEN a metal is plastically deformed, its physical and mechanical properties generally undergo considerable changes and by subsequent annealing these changes are partly or wholly annihilated. Thus, a recovery process can be discussed, taking this term in its general sense. In practice, however, there is reason to discriminate between two apparently different processes, one most easily followed at low temperatures, in which the properties return to an almost constant value between that of the cold worked and fully annealed material, and a second process in which the properties return to their original values before cold working and which is accompanied by the formation and growth of new grains having an orientation different from that of the matrix. In this paper the word *recovery* will be taken to mean the changes in some property as a function of annealing time which occur either without the appearance of new grains or under conditions such that the new recrystallized grains are very small ($\triangleq$ 2 microns), are very few in number, and substantially do not affect the property being measured. This definition is rather abitrary, for it will depend upon the sensitivity of the technique used for the observation of new recrystallized grains, which in the present work was about 1 to 2 microns. However, it is helpful to use the term recovery in this sense and to reserve the term *recrystallization* for the processes of nucleation and growth of new grains in the cold worked matrix.

Although considerable work has been done on recovery and recrystallization, most workers have based their study on the measurement of one or perhaps two parameters. Since very small amounts of impurities have such a profound effect on the recrystallization characteristics of a pure metal, it becomes extremely difficult to correlate one piece of work with another. With this in mind, the present work on recovery and recrystallization was done on the same material.

E. C. W. PERRYMAN is Physical Metallurgist, Physical Metallurgy Div., Aluminium Laboratories Ltd., Kingston, Ont., Canada, and at present is associated with Atomic Energy of Canada Ltd., Chalk River, Ont., Canada.

Discussion of this paper, TP 3984E, may be sent, 2 copies, to AIME by Nov. 1, 1955. Manuscript, Sept. 17, 1954. Chicago Meeting, February 1955.

Experimental Procedure

Material Used and Fabrication: The composition of the superpurity aluminum used throughout this investigation was 0.002 pct Cu, 0.003 pct Fe, 0.003 pct Si, and <0.001 pct Mg. The ingot was hot rolled to 0.250 in., annealed, and cold rolled to 0.034 in. A large number of reductions and intermediate anneals were carried out so as to produce material with a minimum of preferred orientation and maximum homogeneity. For the recovery part of the investigation, the final cold reduction was 20 and 80 pct and for the recrystallization part, 20 pct. After each pass in the cold rolling process, the material was quenched in cold water in order to keep the rolling temperature as near room temperature as possible.

Annealing Procedure: For the recrystallization work, specimens 1x1 in. were cut from the 0.034 in. cold rolled sheet and a hole was drilled in each through which a wire was threaded to support it in the salt bath. The temperature of the salt bath was controlled to ±2°C and the time taken for a specimen to reach temperature was approximately 5 sec. These 1 in. squares were then divided into three groups, one of which was given 5 min at 318°C and another 2 hr at 244°C. These treatments were such that recovery was almost complete and a well defined subgrain structure produced. Separate specimens of each group were annealed for different times at 301°, 318°, 355°, and 373°C, i.e., three specimens for each annealing time. The delay between finish of cold working and start of annealing was about 1 hr.

For the recovery work, strips 0.062 in. thick were cut from the cold worked sheet, annealed, and then given the last cold rolling operation. This was done for each annealing temperature. By this means it was possible to minimize the delay between cold working and annealing. In general, all measurements were carried out within 1 hr of the last cold rolling operation. Annealing at low temperatures was done in an oil bath the temperature of which was maintained constant to ±1°C.

Electrical Resistivity Measurements: Strips 20x0.5x0.05 in. were machined and the electrical resistance measured using a Kelvin double bridge. Measurements were made in an oil bath maintained at 20±0.1°C. The same specimen was used for the complete isothermal annealing curve.

Density Measurements: Specimens 4x1½x0.05 in., weighing about 14 g, were weighed in air and water, precautions being taken to deaerate the water and prevent the formation of air bubbles on the specimen surface. With a 50 g sample, the standard error using this technique has been found to be ±0.0002 g per cu cm. With the lighter samples used here, the standard error would be slightly larger.

Measured X-Ray Half-Peak Breadth: Separate samples were annealed for different times at constant temperature and after annealing were heavily etched to remove the heavily deformed skin. Back-reflection Laue photographs were taken using unfiltered copper radiation and a continuously rotating film. The exposure time varied, being greater for cold worked than for recovered specimens, but was adjusted to give the required line density. A trace of the (333) $K\alpha_1$ line was obtained using a Leeds and Northrup densitometer and the half-peak breadth determined. In no case was it necessary to separate the α_1 and α_2 reflections, since the overlap was very small.

Hardness Testing: The Vhn of each specimen was determined, using a 2½ kg load. Hardness tests were made after electropolishing and five measurements were made on each specimen.

Metallographic Examination: All samples were electrolytically polished and either etched electrolytically or in a solution containing 25 pct HNO_3, 2 pct HF, and 73 pct H_2O in the way described previously.[3] Phase contrast was used for the examination of recovery structures, while polarized light was used for the recrystallization work. Using this technique, the smallest recrystallized grain which could be measured was about 2×10^{-4} cm. To determine the percentage of recrystallization, rate of nucleation N, and growth G, five photographs were taken from each sample at a magnification of X50 and analyzed by the method described by Anderson and Mehl.[5]

Results

Recovery—In all cases the fractional change in the property being measured has been taken as a measure of the amount of recovery. This fractional change is given by $(P_o - P_t)/(P_o - P_f)$, where P_o is the value directly after cold working, P_t is the value at time t, and P_f is the value for completely recrystallized material.

Electrical Resistivity Measurements: The total change in electrical resistivity brought about by 20 pct cold reduction was 0.25 pct. The fractional change in electrical resistivity as a function of annealing time at 74°, 100°, and 127°C is given in Fig. 1. Measurements were continued after much longer annealing times than shown in Fig. 1 but in all cases there was no further change in electrical resistivity. Only part of the increase in resistivity due to cold working is recovered during low temperature annealing and the amount recovered increases slightly with temperature. By plotting the logarithm of the reciprocal of the time for complete recovery against the reciprocal of the annealing temperature T°K, an activation energy of 7,700±100 cal per gram-atom was obtained. If, however, times such that 50 pct of the recovery process had taken place were used, a higher value was obtained—15,500 cal per gram-atom. Seitz[4] recently described the increase in electrical resistivity after cold working in terms of an increase in the number of vacancies. If this is the case, then cold work should decrease the density. A simple calculation shows that if it is assumed that the complete increase in electrical resistivity is due to vacancies, then for aluminum the density of vacancies would be about 3.8×10^{18} per cu cm, giving a density change of 0.006 pct which is smaller than could be measured. To check this, some density

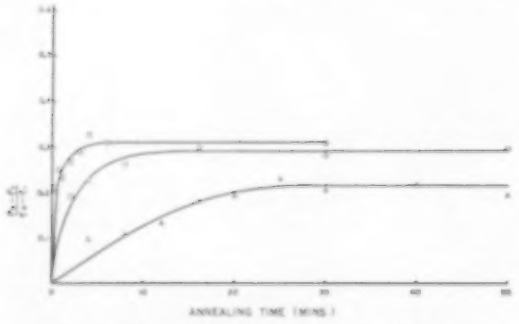

Fig. 1—Fractional change of electrical resistivity is shown as a function of annealing time for superpurity aluminum cold worked 20 pct. Symbols represent various annealing temperatures: triangles, 74°C; circles, 100°C; and squares, 127°C.

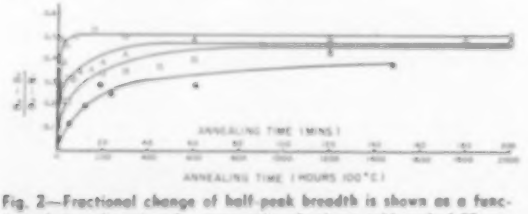

Fig. 2—Fractional change of half-peak breadth is shown as a function of annealing time for superpurity aluminum cold worked 20 pct. Symbols represent various annealing temperatures: open circles, 281°C; triangles, 250°C; squares, 210°C; and filled circles, 100°C. Note change of scale for 100°C anneal.

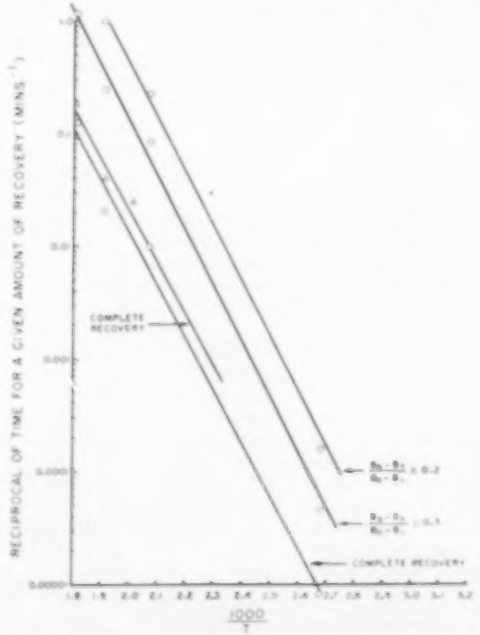

Fig. 3—Times and temperatures are given for recovery of X-ray line breadth for superpurity aluminum cold worked 20 and 80 pct. Symbols represent percentage of cold work: circles, 20 pct; and triangles, 80 pct.

Table I. Recovery of Superpurity Aluminum Cold Worked 20 and 80 Pct

Annealing Temperature, °C	Time for Complete Recovery, Min					Time for Appearance of New Recrystallized Grains, Min, 20 Pct CW*
	Electrical Resistivity, 20 Pct CW*	X-Ray Line Breadth		Hardness		
		20 Pct CW*	80 Pct CW*	20 Pct CW*	80 Pct CW*	
74	26.5	—	—	—	—	—
100	12.0	120,000	—	—	—	—
127	6.0	—	—	—	—	—
210	—	100	—	—	—	—
225	—	—	40	—	250	—
250	—	48	25	500	52	480
281	—	8	5.5	100	24	60
301	—	—	—	34	10	10
318	—	—	—	14	—	3
Activation energy, cal per gram-atom	7700±100	22,400±2000	20,000±5000	31,800±2600	22,500±2400	—

* CW stands for cold worked.

measurements were done on the cold worked, recovered, and fully recrystallized material. No significant differences were found between any of the samples, the values all lying between 2.6984 and 2.6990 g per cu cm.

X-Ray Half-Peak Breadth Measurements: Isothermal annealing curves for material cold worked 20 pct are shown in Fig. 2. Similar curves were obtained for material cold worked 80 pct, the final steady value being the same as that for 20 pct cold work. The half-peak breadth of the (333) $K\alpha_1$ line was 12.6′ of arc for fully recrystallized material and 42.8′ and 54.6′ of arc after cold working 20 and 80 pct, respectively. About 47 and 57 pct of the line broadening in material cold rolled 20 and 80 pct, respectively, is recovered during annealing for temperatures and times such that no recrystallization has commenced. Furthermore, the magnitude of this recovery within the experimental error is independent of temperature. The activation energy plot is shown in Fig. 3. The slopes of the straight lines are independent of the amount of recovery and the average slope gives an activation energy of 22,400±2000 and 20,000±5000 cal per gram-atom for 20 and 80 pct cold work, respectively.

Hardness Measurements: Isothermal annealing curves for material cold worked 20 pct are shown in Fig. 4. Similar curves were obtained for material cold worked 80 pct except that the recovery times were smaller. The Vhn of the fully recrystallized material was 14.2 and directly after cold working was 28.8 and 42.2 for 20 and 80 pct cold work, respectively. Only 30 to 40 pct softening occurs during recovery and, in agreement with previous work,[4,5] this is independent of the amount of cold work. The final steady hardness value, however, increases with cold work and decreasing annealing temperature. Activation energy plots of the complete recovery times gave activation energies of 32,100±500 and 22,500±2400 cal per gram-atom for 20 and 80 pct, respectively. As was the case with the X-ray half-peak breadth, the activation energy was almost independent of the amount of recovery.

Table I gives a summary of the recovery times and the activation energies for the different processes. Also included in Table I is the time taken for the appearance of new recrystallized grains. It will be seen that new recrystallized grains first appear just before recovery of hardness is complete. It might be thought that these new recrystallized grains would have an effect on the hardness, but it must be remembered that at this stage they are very small (1 to 2 microns) and are very few in number —possibly three or four could be seen in 1 sq in.

Metallographic Examination: Substructures similar to those described previously[4] were observed directly after cold working. The subgrain size, 1 to 2 microns, was about the same for 20 and 80 pct cold work. However, subgrains and deformation bands were much more easily seen in material cold worked 80 pct than in that cold worked 20 pct. On annealing, the structures became much sharper, and after annealing times such that the X-ray line breadth had recovered, the deformation bands could be seen to be split into subgrains, Fig. 5. As the annealing time increased, further deformation bands became split up and by the time the hardness had fully recovered, most areas showed a well defined equiaxed subgrain structure, as seen in Fig. 6. Even after these long annealing times, a large number of grains still showed no substructure. With increased annealing times, there was no apparent sign of subgrain growth, the only observable difference being an increase in contrast between adjacent subgrains. The subgrain size increased slightly with increasing temperature (see Figs. 7 and 8) and decreased with increasing amounts of cold work (see Figs. 5 through 7 and 9).

Kinetics of Recovery: From the results given so far, it is clear that recovery is not a single process as in the classical picture of recrystallization. The three properties studied recover at different rates, the rate of recovery decreasing in the order: electrical resistivity, X-ray line breadth, and hardness. Similar results were obtained by Tammann[6] for cold worked iron and more recently A. H. Lutts and P. A. Beck[7]

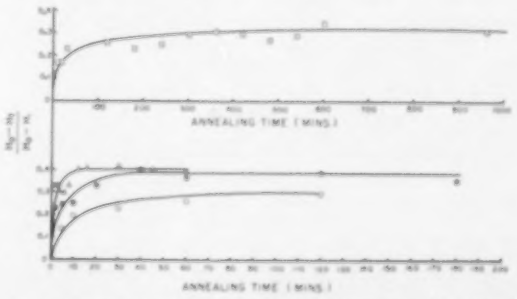

Fig. 4—Fractional change of hardness is shown as a function of annealing time for superpurity aluminum cold worked 20 pct. Symbols represent various annealing temperatures: squares, 247°C; circles, 281°C; encircled crosses, 301°C; and triangles, 318°C.

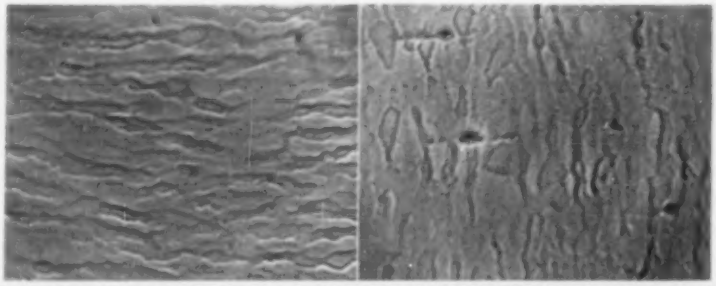

Fig. 5—Superpurity aluminum was cold worked 20 pct and annealed for 1 hr at 250°C. Specimen was etched in 73 pct H_2O, 25 pct HNO_3, and 2 pct HF at 50°C and photographed with phase contrast. X1000. Area reduced approximately 35 pct for reproduction.

Fig. 6—Superpurity aluminum was cold worked 20 pct and annealed for 11 hr at 250°C. Specimen was etched in 73 pct H_2O, 25 pct HNO_3, and 2 pct HF at 50°C and photographed with phase contrast. X1000. Area reduced approximately 35 pct for reproduction.

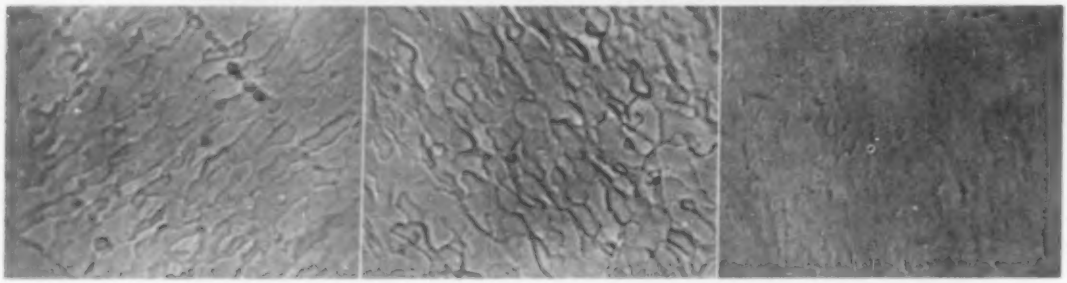

Fig. 7—Superpurity aluminum was cold worked 20 pct and annealed for 2 days at 250°C. Specimen was etched in 73 pct H_2O, 25 pct HNO_3, and 2 pct HF at 50°C and photographed with phase contrast. X1000. Area reduced approx. 35 pct for reproduction.

Fig. 8—Superpurity aluminum was cold worked 20 pct and annealed for 45 min at 318°C. Specimen was etched in 73 pct H_2O, 25 pct HNO_3, and 2 pct HF at 50°C and photographed with phase contrast. X1000. Area reduced approx. 35 pct for reproduction.

Fig. 9—Superpurity aluminum was cold worked 80 pct and annealed for 1 hr at 250°C. Specimen was etched in 73 pct H_2O, 25 pct HNO_3, and 2 pct HF at 50°C and photographed with phase contrast. X1000. Area reduced approx. 35 pct for reproduction.

have shown that, for a heavily cold worked aluminum single crystal, the X-ray line breadth recovers much faster than the hardness.

The recovery results were analyzed to see if they would fit the single stage process proposed by Cook and Richards[8] and the theory proposed by Cottrell and Aytekin.[9] In neither case could the author's results be fitted to the proposed equations. It was found however, see Fig. 10, that these results could be fitted reasonably well to an equation of the type proposed by Betteridge[10]

$$\frac{1}{P-x} = \frac{1}{P_0-x} - at \qquad [1]$$

where P is the value of property being measured at some annealing time t, P_0 is the value of property directly after cold working, and x is the steady value of P after long annealing times.

Recrystallization—The object of this part of the investigation was twofold: 1—to investigate the kinetics of recrystallization and 2—to determine whether prior recovery has any effect on the kinetics of recrystallization, rate of nucleation N, or rate of growth G. After annealing, samples were electrolytically polished and etched and five photographs, using a direct positive process, were taken from each sample at a magnification of X50. First, the maximum and minimum diameters of the largest grain visible which had not impinged upon another growing grain were measured. The two measurements were made because, in general, the new grains tended to be elliptical. Next, the number of recrystallized grains per unit area was counted and then the combined area of the recrystallized grains was measured using a planimeter. The results from the five photographs were averaged. Isothermal annealing curves were determined at 301°, 318°, 355°, and 375°C for material cold worked 20 pct and also for material which had been recovered for 2 hr at 244°C and 5 min at 318°C. After these two recovery treatments, well defined subgrains were visible and it will be seen from Table II that both these treatments are such that the line breadth was fully recovered and that recovery of the hardness was almost complete. Actual measurements after these two recovery treatments are given in Table II.

Measurement of Percentage of Recrystallization: Fig. 11 shows the isothermal recrystallization curves for superpurity aluminum cold worked 20 pct both with and without prior recovery. It is clear that within the experimental error, recovery annealing prior to recrystallization has had no effect. As shown

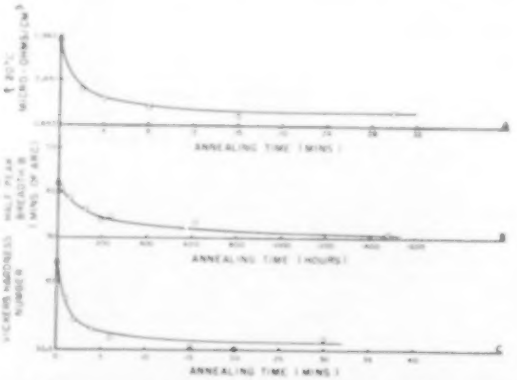

Fig. 10—Theoretical recovery curves are plotted. Section *A* shows curve for superpurity aluminum cold worked 20 pct and annealed at 100°C. $1/(\rho\text{-}2.6602) = (1/0.00165) + 515t$. Curve *B* is for superpurity aluminum cold worked 20 pct and annealed at 100°C. $1/(B\text{-}30) = (1/12.1) + 0.00069t$. Curve *C* is for superpurity aluminum cold worked 80 pct and annealed at 280°C. $1/(H\text{-}33) = (1/9.2) + 0.110t$.

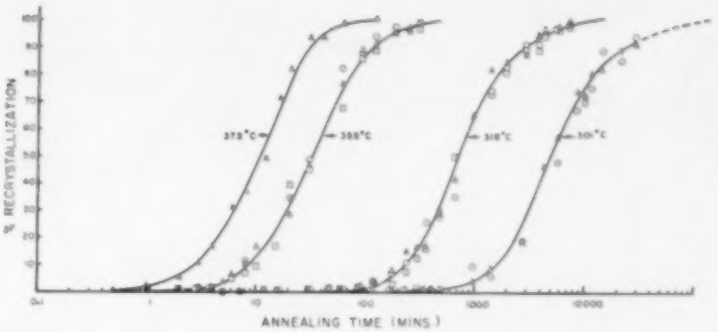

Fig. 11—Isothermal recrystallization curves are plotted for superpurity aluminum cold worked 20 pct. Triangles represent specimens annealed directly after cold working; squares, specimens recovered 2 hr at 244°C before annealing; and circles, specimens recovered 5 min at 318°C before annealing.

Table II. Measurements of Half-Peak Breadth and Hardness after Recovery Treatments

Condition	Half-Peak Breadth, Min of Arc	Vhn
As cold worked 20 pct	42.8	30
Cold worked 20 pct; 2 hr at 244°C	29	24
Cold worked 20 pct; 5 min at 318°C	31	23

before,[1] there was a tendency for groups of new recrystallized grains to form rather than separate ones and, furthermore, these formed preferentially at the grain boundaries. Fig. 12 shows the percentage of softening plotted against the percentage of recrystallization. This graph also includes the results of a previous investigation[3] so that it is made up from results on material cold worked different amounts from 20 to 60 pct and annealed at various temperatures in the range 301° to 375°C. As shown before,[1,3] the softening is more rapid in the early stages of recrystallization because recovery and recrystallization are proceeding together. Once recovery is complete, there is a linear relationship between the percentage of softening and percentage of recrystallization, as would be expected on statistical grounds. It is quite clear that misleading results will be obtained if the hardness is taken as a linear function of percentage of recrystallization. Activation energy plots were made at various degrees of recrystallization; the results are given in Table III. It will be seen that none of the values given in Table III are significantly different, resulting in an average value of 64,800±2000 cal per gram-atom. In previous work,[3] a figure of 56,000 cal per gram-atom was obtained for a slightly higher purity aluminum cold worked 20 pct.

Measurement of Growth Rate: Figs. 13 through 15 show the variation in maximum diameter of the largest unimpinged grain with annealing time for samples cold worked 20 pct, annealed directly after cold working, and annealed after two different recovery treatments. Similar curves were obtained for the minimum diameter. It is commonly supposed that the growth of new recrystallized grains is linear and then the rate of growth decreases because of impingement with other grains. It will be seen from Figs. 13 through 15 that the departure from linearity occurs at very small amounts of total recrystallization (≃ 3 pct) and it seems rather doubtful that at this level of recrystallization there will be impingement. It is interesting to note that all the curves extrapolate back to zero time, thus indicating that under the conditions investigated there is no incubation period. Prior recovery appears to have no significant effect on the rate of growth which is in agreement with the observations of Muller[13] and Kornfeld and Pavlov.[19] Similarly Reiter[16] found that strain aging of low carbon steel has no influence on the rate of growth G.

The growth rate measurements are summarized in Table IV.

Table III. Activation Energies for Recrystallization

Pct Recrystallization	Activation Energy, Cal per Gram-Atom
10	65,700±1600
30	63,500±2700
50	62,400±2700
80	64,100±2700
100	68,400±3200

Table IV. Measurements of Growth Rate G for Superpurity Aluminum Cold Worked 20 Pct

Annealing Temperature, °C	G_n, Long Direction, Cm per Sec	G_n, Short Direction, Cm per Sec
301	5.4×10^{-7}	2.7×10^{-7}
318	8.2×10^{-6}	4.1×10^{-6}
355	5.2×10^{-5}	2.6×10^{-5}
375	1.9×10^{-4}	1.0×10^{-4}

For a constant strain, the dependence of G upon temperature has been described by the relation

$$G = G_o e^{-Q_G/RT}. \qquad [2]$$

Fig. 16 shows log G as a function of $1/T$ from which a value of 55,400±8800 cal per gram-atom and 1.3×10^{13} cm per sec is obtained for Q_G and G_o, respectively. These values are in quite good agreement with the values of 55,000 cal per gram-atom and 1.5×10^{13} cm per sec obtained by Anderson and Mehl[3] for high purity aluminum (99.95 pct) strained 15 pct. Turnbull[14] has recently derived the following equation relating G_o, the constant in Eq. 2, with the jump distance of atoms in diffusion λ, the energy stored in the lattice by cold working ΔF, and the entropy of activation for grain boundary migration (ΔS_a).

$$G_o = e\,\lambda\left(\frac{kT}{h}\right)\left(\frac{\Delta F}{RT}\right)e^{(\Delta F_a/Q)/R} \qquad [3]$$

where k and h are Boltzmann and Planck's constants, respectively. Assuming that the driving force for recrystallization is of the same order of magnitude as the energy stored during cold working, the author will take for ΔF the value of 21.6 cal per gram-atom found by Kansaki[20] for 99.9 pct Al compressed 60 pct. This is a reasonable assumption,

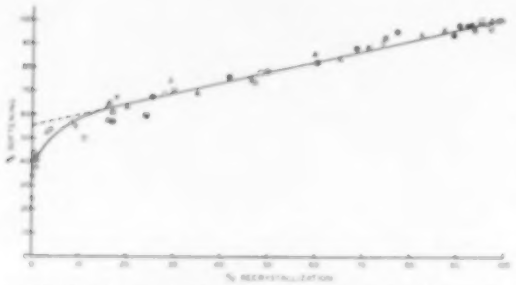

Fig. 12—Percentage of softening is shown as a function of the percentage of recrystallization for superpurity aluminum. Symbols represent: open triangles, cold rolled 20 pct and annealed at 318°C; open circles, cold rolled 20 pct and annealed at 355°C; encircled crosses, cold rolled 20 pct and annealed at 375°C, data taken from previous work; filled triangles, cold rolled 40 pct and annealed at 375°C, data taken from previous work; filled circles, cold rolled 60 pct and annealed at 350°C, data taken from previous work; squares, cold rolled 60 pct and annealed at 375°C, data taken from previous work; half-filled circles, cold rolled 20 pct and annealed at 375°C; and inverted open triangles, cold rolled 20 pct and annealed at 301°C.

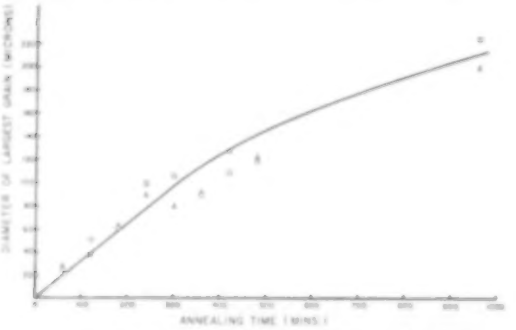

Fig. 13—Diameter of the largest grain (long direction) is shown as a function of annealing time at 301°C. Triangles represent specimen annealed directly after cold working and circles, specimen recovered 5 min at 318°C before annealing.

for the results of Borelius et al.[26] indicate that for aluminum most of the stored energy is released during recrystallization. Furthermore, $(\Delta S_s)_a$ is quite insensitive to changes in ΔF. The grain boundary thickness and diffusion distance λ is taken to be 2×10^{-8} cm. Using Eq. 3, then a value of 50.5 cal per degree per gram-atom is found for $(\Delta S_s)_a$. The free energy of activation for grain boundary migration $(\Delta F_s)_a$ can now be found using the equation

$$(\Delta F_s)_a = Q_a - T(\Delta S_s)_a - RT \qquad [4]$$

where Q_a is the measured activation energy for grain growth. Using this equation, then, a value of 23,200 cal per gram-atom is found for $(\Delta F_s)_a$ at 340°C. These values are in good agreement with those calculated from the results of Anderson and Mehl[5] and Kornfeld and Pavlov,[27] see Table V. For comparison, the activation energy Q_d, entropy of activation $(\Delta S_s)_d$, and free energy of activation $(\Delta F_s)_d$ for self-diffusion are also given in Table V. It is interesting to note that the values of $(\Delta F_s)_a$ are in very good agreement with one another and that $(\Delta F_s)_a$ is much smaller than the free energy of activation for self-diffusion within the grains. As pointed out by Turnbull,[24] the value for grain boundary self-diffusion would be a more appropriate figure for comparison.

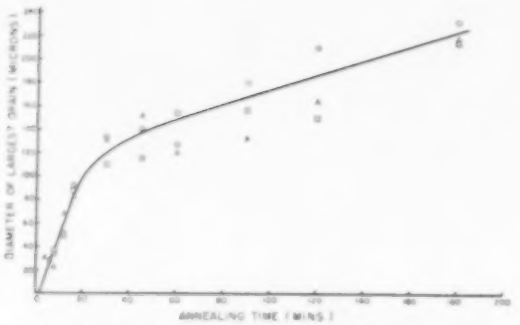

Fig. 14—Diameter of the largest grain (long direction) is shown as a function of annealing time at 318°C. Triangles represent specimen annealed directly after cold working; circles, specimen recovered 5 min at 318°C before annealing; and squares, recovered 2 hr at 244°C before annealing.

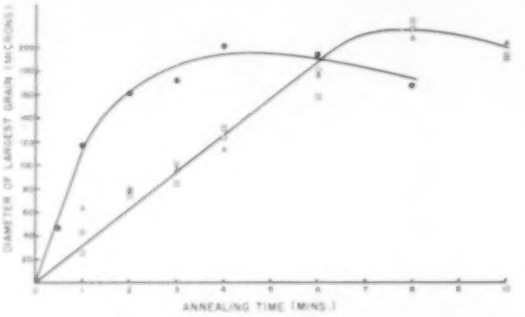

Fig. 15—Diameter of the largest grain (long direction) is shown as a function of annealing time. Filled circles represent specimen annealed at 373°C directly after cold working; triangles, specimen annealed at 355°C directly after cold working; open circles, specimen recovered 5 min at 318°C before annealing at 355°C; and squares, specimen recovered 2 hr at 244°C before annealing at 355°C.

Measurement of Planar Rate of Nucleation N: The measurement of N is a very difficult and time-consuming process for three dimensional recrystallization. However, Phillips and Phillips,[17] working with heavily cold worked copper, found that the ratio of the number of spherical grains per unit volume to the number of grains per unit area was almost constant for all the materials they investigated, which indicates that for a qualitative comparison it is sufficient to measure the planar rate of nucleation. The number of new grains per sq cm is shown as a function of the logarithm of the annealing time in Fig. 17 for material annealed directly after cold working and after two different recovery treatments. It is clear from Fig. 17 that prior recovery has had no significant effect on the number of grains per sq cm and therefore has no effect on the rate of nucleation. It is interesting to note the decrease in the number of grains which has occurred after long annealing times at 355° and 373°C. This, as can be seen micrographically, is because of primary grain growth within the recrystallized areas. With lower annealing temperatures such as 301° and 318°C, the rate of primary grain growth is not sufficient to give this decrease but is such that it counterbalances the rate of formation of new grains and so the number of grains remains almost constant. It is clear, therefore, that any theory which is used for the assessment of the as-recrystallized grain size must take the rate of primary grain growth into consideration

Table V. Comparison of Energy, Entropy, and Free Energy of Activation in Self-Diffusion and Grain Boundary Migration for Aluminum

Strain	Temperature Range, °C	G_0, Cm per Sec	ΔS_A Cal per Degree, Gram-Atom		Q, Kcal per Gram-Atom		ΔF_A, Kcal per Gram-Atom	
			$(\Delta S_A)_L$	$(\Delta S_A)_G$	Q_L	Q_G	$(\Delta F_A)_L$	$(\Delta F_A)_G$
4 pct[12]	425 to 540	4.5×10^{7}	—	22.2	—	34	30.5	17.2
5 pct[9]	310 to 370	1.5×10^{16}	9.2	60.7	37.5	59	32.0	21.8
20 pct cold reduction by rolling	310 to 375	1.3×10^{15}	—	50.5	—	55.4	32.0	23.2

as well as the rate of nucleation N and rate of growth G.

In order to determine the rate of nucleation, enlarged linear plots were made of the number of new grains per sq cm vs the annealing time. The slope of the resultant curve at any time period, divided by the fractional area of unrecrystallized matrix at the same time period, then gave the rate of nucleation N. Fig. 8 shows a typical linear plot of the number of new recrystallized grains as a function of annealing time for 318°C. In this graph the three points for each annealing time shown in Fig. 17 have been averaged. For all annealing temperatures the number of grains was, within the experimental error, a linear function of annealing time up to the time for about 30 pct recrystallization and extrapolated back to zero time. Thus these results confirm those of the grain growth measurements in that under the condition used there is no incubation period. The rate of nucleation N as a function of annealing time is shown in Figs. 19 and 20. N increases slightly with annealing time and then decreases sharply at about 10 pct recrystallization. From these curves it appears that recrystallization has started from the very first instance, which indicates that the germ nuclei or embryos are already present in the cold worked material. The shapes of the nucleation time curves are very different from those found by Anderson and Mehl[2] and Reiter[16] for the recrystallization of lightly strained aluminum and low carbon steel, respectively. Anderson and Mehl, however, did some work on heavily rolled aluminum (90 pct reduction) and concluded that the rate of nucleation N shows either a maximum at short annealing times or steadily decreases from the beginning. The only other work which has been done on heavily cold worked material using the micrographic technique is that of Phillips and Phillips[17] on copper. They found that the rate of nucleation decreased with time similar to that shown in Figs. 19 and 20. Unfortunately their measurements of N did not extend back to the early stages of recrystallization, the first point on their curve being at about 10 pct recrystallization. It is clear from Fig. 17 that prior recovery has exerted no influence on the rate of nucleation N.

Since the rate of nucleation N is a sensitive function of time it is difficult to know how to compare N at different temperatures. Other workers in this field have compared N at various temperatures for a constant percentage of recrystallization and have found that N can be expressed as a function of temperature by the equation

$$N = N_0 e^{-Q_N/RT}. \qquad [5]$$

Thus by plotting log N against the reciprocal of the absolute temperature Q_N can be determined. Fig 16 shows this plot for N at 5 pct recrystallization from which a value of 62,500±2800 cal per gram-atom is obtained for Q_N. This is slightly larger than the value of 53,500 cal per gram-atom found by Anderson and Mehl.[2] However, it will be seen that the activation energies for nucleation and growth, Q_N and Q_G, are not significantly different. Burke and Turnbull,[15] in their discussion of recrystallization, conclude that if $Q_N = Q_G$, the as-recrystallized grain size should be independent of temperature. This was found[1] to be the case for superpurity aluminum in the temperature range 350° to 400°C.

Kinetics of Recrystallization: A very full and complete discussion of the kinetics of recrystallization has been given by Burke and Turnbull[15] and there is no need to review these here. Johnson and Mehl[19] and Avrami[20] have presented equations based on the nucleation and growth hypothesis. Both theories lead to the following equation

$$\text{Ln}\frac{1}{1-x} = f\,G_x G_y G_z \int_o^t (t-\tau)^3 N d\tau \qquad [6]$$

where x is the fraction recrystallized in time t, $G_x G_y G_z$ are the rates of growth in x, y, and z directions, τ is the nucleation period, and N is the rate of nucleation.

The Johnson and Mehl and Avrami treatments differ only in their assumptions as to how N varies with time. Johnson and Mehl say that this must be

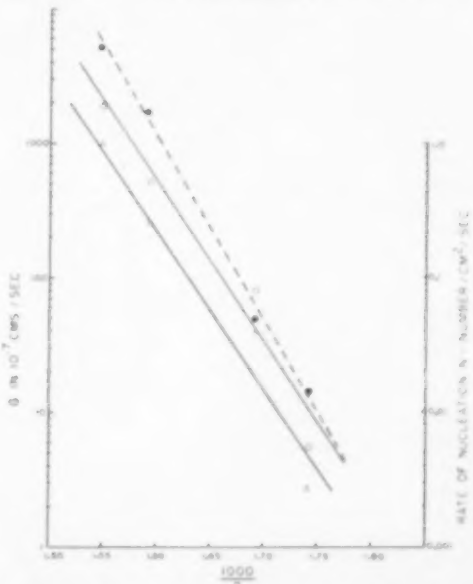

Fig. 16—Log G and log N are shown as a function of $1/T$ in recrystallization of superpurity aluminum cold worked 20 pct. Symbols represent: filled circles and dotted line, rate of nucleation N; open circles, G, long direction; and triangles, G, short direction.

determined by experiment and is shown by Stanley and Mehl[10] to be of the form $N = ae^{bt}$. Clearly this equation cannot represent the author's results where the rate of nucleation is almost constant with time and then decreases sharply at about 10 pct recrystallization.

Avrami, on the other hand, says that there are pre-existing in the unrecrystallized matrix a certain number of preferred nucleation sites which, for example, might be suitably oriented subgrains or regions of high strain. During recrystallization, these sites are used up by becoming active growth nuclei and through being consumed by growth of new recrystallized grains. Let the number of germ nuclei per unit volume be $\bar{N}$. As stated previously, these germ nuclei become used up in two ways. Some of these will become growth nuclei whose number will be N' and others N'' will be consumed by the growing recrystallized grains. Avrami points out that if the probability of formation of growth nuclei per germ nucleus per unit time is large so that almost all of the germ nuclei start growing before any are consumed by the growing grains, then the rate of nucleation N is given by

$$N = \bar{N}e^{-nt} \qquad [7]$$

where n is the probability of formation of growth nuclei. Avrami then goes on to show that the number of growth nuclei N' at any time t is given by

$$N' = \bar{N}\,(1\text{-}e^{-nt}) \qquad [8]$$

which for small values of t gives

$$N' = \bar{N}nt. \qquad [9]$$

Thus in the early stages of recrystallization, the number of new grains will be linear with t and then decrease rapidly. This theory seems to fit the author's results very well; see Fig. 18.

Avrami now substitutes Eq. 7 in Eq. 6 and assumes $G_x = G_y = G$, and arrives at the following general equation for the kinetics of recrystallization

$$x = 1\text{-}e^{-Bt^k}. \qquad [10]$$

He then shows that, for polyhedral growth, k lies between 3 and 4 depending upon whether n is large or small, respectively. If the new grains are plate-like, then k lies between 2 and 3 and if growth is one dimensional, k lies between 1 and 2 for n large or small, respectively. To determine the constants in Eq. 10 loglog $1/(1\text{-}x)$ was plotted against log t; see Fig. 21. Quite good straight lines are obtained considering that at low and high values of x a small

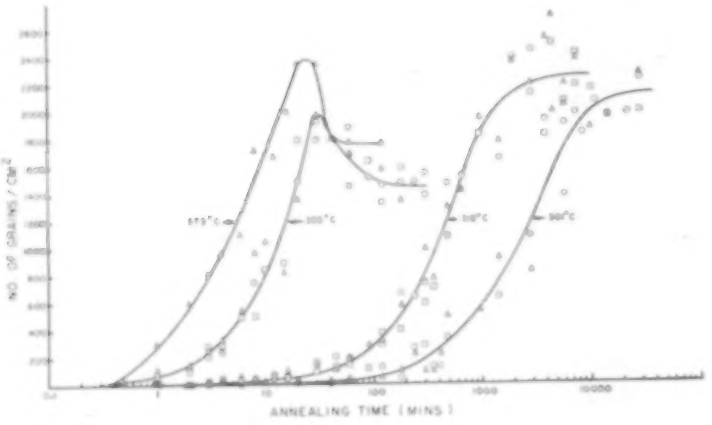

Fig. 17—Number of new recrystallized grains is shown as a function of annealing time for superpurity aluminum cold worked 20 pct. Triangles represent specimen annealed directly after cold working; squares, specimen recovered 2 hr at 244°C before annealing; and circles, specimen recovered 5 min at 318°C before annealing.

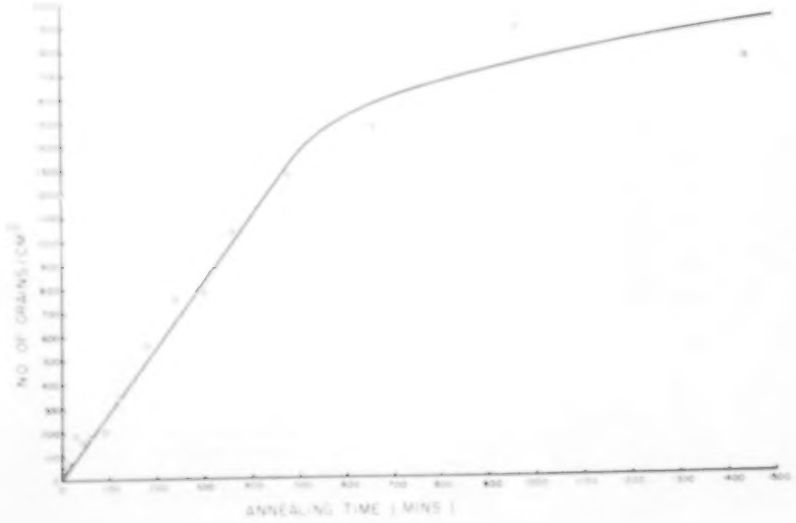

Fig. 18—Number of new recrystallized grains is shown as a function of annealing time for superpurity aluminum cold worked 20 pct and annealed at 318°C.

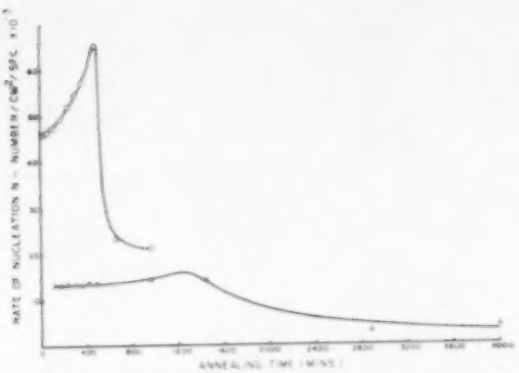

Fig. 19—Rate of nucleation is plotted as a function of annealing time at 301° and 318°C.

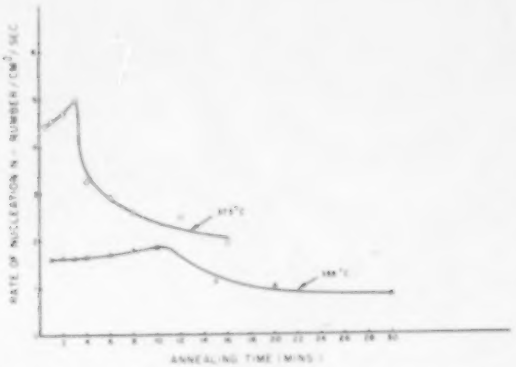

Fig. 20—Rate of nucleation is plotted as a function of annealing time at 355° and 373°C.

error in x will give a very large error in the function loglog $1/(1-x)$. The slopes of these lines are almost the same, giving values of k lying between 1.40 and 1.43. Using these values of k and also values of B derived from Fig. 21, the percentage of recrystallization was calculated and is shown plotted in Fig. 22 together with the experimental points. The agreement between the experimental and calculated values is very good up to about 80 pct recrystallization, this corresponding to the departure from linearity in Fig. 21.

Two alternative theories for the kinetics of recrystallization which are both independent of N and G have been proposed by Krupkowski and Balicki[10] and Cook and Richards.[9] Both theories lead to equations of the same kind as Avrami's with $k = 1$ and $k = 2$. Clearly neither of these can be applied to the author's results. Thorley,[11] using the same hypothesis as Cook and Richards but without making any assumptions, has given the following equation

$$\text{Ln}\frac{1}{1-x} = A\left[t + \frac{1}{\beta}(e^{-\beta t}-1)\right] \qquad [11]$$

where A and β are constants. The variations of A and β with temperature is given by $\beta = be^{-P/RT}$ and $A = ae^{-Q/RT}$ where P and Q are the activation energies for the first and second stages of the recrystallization. Thorley considers that the first stage is recovery. If t is large, $e^{-\beta t} = 0$ and Eq. 11 becomes

$$\text{Ln}\frac{1}{1-x} = A(t-t_o) \qquad [12]$$

where $t_o = \frac{1}{\beta}$. A and β were determined by plotting log $1/(1-x)$ against t, a typical plot being shown in Fig. 23. Using these values of A and β the percentage of recrystallization was calculated and is shown plotted together with the experimental points in Fig. 24. As in previous work,[1] the agreement between the calculated and experimental points is very good except for a slight discrepancy towards the end of the recrystallization process.

Log A and log t_o were plotted against the reciprocal of the absolute temperature and values of 64,800±400 and 63,600±2900 cal per gram-atom were obtained for P and Q, respectively. For comparison, Table VI gives a summary of the activation energies determined during this investigation.

It will be seen from Table VI that the activation energy for recovery P, determined from Thorley's equation, does not agree with the activation energy of any of the recovery processes studied. Varley[12] claims to have shown that, for commercial purity aluminum cold worked 75 pct, the activation energy for recovery and recrystallization are the same. This does not invalidate the author's results because in an earlier paper[1] it has been shown that superpurity aluminum cold worked 80 pct gives an activation energy for recrystallization of about 36,000 cal per gram-atom, which is not too dissimilar from the activation energy for the recovery of hardness; see Table I. Thus the activation energies for recovery and recrystallization will be similar for high amounts of cold work but very different at low amounts.

It is interesting to note that P has a value similar to that for nucleation. A similar correspondence was found by Phillips and Phillips[13] for copper. Although Thorley's equation can be fitted to the results, the theoretical basis on which it is derived breaks down on three counts: 1—the equation describing recovery as a first order rate process does not fit the author's recovery results, 2—the so-called activation energy for recovery P is in wide disagreement with the determined activation energies for recovery, and 3—prior recovery has no influence on the recrystallization process.

Table VI. Activation Energies for Recovery and Recrystallization of Superpurity Aluminum Cold Worked 20 Pct

Property Measured	Activation Energy, Cal per Gram-Atom
Electrical Resistance—recovery	7,700±100
X-ray line breadth—recovery	22,400±2000
Hardness—recovery	31,800±2600
Recrystallization	64,800±2600
Rate of growth G	55,400±8800
Rate of nucleation N	62,500±2800
P, Thorley's recovery	64,800±400
Q, Thorley's recrystallization	63,600±2900

Discussion of Results

The results of this work have shown that recovery and recrystallization are two distinct processes, although the two may overlap each other to a certain extent.

For discussing the recovery process it will be convenient to take the X-ray line broadening results first. First, it can be safely assumed that the broadening observed throughout this work due to strain for particle sizes greater than 1 micron will not be effective in this respect. Hall and Williamson[14, 15] have investigated the shapes and intensities of

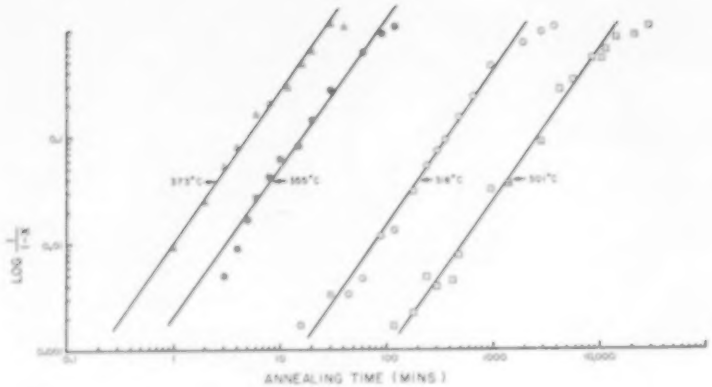

Fig. 21—Loglog $1/(1-x)$ is plotted against log t.

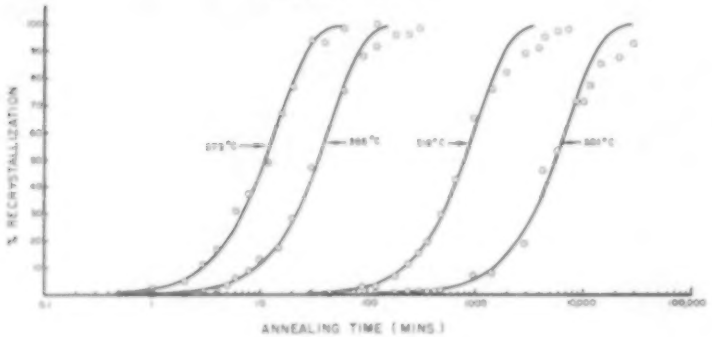

Fig. 22—Theoretical isothermal annealing curves are derived from Avrami's equation: $x = 1 - e^{-\alpha t^k}$.

X-ray reflections from cold worked aluminum and concluded that line breadth is determined by long range strains and hence by the distribution of dislocations, whereas the increase in background and decrease in line intensity is determined by the volume of metal containing intense local strains and hence by the density of dislocations. Their results also showed that on recovery the line breadth changed before the background intensity did, thus indicating that a redistribution of dislocations occurs before annihilation. The results reported here agree with this conception, for the hardness, which would be expected to be a function of both the distribution, density of dislocations, and subgrain size, took a longer time to recover than line breadth. The work of Harper[7] indicates that the density of dislocations reaches a saturation value at relatively low amounts of cold work and so for 20 and 80 pct cold reduction used here the dislocation density would be similar. The fact that the activation energy for recovery of line breadth and the value of the recovered line breadth were both independent of the amount of cold work thus supports the contention that line breadth is reduced by a redistribution of dislocations. The microstructures after recovery can also be explained on this basis, for after recovery there is much greater contrast between subgrains and, furthermore, the subgrain boundaries appear darker (i.e., preferentially attacked) than the interior of the subgrains. This is what would be expected if dislocations diffused and became locked in the subgrain boundaries.

The hardness of cold worked material after recovery will depend upon the density of dislocations and the subgrain size. Thus after recovery the hardness should increase with the amount of previous cold work because of the finer subgrain size and should decrease with increasing annealing because of increasing subgrain size. It should be noted that, although the line breadth is recovered before the hardness, considerable softening has occurred by the time that the line breadth has fully recovered, thus indicating that the major part of the softening is due to redistribution of dislocations.

The observation that the contrast between subgrains is much greater after recovery than directly after cold working suggests that the orientation difference between adjacent subgrains increases during recovery as would be expected if dislocations became locked in the subgrain boundaries. Furthermore, the present work suggests that the orientation difference between subgrains directly after cold working is smaller for 20 pct than 80 pct cold work. Recent work on polygonization[8] indicates that low angle boundaries with an orientation difference between adjacent grains of less than 1° are very mobile. This mobility decreases with increasing orientation difference until with an orientation difference of about 10° the mobility increases with further increase in orientation difference. It is therefore possible that with 20 pct cold work the mobility of the subgrain boundaries directly after cold working is greater than with 80 pct cold work. This explains the larger subgrain size with 20 pct than with 80 pct after annealing. After annealing, however, the orientation difference increases, thus reducing the mobility of the subgrain boundaries and thereby explaining the stability of subgrain size on further annealing.

The increase in electrical resistivity which is brought about by cold working has been described in terms of dislocation and vacancies. The relative effects of these two factors are far from clear at the present time. However, the present work shows that 30 pct of the electrical resistance is recovered very

much more quickly than line breadth and hardness, both of which involve the diffusion of dislocations. For example, at 100°C the electrical resistivity is fully recovered in 12 min, while the line breadth takes 120,000 min. This suggests that the part of the electrical resistance which is recovered during low temperature annealing is due to vacancies or vacancy pairs either forming into aggregates during annealing, which are sufficiently large to produce less scattering than single vacancies, or by diffusing and becoming trapped at high angle grain boundaries.

These results strongly indicate that after recovery most of the strain energy produced by cold working still remains. This agrees with the findings of Borelius et al.[10] that only a small fraction (≏4 pct) of the stored energy is released during recovery. The residual stored energy left after recovery is the driving force for recrystallization.

The recrystallization results agree very well with Avrami's theory[20] except that the determined value of 1.4 for k is lower than would be expected. This figure however agrees with previous work[1] where values of k varying between 1.1 and 1.6 were obtained for superpurity aluminum and superpurity base Al-Mg alloys cold worked 20 to 60 pct. Laurent and Batisse[20] have analyzed the results of other workers on the basis of Avrami's theory and finds that for a wide variety of conditions k for aluminum lies between 1 and 1.7. The only exception seems to be the value of 4.5 to 7.5 found by Anderson and Mehl[2] for lightly strained aluminum. There is, however, an inconsistency between Anderson and Mehl's results using the micrographic technique and those of Laurent and Batisse using hardness measurements. Both groups of workers used low tensile strains; yet the former found k between 4.5 to 7.5 and the latter, 1.65 to 2. Apart from these inconsistencies, it is clear from the survey of Laurent and Batisse and the present results that for rolled material k lies between 1 and 1.7. On the basis of Avrami's theory, a value of between 2 and 3 would be expected for recrystallization in sheet. It was mentioned earlier that the rate of growth started to decrease at very small amounts of recrystallization (≏ 3 pct). This decrease in G together with the fact that the rate of nucleation N decreases with time could explain these low values of k. In contrast to some earlier investigations on this subject, no incubation period was observed in this work. A possible reason for this is the much more sensitive metallographic techniques used in the present work.

The question as to what constitutes the driving force for recrystallization has recently been the subject of controversy. The present results indicate that the driving force is strain energy, most of which is concentrated at the subgrain boundaries because: 1—the recovered values of electrical resistivity, line breadth, and hardness are much greater than the fully annealed values and 2—measurements of the rate of nucleation indicate that the germ nuclei are already present in the cold worked material. This is also indicated by the fact that Avrami's equation, which is based on this postulate, fits the results. Measurements on the isothermal release of stored energy made by Borelius et al.[10] also support this contention. All the measurements which have been made so far on the release of stored energy have shown that a large part of the stored energy is released during recrystallization. The only exception is Suzuki's[20] work on copper which showed that all the energy was released during recovery. The only

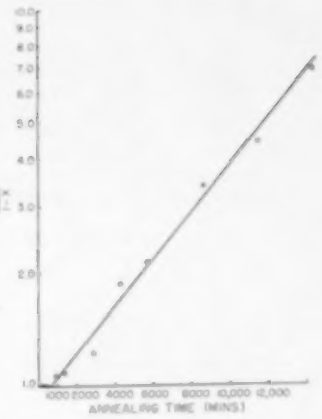

Fig. 23—Log 1/(1-x) is plotted as a function of t for superpurity aluminum cold worked 20 pct and annealed at 301°C.

work on the release of stored energy in aluminum is that of Kanzaki.[10] It would appear from Kanzaki's curves that the major part of the stored energy is released during recrystallization.

The present results suggest that the germ nuclei are present in the cold worked metal. It is not possible to say what these are; they may be certain subgrains which are suitably oriented to become growth nuclei or certain regions of high lattice curvature. As discussed previously,[1] the latter seems more likely. The fact that there is no effect of prior recovery suggests that if subgrains are germ nuclei, perfection of these subgrains is not necessary for them to become growth nuclei.

Discussion of this paper, if any, will appear in JOURNAL OF METALS, May 1956, and in AIME Metals Branch *Transactions*, Vol. **206**, 1956.

References

[1] E. C. W. Perryman: *Trans.* AIME (1955) **203**, p. 369; JOURNAL OF METALS (February 1955).

[2] W. A. Anderson and R. F. Mehl: *Trans.* AIME (1945) **161**, p. 140; METALS TECHNOLOGY (February 1945).

[3] F. Seitz: *Advances in Physics* (1952) **1**, p. 43.

[4] E. C. W. Perryman: *Acta Metallurgica* (1954) **2**, p. 26.

[5] M. O. Kornfeld: *Physik Ztsch. Sowjetunion* (1934) **6**, p. 329.

[6] C. S. Barrett: *Structure of Metals*, (1943) p. 376. New York. McGraw-Hill Book Co. Inc.

[7] A. H. Lutts and P. A. Beck: *Trans.* AIME (1954) **200**, p. 257; JOURNAL OF METALS (February 1954).

[8] M. Cook and T. L. E. Richards: *Journal* Inst. of Metals (1947) **73**, p. 1.

[9] A. H. Cottrell and V. Aytekin: *Journal* Inst. of Metals (1950) **77**, p. 389.

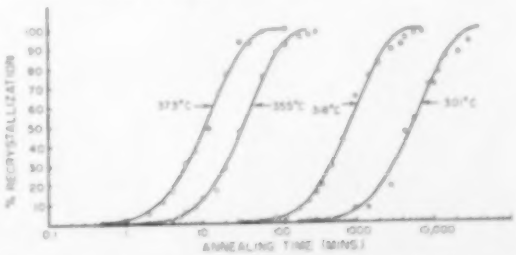

Fig. 24—Theoretical isothermal annealing curves are derived from Thorley's equation: $\text{Ln}\,\frac{1}{1-x} = A\left[t + \frac{1}{\beta}\left(e^{-\beta t} - 1\right)\right]$.

[9] W. Betteridge: *Journal* Inst. of Metals (1953-1954) **82**, p. 149.
[10] H. G. Muller: *Ztsch. für Physik* (1930) **60**, p. 464.
[11] M. Kornfeld and W. Pavlov: *Physik Ztsch. Sowjetunion* (1934) **6**, p. 537; (1937) **12**, p. 658.
[12] S. F. Reiter: *Trans.* AIME (1952) **194**, p. 972; JOURNAL OF METALS (September 1952).
[13] D. Turnbull: *Trans.* AIME (1951) **191**, p. 661; JOURNAL OF METALS (August 1951).
[14] H. Kanzaki: *Journal* Physical Soc., Japan (1951) **6**, p. 90.
[15] G. Borelius, S. Berglund, and S. Sjoberg: *Arkiv für Fysik* (1953) **6**, p. 143.
[16] V. A. Phillips and A. Phillips: *Journal* Inst. of Metals (1952-1953) **81**, p. 185.
[17] J. E. Burke and D. Turnbull: *Progress in Metal Physics* (1951) **3**, p. 220.
[18] W. A. Johnson and R. F. Mehl: *Trans.* AIME (1939) **135**, p. 416; METALS TECHNOLOGY (August 1939).
[19] M. Avrami: *Journal of Chemical Physics* (1939) **7**, p. 1103; (1940) **8**, p. 212; (1941) **9**, p. 177.
[20] J. K. Stanley and R. F. Mehl: *Trans.* AIME (1942) **150**, p. 260; METALS TECHNOLOGY (February 1942).
[21] A. Krupkowski and M. Balicki: *Annalen Akademie Sic. Tech. Varsovie* (1937) **4**, p. 270.
[22] N. Thorley: *Journal* Inst. of Metals (1950) **77**, p. 141.
[23] P. C. Varley: *Journal* Inst. of Metals (1948-1949) **75**, p. 185.
[24] W. H. Hall and G. K. Williamson: *Proceedings* Physical Soc. B (1951) **64**, p. 937.
[25] G. K. Williamson and W. H. Hall: *Acta Metallurgica* (1953) **1**, p. 22.
[26] S. Harper: *Physical Review* (1951) **83**, p. 709.
[27] A. H. Cottrell: *Dislocation and Plastic Flow in Crystals.* (1953) Oxford. Oxford University Press.
[28] P. Laurent and N. Batisse. *Révue de Metallurgie* (1952) **49**, pp. 485, 593.
[29] T. Suzuki: *Science Reports of the Research Inst.* Tôhoku University, Japan (1949) **1**, p. 193.

Technical Note

On the Casting, Rolling, and Annealing Textures of Chromium

by W. H. Smith

IN the course of an investigation on chromium containing minor amounts of alloying elements, the information herein has been obtained on the crystallographic orientations resulting from arc melting, rolling, and annealing.

The chromium used in this investigation was electrolytic flake obtained from the Electro Metallurgical Co. This material was heated for 20 hr at 1600°C in hydrogen with a dew point of about −100°C. The oxygen and nitrogen content of the chromium after this treatment was 0.0003 pct O and 0.005 pct N.

Five pounds of this chromium were arc melted in a water-cooled copper crucible. After arc melting, the oxygen and nitrogen contents were 0.002 and 0.025 pct, respectively. A section of this ingot is shown in Fig. 1. By means of a back-reflection Laue technique, the crystal habit of the cast ingot was determined. As expected, it was found that the [100] was approximately the axis of the columnar grains. In this respect, chromium behaves like other body-centered-cubic metals in that a cubic axis is normal to the cold surface of the mold.

W. H. SMITH is associated with Alloy Studies Research, Research Laboratory, General Electric Co., Schenectady.
TN 272E. Manuscript, Oct. 25, 1954.

A slab cut from this ingot was rolled at 600°C as follows: four 30 pct reductions were made with intermediate anneals at 1200°C for 15 min. Rolling was done with the [100] of the columnar grains in the rolling direction. Following the final anneal, an 80 pct reduction was taken at 600°C. The final sheet thickness was ten mils. By polishing and etching, the thickness was reduced to four mils and the grain orientation determined by the transmission Laue method using molybdenum radiation with a zirconium filter. Fig. 2 is the (110) pole figure for this material with the ideal (100)[011] and (111)[11$\bar{2}$] orientations indicated. The orientation is typical of most cold rolled body-centered-cubic metals having the [110] of the grains approximately in the rolling direction and the (100) planes approximately in the plane of the rolled sheet. There is also evidence of some (110)[112] orientation.

The grain orientation of sheet rolled 40 and 80 pct in the same direction as before at 600°C followed by recrystallization at 1200°C for 15 min was determined by a back-reflection Laue technique. A random texture was found in both cases. This 1200°C 15 min anneal was found to give complete recrystallization and some grain growth.

Fig. 1 — Section through arc-melted chromium ingot is shown.

Fig. 2—(110) pole figure is for chromium reduced 80 pct at 600°C. Ideal orientations are indicated as follows: square, (100) [011] and triangle, (111) [112].

Appreciation is gratefully acknowledged to the following organizations whose support has helped to make possible AIME's extensive publications program of metallurgical research:

Allis-Chalmers Mfg. Co.
Aluminum Co. of America
American Brake Shoe Co.
American Iron & Steel Institute
American Metal Co. Ltd.
American Smelting & Refining Co.
American Zinc, Lead & Smelting Co.
Anaconda Co.
Bridgeport Brass Co.
Bunker Hill & Sullivan Mining & Concentrating Co.
Calumet & Hecla, Inc.
Cerro de Pasco Corp.
Clevite Corp.
Climax Molybdenum Co.
Consolidated Coppermines Corp.
Consolidated Mining & Smelting Co. of Canada Ltd.
Copper Range Co.
Crane Co.
Cyprus Mines Corp.
Dow Chemical Co.
Wilbur B. Driver Co.
Electro Metallurgical Co., div. of Union Carbide & Carbon Corp.
Engineering Foundation
Ford Motor Co.
Freeport Sulphur Co.
General Electric Co.
General Motors Corp.
Howe Sound Co.
Hudson Bay Mining & Smelting Co. Ltd.
International Nickel Co., Inc.
Kennecott Copper Corp.
Magma Copper Co.
Mallory-Sharon Titanium Corp.
Miami Copper Co.
Molybdenum Corp. of America
National Lead Co.
New Jersey Zinc Co.
Newmont Mining Corp.
Noranda Mines, Ltd.
Phelps Dodge Corp.
Raytheon Mfg. Co.
Rem-Cru Titanium Inc.
Revere Copper & Brass Inc.
St. Joseph Lead Co.
Texas Gulf Sulphur Co.
Titanium Metals Corp. of America
U. S. Smelting, Refining & Mining Co.
Vanadium Corp. of America